Measurement of Muon Neutrino Disappearance with Non-Fiducial Interactions in the NOνA Experiment

A THESIS
SUBMITTED TO THE FACULTY OF THE GRADUATE SCHOOL
OF THE UNIVERSITY OF MINNESOTA
BY

Nicholas Jacob Raddatz

IN PARTIAL FULFILLMENT OF THE REQUIREMENTS
FOR THE DEGREE OF
DOCTOR OF PHILOSOPHY

Professor Daniel P. Cronin-Hennessy

April, 2016

Acknowledgements

I would like to thank the NOνA collaboration for the data and the hard work and advice of many collaborators both of which where necessary for this thesis to exist. I would also like to thank my advisor, Daniel Cronin-Hennessy, for his guidance and support in my completion of this degree. To my fellow students, Susan, Dominick, Kanika, and Jan, thank you for providing simple distractions from work, igniting thought provoking discussions, and all of the innumerable things in-between. I would not have wanted to make this journey with anyone else. Finally I would like to thank my family for everything they have done for me. In particular my parents for showing me unconditional love and support in this pursuit, my wife for always believing in me, and my son for showing me the true meaning of happiness.

Dedication

[redacted]

Abstract

The NuMI[1] Off-Axis ν_e Appearance (NOνA) experiment is a long baseline neutrino oscillation experiment. The experiment measures the oscillations of a primarily muon neutrino beam using two functionally identical liquid scintillator tracking calorimeters detectors placed 810 km apart and 14 milliradians off-axis to the NuMI beam. The oscillation parameters $\sin^2\theta_{23}$ and $\left|\Delta m^2_{32}\right|$ are measured from the disappearance of muon neutrinos as they propagate between the two detectors using the first data collected in 2014 and 2015. The primary NOνA analysis uses charged current events only in the fiducial volume of the far detector. This analysis also includes a non-fiducial sample of interactions that originate in the fiducial volume of the far detector but escape the detector. This analysis measures the oscillation parameters as $\sin^2\theta_{23} = 0.31$-0.71 and $\left|\Delta m^2_{32}\right| = 2.15$-$2.91\times10^{-3}$ eV^2 at 90% confidence limits.

[1] Neutrinos at the Main Injector

Contents

Acknowledgements i

Dedication ii

Abstract iii

List of Tables ix

List of Figures x

1 Introduction 1

2 Physics of Neutrinos 3

2.1 The Standard Model 3

2.2 Brief History of Neutrino Physics 5

2.3 Neutrino Flavor Oscillations 7

2.4 Matter Effects and the Mass Hierarchy 9

2.5 Current Knowledge of Neutrino Oscillations 11

2.6 Theoretical Interest 13

3 The NOνA Experiment 15

3.1 NOνA Experiment 15

3.2 NuMI Beam 15

3.2.1 Run Periods Used 16

3.3 NOνA Detectors 17

3.3.1 Detector Design 17

3.3.2 Data Acquisition . . . 20
3.3.3 The Near Detector . . . 21
3.3.4 The Far Detector . . . 25
3.3.5 Off-Axis Detector Placement . . . 29
3.4 Neutrino Interactions in NOνA . . . 33
3.5 NOνA Oscillation Measurements . . . 34

4 Simulation **36**
4.1 Introduction . . . 36
4.2 Beam . . . 36
4.3 Neutrino Interactions . . . 37
4.4 Cosmic Rays . . . 38
4.5 Particle Propagation . . . 38
4.6 Detector Response . . . 38
4.6.1 Simulation Tuning . . . 40

5 Event Reconstruction and Calibration **43**
5.1 Slicing . . . 43
5.2 Tracking . . . 47
5.2.1 Kalman Filters . . . 47
5.2.2 Kalman Filter Tracking . . . 48
5.2.3 Performance . . . 54
5.3 Calibration . . . 65

6 ν_μ CC Selection **71**
6.1 Features of Signal and Background . . . 71
6.1.1 Muon Identification Variables . . . 78
6.2 Multivariate Analysis . . . 85
6.2.1 k-Nearest Neighbour Classifier . . . 85
6.2.2 Training . . . 86
6.3 Performance . . . 91

7 Energy Estimation and Event Separation **96**
7.1 Energy Estimation . . . 96
7.2 Event Separation . . . 102
7.2.1 Features of ν_μ CC QE Events and Backgrounds . . . 102
7.2.2 QE Variables . . . 107
7.2.3 Multivariate Analysis . . . 109
7.2.4 Performance . . . 116

8 Cosmic Rejection **122**
8.1 Contained Population . . . 123
8.2 Escaping Population . . . 151

9 Event Selection **168**
9.1 Data Quality . . . 168
9.2 Near Detector Selection . . . 171
9.2.1 Data-Simulation Comparisons . . . 171
9.3 Far Detector Selection . . . 198
9.3.1 Cosmic Background Subtraction . . . 198

10 Far Detector Prediction **202**

11 Systematics **213**
11.1 Beam . . . 213
11.2 Neutrino Interactions . . . 218
11.2.1 Large GENIE uncertainties . . . 218
11.2.2 Small GENIE uncertainties . . . 226
11.3 Detector Mass . . . 229
11.3.1 Absolute Normalization . . . 229
11.3.2 Relative Normalization . . . 229
11.3.3 Muon Energy Scale . . . 229
11.4 POT Accounting . . . 232
11.5 Calibration . . . 232
11.5.1 Absolute Energy Scale . . . 232

11.5.2 Uniform Simulation Calibration . . . 235
11.5.3 Thresholds . . . 235
11.6 Alignment . . . 235
11.7 Bad Channels . . . 236
11.8 Hadronic Modeling . . . 236
11.8.1 GEANT4 Particle Propagation . . . 236
11.8.2 Birks' Law . . . 237
11.8.3 Number of Hadronic Hits . . . 238
11.9 Total Systematics . . . 244

12 Results **248**
12.1 Far Detector Events . . . 249
12.2 Oscillation Parameter Measurement . . . 278
12.2.1 Statistical Error Only Result . . . 280
12.2.2 Systematic Error Result . . . 280
12.2.3 Feldman-Cousins Anaylsis . . . 284
12.2.4 Comparison to MINOS and T2K . . . 284

13 Conclusion **286**

References **288**

Appendix A. Extrapolation **294**
A.1 Near Detector Non-QE sample . . . 294
A.1.1 $\nu_\mu \rightarrow \nu_\mu$ Channel . . . 294
A.1.2 $\bar{\nu}_\mu \rightarrow \bar{\nu}_\mu$ Channel . . . 298
A.1.3 NC $\rightarrow$ NC Channel . . . 302
A.2 Near Detector QE sample . . . 302
A.2.1 $\nu_\mu \rightarrow \nu_\mu$ Channel . . . 302
A.2.2 $\bar{\nu}_\mu \rightarrow \bar{\nu}_\mu$ Channel . . . 307
A.2.3 NC $\rightarrow$ NC Channel . . . 311

Appendix B. Systematics **313**
B.1 Beam . . . 313

B.2 Large GENIE uncertainties 317
B.2.1 Small GENIE uncertainties 336
B.3 Normalization 340
B.4 Absolute Energy Scale 347
B.5 Hadronic Hit 354

Appendix C. Hadronic Model Systematic Simulation 361

List of Tables

2.1 Best fit values of oscillation parameters. No measurements of δ with greater than 3σ significance currently exist. [1]. 13

3.1 Summary of recorded beam data at the far detector. 17

12.1 Predicted event count in the far detector under the oscillation parameters listed in table 2.1, Osc., and with no oscillations, No Osc. 248

12.2 Selected events in the QE sample in the far detector. 249

12.3 Selected events in the NonQE sample in the far detector. 250

12.4 Selected events in the escaping sample in the far detector. 251

12.5 Best fit values of each systematic error from the marginalization fitting procedure in units of σ deviations defined for each systematic error. . . 282

List of Figures

2.1 Elementary particles in the standard model. Coloring (blue, red, green) corresponds to type of particle (quark, lepton, boson). 4
2.2 Feynman diagrams of neutrino interactions 5
2.3 Possible mass ordering of neutrinos. Left: Normal mass hierarchy. Right: Inverted mass hierarchy. The vertical axis represents increasing mass and the color represents flavor content of each mass state, note that the color coding is not to scale. 10
2.4 Feynman diagrams of neutrino forward elastic scattering with normal matter. Time is in the vertical direction 11
3.1 NuMI beam [2]. 16
3.2 Fiber emission spectra and quantum efficiencies of APDs and PMTs[3]. 18
3.3 APD[4] 19
3.4 The NOνA detectors. 20
3.5 DAQ schematic. 22
3.6 NOνA near detector. 23
3.7 NOνA far detector 27
3.8 Hit efficiency in the far detector. Differences between horizontal and vertical modules arise from voids of scintillator in the horizontal modules. 28
3.9 Neutrino energy as a function of parent pion energy for various off-axis locations. 30
3.10 Unoscillated neutrino energy spectrum of CC events in the far detector. 30
3.11 Oscillated neutrino energy spectrum of CC events in the far detector. . 31
3.12 NOνA detector placement relative to NuMI beam 32
3.13 Neutrino cross section as a function of energy[5]. 33

4.1 Template function of collection rate of scintillation photons. 39
4.2 Comparison of detector response to cosmic ray muons between data and simulation in the far detector. The discrepancy between data and simulation at high photo-electrons results from the gain being set on each cell individually in the detector while the simulation models that gain as a single value across all cells. 41
4.3 Comparison of detector response to cosmic ray muons between data and simulation in the near detector. The discrepancy between data and simulation at high photo-electrons results from the gain being set on each cell individually in the detector while the simulation models that gain as a single value across all cells. 42
5.1 Typical trigger window in simulated near detector data. Slices are indicated by color with hits from the same slice being drawn in the same color. 45
5.2 Typical trigger window in simulated far detector cosmic data. Slices are indicated by color with hits from the same slice being drawn in the same color. 46
5.3 Typical muon multiple scattered track. Blue dashed line shows the true trajectory of a muon from a simulated ν_μ CC interaction in the far detector. 50
5.4 Muon track with a hard scatter. Blue dashed line shows the true trajectory of a muon from a simulated ν_μ CC interaction in the far detector. Hard scattering occurs near z position of 5300 cm in the x-z detector view. 51
5.5 Typical muon multiple scattered track an charged pion track with a hard scatter. Blue dashed line shows the true trajectory of a muon and the magenta dashed line shows the true trajectory of a charged pion. Both particles come from a simulated ν_μ CC interaction in the far detector. . 52
5.6 Reconstructed tracks in a typical trigger window in simulated near detector data. Tracks are indicated by color with hits from the same slice being drawn in the same color. The track fitted trajectory is drawn as a dashed line. 55

5.7 Reconstructed tracks in a typical trigger window in simulated far detector data. Tracks are indicated by color with hits from the same slice being drawn in the same color. The track fitted trajectory is drawn as a dashed line. 56
5.8 Reconstructed tracks in a typical trigger window in simulated far detector data. Tracks are indicated by color with hits from the same slice being drawn in the same color. The track fitted trajectory is drawn as a dashed line. 57
5.9 Muon track completeness as a function of the initial muon momentum in far detector simulated ν_μ CC interactions. 58
5.10 Muon track completeness as a function of the initial muon momentum in different interaction types in far detector simulated ν_μ CC interactions. 58
5.11 Muon track completeness as a function of the initial position of the muon in far detector simulated ν_μ CC interactions. 59
5.12 Muon track purity as a function of the initial muon momentum in far detector simulated ν_μ CC interactions. 59
5.13 Muon track purity as a function of the initial muon momentum in different interaction types in far detector simulated ν_μ CC interactions. 60
5.14 Muon track purity as a function of the initial position of the muon in far detector simulated ν_μ CC interactions. 60
5.15 Muon track completeness as a function of the initial muon momentum in near detector simulated ν_μ CC interactions. 61
5.16 Muon track completeness as a function of the initial muon momentum in different interaction types in near detector simulated ν_μ CC interactions. 61
5.17 Muon track completeness as a function of the initial position of the muon in near detector simulated ν_μ CC interactions. 62
5.18 Muon track purity as a function of the initial muon momentum in near detector simulated ν_μ CC interactions. 62
5.19 Muon track purity as a function of the initial muon momentum in different interaction types in near detector simulated ν_μ CC interactions. 63
5.20 Muon track purity as a function of the initial position of the muon in near detector simulated ν_μ CC interactions. 63

5.21 Resolution of reconstructed track length of muons in far detector simulated ν_μ CC interactions. 64
5.22 Resolution of reconstructed track length of muons in near detector simulated ν_μ CC interactions. 64
5.23 Diagram of tricell criteria. 66
5.24 Cell response as function distance from the center of the cell for and example far detector cell. 67
5.25 Cell response before and after calibration in the x view. 67
5.26 Cell response before and after calibration in the y view. 68
5.27 Corrected detector response as a function of distance from the track end in far detector data. 68
5.28 Corrected detector response as a function of distance from the track end in far detector simulation. 69
5.29 Corrected detector response as a function of distance from the track end in far detector data. 69
5.30 Corrected detector response as a function of distance from the track end in far detector simulation. 70
6.1 Example event display of an ν_μ CC quasi-elastic interaction resulting in a muon and proton in the final state. The muon is represented by the blue line and the proton by the purple. 72
6.2 Example event display of an NC interaction with a similar topology to a ν_μ CC QE interaction. This event creates a proton, shown in purple, and π^-, shown in magenta, in the final state. 73
6.3 Example event display of a typical ν_μ CC deep inelastic interaction with a visible muon track and visible hadronic activity. This interaction results in a muon in, shown in blue, along with a hadronic shower. 74
6.4 Example event display of an NC interaction with a charged pion track, shown in magenta, extending out from hadronic activity. 75
6.5 Example event display of an ν_μ CC deep inelastic interaction. Note the final state charged pion, shown in magenta, is longer than the final state muon, shown in blue, in this interaction. 76

6.6 Example event display of an ν_e interaction resulting in an electromagnetic shower from the final state electron, shown in red. 77
6.7 Probability distribution of muon $\frac{dE}{dx}$ at a distance of 500 cm from the end of the track. 79
6.8 Profile of distribution of muon $\frac{dE}{dx}$ as a function of the distance from the end of the reconstructed track. The error bars show the RMS of the distribution. 80
6.9 Profile of distributions of $\frac{dE}{dx}$ as a function of the distance from the end of the reconstructed track under the muon and charged pion particle assumptions. The error bars show the RMS of the distribution. 81
6.10 Probability distributions of $\frac{dE}{dx}$ at a distance of 500 cm from the end of the track under the muon and charged pion particle assumptions. 82
6.11 Profile of distributions of scattering as a function of the distance from the end of the reconstructed track. The data points are located at the peak of the distribution, 0, and the error bars show the RMS of the distribution from 0. 83
6.12 Probability distributions of scattering at a distance of 500 cm from the end of the track. 84
6.13 Distribution of the $\frac{dE}{dx}$ LL variable in kNN training sample. 86
6.14 Distribution of the scattering LL variable in kNN training sample. . . . 87
6.15 Distribution the track length variable in kNN training sample. 88
6.16 Distribution of the plane fraction variable in kNN training sample. Note the spiked behavior of the distribution coming from the discrete nature of the number of planes crossed and number of planes with $\frac{dE}{dx}$ measurements 88
6.17 Overtraining test of PID output distributions of signal and background events. 89
6.18 Training sample efficiencies, purities, and FOM in a testing sample as a function of PID cut value. 90
6.19 PID distribution of signal and background events in simulated far detector neutrino interactions. 92
6.20 Distribution of PID input variable, $\frac{dE}{dx}$ LL, of signal and background events in simulated far detector neutrino interactions. 92

6.21 Distribution of PID input variable, scattering LL, of signal and background events in simulated far detector neutrino interactions 93
6.22 Distribution of PID input variable, track length, of signal and background events in simulated far detector neutrino interactions 93
6.23 Distribution of PID input variable, non-hadronic plane fraction, of signal and background events in simulated far detector neutrino interactions . 94
6.24 ν_μ CC selection efficiency as a function of PID cut value. 94
6.25 ν_μ CC selection purity as a function of PID cut value. 95
7.1 Muon energy fit. 98
7.2 Muon energy fractional resolution. 99
7.3 Hadronic energy fit for NonQE interaction types. 99
7.4 Hadronic energy fractional resolution for NonQE interaction types. . . . 100
7.5 Fractional neutrino energy resolution for QE interactions. 100
7.6 Fractional neutrino energy resolution for NonQE interactions. 101
7.7 Example event display of an ν_μ CC QE interaction with only a visible muon in the final state. 103
7.8 Example event display of an ν_μ CC QE interaction with a visible muon and proton in the final state. 104
7.9 Example event display of a typical ν_μ CC resonance interaction with a visible muon track and multiple proton prongs. 105
7.10 Example event display of a typical ν_μ CC deep inelastic interaction with a visible muon track and visible hadronic activity. 106
7.11 Distribution of the off track energy in the one track kNN training sample. 110
7.12 Distribution of the off track energy in the two track kNN training sample. 111
7.13 Distribution of the fractional energy difference variable in the one track kNN training sample. 111
7.14 Distribution of the fractional energy difference variable in the two track kNN training sample. 112
7.15 Distribution of the fractional energy difference z-test variable in the one track kNN training sample. 112
7.16 Distribution of the fractional energy difference z-test variable in the two track kNN training sample. 113

7.17 Distribution of the $\frac{dE}{dx}$ ratio variable in the two track kNN training sample. 113
7.18 Training and testing sample PID output distributions of signal and background in the one track sample. Note spikes in the distributions are from the default binning in the TMVA training algorithm. 114
7.19 Training and testing sample PID output distributions of signal and background in the two track sample. Note spikes in the distributions are from the default binning in the TMVA training algorithm. 114
7.20 Sample efficiencies, purities, and FOM as a function of PID cut value of a testing sample in the one track sample. 115
7.21 Sample efficiencies, purities, and FOM as a function of PID cut value of a testing sample in the two track sample. 115
7.22 PID distribution of signal and background events in the one track sample. 117
7.23 PID distribution of signal and background events in the two track sample. 117
7.24 Distribution of PID input variable, off-track energy, of signal and background events in simulated far detector neutrino interactions in the one track sample. 118
7.25 Distribution of PID input variable, off-track energy, of signal and background events in simulated far detector neutrino interactions in the two track sample. 118
7.26 Distribution of PID input variable, fractional energy difference, of signal and background events in simulated far detector neutrino interactions in the one track sample. 119
7.27 Distribution of PID input variable, fractional energy difference, of signal and background events in simulated far detector neutrino interactions in the two track sample. 119
7.28 Distribution of PID input variable, fractional energy difference Z-test, of signal and background events in simulated far detector neutrino interactions in the one track sample. 120
7.29 Distribution of PID input variable, fractional energy difference Z-test, of signal and background events in simulated far detector neutrino interactions in the two track sample. 120

7.30 Distribution of PID input variable, $\frac{dE}{dx}$ Ratio, of signal and background events in simulated far detector neutrino interactions in the two track sample. 121
8.1 Diagram of basic topology of cosmic rays and ν_μ CC interactions. Dashed lines indicate particles that are not visible. For cosmic rays this is where the particle is outside of the detector. For ν_μ CC interactions this is representing the initial state neutrino 124
8.2 Diagram of start and stop point of muon like tracks in cosmic rays and ν_μ CC interactions from figure 8.1. 125
8.3 Diagram of positive and negative populations in cosmic rays and ν_μ CC interactions from figure 8.1. 126
8.4 Positive and negative populations for cosmic rays and ν_μ CC interactions. 126
8.5 Negative population track start x and y position distribution in cosmic ray data. 128
8.6 Negative population track start x and y position distribution in simulated neutrino data. 129
8.7 Negative population track start x and z position distribution in cosmic ray data. 129
8.8 Negative population track start x and z position distribution in simulated neutrino data. 130
8.9 Negative population track start y and z position distribution in cosmic ray data. 130
8.10 Negative population track start y and z position distribution in simulated neutrino data. 131
8.11 Negative population track end x and y position distribution in cosmic ray data. 131
8.12 Negative population track end x and y position distribution in simulated neutrino data. 132
8.13 Negative population track end x and z position distribution in cosmic ray data. 132
8.14 Negative population track end x and z position distribution in simulated neutrino data. 133

8.15 Negative population track end y and z position distribution in cosmic ray data. 133
8.16 Negative population track end y and z position distribution in simulated neutrino data. 134
8.17 Positive population track start x and y position distribution in cosmic ray data. 134
8.18 Positive population track start x and y position distribution in simulated neutrino data. 135
8.19 Positive population track start x and z position distribution in cosmic ray data. 136
8.20 Positive population track start x and z position distribution in simulated neutrino data. 136
8.21 Positive population track start y and z position distribution in cosmic ray data. 137
8.22 Positive population track start y and z position distribution in simulated neutrino data. 137
8.23 Positive population track end x and y position distribution in cosmic ray data. 138
8.24 Positive population track end x and y position distribution in simulated neutrino data. 138
8.25 Positive population track end x and z position distribution in cosmic ray data. 139
8.26 Positive population track end x and z position distribution in simulated neutrino data. 139
8.27 Positive population track end y and z position distribution in cosmic ray data. 140
8.28 Positive population track end y and z position distribution in simulated neutrino data. 140
8.29 Distribution of events with all non-muon tracks passing and failing containment cuts in the negative and positive populations in cosmic ray data and simulated neutrino data. 142

8.30 Distribution of fractional transverse momentum in the negative population of cosmic ray data and simulated neutrino data. 143
8.31 Distribution of fractional transverse momentum in the positive population of cosmic ray data and simulated neutrino data. 144
8.32 Distribution of distance to detector edge and track angle in the negative population of cosmic ray data. 145
8.33 Distribution of distance to detector edge and track angle in the negative population of simulated neutrino data. 146
8.34 Distribution of distance to detector edge and track angle in the positive population of cosmic ray data. 146
8.35 Distribution of distance to detector edge and track angle in the positive population of simulated neutrino data. 147
8.36 Event display of an example flasher in the far detector. The instigating cosmic ray slice is drawn in green with the contained flasher slice drawn in yellow. 149
8.37 Distribution of flasher metric for the cosmic ray and simulated neutrino data. 150
8.38 Negative population muon track start x and y position distribution in cosmic ray data. 153
8.39 Negative population muon track start x and y position distribution in simulated neutrino data. 153
8.40 Negative population muon track start x and z position distribution in cosmic ray data. 154
8.41 Negative population muon track start x and z position distribution in simulated neutrino data. 154
8.42 Negative population muon track start y and z position distribution in cosmic ray data. 155
8.43 Negative population muon track start y and z position distribution in simulated neutrino data. 155
8.44 Distribution of distance from the muon track start to the detector edge in the negative population of cosmic ray and simulated neutrino data. . 156

8.45 Positive population muon track start x and y position distribution in cosmic ray data. 156
8.46 Positive population muon track start x and y position distribution in simulated neutrino data. 157
8.47 Positive population muon track start x and z position distribution in cosmic ray data. 157
8.48 Positive population muon track start x and z position distribution in simulated neutrino data. 158
8.49 Positive population muon track start y and z position distribution in cosmic ray data. 158
8.50 Positive population muon track start y and z position distribution in simulated neutrino data. 159
8.51 Distribution of distance from the muon track start to the detector edge in the positive population of cosmic ray and simulated neutrino data. . . 159
8.52 Distribution of fractional transverse momentum in the negative population of cosmic ray data and simulated neutrino data. 161
8.53 Distribution of direction of the muon track start relative to the beam direction negative population of cosmic ray and simulated neutrino data. 161
8.54 Distribution of fractional transverse momentum in the positive population of cosmic ray data and simulated neutrino data. 162
8.55 Distribution of direction of the muon track start relative to the y direction using the KalmanTrack reconstruction in the positive population of cosmic ray and simulated neutrino data. 163
8.56 Distribution of direction of the muon track start relative to the y direction using the CosmicTrack reconstruction in the positive population of cosmic ray and simulated neutrino data. 164
8.57 Distribution of hadronic energy in the negative population of cosmic ray and simulated neutrino data. 165
8.58 Distribution of hadronic energy in the positive population of cosmic ray and simulated neutrino data. 166
8.59 Distribution of hadronic energy overlapping with the muon track in the positive population of cosmic ray and simulated neutrino data. 166

8.60 Distribution of flasher metric for the cosmic ray and simulated neutrino data. 167
9.1 Maximum position in the x direction of any hits in a contained slice. . . 172
9.2 Minimum position in the x direction of any hits in a contained slice. . . 173
9.3 Maximum position in the y direction of any hits in a contained slice. . . 173
9.4 Minimum position in the y direction of any hits in a contained slice. . . 174
9.5 Maximum position in the z direction of any hits in a contained slice. . . 174
9.6 Minimum position in the z direction of any hits in a contained slice. . . 175
9.7 Extent of hits of in a slice in the x direction in contained slices. 175
9.8 Extent of hits of in a slice in the y direction in contained slices. 176
9.9 Extent of hits of in a slice in the z direction in contained slices. 176
9.10 Number of hits in contained slices. 177
9.11 Length of the most muon like track in contained slices. 178
9.12 Number of hits in the most muon like track in contained slices. 179
9.13 Track direction with respect to the x direction in the most muon like track in contained slices. 179
9.14 Track direction with respect to the y direction in the most muon like track in contained slices. 180
9.15 Track direction with respect to the z direction in the most muon like track in contained slices. 180
9.16 Track start x position in the most muon like track in contained slices. . 181
9.17 Track start y position in the most muon like track in contained slices. . 181
9.18 Track start z position in the most muon like track in contained slices. . 182
9.19 Number of hits in the most muon like track in contained slices. 182
9.20 Track end x position in the most muon like track in contained slices. . . 183
9.21 Track end y position in the most muon like track in contained slices. . . 183
9.22 Track end z position in the most muon like track in contained slices. . . 184
9.23 ReMId distribution in contained slices. 185
9.24 ReMId $\frac{dE}{dx}$ LL distribution in contained slices. 186
9.25 ReMId scattering LL distribution in contained slices. 186
9.26 ReMId non-hadronic plane fraction distribution in contained slices. . . . 187
9.27 Track length of muon track in contained slices passing ν_μ CC selection. 188

9.28 Number of hits in the muon track in contained slices passing ν_μ CC selection. 189
9.29 Number of hadronic hits in contained slices passing ν_μ CC selection. . . 189
9.30 Hadronic energy not overlapping with the muon track in contained slices passing ν_μ CC selection. 190
9.31 Hadronic energy overlapping with the muon track in contained slices passing ν_μ CC selection. 190
9.32 Average visible hadronic energy per hadronic hit in contained slices passing ν_μ CC selection. 191
9.33 Energy spectrum of QE selected events. 192
9.34 Energy spectrum of NonQE selected events. 193
9.35 QePID distribution in contained slices passing ν_μ CC selection with one reconstructed track. 193
9.36 QePID distribution in contained slices passing ν_μ CC selection with two reconstructed track. 194
9.37 Off-track energy ratio distribution in contained slices passing ν_μ CC selection with one reconstructed track. 194
9.38 Off-track energy ratio distribution in contained slices passing ν_μ CC selection with two reconstructed track. 195
9.39 Fractional energy difference distribution in contained slices passing ν_μ CC selection with one reconstructed track. 195
9.40 Fractional energy difference distribution in contained slices passing ν_μ CC selection with two reconstructed track. 196
9.41 Fractional energy difference z-test distribution in contained slices passing ν_μ CC selection with one reconstructed track. 196
9.42 Fractional energy difference z-test distribution in contained slices passing ν_μ CC selection with two reconstructed track. 197
9.43 $\frac{dE}{dx}$ ratio distribution in contained slices passing ν_μ CC selection with two reconstructed track. 197

9.44 Energy spectrum of selected cosmic background events in data along with the fit and background estimate in the QE sample. The background estimate is taken from the fit and shows the expected background event count in each energy bin used in the analysis. 199
9.45 Energy spectrum of selected cosmic background events in data along with the fit and background estimate in the NonQE sample. The background estimate is taken from the fit and shows the expected background event count in each energy bin used in the analysis. 200
9.46 Energy spectrum of selected cosmic background events in data along with the fit and background estimate in the escaping sample. The background estimate is taken from the fit and shows the expected background event count in each energy bin used in the analysis. Note the expected background has variable binning making it appear to diverge at high energies. 201
10.1 Proportion of selected QE events in each of the three major signals and backgrounds. 205
10.2 Proportion of selected NonQE events in each of the three major signals and backgrounds. 206
10.3 Selected NonQE events in near detector data and simulation. 207
10.4 Mapping of between reconstructed and true energy of selected NonQE events in near detector. 207
10.5 True energy spectra of selected NonQE events in near detector data and simulation. The reweighed spectrum is determined by the data selected events and the simulation spectrum is determined from the base simulation of near detector events. 208
10.6 True energy spectra of selected NonQE events in far detector data and simulation. The extrapolated spectrum comes from extrapolated data events in the near detector and the simulation is from the base simulation of far detector events. 209
10.7 Mapping of between reconstructed and true energy of selected NonQE events in far detector. 209

10.8 Reconstructed energy spectra of selected NonQE events in far detector data and simulation. The extrapolated spectrum comes from extrapolated data events in the near detector and the simulation is from the base simulation of far detector events. 210
10.9 Reconstructed energy spectra of selected QE events in far detector data and simulation. The extrapolated spectrum comes from extrapolated data events in the near detector and the simulation is from the base simulation of far detector events. 211
10.10Reconstructed energy spectra of selected escaping events in far detector data and simulation. The extrapolated spectrum comes from extrapolated data events in the near detector and the simulation is from the base simulation of far detector events. 212
11.1 Reconstructed energy of selected events in the nonQE sample with the systematic error band from beam uncertainties. All selected simulated events are shown in red with the a red systematic error band. The contribution to the selected events from background in the simulation is shown in blue. For the near detector the data is drawn in black with statistical error bars. For the far detector the oscillation parameters listed in table 2.1 are assumed. 216
11.2 Reconstructed energy of selected events in the escaping sample with the systematic error band from beam uncertainties. All selected simulated events are shown in red with the a red systematic error band. The contribution to the selected events from background in the simulation is shown in blue. For the near detector the data is drawn in black with statistical error bars. For the far detector the oscillation parameters listed in table 2.1 are assumed. 217

11.3 Reconstructed energy of selected events in the nonQE sample with the systematic error band from M_A CC QE. All selected simulated events are shown in red with the a red systematic error band. The contribution to the selected events from background in the simulation is shown in blue. For the near detector the data is drawn in black with statistical error bars. For the far detector the oscillation parameters listed in table 2.1 are assumed. 220
11.4 Reconstructed energy of selected events in the nonQE sample with the systematic error band from M_A CC RES. All selected simulated events are shown in red with the a red systematic error band. The contribution to the selected events from background in the simulation is shown in blue. For the near detector the data is drawn in black with statistical error bars. For the far detector the oscillation parameters listed in table 2.1 are assumed. 221
11.5 Reconstructed energy of selected events in the nonQE sample with the systematic error band from M_v CC RES. All selected simulated events are shown in red with the a red systematic error band. The contribution to the selected events from background in the simulation is shown in blue. For the near detector the data is drawn in black with statistical error bars. For the far detector the oscillation parameters listed in table 2.1 are assumed. 222
11.6 Reconstructed energy of selected events in the nonQE sample with the systematic error band from M_A NC RES. All selected simulated events are shown in red with the a red systematic error band. The contribution to the selected events from background in the simulation is shown in blue. For the near detector the data is drawn in black with statistical error bars. For the far detector the oscillation parameters listed in table 2.1 are assumed. 223

11.7 Reconstructed energy of selected events in the nonQE sample with the systematic error band from M_v NC RES. All selected simulated events are shown in red with the a red systematic error band. The contribution to the selected events from background in the simulation is shown in blue. For the near detector the data is drawn in black with statistical error bars. For the far detector the oscillation parameters listed in table 2.1 are assumed. 224
11.8 Reconstructed energy of selected events in the nonQE sample with the systematic error band from M_A NC elastic. All selected simulated events are shown in red with the a red systematic error band. The contribution to the selected events from background in the simulation is shown in blue. For the near detector the data is drawn in black with statistical error bars. For the far detector the oscillation parameters listed in table 2.1 are assumed. 225
11.9 Reconstructed energy of selected events in the nonQE sample with the systematic error band from the small GENIE uncertainties. All selected simulated events are shown in red with the a red systematic error band. The contribution to the selected events from background in the simulation is shown in blue. For the near detector the data is drawn in black with statistical error bars. For the far detector the oscillation parameters listed in table 2.1 are assumed. 228
11.10 Reconstructed energy of selected events in the nonQE sample with the systematic error band from the absolute normalization uncertainty. All selected simulated events are shown in red with the a red systematic error band. The contribution to the selected events from background in the simulation is shown in blue. For the near detector the data is drawn in black with statistical error bars. For the far detector the oscillation parameters listed in table 2.1 are assumed. 230

11.11Reconstructed energy of selected events in the nonQE sample with the systematic error band from the relative normalization uncertainty. All selected simulated events are shown in red with the a red systematic error band. The contribution to the selected events from background in the simulation is shown in blue. For the near detector the data is drawn in black with statistical error bars. For the far detector the oscillation parameters listed in table 2.1 are assumed. 231
11.12Reconstructed energy of selected events in the nonQE sample with the systematic error band from the absolute energy uncertainty in the near detector. All selected simulated events are shown in red with the a red systematic error band. The contribution to the selected events from background in the simulation is shown in blue. For the near detector the data is drawn in black with statistical error bars. For the far detector the oscillation parameters listed in table 2.1 are assumed. 233
11.13Reconstructed energy of selected events in the nonQE sample with the systematic error band from the absolute energy uncertainty in the far detector. All selected simulated events are shown in red with the a red systematic error band. The contribution to the selected events from background in the simulation is shown in blue. For the near detector the data is drawn in black with statistical error bars. For the far detector the oscillation parameters listed in table 2.1 are assumed. 234
11.14Energy spectrum of QE selected events. 239
11.15Energy spectrum of Non-QE selected events. 240
11.16Number of hadronic hits in contained slices passing ν_μ CC selection. . . 240
11.17QePID distribution in contained slices passing ν_μ CC selection with one reconstructed track. 241
11.18QePID distribution in contained slices passing ν_μ CC selection with two reconstructed track. 241

11.19Reconstructed energy of selected events in the nonQE sample with the systematic error band from the hadronic modeling uncertainty in the near detector. All selected simulated events are shown in red with the a red systematic error band. The contribution to the selected events from background in the simulation is shown in blue. For the near detector the data is drawn in black with statistical error bars. For the far detector the oscillation parameters listed in table 2.1 are assumed. 242
11.20Reconstructed energy of selected events in the nonQE sample with the systematic error band from the hadronic modeling uncertainty in the far detector. All selected simulated events are shown in red with the a red systematic error band. The contribution to the selected events from background in the simulation is shown in blue. For the near detector the data is drawn in black with statistical error bars. For the far detector the oscillation parameters listed in table 2.1 are assumed. 243
11.21Reconstructed energy of selected events in the QE sample with the total systematic error band. All selected simulated events are shown in red with the a red systematic error band. The contribution to the selected events from background in the simulation is shown in blue. For the near detector the data is drawn in black with statistical error bars. For the far detector the oscillation parameters listed in table 2.1 are assumed. . 245
11.22Reconstructed energy of selected events in the nonQE sample with the total systematic error band. All selected simulated events are shown in red with the a red systematic error band. The contribution to the selected events from background in the simulation is shown in blue. For the near detector the data is drawn in black with statistical error bars. For the far detector the oscillation parameters listed in table 2.1 are assumed. . 246
11.23Reconstructed energy of selected events in the escaping sample with the total systematic error band. All selected simulated events are shown in red with the a red systematic error band. The contribution to the selected events from background in the simulation is shown in blue. For the near detector the data is drawn in black with statistical error bars. For the far detector the oscillation parameters listed in table 2.1 are assumed. . 247

12.1 Event display of a selected QE event from run 17953 subrun 38 event 256887. Colored dots correspond to hits in reconstructed tracks. Hits in the readout not in the beam time window displayed are shown in gray. The display is zoomed in time and to the region of interest in the detector. 253
12.2 Event display of a selected NonQE event from run 18791 subrun 48 event 765587. Colored dots correspond to hits in reconstructed tracks. Hits in the readout not in the beam time window displayed are shown in gray. The display is zoomed in time and to the region of interest in the detector. 254
12.3 Event display of a selected escaping event from run 16270 subrun 8 event 34539. Colored dots correspond to hits in reconstructed tracks. Hits in the readout not in the beam time window displayed are shown in gray. The display is zoomed in time and to the region of interest in the detector. The blue line represents the end of the instrumented region of the detector. 255
12.4 Total number of hits in the slice of selected non QE events in the far detector data. The prediction is drawn in red with the systematic errors shown in the error bands. The major sources of background are shown in magenta and green. 256
12.5 Total number of hits in the slice of selected QE events in the far detector data. The prediction is drawn in red with the systematic errors shown in the error bands. The major sources of background are shown in magenta and green. 257
12.6 Total number of hits in the slice of selected escaping events in the far detector data. The prediction is drawn in red with the systematic errors shown in the error bands. The major sources of background are shown in magenta and green. 257
12.7 Total number of hits in the most muon like track in selected non QE events in the far detector data. The prediction is drawn in red with the systematic errors shown in the error bands. The major sources of background are shown in magenta and green. 258

12.8 Total number of hits in the most muon like track in selected QE events in the far detector data. The prediction is drawn in red with the systematic errors shown in the error bands. The major sources of background are shown in magenta and green. 258
12.9 Total number of hits in the most muon like track in selected escaping events in the far detector data. The prediction is drawn in red with the systematic errors shown in the error bands. The major sources of background are shown in magenta and green. 259
12.10 Track starting x position of the most muon like track in selected non QE events in the far detector data. The prediction is drawn in red with the systematic errors shown in the error bands. The major sources of background are shown in magenta and green. 259
12.11 Track starting x position of the most muon like track in selected QE events in the far detector data. The prediction is drawn in red with the systematic errors shown in the error bands. The major sources of background are shown in magenta and green. 260
12.12 Track starting x position of the most muon like track in selected escaping events in the far detector data. The prediction is drawn in red with the systematic errors shown in the error bands. The major sources of background are shown in magenta and green. 260
12.13 Track starting y position of the most muon like track in selected non QE events in the far detector data. The prediction is drawn in red with the systematic errors shown in the error bands. The major sources of background are shown in magenta and green. 261
12.14 Track starting y position of the most muon like track in selected QE events in the far detector data. The prediction is drawn in red with the systematic errors shown in the error bands. The major sources of background are shown in magenta and green. 262
12.15 Track starting x position of the most muon like track in selected escaping events in the far detector data. The prediction is drawn in red with the systematic errors shown in the error bands. The major sources of background are shown in magenta and green. 262

12.16Track starting z position of the most muon like track in selected non QE events in the far detector data. The prediction is drawn in red with the systematic errors shown in the error bands. The major sources of background are shown in magenta and green. 263
12.17Track starting z position of the most muon like track in selected QE events in the far detector data. The prediction is drawn in red with the systematic errors shown in the error bands. The major sources of background are shown in magenta and green. 263
12.18Track starting z position of the most muon like track in selected escaping events in the far detector data. The prediction is drawn in red with the systematic errors shown in the error bands. The major sources of background are shown in magenta and green. 264
12.19Track stopping x position of the most muon like track in selected non QE events in the far detector data. The prediction is drawn in red with the systematic errors shown in the error bands. The major sources of background are shown in magenta and green. 264
12.20Track stopping x position of the most muon like track in selected QE events in the far detector data. The prediction is drawn in red with the systematic errors shown in the error bands. The major sources of background are shown in magenta and green. 265
12.21Track stopping y position of the most muon like track in selected escaping events in the far detector data. The prediction is drawn in red with the systematic errors shown in the error bands. The major sources of background are shown in magenta and green. 265
12.22Track stopping y position of the most muon like track in selected non QE events in the far detector data. The prediction is drawn in red with the systematic errors shown in the error bands. The major sources of background are shown in magenta and green. 266
12.23Track stopping y position of the most muon like track in selected QE events in the far detector data. The prediction is drawn in red with the systematic errors shown in the error bands. The major sources of background are shown in magenta and green. 266

12.24Track stopping x position of the most muon like track in selected escaping events in the far detector data. The prediction is drawn in red with the systematic errors shown in the error bands. The major sources of background are shown in magenta and green. 267
12.25Track stopping z position of the most muon like track in selected non QE events in the far detector data. The prediction is drawn in red with the systematic errors shown in the error bands. The major sources of background are shown in magenta and green. 267
12.26Track stopping z position of the most muon like track in selected QE events in the far detector data. The prediction is drawn in red with the systematic errors shown in the error bands. The major sources of background are shown in magenta and green. 268
12.27Track stopping z position of the most muon like track in selected escaping events in the far detector data. The prediction is drawn in red with the systematic errors shown in the error bands. The major sources of background are shown in magenta and green. 268
12.28Direction with respect to the beam of the most muon like track in selected non-QE events in the far detector data. The prediction is drawn in red with the systematic errors shown in the error bands. The major sources of background are shown in magenta and green. 269
12.29Direction with respect to the beam of the most muon like track in selected QE events in the far detector data. The prediction is drawn in red with the systematic errors shown in the error bands. The major sources of background are shown in magenta and green. 270
12.30Direction with respect to the beam of the most muon like track in selected escaping events in the far detector data. The prediction is drawn in red with the systematic errors shown in the error bands. The major sources of background are shown in magenta and green. 270
12.31ReMId value of the most muon like track in selected non-QE events in the far detector data. The prediction is drawn in red with the systematic errors shown in the error bands. The major sources of background are shown in magenta and green. 271

12.32ReMId value of the most muon like track in selected QE events in the far detector data. The prediction is drawn in red with the systematic errors shown in the error bands. The major sources of background are shown in magenta and green. 272
12.33ReMId value of the most muon like track in selected escaping events in the far detector data. The prediction is drawn in red with the systematic errors shown in the error bands. The major sources of background are shown in magenta and green. 272
12.34$\frac{dE}{dx}$ log-likelihood value of the most muon like track in selected non-QE events in the far detector data. The prediction is drawn in red with the systematic errors shown in the error bands. The major sources of background are shown in magenta and green. 273
12.35$\frac{dE}{dx}$ log-likelihood value of the most muon like track in selected QE events in the far detector data. The prediction is drawn in red with the systematic errors shown in the error bands. The major sources of background are shown in magenta and green. 273
12.36$\frac{dE}{dx}$ log-likelihood value of the most muon like track in selected escaping events in the far detector data. The prediction is drawn in red with the systematic errors shown in the error bands. The major sources of background are shown in magenta and green. 274
12.37Scattering log-likelihood value of the most muon like track in selected non-QE events in the far detector data. The prediction is drawn in red with the systematic errors shown in the error bands. The major sources of background are shown in magenta and green. 274
12.38Scattering log-likelihood value of the most muon like track in selected QE events in the far detector data. The prediction is drawn in red with the systematic errors shown in the error bands. The major sources of background are shown in magenta and green. 275
12.39Scattering log-likelihood value of the most muon like track in selected escaping events in the far detector data. The prediction is drawn in red with the systematic errors shown in the error bands. The major sources of background are shown in magenta and green. 275

12.40Hadronic energy in selected non-QE events in the far detector data. The prediction is drawn in red with the systematic errors shown in the error bands. The major sources of background are shown in magenta and green. 276
12.41Hadronic energy in selected QE events in the far detector data. The prediction is drawn in red with the systematic errors shown in the error bands. The major sources of background are shown in magenta and green. 276
12.42Hadronic energy in selected escaping events in the far detector data. The prediction is drawn in red with the systematic errors shown in the error bands. The major sources of background are shown in magenta and green. 277
12.43Neutrino energy in selected NonQE events in the far detector data. The prediction is drawn in red with the systematic errors shown in the error bands. The major sources of background are shown in magenta and green. 278
12.44Neutrino energy in selected QE events in the far detector data. The prediction is drawn in red with the systematic errors shown in the error bands. The major sources of background are shown in magenta and green. 279
12.45Neutrino energy in selected escaping events in the far detector data. The prediction is drawn in red with the systematic errors shown in the error bands. The major sources of background are shown in magenta and green. 279
12.4690% confidence limits on the measurement of the oscillation parameters $\sin^2\theta_{23}$ and $\left|\Delta m^2_{32}\right|$ considering only statistical errors. 280
12.4790% confidence limits on the measurement of the oscillation parameters $\sin^2\theta_{23}$ and $\left|\Delta m^2_{32}\right|$ considering both statistical and systematic errors. . 281
12.4890% confidence limits on the measurement of the oscillation parameters $\sin^2\theta_{23}$ and $\left|\Delta m^2_{32}\right|$ for the combined result of the statistical only and statistical and systematic error cases. 283
12.4990% confidence limits on the measurement of the oscillation parameters $\sin^2\theta_{23}$ and $\left|\Delta m^2_{32}\right|$ for the combined result including the escaping sample and not including the escaping sample. 283
12.5090% confidence limits on the measurement of the oscillation parameters $\sin^2\theta_{23}$ and $\left|\Delta m^2_{32}\right|$ compared to measurements from the T2K and MINOS experiments with data taken from [6] and [7] respectively. 285
A.1 Selected Non-QE events in near detector data and simulation. 295

A.2 Mapping of between reconstructed and true energy of selected Non-QE events in near detector. 295
A.3 True energy spectra of selected Non-QE events in near detector data and simulation. The reweighed spectrum is determined by the data selected events and the simulation spectrum is determined from the base simulation of near detector events. 296
A.4 True energy spectra of selected Non-QE events in far detector data and simulation. The extrapolated spectrum comes from extrapolated data events in the near detector and the simulation is from the base simulation of far detector events. 296
A.5 Mapping of between reconstructed and true energy of selected Non-QE events in far detector. 297
A.6 Reconstructed energy spectra of selected Non-QE events in far detector data and simulation. The extrapolated spectrum comes from extrapolated data events in the near detector and the simulation is from the base simulation of far detector events. 297
A.7 Selected Non-QE events in near detector data and simulation. 298
A.8 Mapping of between reconstructed and true energy of selected Non-QE events in near detector. 299
A.9 True energy spectra of selected Non-QE events in near detector data and simulation. The reweighed spectrum is determined by the data selected events and the simulation spectrum is determined from the base simulation of near detector events. 299
A.10 True energy spectra of selected Non-QE events in far detector data and simulation. The extrapolated spectrum comes from extrapolated data events in the near detector and the simulation is from the base simulation of far detector events. 300
A.11 Mapping of between reconstructed and true energy of selected Non-QE events in far detector. 300

A.12 Reconstructed energy spectra of selected Non-QE events in far detector data and simulation. The extrapolated spectrum comes from extrapolated data events in the near detector and the simulation is from the base simulation of far detector events. 301
A.13 Selected Non-QE events in near detector data and simulation. 302
A.14 Reconstructed energy spectra of selected Non-QE events in far detector data and simulation. The extrapolated spectrum comes from extrapolated data events in the near detector and the simulation is from the base simulation of far detector events. 303
A.15 Selected QE events in near detector data and simulation. 303
A.16 Mapping of between reconstructed and true energy of selected QE events in near detector. 304
A.17 True energy spectra of selected QE events in near detector data and simulation. The reweighed spectrum is determined by the data selected events and the simulation spectrum is determined from the base simulation of near detector events. 304
A.18 True energy spectra of selected QE events in far detector data and simulation. The extrapolated spectrum comes from extrapolated data events in the near detector and the simulation is from the base simulation of far detector events. 305
A.19 Mapping of between reconstructed and true energy of selected QE events in far detector. 305
A.20 Reconstructed energy spectra of selected QE events in far detector data and simulation. The extrapolated spectrum comes from extrapolated data events in the near detector and the simulation is from the base simulation of far detector events. 306
A.21 Selected QE events in near detector data and simulation. 307
A.22 Mapping of between reconstructed and true energy of selected QE events in near detector. 308

A.23 True energy spectra of selected QE events in near detector data and simulation. The reweighed spectrum is determined by the data selected events and the simulation spectrum is determined from the base simulation of near detector events. 308
A.24 True energy spectra of selected QE events in far detector data and simulation. The extrapolated spectrum comes from extrapolated data events in the near detector and the simulation is from the base simulation of far detector events. 309
A.25 Mapping of between reconstructed and true energy of selected QE events in far detector. 309
A.26 Reconstructed energy spectra of selected QE events in far detector data and simulation. The extrapolated spectrum comes from extrapolated data events in the near detector and the simulation is from the base simulation of far detector events. 310
A.27 Selected QE events in near detector data and simulation. 311
A.28 Reconstructed energy spectra of selected QE events in far detector data and simulation. The extrapolated spectrum comes from extrapolated data events in the near detector and the simulation is from the base simulation of far detector events. 312
B.1 Reconstructed energy of selected events in the QE sample with the systematic error band from beam uncertainties. All selected simulated events are shown in red with the a red systematic error band. The contribution to the selected events from background in the simulation is shown in blue. For the near detector the data is drawn in black with statistical error bars. For the far detector the oscillation parameters listed in table 2.1 are assumed. 314

B.2 Reconstructed energy of selected events in the nonQE sample with the systematic error band from beam uncertainties. All selected simulated events are shown in red with the a red systematic error band. The contribution to the selected events from background in the simulation is shown in blue. For the near detector the data is drawn in black with statistical error bars. For the far detector the oscillation parameters listed in table 2.1 are assumed. 315
B.3 Reconstructed energy of selected events in the escaping sample with the systematic error band from beam uncertainties. All selected simulated events are shown in red with the a red systematic error band. The contribution to the selected events from background in the simulation is shown in blue. For the near detector the data is drawn in black with statistical error bars. For the far detector the oscillation parameters listed in table 2.1 are assumed. 316
B.4 Reconstructed energy of selected events in the QE sample with the systematic error band from M_A CC QE. All selected simulated events are shown in red with the a red systematic error band. The contribution to the selected events from background in the simulation is shown in blue. For the near detector the data is drawn in black with statistical error bars. For the far detector the oscillation parameters listed in table 2.1 are assumed. 318
B.5 Reconstructed energy of selected events in the QE sample with the systematic error band from M_A CC RES. All selected simulated events are shown in red with the a red systematic error band. The contribution to the selected events from background in the simulation is shown in blue. For the near detector the data is drawn in black with statistical error bars. For the far detector the oscillation parameters listed in table 2.1 are assumed. 319

B.6 Reconstructed energy of selected events in the QE sample with the systematic error band from M_v CC RES. All selected simulated events are shown in red with the a red systematic error band. The contribution to the selected events from background in the simulation is shown in blue. For the near detector the data is drawn in black with statistical error bars. For the far detector the oscillation parameters listed in table 2.1 are assumed. 320
B.7 Reconstructed energy of selected events in the QE sample with the systematic error band from M_A NC RES. All selected simulated events are shown in red with the a red systematic error band. The contribution to the selected events from background in the simulation is shown in blue. For the near detector the data is drawn in black with statistical error bars. For the far detector the oscillation parameters listed in table 2.1 are assumed. 321
B.8 Reconstructed energy of selected events in the QE sample with the systematic error band from M_v NC RES. All selected simulated events are shown in red with the a red systematic error band. The contribution to the selected events from background in the simulation is shown in blue. For the near detector the data is drawn in black with statistical error bars. For the far detector the oscillation parameters listed in table 2.1 are assumed. 322
B.9 Reconstructed energy of selected events in the QE sample with the systematic error band from M_A NC elastic. All selected simulated events are shown in red with the a red systematic error band. The contribution to the selected events from background in the simulation is shown in blue. For the near detector the data is drawn in black with statistical error bars. For the far detector the oscillation parameters listed in table 2.1 are assumed. 323

B.10 Reconstructed energy of selected events in the nonQE sample with the systematic error band from M_A CC QE. All selected simulated events are shown in red with the a red systematic error band. The contribution to the selected events from background in the simulation is shown in blue. For the near detector the data is drawn in black with statistical error bars. For the far detector the oscillation parameters listed in table 2.1 are assumed. 324
B.11 Reconstructed energy of selected events in the nonQE sample with the systematic error band from M_A CC RES. All selected simulated events are shown in red with the a red systematic error band. The contribution to the selected events from background in the simulation is shown in blue. For the near detector the data is drawn in black with statistical error bars. For the far detector the oscillation parameters listed in table 2.1 are assumed. 325
B.12 Reconstructed energy of selected events in the nonQE sample with the systematic error band from M_v CC RES. All selected simulated events are shown in red with the a red systematic error band. The contribution to the selected events from background in the simulation is shown in blue. For the near detector the data is drawn in black with statistical error bars. For the far detector the oscillation parameters listed in table 2.1 are assumed. 326
B.13 Reconstructed energy of selected events in the nonQE sample with the systematic error band from M_A NC RES. All selected simulated events are shown in red with the a red systematic error band. The contribution to the selected events from background in the simulation is shown in blue. For the near detector the data is drawn in black with statistical error bars. For the far detector the oscillation parameters listed in table 2.1 are assumed. 327

B.14 Reconstructed energy of selected events in the nonQE sample with the systematic error band from M_v NC RES. All selected simulated events are shown in red with the a red systematic error band. The contribution to the selected events from background in the simulation is shown in blue. For the near detector the data is drawn in black with statistical error bars. For the far detector the oscillation parameters listed in table 2.1 are assumed. 328
B.15 Reconstructed energy of selected events in the nonQE sample with the systematic error band from M_A NC elastic. All selected simulated events are shown in red with the a red systematic error band. The contribution to the selected events from background in the simulation is shown in blue. For the near detector the data is drawn in black with statistical error bars. For the far detector the oscillation parameters listed in table 2.1 are assumed. 329
B.16 Reconstructed energy of selected events in the escaping sample with the systematic error band from M_A CC QE. All selected simulated events are shown in red with the a red systematic error band. The contribution to the selected events from background in the simulation is shown in blue. For the near detector the data is drawn in black with statistical error bars. For the far detector the oscillation parameters listed in table 2.1 are assumed. 330
B.17 Reconstructed energy of selected events in the escaping sample with the systematic error band from M_A CC RES. All selected simulated events are shown in red with the a red systematic error band. The contribution to the selected events from background in the simulation is shown in blue. For the near detector the data is drawn in black with statistical error bars. For the far detector the oscillation parameters listed in table 2.1 are assumed. 331

B.18 Reconstructed energy of selected events in the escaping sample with the systematic error band from M_v CC RES. All selected simulated events are shown in red with the a red systematic error band. The contribution to the selected events from background in the simulation is shown in blue. For the near detector the data is drawn in black with statistical error bars. For the far detector the oscillation parameters listed in table 2.1 are assumed. 332
B.19 Reconstructed energy of selected events in the escaping sample with the systematic error band from M_A NC RES. All selected simulated events are shown in red with the a red systematic error band. The contribution to the selected events from background in the simulation is shown in blue. For the near detector the data is drawn in black with statistical error bars. For the far detector the oscillation parameters listed in table 2.1 are assumed. 333
B.20 Reconstructed energy of selected events in the escaping sample with the systematic error band from M_v NC RES. All selected simulated events are shown in red with the a red systematic error band. The contribution to the selected events from background in the simulation is shown in blue. For the near detector the data is drawn in black with statistical error bars. For the far detector the oscillation parameters listed in table 2.1 are assumed. 334
B.21 Reconstructed energy of selected events in the escaping sample with the systematic error band from M_A NC elastic. All selected simulated events are shown in red with the a red systematic error band. The contribution to the selected events from background in the simulation is shown in blue. For the near detector the data is drawn in black with statistical error bars. For the far detector the oscillation parameters listed in table 2.1 are assumed. 335

B.22 Reconstructed energy of selected events in the QE sample with the systematic error band from the small GENIE uncertainties. All selected simulated events are shown in red with the a red systematic error band. The contribution to the selected events from background in the simulation is shown in blue. For the near detector the data is drawn in black with statistical error bars. For the far detector the oscillation parameters listed in table 2.1 are assumed. 337
B.23 Reconstructed energy of selected events in the nonQE sample with the systematic error band from the small GENIE uncertainties. All selected simulated events are shown in red with the a red systematic error band. The contribution to the selected events from background in the simulation is shown in blue. For the near detector the data is drawn in black with statistical error bars. For the far detector the oscillation parameters listed in table 2.1 are assumed. 338
B.24 Reconstructed energy of selected events in the escaping sample with the systematic error band from the small GENIE uncertainties. All selected simulated events are shown in red with the a red systematic error band. The contribution to the selected events from background in the simulation is shown in blue. For the near detector the data is drawn in black with statistical error bars. For the far detector the oscillation parameters listed in table 2.1 are assumed. 339
B.25 Reconstructed energy of selected events in the QE sample with the systematic error band from the absolute normalization uncertainty. All selected simulated events are shown in red with the a red systematic error band. The contribution to the selected events from background in the simulation is shown in blue. For the near detector the data is drawn in black with statistical error bars. For the far detector the oscillation parameters listed in table 2.1 are assumed. 341

B.26 Reconstructed energy of selected events in the QE sample with the systematic error band from the relative normalization uncertainty. All selected simulated events are shown in red with the a red systematic error band. The contribution to the selected events from background in the simulation is shown in blue. For the near detector the data is drawn in black with statistical error bars. For the far detector the oscillation parameters listed in table 2.1 are assumed. 342
B.27 Reconstructed energy of selected events in the nonQE sample with the systematic error band from the absolute normalization uncertainty. All selected simulated events are shown in red with the a red systematic error band. The contribution to the selected events from background in the simulation is shown in blue. For the near detector the data is drawn in black with statistical error bars. For the far detector the oscillation parameters listed in table 2.1 are assumed. 343
B.28 Reconstructed energy of selected events in the nonQE sample with the systematic error band from the relative normalization uncertainty. All selected simulated events are shown in red with the a red systematic error band. The contribution to the selected events from background in the simulation is shown in blue. For the near detector the data is drawn in black with statistical error bars. For the far detector the oscillation parameters listed in table 2.1 are assumed. 344
B.29 Reconstructed energy of selected events in the escaping sample with the systematic error band from the absolute normalization uncertainty. All selected simulated events are shown in red with the a red systematic error band. The contribution to the selected events from background in the simulation is shown in blue. For the near detector the data is drawn in black with statistical error bars. For the far detector the oscillation parameters listed in table 2.1 are assumed. 345

B.30 Reconstructed energy of selected events in the escaping sample with the systematic error band from the relative normalization uncertainty. All selected simulated events are shown in red with the a red systematic error band. The contribution to the selected events from background in the simulation is shown in blue. For the near detector the data is drawn in black with statistical error bars. For the far detector the oscillation parameters listed in table 2.1 are assumed. 346
B.31 Reconstructed energy of selected events in the QE sample with the systematic error band from the absolute energy uncertainty in the near detector. All selected simulated events are shown in red with the a red systematic error band. The contribution to the selected events from background in the simulation is shown in blue. For the near detector the data is drawn in black with statistical error bars. For the far detector the oscillation parameters listed in table 2.1 are assumed. 348
B.32 Reconstructed energy of selected events in the QE sample with the systematic error band from the absolute energy uncertainty in the far detector. All selected simulated events are shown in red with the a red systematic error band. The contribution to the selected events from background in the simulation is shown in blue. For the near detector the data is drawn in black with statistical error bars. For the far detector the oscillation parameters listed in table 2.1 are assumed. 349
B.33 Reconstructed energy of selected events in the nonQE sample with the systematic error band from the absolute energy uncertainty in the near detector. All selected simulated events are shown in red with the a red systematic error band. The contribution to the selected events from background in the simulation is shown in blue. For the near detector the data is drawn in black with statistical error bars. For the far detector the oscillation parameters listed in table 2.1 are assumed. 350

B.34 Reconstructed energy of selected events in the nonQE sample with the systematic error band from the absolute energy uncertainty in the far detector. All selected simulated events are shown in red with the a red systematic error band. The contribution to the selected events from background in the simulation is shown in blue. For the near detector the data is drawn in black with statistical error bars. For the far detector the oscillation parameters listed in table 2.1 are assumed. 351
B.35 Reconstructed energy of selected events in the escaping sample with the systematic error band from the absolute energy uncertainty in the near detector. All selected simulated events are shown in red with the a red systematic error band. The contribution to the selected events from background in the simulation is shown in blue. For the near detector the data is drawn in black with statistical error bars. For the far detector the oscillation parameters listed in table 2.1 are assumed. 352
B.36 Reconstructed energy of selected events in the escaping sample with the systematic error band from the absolute energy uncertainty in the far detector. All selected simulated events are shown in red with the a red systematic error band. The contribution to the selected events from background in the simulation is shown in blue. For the near detector the data is drawn in black with statistical error bars. For the far detector the oscillation parameters listed in table 2.1 are assumed. 353
B.37 Reconstructed energy of selected events in the QE sample with the systematic error band from the hadronic modeling uncertainty in the near detector. All selected simulated events are shown in red with the a red systematic error band. The contribution to the selected events from background in the simulation is shown in blue. For the near detector the data is drawn in black with statistical error bars. For the far detector the oscillation parameters listed in table 2.1 are assumed. 355

B.38 Reconstructed energy of selected events in the QE sample with the systematic error band from the hadronic modeling uncertainty in the far detector. All selected simulated events are shown in red with the a red systematic error band. The contribution to the selected events from background in the simulation is shown in blue. For the near detector the data is drawn in black with statistical error bars. For the far detector the oscillation parameters listed in table 2.1 are assumed. 356
B.39 Reconstructed energy of selected events in the nonQE sample with the systematic error band from the hadronic modeling uncertainty in the near detector. All selected simulated events are shown in red with the a red systematic error band. The contribution to the selected events from background in the simulation is shown in blue. For the near detector the data is drawn in black with statistical error bars. For the far detector the oscillation parameters listed in table 2.1 are assumed. 357
B.40 Reconstructed energy of selected events in the nonQE sample with the systematic error band from the hadronic modeling uncertainty in the far detector. All selected simulated events are shown in red with the a red systematic error band. The contribution to the selected events from background in the simulation is shown in blue. For the near detector the data is drawn in black with statistical error bars. For the far detector the oscillation parameters listed in table 2.1 are assumed. 358
B.41 Reconstructed energy of selected events in the escaping sample with the systematic error band from the hadronic modeling uncertainty in the near detector. All selected simulated events are shown in red with the a red systematic error band. The contribution to the selected events from background in the simulation is shown in blue. For the near detector the data is drawn in black with statistical error bars. For the far detector the oscillation parameters listed in table 2.1 are assumed. 359

B.42 Reconstructed energy of selected events in the escaping sample with the systematic error band from the hadronic modeling uncertainty in the far detector. All selected simulated events are shown in red with the a red systematic error band. The contribution to the selected events from background in the simulation is shown in blue. For the near detector the data is drawn in black with statistical error bars. For the far detector the oscillation parameters listed in table 2.1 are assumed. 360
C.1 Maximum position in the x direction of any hits in a contained slice. . . 361
C.2 Minimum position in the x direction of any hits in a contained slice. . . 362
C.3 Maximum position in the y direction of any hits in a contained slice. . . 362
C.4 Minimum position in the y direction of any hits in a contained slice. . . 363
C.5 Maximum position in the z direction of any hits in a contained slice. . . 363
C.6 Minimum position in the z direction of any hits in a contained slice. . . 364
C.7 Extent of hits of in a slice in the x direction in contained slices. 364
C.8 Extent of hits of in a slice in the y direction in contained slices. 365
C.9 Extent of hits of in a slice in the z direction in contained slices. 365
C.10 Number of hits in contained slices. 366
C.11 Length of the most muon like track in contained slices. 367
C.12 Number of hits in the most muon like track in contained slices. 368
C.13 Track direction with respect to the x direction in the most muon like track in contained slices. 368
C.14 Track direction with respect to the y direction in the most muon like track in contained slices. 369
C.15 Track direction with respect to the z direction in the most muon like track in contained slices. 369
C.16 Track start x position in the most muon like track in contained slices. . 370
C.17 Track start y position in the most muon like track in contained slices. . 370
C.18 Track start z position in the most muon like track in contained slices. . 371
C.19 Number of hits in the most muon like track in contained slices. 371
C.20 Track end x position in the most muon like track in contained slices. . . 372
C.21 Track end y position in the most muon like track in contained slices. . . 372
C.22 Track end z position in the most muon like track in contained slices. . . 373

C.23 ReMId distribution in contained slices. 374
C.24 ReMId $\frac{dE}{dx}$ LL distribution in contained slices. 375
C.25 ReMId scattering LL distribution in contained slices. 375
C.26 ReMId non-hadronic plane fraction distribution in contained slices. . . . 376
C.27 Track length of muon track in contained slices passing ν_μ CC selection. 377
C.28 Number of hits in the muon track in contained slices passing ν_μ CC selection. 378
C.29 Number of hadronic hits in contained slices passing ν_μ CC selection. . . 378
C.30 Hadronic energy not overlapping with the muon track in contained slices passing ν_μ CC selection. 379
C.31 Hadronic energy overlapping with the muon track in contained slices passing ν_μ CC selection. 379
C.32 Average visible hadronic energy per hadronic hit in contained slices passing ν_μ CC selection. 380
C.33 Energy spectrum of QE selected events. 381
C.34 Energy spectrum of Non-QE selected events. 382
C.35 QePID distribution in contained slices passing ν_μ CC selection with one reconstructed track. 382
C.36 QePID distribution in contained slices passing ν_μ CC selection with two reconstructed track. 383
C.37 Off-track energy ratio distribution in contained slices passing ν_μ CC selection with one reconstructed track. 383
C.38 Off-track energy ratio distribution in contained slices passing ν_μ CC selection with two reconstructed track. 384
C.39 Fractional energy difference distribution in contained slices passing ν_μ CC selection with one reconstructed track. 384
C.40 Fractional energy difference distribution in contained slices passing ν_μ CC selection with two reconstructed track. 385
C.41 Fractional energy difference z-test distribution in contained slices passing ν_μ CC selection with one reconstructed track. 385
C.42 Fractional energy difference z-test distribution in contained slices passing ν_μ CC selection with two reconstructed track. 386

C.43 $\frac{dE}{dx}$ ratio distribution in contained slices passing ν_μ CC selection with two reconstructed track. 386

Chapter 1

Introduction

The NuMI[1] Off-Axis ν_e Appearance (NOνA) experiment is a long baseline neutrino oscillation experiment. The experiment consists of two detectors separated by a baseline of 810 km sitting 14 mrad off-axis to a beam of neutrinos. The near detector, placed close to the source of the neutrino beam, measures the initial composition of the beam while the far detector measures the composition of the beam after the neutrinos have propagated far enough to undergo a significant amount of oscillation. By comparing the composition of the beam between the two detectors, parameters governing the oscillations between the two detectors are measured. This analysis focuses on measuring the oscillation parameters $\sin^2\theta_{23}$ and $\left|\Delta m^2_{32}\right|$ from disappearance of muon neutrinos (ν_μ's) between the near and far detectors. Chapters 2 and 3 detail the theory of neutrino oscillations and describe the beam and detectors that make up the experiment.

Charged current interactions of ν_μ's usually result in a visible muon and hadronic particles in the NOνA detectors. In general the muon appears as a long track in the detector. Correctly reconstructing the muon track and identifying it as a muon emerging from a neutrino interaction provides a method for determining the ν_μ composition in each detector. Chapter 5 discusses the reconstruction of the data from the detectors and chapter 6 describes the identification of ν_μ charged current events from background neutrino events.

In order to best determine the ν_μ disappearance oscillation a fit is performed on the neutrino energy spectrum. The neutrino energy is determined from summing the

[1] Neutrinos at the Main Injector

energy in both the muon and hadronic components of the events. This method is described in chapter 7. In addition to estimating overall neutrino energy determining event energy topologies allows for the separation of the ν_μ events into subcategories with different energy resolutions. The separation of ν_μ events by energy resolution allows for performing a weighted fit enhancing the overall measurement sensitivities. The process of separating signal events into sub-samples is also described in chapter 7.

The main background to this analysis comes from cosmic rays. This results from the far detector being placed on the surface of the Earth with only minimal overburden exposing it to a large flux of cosmic ray muons which can mimic the final state muon produced in a ν_μ charged current interaction. Neutrino events in which the whole interaction is located within the fiducial volume of the detector provide the best energy estimate, because all the kinetic energy of the particles is lost in the detector, and are also relatively easy to separate from cosmic ray background. However, ν_μ interactions in which either the muon or hadronic component of the final state particles are not contained within the detector exist and can provide additional information on the oscillation parameters. This is especially true in the case of this analysis in which the statistics of neutrino interactions in the far detector is low. Furthermore these non-fiducial events tend to come from the high energy tail in the beam energy spectrum where the probability of oscillation is low. By measuring this part of the energy spectrum the overall normalization of the beam is more constrained enhancing the power in the fit for oscillation parameters. Chapter 8 focuses on the rejection of cosmic rays from this analysis and also the separation of ν_μ events into fiducial and non-fiducial sub-samples.

This analysis consists of comparing the rate of interactions of ν_μ events in the near and far detectors as a function of neutrino energy. Chapter 9 gives the definitions of the samples and event selections used for both the near and far detectors. Chapter 10 describes the method in which events measured in the near detector are extrapolated to the far detector. Chapter 11 explains the systematic uncertainties in this method and presents the affect on the analysis and chapter 12 gives the results of this analysis. Finally chapter 13 has concluding remarks.

Chapter 2

Physics of Neutrinos

2.1 The Standard Model

The standard model is the theory describing the fundamental strong, weak, and electromagnetic forces and the elementary particles that interact through these forces.[1] The basic components of the theory started in 1961 with Glashow combining the electromagnetic and weak interactions into the electroweak theory[8] and was extended throughout the 1960's and 1970's to incorporate the Higgs boson[9] and strong interactions. The basic particles and forces described by the standard model are summarized in figure 2.1. Two kinds of particles exist in the standard model fermions (such as quarks, leptons) and bosons which are depicted in figure 2.1. The quarks and leptons are the elementary particles that make up matter and the bosons are the particles that mediate the interactions of particles.

Quarks and leptons are elementary particles of spin 1/2, fermions. In total there are six quarks, up, down, charm, strange, top and bottom, and there are six leptons, electron, electron neutrino, muon, muon neutrino, tau, and tau neutrino, with each of these having a corresponding antiparticle. They are categorized by what types of forces they can interact with; quarks interact with all three fundamental forces, whereas leptons do not interact with the strong force. Although neutrinos belong to the lepton family which can electromagnetically interact, they have no electric charge leaving them with the ability to only interact through the weak force. Additionally the quarks and

[1] The standard model does not account for the fourth fundamental force, gravity

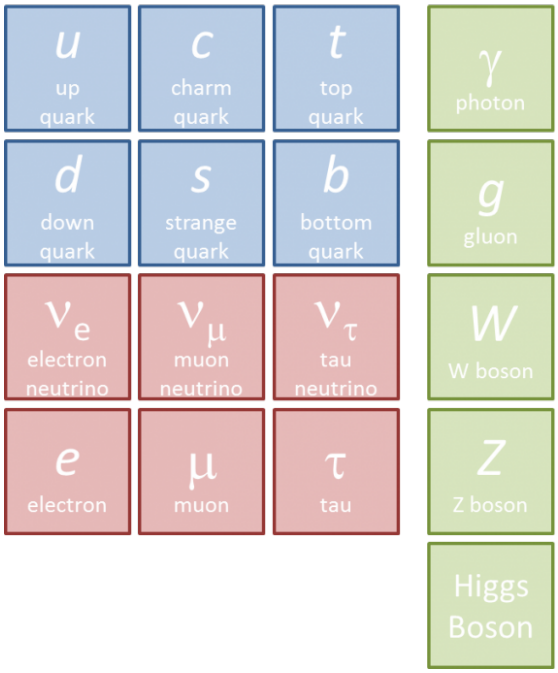

Figure 2.1: Elementary particles in the standard model. Coloring (blue, red, green) corresponds to type of particle (quark, lepton, boson).

leptons are organized into generations denoted as columns in 2.1 with each generation of matter having the same properties as the previous except with larger masses.[2] The lightest generation of matter is made up of the up quark, down quark, electron, and electron neutrino and is stable forming the basis of nucleons, nuclei, and atoms.

Bosons are particles that mediate the interactions in the standard model. In particular strong interactions are described by gluon exchange, weak interactions are described by $W^{\pm}$ and Z° exchanges and electromagnetic interactions are described by photon exchanges. Because neutrinos only interact weakly, all neutrino interactions can be described by the exchanges shown in the Feynman diagrams in Figure 2.2. These interactions are categorized into charged-current (CC) interactions in which a $W^{\pm}$ is exchanged and neutral current (NC) interactions in which a Z° is exchanged. An additional boson, the Higgs, does not immediately represent the interactions of particles

[2] This is yet to be experimentally shown for neutrinos see Section 2.4

that lead to one of the fundamental forces, but instead describes interactions that give the particles in the standard model mass.

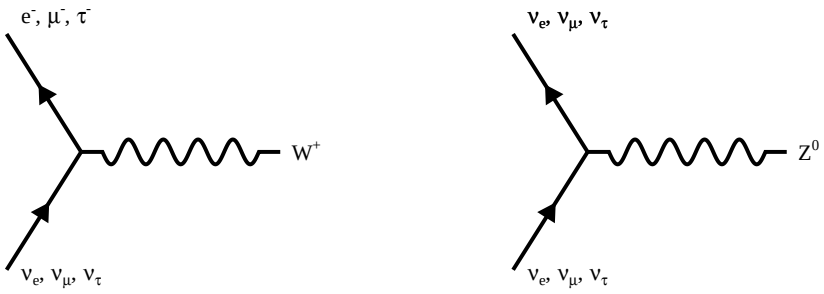

(a) CC Interaction (b) NC Interaction

Figure 2.2: Feynman diagrams of neutrino interactions

The standard model achieved great success in predicting and describing the basic properties and interactions of elementary particles over the last 40 years. Moreover, the discovery of the Higgs boson in 2012[10, 11] solidified the theory by removing the long standing issue of the Higgs existence. However in some ways the known properties of neutrinos do not fit into the basic structure of the standard model. This topic will be revisited in Section 2.6 after a brief overview of neutrino physics.

2.2 Brief History of Neutrino Physics

In 1914 James Chadwick measured the energy spectrum of beta decays [12]. At that time a parent nucleus was thought to decay to only a daughter nucleus and an electron. Chadwick found that the electron energy spectrum was continuous unlike other two body decay products which possessed unique energies. This raised the question as to what happened to the missing energy in the decay. In 1930, Wolfgang Pauli proposed the neutrino as a solution to the neutron decay problem [13]. By introducing an undetectable, light, and neutral particle, Pauli made neutron decay a three body process allowing for a continuous electron energy spectrum while still maintaining energy and momentum conservation.

The existence of neutrinos was not experimentally confirmed until 1956. In their experiment, Reines and Cowan measured the production of positrons by placing protons in front of a source of antineutrinos produced by neutron decays in a nuclear reactor through the reactions [14]:

$$n \longrightarrow pe^{-}\bar{\nu_e} \text{ (reactor)} \tag{2.1}$$

$$\bar{\nu_e}p \longrightarrow e^{+}n \text{ (detector)} \tag{2.2}$$

After production the positron combines with an electron to annihilate into two photons while on a longer time scale a nucleus captures the neutron resulting in another photon being produced. By measuring the signal of the two annihilation photons followed by a single photon they proved that neutrinos exist.

Following Reines and Cowan's discovery it was found in 1962 that more than one flavor of neutrino exists. The measurement of the muon neutrino from the decay of a pion into a muon and muon neutrino at Brookhaven National Laboratory made two observed flavors [15]. In 1989 the ALEPH collaboration at the Large Electron Positron (LEP) collider measured the invisible decay width of Z° bosons, corresponding to decay modes involving neutrinos, to be consistent with three flavors of light, weakly interacting neutrinos [16]. The observation of the tau neutrino in 2000 by the DONUT experiment completed the detection of light neutrinos at three flavors corresponding to the electron, muon, and tau [17]. This was consistent to standard model generational pairing of the neutrinos with a charged lepton.

With the existence of multiple neutrino types, neutrino oscillations between types became possible. Even before the existence of multiple flavors was discerned, Bruno Pontecorvo proposed the idea of neutrinos oscillating between states in 1957 [18]. Because only the electron neutrino existed at that time, he envisioned electron neutrinos oscillating between neutrino and antineutrino.[3] As neutrino flavors came into existence Maki, Nakagawa, and Sakata described the oscillation between electron and muon flavors by carrying over Pontecorvo's framework for two neutrino state oscillation [19]. Later an extension to the theory was developed to include all three neutrino flavors.

[3] Under typical oscillation models, oscillations between antineutrinos and neutrinos do not exist as they would require a right handed neutrino or left handed antineutrino which have never been observed.

The theory of neutrino oscillations, with the inclusion of matter effects, gave an explanation to the experimentally determined solar neutrino problem. In the 1960's Ray Davis detected fewer than the expected number of solar neutrinos predicted from standard solar models in the Homestake experiment [20]. Other later experiments such as Super-Kamiokande (Super-K) and Sudbury Neutrino Observatory (SNO) also confirmed the deficit. In particular the SNO results show direct evidence of neutrino oscillations and solved the solar neutrino problem because of its ability to measure neutral current neutrino interactions in addition to charged current interactions giving an overall neutrino interaction rate for all flavors [21, 22]. The KamLAND experiment confirmed the solar neutrino oscillation parameters found in these experiments using neutrinos from nuclear reactors [23].

2.3 Neutrino Flavor Oscillations

In the standard model neutrinos of definite flavor interact through the weak force with the exchange of Z$^\circ$ and $W^\pm$ bosons, as shown in Figure 2.2. The states of definite flavor are eigenstates of the weak force and the states of definite mass are eigenstates of the Dirac equation applied to the vacuum, but the flavor eigenstates are not the same as the mass eigenstates. Instead the flavor eigenstates can be represented as a superposition of the mass eigenstates. This is represented by the following:

$$|\nu_\alpha\rangle = \sum_{i=1}^{3} U^*_{\alpha i}|\nu_i\rangle \tag{2.3}$$

Where the U matrix is the matrix that rotates the three mass eigenstates into the three flavor eigenstates. This is similar to the common practice in rigid body mechanics of transforming between two Cartesian coordinate systems by use of Euler angles with the addition of the complex phase δ which if nonzero provides charge-parity (CP) violation.

$$U = \begin{pmatrix} c_{12}c_{13} & s_{12}c_{13} & s_{13}e^{-i\delta} \\ -s_{12}c_{23} - c_{12}s_{23}s_{13}e^{i\delta} & c_{12}c_{23} - s_{12}s_{23}s_{13}e^{i\delta} & s_{23}c_{13} \\ s_{12}s_{23} - c_{12}c_{23}s_{13}e^{i\delta} & c_{12}s_{23} - s_{12}c_{23}s_{13}e^{i\delta} & c_{23}c_{13} \end{pmatrix} \tag{2.4}$$

where $s_{ij} = \sin\theta_{ij}$ and $c_{ij} = \cos\theta_{ij}$.

This representation describes the propagation of the neutrino flavors through a vacuum using plane wave solutions to the Dirac equation for the mass eigenstates:

$$|\nu_i(t)\rangle = e^{-i(E_i t - \vec{p_i}\cdot\vec{x})}|\nu_i(0)\rangle \tag{2.5}$$

Using the small mass approximation for neutrinos we can simplify the above by noting that:

$$E_i = \sqrt{p_i^2 + m_i^2} \simeq p_i\left(1 + \frac{m_i^2}{2p_i^2}\right) \simeq E_i + \frac{m_i^2}{2E_i} \tag{2.6}$$

and that the time it takes for a neutrino to travel a distance L is t $\sim$ L resulting in:

$$|\nu_i(L)\rangle = e^{-i\frac{m_i^2 L}{2E_i}}|\nu_i(0)\rangle \tag{2.7}$$

Assuming a neutrino has a well defined energy, E_i can be replaced by E and we can insert equation 2.7 into equation 2.3 to find the flavor content of a neutrino as a function of distance it propagates from the source. Since neutrinos of different mass will propagate at different speeds there is interference between the mass states in the final state allowing for the flavor of the neutrino to oscillate.

Using standard quantum mechanics techniques, the probability that a neutrino that is initially in state α is in state β after it travels a distance L is:

$$P_{\alpha\to\beta} = |\langle\nu_\beta(L)|\nu_\alpha(0)\rangle|^2 = \left|\sum_{i=1}^{3} U_{\alpha i}^* U_{\beta i} e^{i\frac{m_i^2 L}{2E}}\right|^2 \tag{2.8}$$

which results in:

$$P_{\alpha\to\beta} = \sum_{i=1}^{3}\sum_{j=1}^{3} U_{\alpha j}U_{\beta j}^* U_{\alpha i}^* U_{\beta i} e^{-i\frac{m_j^2 L}{2E}} e^{i\frac{m_i^2 L}{2E}} \tag{2.9}$$

This can be further rewritten by making use of the unitarity of U and trigonometric identities as:

$$\begin{aligned} P_{\alpha\to\beta} &= \delta_{\alpha\beta} - 4\sum_{i>j}\Re(U_{\alpha j}U_{\beta j}^* U_{\alpha i}^* U_{\beta i})\sin^2\frac{\Delta m_{ij}^2 L}{4E} \\ &\quad + 2\sum_{i>j}\Im(U_{\alpha j}U_{\beta j}^* U_{\alpha i}^* U_{\beta i})\sin\frac{\Delta m_{ij}^2 L}{2E} \end{aligned} \tag{2.10}$$

where $\Delta m_{ij}^2 = m_i^2 - m_j^2$.

The same formulation to flavor oscillations applies to antineutrinos as well. Transforming to the antineutrino case only requires taking the complex conjugate of the mixing matrix U in the previous equations leaving the oscillation probability, Equation 2.10, unchanged except for the sign of the imaginary terms.

This form is particularly helpful in that if no CP violation occurs, $\delta = 0$, U is a real matrix and the third term completely drops out of the equation. Also, the first term of the equation is only relevant if the neutrino stays in the same flavor state making the second term the term of primary importance in describing oscillations between different flavors. The second term still dominates in the event that CP violation occurs because experiments constrain its effects to be small. Using the framework setup in this section it is evident that six parameters (three angles, two mass differences, and a CP violating phase) completely govern neutrino flavor oscillations in a vacuum.

2.4 Matter Effects and the Mass Hierarchy

Vacuum flavor oscillations provide insight into the properties of neutrinos, but they give no information about the basic attributes of overall mass and the ordering of the mass states known as the mass hierarchy. When neutrinos propagate through matter, they not only oscillate but they do so in such a way that depends on the mass hierarchy because of interactions with matter. Based on current measurements, that determined the mass of ν_1 to be less than that of ν_2 [24], two possible mass hierarchy cases exist as seen in figure 2.3.

While propagating through matter neutrinos can interact with neutrons, protons, and electrons that make up normal matter. It is possible for the matter to modify the oscillations that are seen when neutrinos propagate through vacuum. The only interactions that will modify the oscillations force the initial and final states to be the same, allowing for only forward elastic scattering of neutrinos on the particles in the medium. Quarks comprise the proton and neutron, making the only possible interaction that could potentially modify oscillations the elastic scattering through Z° exchange. Neutrinos scattering on electrons also scatter through the neutral current process, but because they are leptons they can forwardly elastic scatter through $W^\pm$ exchange. Since the weak interaction conserves not only overall lepton number, but also lepton family

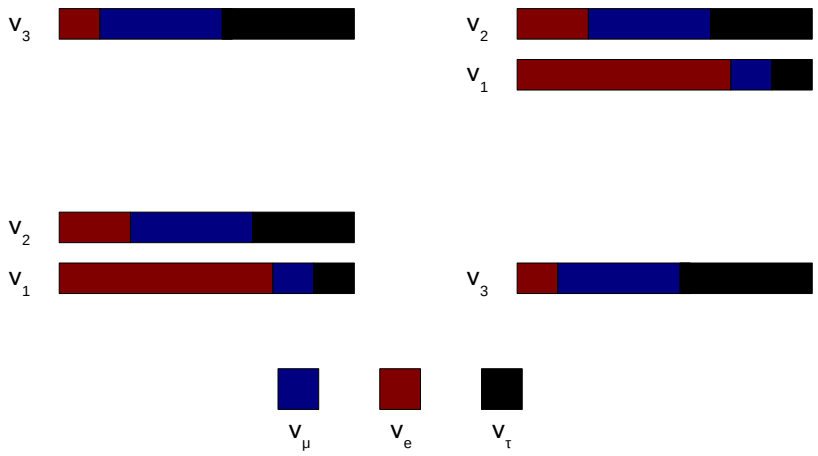

Figure 2.3: Possible mass ordering of neutrinos. Left: Normal mass hierarchy. Right: Inverted mass hierarchy. The vertical axis represents increasing mass and the color represents flavor content of each mass state, note that the color coding is not to scale.

number only the electron neutrino interacts with the electrons making up ordinary matter through the exchange of W^-. Figure 2.4 summarizes all of the possible types of elastic interactions between neutrinos and ordinary matter that modify oscillations.

Including the matter interactions modifies the Hamiltonian governing neutrino propagation to include an extra term for the ν_e to account for the CC interaction and a common term for all three flavors of neutrino to account for the NC interaction. The observation of neutrino oscillations depends on the square of the probability amplitude for seeing a specific flavor of neutrino making any processes common to all three neutrino flavors irrelevant and the only effect on oscillations results from the additional term from the CC process. Antineutrinos also follow this behavior with only the electron antineutrino getting an additional CC interaction added to the Hamiltonian. Inserting the interaction Hamiltonian into the Dirac equation and carrying out the calculation for the probability of flavor oscillations between states results in the same as Equation 2.10 with the following changes [25]:

$$\sin\frac{\Delta m^2_{ij}L}{2E} \longrightarrow \frac{\Delta m^2_{ij}}{\Delta m^2_{ij} \pm 2Ea}\sin\left(\frac{\Delta m^2_{ij}L}{2E} \pm aL\right) \tag{2.11}$$

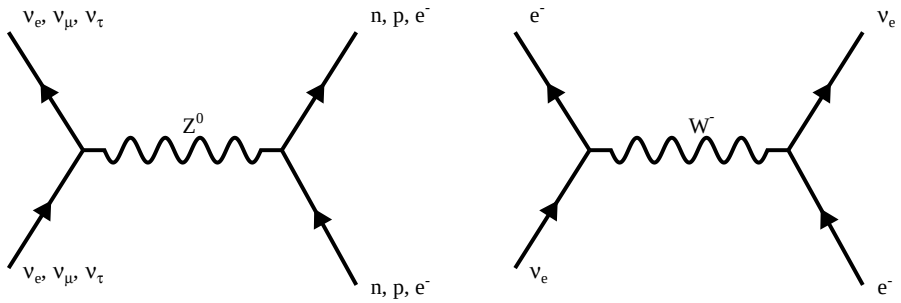

(a) NC forward elastic scattering (b) CC forward elastic scattering

Figure 2.4: Feynman diagrams of neutrino forward elastic scattering with normal matter. Time is in the vertical direction

where

$$a = \frac{G_F n_e E}{\sqrt{2}} \tag{2.12}$$

for $j = 1$, $i = 2, 3$, G_F as Fermi's constant, and n_e as the electron density of matter. The minus sign refers to the case of neutrinos and the plus sign refers to the case of antineutrinos. The neutrino and antineutrino cases come with different signs because the direction of the neutrino arrow reverses in the Feynman diagram of the CC interaction when the antineutrino replaces the neutrino altering the expression of energy and momentum conservation at the diagrams vertices.

For the two choices of mass hierarchy equation 2.11 shows different behaviors for the neutrinos and antineutrinos. For example, the fraction of muon neutrinos oscillating into electron neutrinos increases while the fraction of muon antineutrinos oscillating into electron antineutrinos decreases compared to the oscillations in vacuum for the normal mass hierarchy. The opposite effect occurs for the inverted mass hierarchy.

2.5 Current Knowledge of Neutrino Oscillations

Neutrino oscillation experiments seek to measure the six parameters governing oscillations ($\Delta m^2_{21}, \Delta m^2_{32}, \theta_{12}, \theta_{23}, \theta_{13}$, and δ). Two basic types of experiments exist. Appearance experiments look at the probability for the appearance of a specific neutrino

flavor as a function of energy , $P_{\alpha\to\beta}(E)$, by propagating a known source of neutrinos of flavor α and detecting the number of neutrinos with flavor β at a given distance from the source. Disappearance experiments look at the probability for the disappearance of a specific neutrino flavor, by propagating a known source of neutrinos of flavor α and detecting the number of neutrinos with flavor α at a given distance from the source. A common example of an oscillation experimental setup consists of an initial neutrino source made up of one flavor and known energy with a detector situated a known distance away measuring the appearance of other flavors for the appearance experiment or the number of interactions involving the original neutrino flavor for a disappearance experiment.

The experiments Super-K[26] , SNO[27], and KamLAND[28] provided the first precision measurements of oscillation parameters, measuring θ_{12} and Δm^2_{21}. Super-Kamiokande used a 50 kT water Cherenkov detector to study the interactions of neutrinos generated in the sun, solar neutrinos. The experiment measured a deficit in the angular (baseline) and energy distributions to be consistent with neutrino oscillations. SNO made precision measurements of solar neutrinos using a 1 kT heavy water Cherenkov detector. The experiment compared the electron and non electron component of the solar neutrino spectrum using charged current and neutral current interactions on deuterium. Finally KamLAND measured the disappearance of $\bar{\nu}_e$ from nuclear power plants.

Later experiments focused on measuring the parameters θ_{23} and Δm^2_{32}. Super-K[29] used measurements of neutrinos generated in the Earth's atmosphere, atmospheric neutrinos, to determine the parameters. Similarly IceCube[30] used the ice in the south pole as a Cherenkov detector to measure the atmospheric neutrino rate. The MINOS[7], K2K[31], and T2K[6] experiments are multiple detector experiments looking for the disappearance of an accelerator source of ν_μ's to make the measurement.

Most recently the value of θ_{13} has been measured. The strongest measurements coming from reactor experiments, Daya Bay[32], RENO[33], and Double Chooz[34], similar to KamLAND that measure the disappearance of $\bar{\nu}_e$ coming from nuclear power plants. These experiments differ from KamLAND in that the oscillation baseline is much smaller to be sensitive to oscillations from the θ_{13} and Δm^2_{32} parameters. Additionally these experiments made use of a multiple detector arrangement in which some detectors

were placed near the source and others at the desired baseline far from the near detectors. Other measurements of θ_{13} have been made by the T2K[35] and MINOS[7] experiments making use of the appearance of ν_e in a ν_μ beam.

Of the six parameters that determine neutrino flavor oscillations, experimental data determines five of the parameters reasonably well. Only the CP violating phase δ and mass hierarchy are yet to be determined. Table 2.1 summarizes the best global fit to all the neutrino oscillation data to the oscillation parameters. The CP phase δ is excluded from the table as it has yet to be measured.[4] Of the measured parameters the least well known parameter is the mixing angle θ_{23} which is only known to within roughly 6°.

Table 2.1: Best fit values of oscillation parameters. No measurements of δ with greater than 3σ significance currently exist. [1].

Parameter	Best-Fit
Δm^2_{21}	$7.53 \pm 0.18 \times 10^{-5}$ eV^2
$\lvert\Delta m^2_{32}\rvert$	$2.44 \pm 0.06 \times 10^{-3}$ eV^2 (normal mass hierarchy)
$\lvert\Delta m^2_{32}\rvert$	$2.49 \pm 0.06 \times 10^{-3}$ eV^2 (inverted mass hierarchy)
$\sin^2\theta_{12}$	0.304 ± 0.014
$\sin^2\theta_{23}$	$0.514^{+0.055}_{-0.056}$ (normal mass hierarchy)
$\sin^2\theta_{23}$	0.511 ± 0.055 (inverted mass hierarchy)
$\sin^2\theta_{13}$	0.0219 ± 0.0012

2.6 Theoretical Interest

With neutrinos making up part of the fundamental particles in the standard model it is important to understand their basic properties, like mass, in order to have a full understanding of the theory. Non-neutrino particles in the standard model get their mass from couplings to Higgs boson which link the left and right handed states of the

[4] T2K shows a slight favoring of δ near -$\pi/2$ when constrained by the reactor experiments measurements of θ_{13}[36].

particle through Lagrangian terms of the following sort:

$$\mathscr{L}_{Dirac} = -m\left(\bar{\psi}_L\psi_R + \bar{\psi}_R\psi_L\right). \tag{2.13}$$

However, neutrinos in the standard model only have a left helicity state in each generation so they can not get their mass from the same type of mass term without introduction of another right handed neutrino that they could couple to. Other Lagrangian terms could be responsible for neutrino mass such as a Majorana mass term of the following form:

$$\mathscr{L}_{Majorana} = -\frac{m}{2}\left(\bar{\psi}_L\right)^C\psi_L + h.c. \tag{2.14}$$

These mass terms would imply that neutrino are their own antiparticles and do not conserve lepton number. Measurements of neutrino oscillations provide definitive proof of a nonzero neutrino mass. Furthermore, to date they are the only direct method able to determine neutrino masses to be nonzero. As such it is important to continue to probe neutrino oscillations as a handle on neutrino mass. In particular obtaining precision measurements of the oscillations parameters could prove to be useful. With θ_{23} being the least well known oscillation parameter, aside from δ, further measurements of this parameter along with the mass splittings could be useful.

Oscillations may also provide insight into the the matter-antimatter asymmetry in the Universe. Under the assumption that the Universe started with equal amounts of matter and antimatter a mechanism needs to exist that can generate the excess in matter seen today. One such mechanism requires processes that violate lepton number and CP symmetry[37]. Direct measurements of the oscillation parameter δ determine if neutrino oscillations could fulfill some part of the CP violating processes necessary in such a model. However, measuring a non-zero value of δ does not determine whether neutrinos are responsible for the asymmetry of matter and antimatter. Current experiments trying to measure such δ, T2K and NOνA, do so through the measurement of ν_e and $\bar{\nu}_e$ appearance in a ν_μ beam. Using this technique makes the oscillation probabilities dependent on all three mixing angles. Improvement of the precision in the measurements of the mixing angles, specifically the least well known θ_{23}, improves the ability to measure δ.

Chapter 3

The NOνA Experiment

3.1 NOνA Experiment

The NOνA experiment measures the oscillation of the neutrinos from an accelerator source of neutrinos created at Fermilab. The NOνA experiment was designed before the value of the θ_{13} was known with the primary goal of detecting ν_e appearance. It is made up of two main components, a beam of neutrinos described in section 3.2 and the detectors used to measure neutrino interactions described in section 3.3. Finally section 3.5 describes the oscillation measurements in the context of the NOνA experiment.

3.2 NuMI Beam

The Neutrinos at the Main Injector (NuMI) facility at Fermilab was originally built for the Main Injector Neutrino Oscillation Search (MINOS) experiment[38] and has undergone upgrades for the NOνA experiment. The facility produces a high intensity beam of muon neutrinos using 120 GeV protons from the Main Injector. A 10 μs pulse of protons from the Main Injector are delivered to a graphite target every 1.33 s. This pulse is called a beam spill or simply a spill.

Interactions of the protons with the target produce secondary particles which are mostly comprised of pions and kaons. The target is made of 50 collinear graphite fins with each fin 7.4 mm wide and 24 mm long[39]. Figure 3.1 depicts the NuMI beam. Magnetic horns sitting behind the target are used to focus the charged particles resulting

from the collisions of the protons with the target into a decay pipe. The decay pipe is 675 m long and 2 m in diameter. In the decay pipe, the secondary pions and kaons decay. More than 99% of pions and over 63% of kaons decay into anti-muons and ν_μ creating a source of neutrinos. Changing the direction of current in the magnetic horns changes the sign of the charged particles that get into the decay pipe. Allowing positively charged particles results in a beam of anti-muons and ν_μ's whereas negatively charged particles result in muons and $\bar{\nu}_\mu$'s. At the end of the decay pipe lies a monitor to detect hadrons and an absorber to absorb any particles coming from the target other than muons and neutrinos. Finally, a series of muon detectors and rock are placed in the beam path to remove muons from the beam creating a beam of muon flavored (anti)neutrinos. The NuMI beam is aimed at the MINOS near detector located at Fermilab and far detector located in the Soudan mine in northern Minnesota. The total beam exposure is measured in units of protons on target, POT, as this determines how many interactions occur in the target that could result in a neutrino being produced. On average each spill in this analysis had 2.5×10^{13} POT.

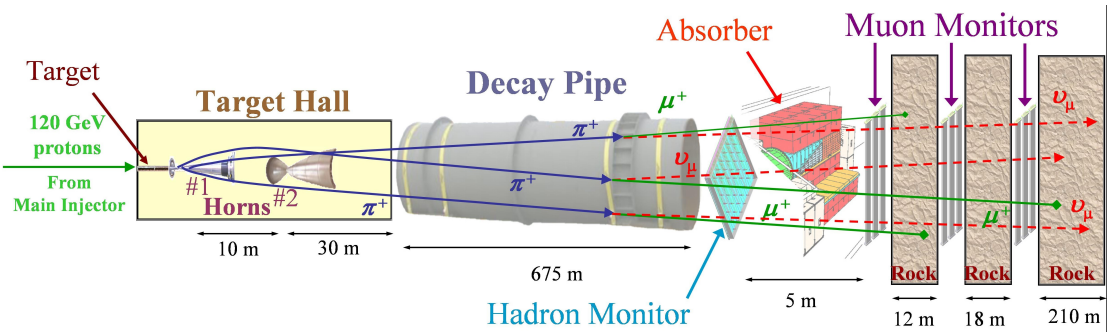

Figure 3.1: NuMI beam [2].

3.2.1 Run Periods Used

In order to facilitate the long term goals of the NOνA experiment, the Main Injector and Recycler beam facilities at Fermilab underwent upgrades to bring the maximum power up to 700 kW from the 500 kW original design. The beam data used in this analysis comes from two major running periods. The first period, pre-shutdown, comes

from March 2014 to August 2014. During this time period not all beam upgrades to reach 700 kW design power were completed and the beam typically operated at 250 kW. At the end of the first period, a shutdown occurred in which the remaining upgrades to the Recycler were completed to achieve a maximum beam power of 700 kW. The second period, post-shutdown, comes from November 2014 to May 2015 following the shutdown period. During this period, the beam power was slowly ramped up to test all systems upgraded. During the post-shutdown period the beam power started at 250 kW and reached 420 kW near the end of the period. Table 3.1 shows the total exposure recorded at the far detector during these run periods.

Table 3.1: Summary of recorded beam data at the far detector.

	POT/10^{20}	Livetime (s)
Pre-shutdown	1.27	132
Post-shutdown	2.25	102
Total	3.52	234

3.3 NOνA Detectors

3.3.1 Detector Design

The NOνA experiment consists of two detectors, near and far. The two detectors are designed very similarly to each other in order to minimize systematic uncertainties in the near to far extrapolation. The general design of the detectors is presented here with the following sections presenting information unique to each of the two detectors.

The NOνA detectors are mostly active tracking calorimeters meaning that they have high granularity to distinguish individual particles from each other and also the ability to measure particle energy depositions. The detectors are designed to measure neutrino interactions in the few GeV energy regime through patterns measured in the data. Specifically, the detectors are designed to distinguish electromagnetic showers originating from photons from those originating from electrons. This requirement stems from the aim to separate ν_e CC events which result in electromagnetic showers induced from an electron from NC events which can produce photon induced electromagnetic

showers from π°'s which are a major background to measuring ν_e appearance.

Each detector is based on a cellular structure. A single cell is made from extruded polyvinyl chloride (PVC) doped with titanium dioxide to enhance reflectivity. The cells are 3.6 cm by 5.6 cm in cross section and 4.2 m long in the near detector and 15.2 m long in the far detector. Within the cell is a polystyrene looped wavelength shifting (WLS) fiber. The cell is filled with liquid scintillator which is composed of mineral oil doped with ~5% pseudocumene[1] . Charged particles passing through a cell produce scintillation light that is multiply reflected off of the cell walls. A fraction of the scintillation light impinges on the WLS fiber and is absorbed and remitted isotropically at longer wavelength. Typical scintillation light is in the blue spectrum, but is remitted by the WLS fiber in the green spectrum shown in Figure 3.2. A fraction of the emitted light totally internally reflects in the fiber and is transported to the fiber ends. Each cell is 0.18 radiations lengths wide with a minimum ionizing particle depositing 10 MeV of energy as it passes through the width of the cell.

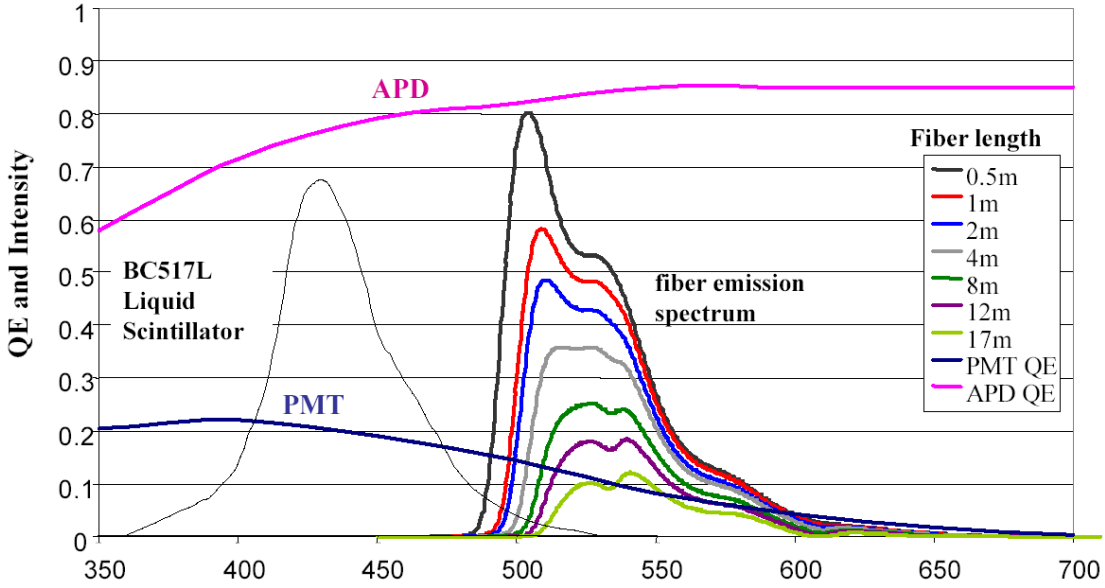

Figure 3.2: Fiber emission spectra and quantum efficiencies of APDs and PMTs[3].

[1] 1,2,4-Trimethylbenzene

Cells are extruded 16 at a time in an extrusion. Within an extrusion each cell is separated from the next by 3.3 mm of PVC. Two extrusions are glued together along the length of the cell to form a planar unit of 32 two cells called a module. All of the fibers from each cell in the module are optically separated from each other but connected to a single optical connector at the fiber ends. The optical connector attaches the module to an avalanche photo diode (APD) shown in Figure 3.3. Each fiber end is connected to the APD with both fiber ends from a single cell connected to one pixel of the APD. APDs were chosen over other technologies such as photo-multiplier tubes (PMTs) because of the higher quantum efficiency in the light spectrum of interest seen in figure 3.2. Each pixel is then read out by the data acquisition (DAQ) system.

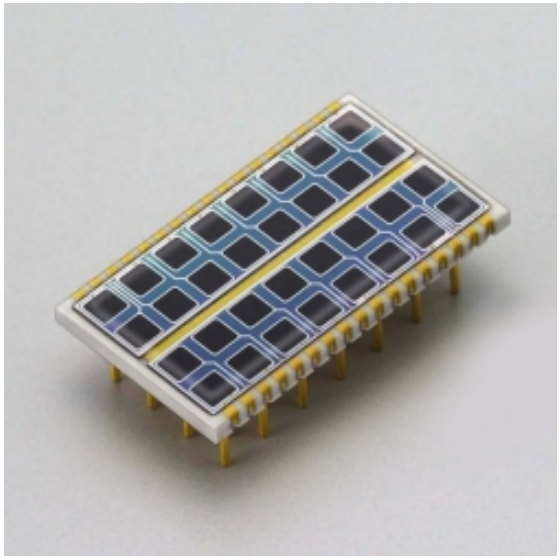

Figure 3.3: APD[4]

Modules are glued together to from planes. In each plane the modules are either vertically or horizontally aligned and each plane is orthogonally rotated with respect to the previous plane. The detectors are placed such that the planes are oriented perpendicularly to the NuMI beam. The alternating orientation of the detector planes gives two independent detector views which can be reconstructed into full three dimensional

events with cells aligned horizontally measuring the height in the detector and the vertically aligned cells measuring the horizontal position in the detector. Coordinates are assigned to the detectors such that increasing plane in the detector defines the z dimension, and the positive x and y directions are the side and top of the detector close to the electronic readout of the modules. The origin of the detectors is defined to be the center of the front face of the first plane of the detector. Figure 3.4 depicts the structure of the detectors.

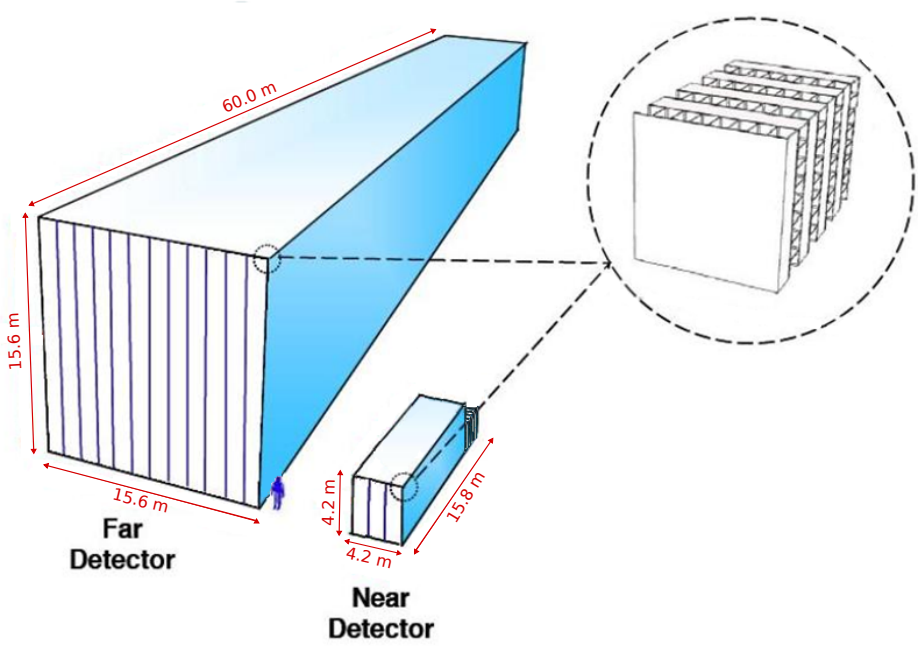

Figure 3.4: The NOνA detectors.

3.3.2 Data Acquisition

When light from a signal is incident on a pixel in an APD an amplified signal is produced. The DAQ system records and stores data from APDs for offline analysis. A schematic of the DAQ system is shown in figure 3.5. The signal from the APD is further amplified and shaped by an ASIC on the front end board (FEB) electronics resulting in an electronic wave-form given in equation 3.1 for the charge as a function of time, $q(t)$, described by

the rise, R, and fall, F, times of the electronics:

$$q(t) \propto \frac{F}{F-R}\left(e^{-\frac{t}{F}} - e^{-\frac{t}{R}}\right) \tag{3.1}$$

This waveform is sampled at discrete intervals separated by 62.5 ns by a high speed ADC to obtain multiple points along the baseline rise and fall of a signal. Additionally each pixel on the APD is sampled in a phased manner so that only 8 pixels on the same APD are sampled at the same time. A dual correlated sampling algorithm determines if the signal is above threshold by comparing the current ADC value to the value three sampling times before. The threshold of each channel is set independently and determined as the value that is four times higher than the standard deviation of the noise ADC distribution. When a signal is above threshold the data from the channel is recorded, as a hit, in the form of a timestamp from a TDC attached to the channel and the ADC values of the channel.

The hits from the FEBs are sent to a data concentrator module (DCM) which aggregates and sorts the hits from 64 FEBs. The DCM is a custom built computer that takes the FEB data and time sorts them. Once the DCM builds a data stream of 5 ms length it sends the data to a buffer node where the data is stored until a trigger decision is made. By design the DAQ system runs in a continuous readout mode so that all hits recorded in the detector are stored until a trigger decision is made. Once stored in the buffer there is 20 s to make a trigger decision. For the beam neutrino analysis a signal sent from the accelerator corresponding to a beam spill is used for triggering. When triggered 550 μs of data centered on the beam spill in the buffer nodes is grouped together as a trigger window and sent to permanent storage.

3.3.3 The Near Detector

The NOνA near detector is located in a cavern at Fermilab 1 km downstream of the NuMI beam and 100 m underground. The layout of the cavern and a picture of the detector are shown in figure 3.6. The detector consists of 20,192 cells arranged in 214 planes with a mass of 280 tons. Each plane is comprised of 3 modules giving the near detector a width and height of 4.2 m (except in the muon catcher) and a length of 15.8 m.

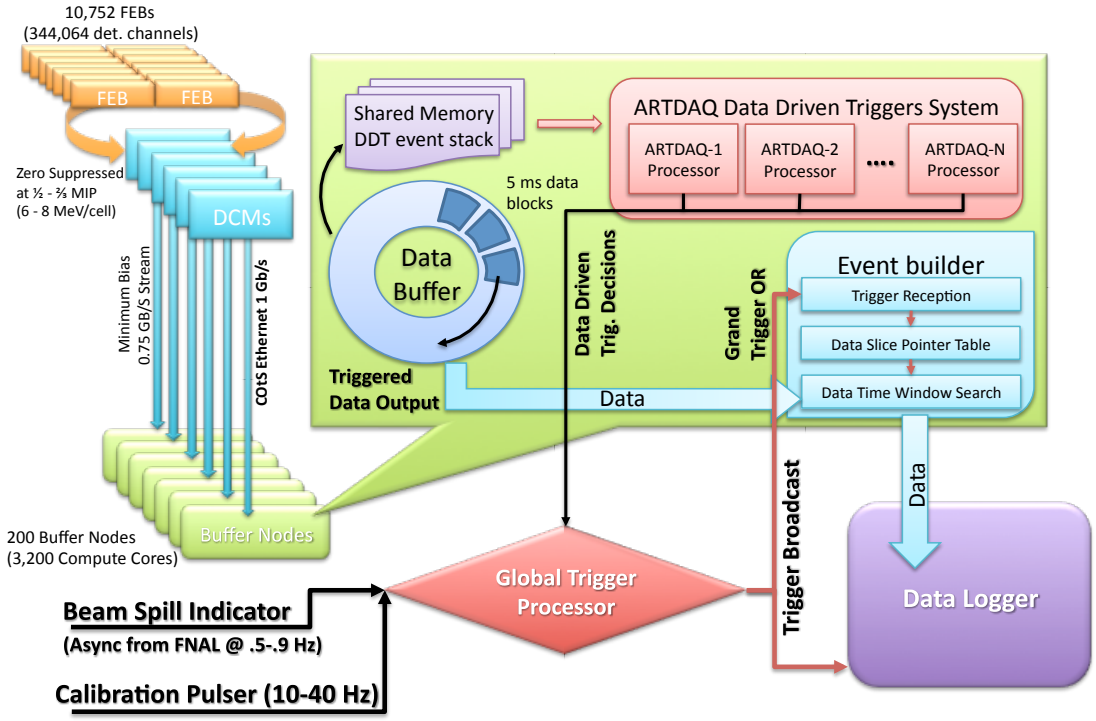

Figure 3.5: DAQ schematic.

Additionally the near detector employs a muon catcher at the downstream end of the detector. In the muon catcher steel planes are interspersed with the active PVC planes. These steel planes are 4 inches thick and are inserted between pairs of vertical and horizontally aligned planes with the final active section of the detector being comprised of three active planes instead of two. In the muon catcher section of the detector the planes are only 2.8 m, two modules, high in the vertical dimension, but still 4.2 m, three modules, wide. The muon catcher is used to range out muons that are produced in the active region of the detector. A muon traversing the full length of the muon catcher would lose on average energy of 1.6 GeV compared to 0.6 GeV if traversing the same length of PVC only planes. The addition of the muon catcher allows for the detector to range out muons emerging from a contained ν_μ interaction of 4.2 GeV total energy.

The rock above the ND cavern is 224 meters water equivalent and provides significant

Figure 3.6: NOνA near detector.

cosmic ray shielding for the detector. The resulting rate of cosmic rays in the near detector is 24 Hz[40] leading to 1 cosmic ray in every 4000 10 μs beam spill. By comparison the data have an average of 9.9 neutrino interactions [41] in every 10 μs beam spill window making the cosmic ray rate negligible compared to the neutrino signal in the near detector.

With the high rate of neutrinos in any given beam spill in the near detector, there is a chance that two neutrino interactions overlap in time and can not be disentangled from each other. This effect is called pile-up and will be discussed more in chapter 5. The FEB settings in the near detectors were set to a rise time of 136 ns and a fall time of 4500 ns to get the best timing resolution of individual hits in order to minimize possibility of pile-up. With these settings the ratio of the ADC value to the number of photo-electrons (PE) incident on the APD is 2.4. Additionally the DAQ was run in a

multipoint sampling mode in which four ADC points along the channel response curve along with the TDC are saved for every hit that falls above threshold. This allowed for a fit to the channel response to a function of the form shown in equation 3.1 which improves the timing and charge measurements compared to any single charge and time measurement. The time resolution of hits as a function of PE was determined from measuring time distribution of hits belonging to single cosmic ray muons correcting for the time of flight [42]. Hits with greater than 200 PE have hit time resolution less than 8 ns.

3.3.4 The Far Detector

The NOνA far detector is located near Ash River in northern Minnesota, 810 km away from the near detector. The far detector is situated in a detector hall such that 1/6 of the detector is above the surface of the Earth and the bottom 5/6 of the detector is below the surface of the Earth. The detector hall roof is constructed with concrete and an 12 inch barite overburden layer. The total overburden provides protection against cosmic rays with the minimum shielding depth of 3 m, 9 radiation lengths. The layout of the detector hall and a picture of the detector are shown in figure 3.7. The detector consists of 344,064 channels arranged in 896 planes with a mass of 14 kT. Each plane is comprised of 12 modules making the FD have a width and height of 15.6 m and a length of 59.6 m.

During the data taking period in this analysis the far detector was undergoing construction and commissioning. This led to taking data in partial detector configurations in which only 4 or more diblocks of the detector were used. Where a diblock is defined as 128 planes, the number of planes of FEBs encompassed by a single DCM. Most of the POT and exposure, POT$\times$detector mass, recorded was in a configuration of 14 diblocks.

The far detector has nearly the opposite event rate characteristics than the near detector. Because the far detector has minimal cosmic shielding and increased size, the cosmic rate in the far detector is much higher than the near detector at 160 kHz in the full 14 kT detector[43]. Additionally because of the distance away from the neutrino beam source the neutrino interaction rate is much smaller with only 1.0 expected ν_μ CC event with total energy less than 5 GeV contained within the detector every 3 days[43] in the full 14 kT detector with 700 kW beam power. In general the primary need of the DAQ system is to precisely measure the topologies of the interactions in the detector in order to identify as many neutrinos as possible while also rejecting as many cosmic rays as possible. The FEB settings in the far detectors were set to a rise time of 432 ns and a fall time of 7000 ns to get the best signal to noise ratio in the channel response measurement. With these settings the ratio of the ADC value to the number of photo-electrons (PE) incident on the APD is 2.3. The DAQ was run in two modes during the course of data taking, single-point and multi-point. The multipoint sampling mode works in the same manner as described for the near detector. The time resolution of hits as a function of PE was determined from measuring time distribution

of hits belonging to single cosmic ray muons correcting for the time of flight[42]. Hits with greater than 200 PE have hit time resolution less than 11 ns. In the pre-shutdown data taking period, the multipoint readout of the electronics was not possible. Instead the far detector operated in single-point readout mode in which only one ADC point along with the TDC was saved for each hit. This prevents fitting to the functional form of the electronics response and results in a worse individual hit time resolution. In the single-point readout mode hits of greater than 200 PE having hit time resolutions of 144 ns[42].

The length of the cells in the far detector leads to significant attenuation in the fiber and the possibility of the energy depositions falling below threshold for making a hit. The rate at which this happens is measured in terms of the efficiency of recording hits and shown in figure 3.8. The efficiency was measured from the rate of missing hits in the expected cells on muon cosmic ray tracks. The efficiency was found to be greater than 90% at the far end of the cell away from the electronic readout[44].

In the far detector the trigger decision for the neutrino beam data is delivered to the detector from a GPS signal. The signal is sent to a master timing distribution unit (TDU) which then synchronizes the detector time by distributing the time to slave TDUs which then propagate the correct time to the DCMs. It was discovered that the master TDU had a failure mode in which the time would be 64 μs off of the normal synchronized time shifting the beam window in which neutrino interactions should be expected[45]. In the pre-shutdown data there was no way to determine when this failure mode occurs. In this data a second timing window shifted by 64 μs is also considered in this analysis. In the post-shutdown data mechanisms were put in place to recognize this failure mode so that only one timing window exists.

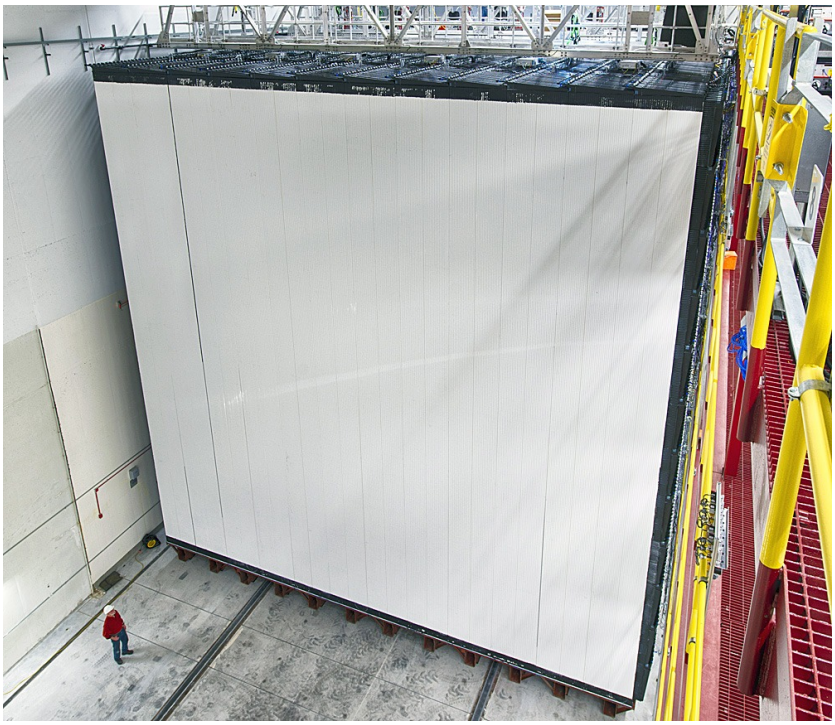

(a) Partially completed NOνA far detector

(b) Top view of NOνA far detector

Figure 3.7: NOνA far detector

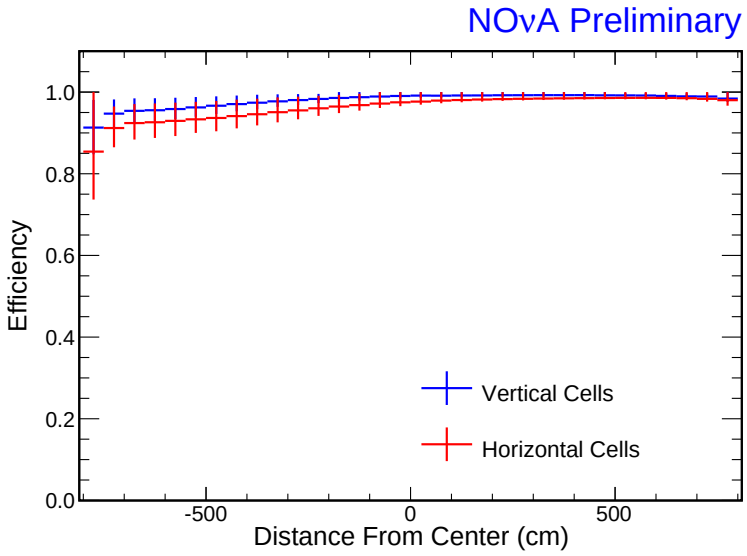

Figure 3.8: Hit efficiency in the far detector. Differences between horizontal and vertical modules arise from voids of scintillator in the horizontal modules.

3.3.5 Off-Axis Detector Placement

The NOνA detectors lie off-axis to the NuMI beam by 14 mrad. By placing the detectors off-axis, the flux and energy of the neutrinos increase the sensitivity of the transition probability measurement. The flux and energy dependency on the off-axis angle simply comes from the relativistic kinematics of the pion and kaon decay which produce the beam of muon neutrinos. In their rest frame pions and kaons decay isotropically giving a uniform distribution of neutrinos. The rest frame of the pions does not coincide with the lab frame since the pions and kaons are moving with respect to the detectors. When boosted to detector frame the flux and energy take on the following relations for neutrinos decaying from pions:

$$F = \left(\frac{2\gamma}{1+\gamma^2\theta^2}\right)^2 \frac{A}{4\pi z^2} \tag{3.2}$$

$$E_\nu = \frac{0.43E_\pi}{1+\gamma^2\theta^2} \tag{3.3}$$

where A is the detector area, z is the distance from the decaying particle, E_π is the energy of the pion, θ is the angle off-axis, and $\gamma = E_\pi/m_\pi$. Decaying kaons produce the same results except with the 0.43 in the energy expression replaced with 0.96 and using kaon energy and mass appropriately. Using these expressions, a neutrino beam of much more narrow width can be constructed off-axis compared to on axis. This relation is seen in figure 3.9 with the resulting unoscillated and oscillated spectrum of CC events in the far detector shown in figure 3.10 and figure 3.11. In order to get the best measurement of ν_e appearance the detectors were placed 14 mrad off-axis to the beam. This results in a beam peak energy of 2 GeV, near the ν_μ oscillation maximum for a baseline of 810 km. Diagrams of the detector placement relative to the beam are shown in figure 3.12.

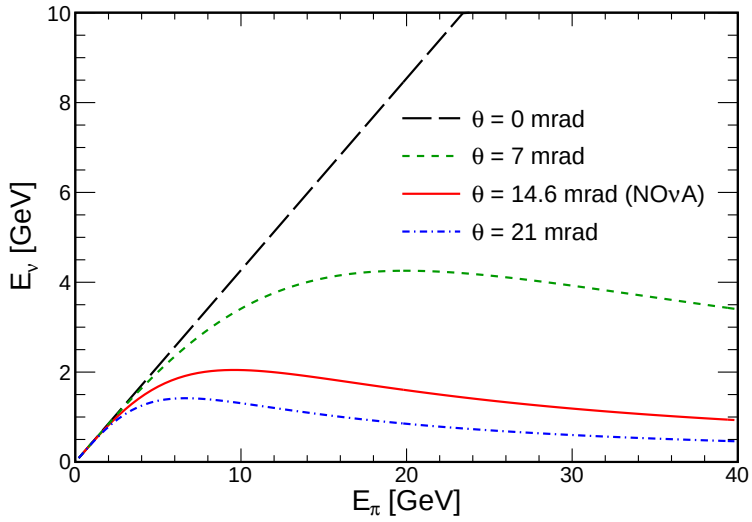

Figure 3.9: Neutrino energy as a function of parent pion energy for various off-axis locations.

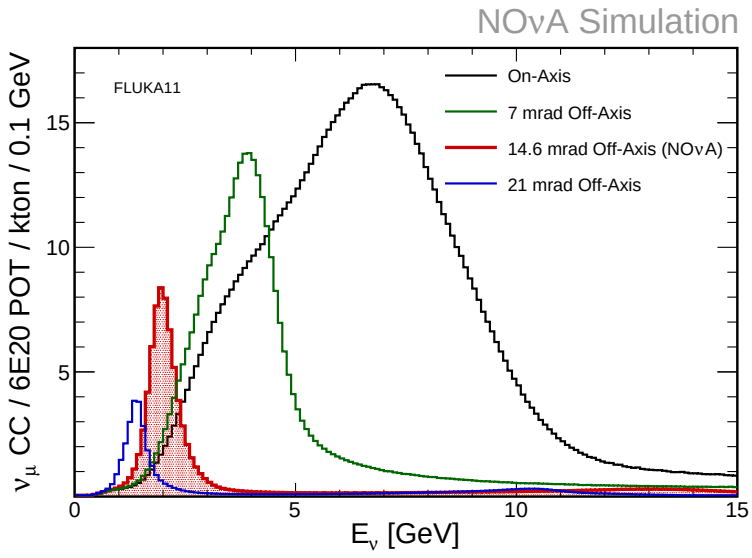

Figure 3.10: Unoscillated neutrino energy spectrum of CC events in the far detector.

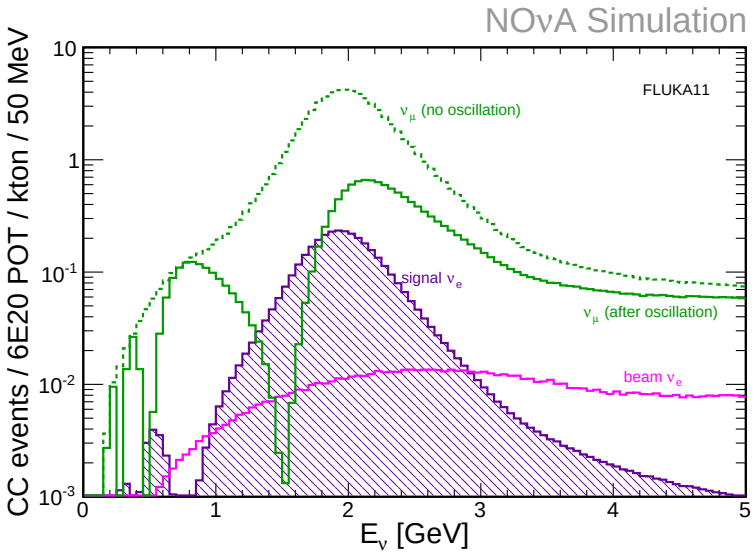

Figure 3.11: Oscillated neutrino energy spectrum of CC events in the far detector.

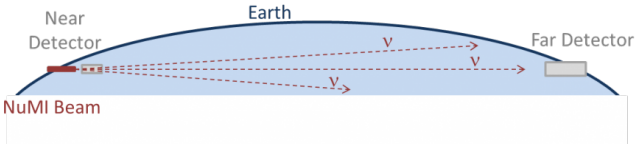

(a)

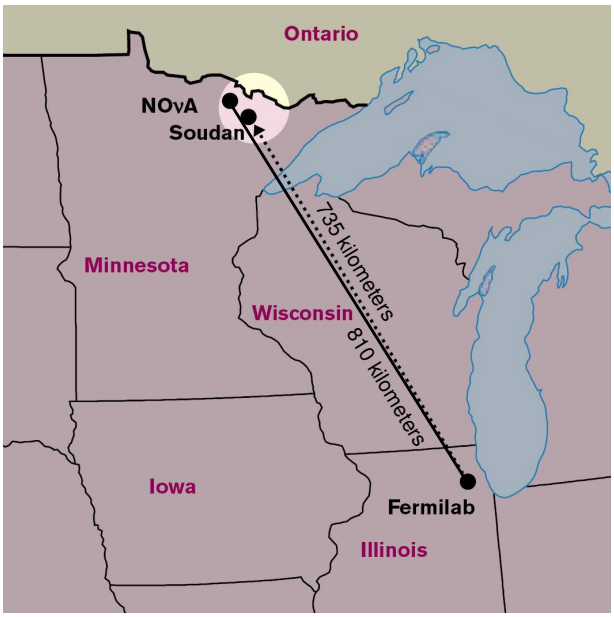

(b)

Figure 3.12: NOνA detector placement relative to NuMI beam

3.4 Neutrino Interactions in NOνA

In the intermediate, ∼0.1 - 20 GeV, beam energy range utilized by NOνA three main categories of neutrino interactions occur: quasielastic (QE) scattering, resonance (RES) scattering, and deep inelastic (DIS) scattering. The total neutrino cross sections and the components of each type of scattering process across the energy range relevant for NOνA are shown in figure 3.13. Near the peak of the beam neutrino energy the three processes roughly occur at the same rate. QE scattering describes the process of a neutrino scattering off of a whole nucleon in a nucleus typically liberating the nucleon (and possibly other nucleon due to internuclear scattering) from the nucleus. RES scattering is the same as QE scattering except that the interaction with the target nucleon results in a baryonic resonance state (Δ and N^*) which decay usually producing mesons. DIS scattering describes the processes in which the neutrino scatters off of individual quarks in the target nucleon. These three types of neutrino interactions lead to a variety of final states and topologies seen in the NOνA detectors. These topologies will be further discussed in chapters 6 and 7 as they relate to signal identification and classification.

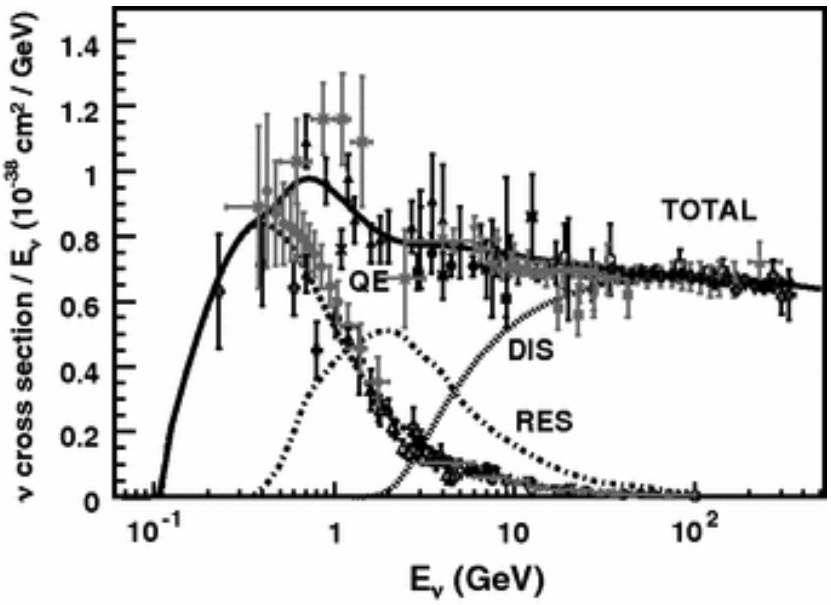

Figure 3.13: Neutrino cross section as a function of energy[5].

3.5 NOνA Oscillation Measurements

There are three potential oscillation measurements the NOνA experiment could make: ν_μ disappearance, ν_e appearance, and ν_τ appearance. These channels are measured through the observation of CC interactions in the near and far detectors. Only CC interactions can be used to measure flavor composition because they result in a lepton of the same flavor as the incoming neutrino flavor. NC interactions result in an outgoing, undetected neutrino and is independent of the neutrino flavor. Given the current knowledge of oscillation parameters the primary oscillation is $\nu_\mu \rightarrow \nu_\tau$; however, measurement of ν_τ appearance through ν_τ CC interactions is kinematically constrained in the peak region. This oscillation channel is yet to be shown as a measurement that can be made by NOνA and will not be discussed further. For the first two oscillation channels, many simplifications to the full oscillation probability, equation 2.10, can be made. The mass splittings are such that $\Delta m^2_{13} \approx \Delta m^2_{23}$ and are much larger than Δm^2_{12}. At the baseline and beam energy L/E combines so that only oscillations from the larger two mass splittings are visible in NOνA. Applying these simplifications results in the leading order expression for the ν_μ survival probability of

$$P_{\nu_\mu \rightarrow \nu_\mu} = 1 - \sin^2(2\theta_{23}) \sin^2\left(1.27 \frac{\Delta m^2_{32} L}{E}\right) \tag{3.4}$$

and the leading order ν_e appearance probability is given by:

$$P_{\nu_\mu \rightarrow \nu_e} = \sin^2(\theta_{23}) \sin^2(2\theta_{13}) \sin^2\left(1.27 \frac{\Delta m^2_{32} L}{E}\right) + P_{CP} \tag{3.5}$$

where the ν_e appearance probability has a CP contributing term, P_{CP} of the following form

$$\begin{aligned} P_{CP} &= \cos\theta_{13} \sin\theta_{12} \sin\theta_{23} \sin\left(1.27 \frac{\Delta m^2_{31} L}{E}\right) \sin\left(1.27 \frac{\Delta m^2_{21} L}{E}\right) \\ &\quad \left(\cos\delta \cos\left(1.27 \frac{\Delta m^2_{32} L}{E}\right) \pm \sin\delta \sin\left(1.27 \frac{\Delta m^2_{32} L}{E}\right)\right) \end{aligned} \tag{3.6}$$

The top sign in P_{CP} corresponds to neutrinos and the bottom sign to antineutrinos. The previous three equations assume that E is in units of GeV, L in units of km, and all Δm^2 in units of eV^2.

This analysis looks at ν_μ disappearance. These measurements are used to determine oscillation parameters θ_{23} and Δm^2_{32}. From equation 3.4 the parameter of Δm^2_{32} can be

interpreted as the location in the energy spectrum at which the maximum oscillation occurs, this is near 1.6 GeV in figure 3.11. The parameter θ_{23} controls the depth of the oscillation dip, i.e. how many ν_μ are expected to disappear.

Even though the NOνA experiment was designed to specifically look for ν_e appearance it can function to measure ν_μ disappearance to the point that it can improve the current measurement of the least known oscillation parameter θ_{23}[46]. This power comes from the high granularity of the detector which allows for precise reconstruction of ν_μ energies, discussed in chapter 7, and the beam peak position being located near the oscillation maximum. Precision energy measurements allow for precise determination of the location of the minimum in the oscillated far detector spectrum and the number of events in the oscillation region. With the beam peak position near the oscillation maximum, many of the expected ν_μ's will have oscillated to a different flavor at the far detector allowing for a high statistics measurement of the number of missing ν_μ's. Additionally without many high energy neutrinos in the beam, background interactions which can fake a ν_μ CC interaction through the feed-down effect, discussed in chapter 6, are minimized. The detailed characteristics of the topology and identification of ν_μ CC events is also discussed in chapter 6.

Appearance of ν_e could also be used to determine θ_{23} as it enters the leading order oscillation probability in equation 3.5. But, unlike the disappearance probability there is also a dependence on the undetermined CP violating phase in the oscillation probability making precision measurements of θ_{23} difficult. Additionally the probability of oscillation to ν_e is small making a high precision measurement difficult due to limited statistics. However, the θ_{23} term comes in without a 2 in the leading sinusoidal term making it sensitive to the octant of θ_{23}, whether $\theta_{23} > 45^\circ$ or not.

Chapter 4

Simulation

4.1 Introduction

This analysis relies on the use of Monte Carlo simulation to predict the spectrum of events at the far detector, develop analysis techniques, evaluate the analysis performance, and perform systematic uncertainty studies. The reliance on the simulation by this analysis make it important that the simulation is accurate and reliable as well as mandates that cross checks be performed to verify the validity of the simulation. There are five main components of the simulation that will be described in this chapter: the beam, neutrino interactions, cosmic ray interactions, propagation of particles emerging from interactions, and the detector response. Analysis cross checks of the simulation are discusses in chapter 9 and systematics due to the uncertainty in the simulation are discussed in chapter 11. In total this analysis uses 2×10^6 simulated trigger windows in the far detector and 40×10^6 simulated trigger windows in the near detector along with additional samples generated for the purpose of calibration of the simulation and systematic studies.

4.2 Beam

Beam simulations determine the neutrino flux that impinge on both the near and far detector. The beam simulation consists of simulating the interactions of 120 GeV protons from the Main Injector with the target and the resulting interactions in the target hall

resulting in a neutrino beam. The beam simulation is done using the FLUGG[47] simulation package. FLUGG combines two simulations FLUKA[48, 49] and GEANT4[50, 51] to get a complete model of the beam. GEANT4 is used to handle the geometry modeling of the target, horns, target hall, and decay volume. FLUKA is used to determine the interactions of particles within the geometry. Secondary particles produced from the initial interaction from protons with the target are propagated through the geometry where they may continue to interact or decay. Neutrinos produced from decay products of particles are saved for further use in the simulation.

4.3 Neutrino Interactions

Neutrinos produced from the beam simulation are used in the simulation of interactions expected in the near and far detector. The interactions of the neutrinos with the detector and surrounding material are performed by the GENIE[52] simulation package. GENIE creates interactions in the detector volumes by sampling the probabilities of the neutrino creation from the beam simulation and the neutrino interaction cross sections. GENIE simulates the type of interaction that the neutrino has with the detector material and determines the final particles emerging from the nucleus.

The simulated detector volume includes the detector itself and the material surrounding the detectors in the detector halls. In the near detector there is a significant amount of neutrino interactions with the rock upstream of the detector that lies outside the detector hall that results in particle interactions in the detector at the same time as neutrinos that interact within the detector. Because they are computationally hard to simulate these rock interactions are simulated separately and independently from the in detector events in smaller total number than would be expected in a complete simulation of the near detector. The resulting rock interactions are then randomly overlaid with the detector events so that the total number of neutrino interactions in the detector is consistent to what is expected. Because of the small statistics the rock interactions are reused many times. Rock interactions are rejected by analysis cuts so this has no significant impact on the results of the analysis. In the far detector no rock interactions are ever expected to overlap with in detector neutrino interactions. Additionally the far detector is simulated in a mode in which every simulated trigger window has a neutrino

interaction.

4.4 Cosmic Rays

In addition to neutrino interactions in the detector, simulation of cosmic rays are important for this analysis. CRY [53] is used to simulate the cosmic ray interactions with the detector. CRY simulates cosmic rays particle shower distributions from tables derived from full simulations of primary cosmic rays in the atmosphere. From this simulation CRY determines a list of particles that cross the simulated detector volume within the trigger time window. The particles are saved and input into the particle propagation step.

4.5 Particle Propagation

Particle propagation takes the list of final state particles determined from neutrino or cosmic ray interactions from GENIE or CRY and simulates the interactions of the particles with the detector. GEANT4 is used to simulate particle propagation which results in further interactions and decay of the final state particles. GEANT4 determines particle propagation from the particle cross sections. The particle propagation as it travels through the detector is recorded in finite steps. In particular the energy depositions and path through each cell is saved. Particle propagation stops when particles have less than 100 eV of kinetic energy remaining.

4.6 Detector Response

The detector response to the energy deposition of particles in the cells determined by GEANT4 is simulated from custom NOνA software[54]. The response involves several steps: propagation of photons in the scintillator, photon capture in fiber, fiber transport, and electronics simulation. These steps assume that all cells in the detector are equivalent to each other. This allows for the use of templates for how energy depositions in a cell behave instead of simulating individual optical photon processes in each detector cell which is very computationally expensive.

The first two steps of the detector response, photon propagation and capture in the fiber, are handled by a template function that determines the collection rate of photons by the fiber as a function of the position of the energy deposition with respect to the fiber and the time in which the energy was deposited, both of which are determined by GEANT4. The template function was determined from a ray tracing simulation. The ray tracing simulation determines the rate at which scintillation photons are collected assuming the following parameters of the detector, 9 ns scintillator emission time, 87.7% cell wall reflectivity, index of reflectivity in oil of 1.46, and an exponential photon capture probability with a capture length of 30.66 cm. Figure 4.1 shows the template function used.

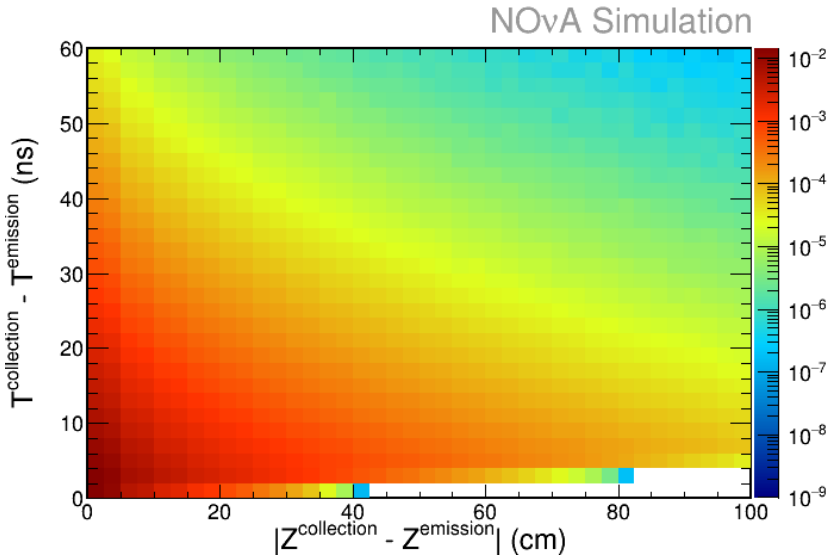

Figure 4.1: Template function of collection rate of scintillation photons.

Fiber transportation determines how many photons are incident on the APD as a function of time given that the photons captured in the fiber. Half of the photons collected in the fiber are sent in each direction of the fiber loop. The mean number of photons that arrive at the APD are determined from an attenuation curve that was measured in bench tests. Finally the number of photoelectrons created by the APD are determined after accounting for the quantum efficiency and Poisson sampling.

Additionally APDs have an excess noise factor that expands the variance of the signal beyond Poisson statistics and is modeled as a log-normal distribution. The time of the photoelectron creation is determined from the energy deposition time in the scintillator combined with the photon transport time through the fiber. The photon transport time through the fiber is determined from a ray tracing simulation of photons traveling at many angles through the fiber.

The final piece of the detector response is the simulation of the front end electronics. For cells with photoelectrons, analog traces of the form shown in equation 3.1 are created starting at the time attributed to the photoelectron creation with the normalization of the trace determined from the total number of photoelectrons. When a cell has photoelectrons created at multiple times, traces are created from each of the photoelectrons individually and added together resulting in the final trace. A constant baseline of 250 ADC is added to the trace. This was the average baseline measured in far detector data. The analog traces are then digitized by sampling the traces every 62.5 ns, truncating the trace to integer values, and clamping values between 0 and 4095 ADC counts. Noise is added to cells with particle energy deposition from both current and voltage noise sources. For cells with no simulated energy deposition, noise is added randomly from a distribution of noise hits measure in cosmic ray data to save computational time of having to generate full traces in the cell. Hits are created from the simulated electronic responses by using the same dual correlated sampling algorithm that is used in the DAQ to record data from the detector. From this point the hits created by the simulation can be treated equivalently to those measured in data except that more information is available about what physics processes created the hit.

4.6.1 Simulation Tuning

Several places in the simulation make use of bench top measurements to inform the model used in the simulation. There is only one tuneable parameter remaining in the simulation of the detector response, the conversion factor between energy deposited in the detector and scintillation photons created. This parameter is estimated to be 3360 photons/MeV for the scintillator used in NOνA . However, the number used in the simulation is tuned using a comparison of the data to the simulation. The simulation conversion factor is tuned to match the detector response, photoelectrons per unit

length, in the minimum ionizing range of the $\frac{dE}{dx}$ in cosmic ray muons. This is similar to the method used for calibration and will be described further in chapter 5. Figures 4.2 and 4.3 show the comparison of the detector responses to cosmic ray muons in the near and far detector between data and the tuned simulation.

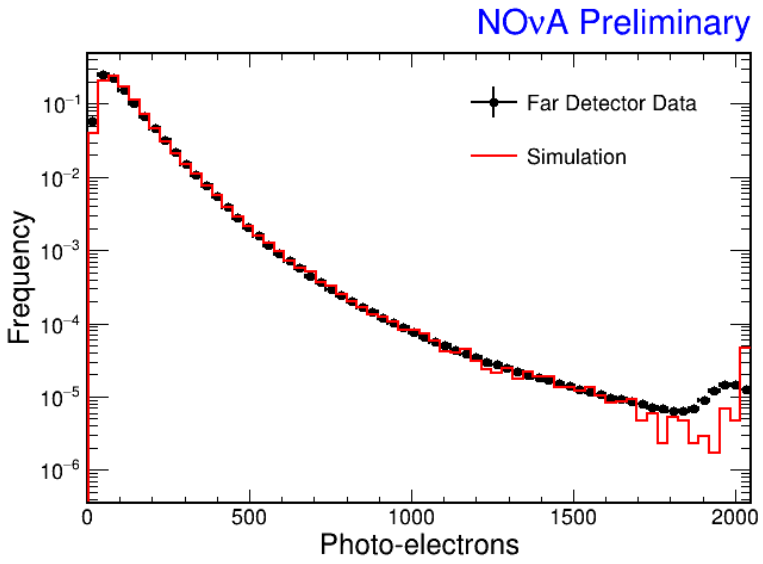

Figure 4.2: Comparison of detector response to cosmic ray muons between data and simulation in the far detector. The discrepancy between data and simulation at high photo-electrons results from the gain being set on each cell individually in the detector while the simulation models that gain as a single value across all cells.

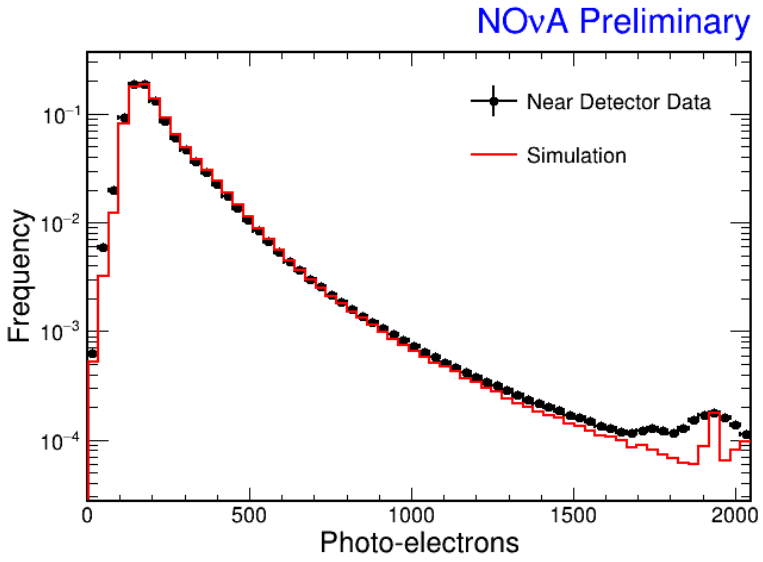

Figure 4.3: Comparison of detector response to cosmic ray muons between data and simulation in the near detector. The discrepancy between data and simulation at high photo-electrons results from the gain being set on each cell individually in the detector while the simulation models that gain as a single value across all cells.

Chapter 5

Event Reconstruction and Calibration

This chapter describes the process of reconstructing interactions from the raw data recorded in a trigger window. This multi-step process separates the data within the trigger into individual interaction events and associates hits that arise from the same particle together within in interaction. The resulting groups of hits allow for the three-dimensional reconstruction of particle trajectories through the detector and also allows for particle identification to be performed as discussed in chapter 6. Additionally the process of calibration is described which allows for the determination of the true energy deposition of particles as they travel through the detector.

5.1 Slicing

Data is recorded in trigger windows of length 550 μs. Within this time window multiple unrelated events can be recorded. The first step in event reconstruction groups the hits into collections of hits called slices that are causally related to each other. This step achieves two objectives in event reconstruction. First it separates unrelated physics interactions from each other and second it removes hits originating from electronic noise from hits originating from physical interactions. This effectively groups hits into individual events to be evaluated for analysis.

Slicing clusters hits that have a high density of hits that are potentially casually

related to each other[55]. It does this by assigning a score to each hit based on the distance in time and space from other hits in the trigger window. The score function is defined as

$$\epsilon = \left(\frac{\Delta T - {}^{\Delta\vec{r}}/_{c}}{T_{res}}\right)^2 + \left(\frac{\Delta Z}{D_Z}\right) + \left(\frac{\Delta V}{D_V}\right), \tag{5.1}$$

where ΔT is the time difference between hits, $\vec{r}$ is the Euclidean distance between hits, ΔZ is the z distance between the two hits and ΔV is the x or y distance between two hits in the same view. The first term in the score function quantifies temporal proximity account for flight time. T_{res} is the timing resolution. The last two terms quantify spatial proximity and count as penalty terms towards the overall score. These terms attempt to remove noise from the clustering as noise hits will be randomly distributed in time and space throughout the detector making them likely isolated from other hits. The second term applies to the z distance between each hit and the third term applies to the distance between the hits in the x or y view. Since individual hits can originate from light being collected from anywhere in the cell only the distance in the cells view is known well and the third term only applies when the two hits in consideration are in the same view. When ϵ falls below a threshold value the two hits are said to be neighbors of each other

Hits with more than a minimum number of neighbors are labeled as core points otherwise they are called border points. Individual slices are made by expanding the cluster around a core point to include all of its neighbors. All of the core points included in the cluster are expanded to include all of their neighbors until the only remaining points that have not been expanded are border points. This process is done iteratively as to find as many slices in a trigger window as possible. Figures 5.1 and 5.2 show examples of slicing in the near and far detectors.

In the near detector multiple neutrinos are seen in the detector in the each beam spill. An average of 9.9 different neutrinos contribute to the hits seen in any beam window, with 6.94[56] coming from neutrinos interacting in the rock outside the detector and 2.96 coming from interactions originating within the detector. This allows for the possibility of multiple overlapping neutrino interactions being reconstructed together in the same slice which could lead to a miscounting of the neutrinos in the near detector. The rate at which neutrinos pile-up in the same slice is less than 1%. In the far detector the pile-up

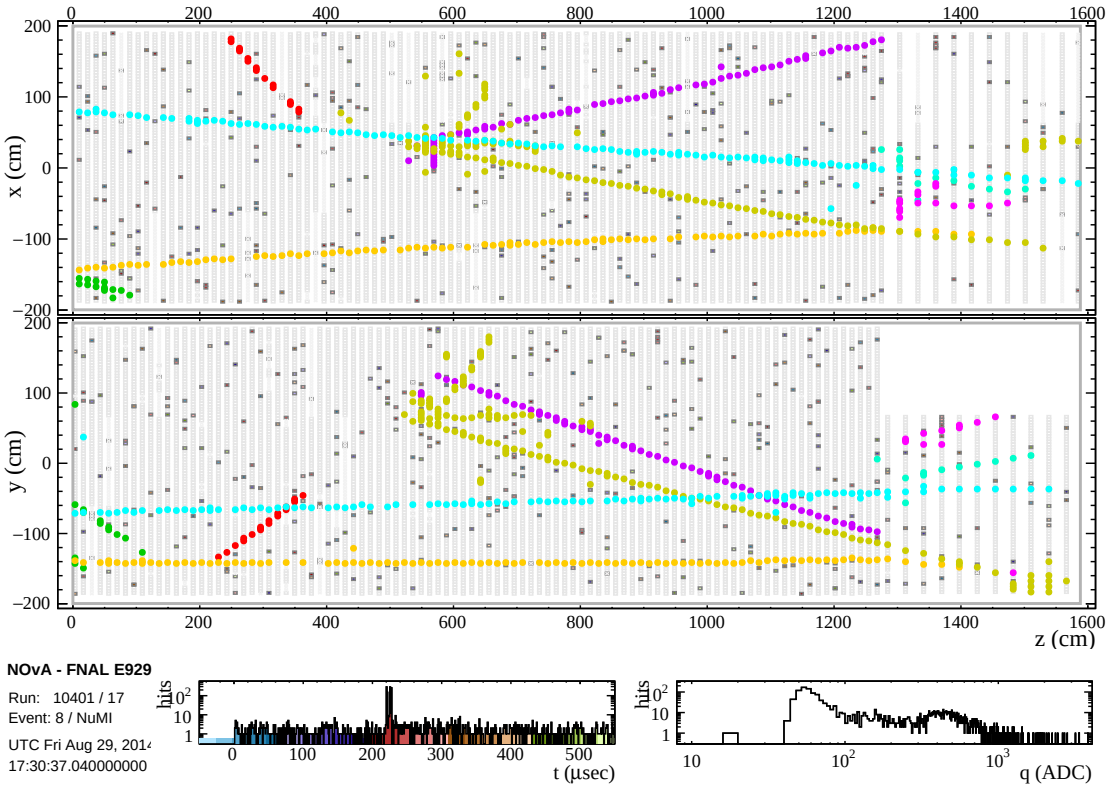

Figure 5.1: Typical trigger window in simulated near detector data. Slices are indicated by color with hits from the same slice being drawn in the same color.

rate refers to slicing multiple cosmic rays together since the neutrino interaction rate is low. The cosmic pile-up rate could lead to a miscounting of background in the final analysis sample. It was determined from cosmic ray simulation that the far detector pile-up rate is less than 1%[57].

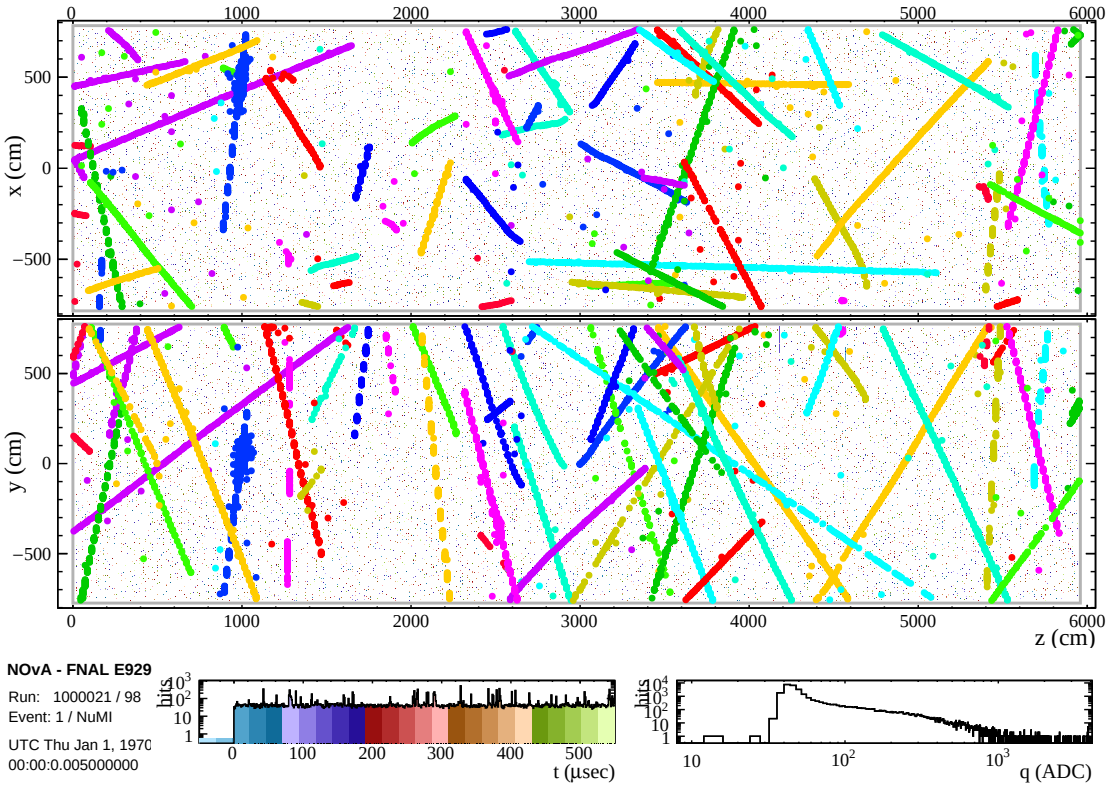

Figure 5.2: Typical trigger window in simulated far detector cosmic data. Slices are indicated by color with hits from the same slice being drawn in the same color.

5.2 Tracking

Tracks are reconstructed on individual slices. The goal of the tracking is to trace the trajectory of individual particles that deposit energy in the detector. This is especially useful in identifying particles that do not create large electromagnetic or hadronic showers, such as muons. The tracking algorithm is based on a Kalman filter and results in reconstructed tracks called Kalman tracks.

5.2.1 Kalman Filters

Kalman filters are a common way of estimating the true value of a measurement based on the amount of error expected in the measurement and the amount of noise in the system. In general Kalman filters solve the problem of estimating the true value of a state, x, at discrete steps k with measurements z. Where the state is a real n dimensional vector that at step k relates to the previous step $k-1$ through equation 5.2.

$$x_k = Ax_{k-1} + Bu_{k-1} + w_{k-1} \tag{5.2}$$

u represents any inputs into the system and w represents the inherent noise in the system process. The matrices A and B transform the state and input at step $k-1$ to k, respectively. Finally measurements of the system relate to the true state of the system through equation 5.3.

$$z_k = Hx_k + v_k \tag{5.3}$$

v_k represents the noise inherent in the measurement process and the matrix H defines how the measurement of the system relates to the true state of the system.

The Kalman filter is a method to determine the best estimate of the state x_k assuming a linear system and the process, w, and measurement, v, noise are independent of each other and their probability is normally distributed with noise covariance matrices Q and R, respectively. The estimate of the state at step k, $\hat{x}_k$, is chosen so that it minimizes the mean square error between the estimated and true state, x_k. It is possible to find a solution that minimizes the error by using a linear sum of the predicted estimate of the state, $\hat{x}_k^-$, and the difference between the predicted state and actual measurement

multiplied by a gain factor K_k, equation 5.4, where the gain factor is calculated, by 5.5 using the estimated error of the predicted state, P_k^-.

$$\hat{x}_k = \hat{x}_k^- + K_k \left(z_k - H\hat{x}_k^- \right) \tag{5.4}$$

$$K_k = \frac{P_k^- H^T}{H P_k^- H^T + R} \tag{5.5}$$

With this formalism a recursive algorithm implementing the following steps results in the estimate of the true state of the system minimizes the error on the estimate:

1. Predict the state of the system given the state at step $k-1$:

$$x_k = Ax_{k-1} + Bu_{k-1} \tag{5.6}$$

2. Calculate the error in the prediction based on the error at step $k-1$ and the process noise:

$$P_k^- = AP_{k-1}A^T + Q \tag{5.7}$$

3. Determine the gain factor to be applied at step k using 5.5

4. Correct the predicted state using the gain to get an estimate of the state using 5.4

5. Update the predicted state error using the measurement information:

$$P_k = (I - K_k H) P_k^- \tag{5.8}$$

5.2.2 Kalman Filter Tracking

In the context of tracking the Kalman filter is used to reconstruct the true position of a particle given the position of the hits recorded in the data. In the language of Kalman filters the true position and direction of the particle represents the state of the system and the goal of tracking is to find and fit the best estimate of the particle path given the measurement of the hits that are present in the detector. The noise associated with the system are the measurement noise originating from the detector cells having finite width and depth and the process noise originating from the possibility of particles undergoing

some scattering process between measurements that deflect the true particle position from the expected.

In the NOνA detectors non-showering charged particles primarily lose energy due to ionization. Because of this and the lack of an external magnetic field (ignoring the effects of the Earth's magnetic field) trackable particles are expected to follow a straight line trajectory making the prediction of the location of the track a simple linear extension of the previous position along the direction of the track. Any deviations from the straight line assumption come from multiple scattering of the charged particle or hard scattering processes. Multiple scattering mainly contributes to small angle scattering. The small angle scattering due to multiple scattering can be approximated as normally distributed with a width given by:

$$\theta_0 = \frac{13.6 \text{ MeV}}{\beta p} z \sqrt{x/X_0} \left[1 + 0.038 \ln \left(x/X_0\right)\right] \tag{5.9}$$

For the case of 2 GeV muons traveling through one plane of the detector, $\theta_0 = 5.4 \times 10^{-3}$ radians. This jitter in the track direction due to small angle multiple scattering is accounted for in the tracking system by determining the covariance matrix R by assuming there is no system noise in the position and the system noise in the direction originates from the multiple scattering process. Large angle scatters are not handled in the initial track finding and fitting procedure as they do not fit the normal, zero-mean assumptions of the system noise that can be input into the Kalman filter. The small angle Gaussian approximation of multiple scattering encompasses 98% of the charged particle scattering making it an accurate approximation for most charged particle scattering. In addition to charged scattering, hadronic particles can undergo scattering processes through strong force interactions. The hadronic interaction length in the NOνA detectors is 60 cm, approximately 10 planes. These hadronic scattering processes tend to result in large angle scatters. In general trackable particles leave characteristic trajectories of long straight sections dominated by small angle multiple scattering with large angle scattering due to electromagnetic or strong interactions occurring intermittently along the track. Figures 5.3-5.5 show characteristic trajectories of trackable particles in the NOνA detector.

The algorithm that performs this process is broken into the tasks of track finding, track fitting, and view matching which are detailed in the following sections. The process

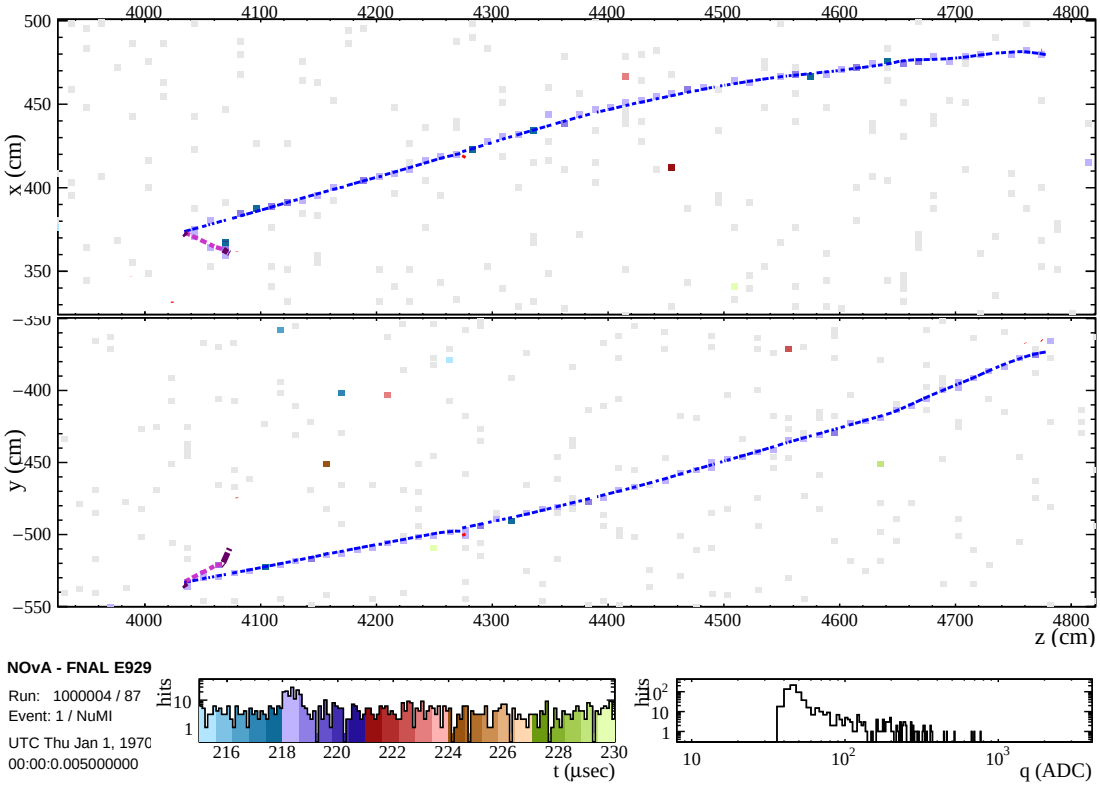

Figure 5.3: Typical muon multiple scattered track. Blue dashed line shows the true trajectory of a muon from a simulated ν_μ CC interaction in the far detector.

of track finding and fitting is performed in each detector view independently since the trajectory in both the x and y view are independent of each other. The goal of these two tasks is to find the hits belonging to long sections of track dominated by small angle multiple scattering and get the best estimate of the true particle position from the pattern of hits in the track. The view matching task then reconstructs the full three dimensional tracks in a slice from the individual tracks found in each view independently. The view matching also recovers tracks that may have been reconstructed in multiple pieces due to the presence of hard scattering.

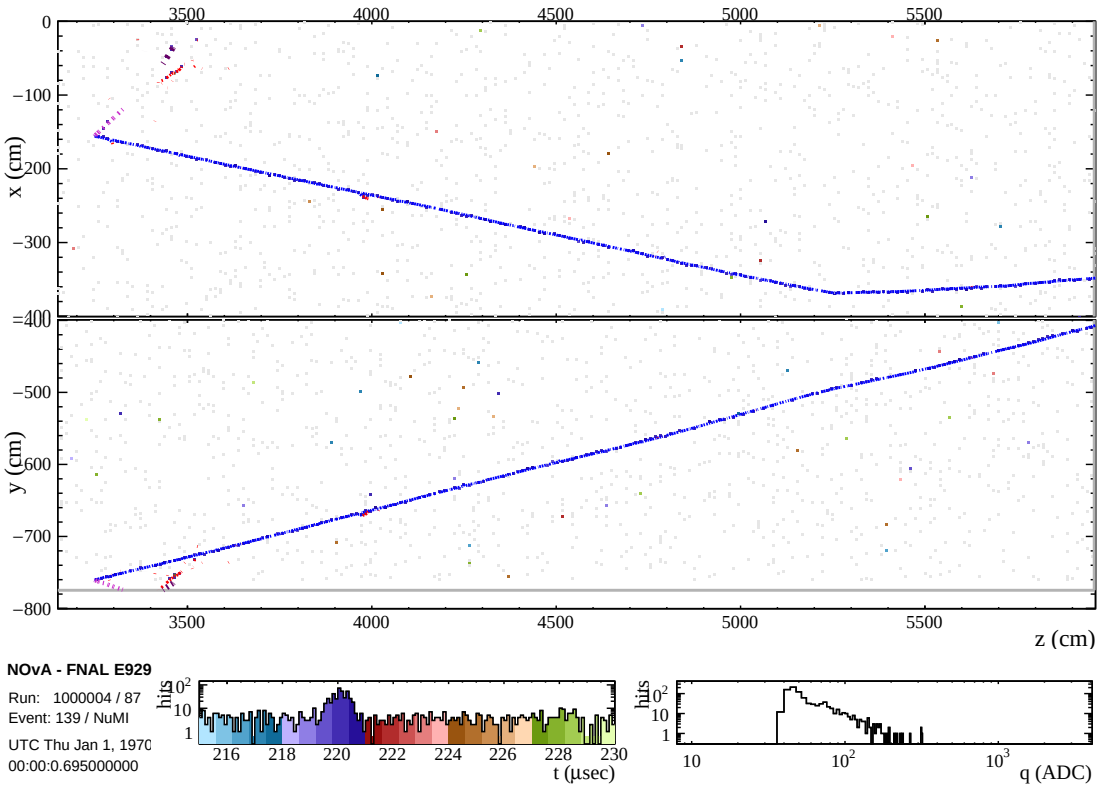

Figure 5.4: Muon track with a hard scatter. Blue dashed line shows the true trajectory of a muon from a simulated ν_μ CC interaction in the far detector. Hard scattering occurs near z position of 5300 cm in the x-z detector view.

Track Finding

Track finding is the process of sorting out which hits in a slice belong together in a single track. This process is accomplished by first finding segments of tracks called seeds and then propagating these seeds using a Kalman filter to extend the track and add additional hits that are consistent with the track.

Track seeds are formed from combinations of two hits that are separated by less than 4 cells apart from each other. The pairs of hits in the track seed are used to estimate the position and slope of the track. Tracks are formed from the seeds through a predict and probe method using the equations 5.2-5.8. The location of adjacent hits

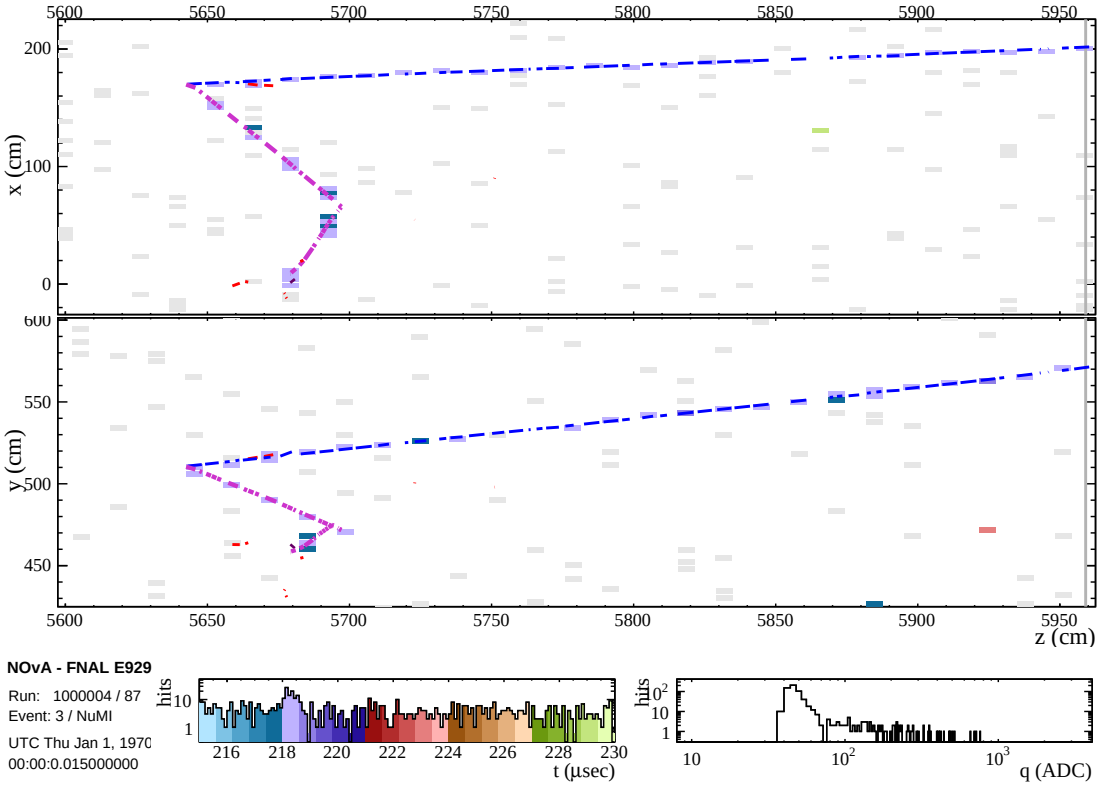

Figure 5.5: Typical muon multiple scattered track an charged pion track with a hard scatter. Blue dashed line shows the true trajectory of a muon and the magenta dashed line shows the true trajectory of a charged pion. Both particles come from a simulated ν_μ CC interaction in the far detector.

is predicted using the estimated position and direction of the track assuming a linear fit and process errors coming from scattering and the measurement errors coming from the uncertainty of the particle location within a hit cell. Hits that are close to the predicted location are added to the track. A hit is determined to be close enough to be added to the track if it is less than 8 in χ^2 units away from the track prediction. Once a hit is added to the track the track's position and direction estimates are updated given the new measurement and the process is repeated until no more hits can be added to the track.

The propagation process initially starts from the downstream beam end of the detector, high z, toward the upstream beam direction as in the downstream region the particles emerging from the interaction should be the most separated from each other. Track propagation is terminated when there are no hits consistent with the track projections or if the probability of a gap existing in a track from one hit to the next is less than 0.0001. Once the tracks have been propagated as far upstream as they can go, the propagation is reversed to go downstream to pick up any hits that may have been missed from the initial propagation. One final propagation is then repeated to go upstream to separate tracks near the interaction vertex using as much information as possible.

From all the tracks found, the track with the most hits is saved. In order to accommodate finding any number of tracks in a given slice, the algorithm is recursively performed on the remaining hits until no more tracks are reconstructed.

Track Fitting

Track fitting is the process of fitting the best particle trajectory to the hits that are determined to belong to the same track. Using the input of the track finding method the fit of the track is determined using equations 5.2-5.8. At any given location, the fit is determined from the the step-wise forward propagation of all hits that came before the current location and a step-wise backward propagation of all hits that came after the current location. A weighted sum of the forward and backward estimated location and direction is used as the final fit to the trajectory. The weights of the forward and backward propagated fits to use determined as the inverse of the error determined in the fit normalized so that the contribution from the forward and backward propagation adds to unity.

View Matching

View Matching combines the two-dimensional tracks found in each view of the detector. The location and direction of the tracks between the two views are independent except for the z dimension. Because of this, two-dimensional tracks are matched together based on a scoring metric, S, that measures the overlap of the two dimensional tracks in the

z dimension.

$$S = \frac{Start_{diff} + Stop_{diff}}{Overlap}, \tag{5.10}$$

where $Start_{diff}$ is the difference in planes between the starting point of the tracks in the two views, $Stop_{diff}$ is the difference in planes between the stopping point of the tracks in the two views, and $Overlap$ is the number of planes that overlap each other over the length of the two tracks. Combinations of two dimensional tracks are ranked against each other and the combination with the lowest value of S are matched together. Only combinations of tracks that overlap at all are considered for matching. Additionally two dimensional tracks are considered to be linked together if it improves the score of the three dimensional match. This accounts for tracks that may have been reconstructed in two or more pieces because of hard scattering processes. Once two dimensional tracks are determined to be a match to each other, they are removed from the pool of matchable tracks. The matching is performed iteratively until no more two dimensional tracks can be matched together to form a three dimensional track.

5.2.3 Performance

Figures 5.6-5.8 show examples of the reconstructed tracks from simulated events in the near and far detectors. The algorithm was also tested to determine how well it can reconstruct muon induced tracks from neutrino events in both the near and far detector. The track *completeness*, ratio of number of hits on the track induced from a muon to the number of total hits induced by a muon, and *purity*, ratio of number of hits on the track induced from a muon to the total number of hits in the track provide measures of how well the algorithm can reconstruct muon tracks. These quantities are shown in figures 5.9-5.20 for simulated neutrino interactions in both the far and near detectors. Additionally the resolution on the reconstructed track length of muons are shown in figures 5.21 and 5.22. In particular the ability to reconstruct the track length well affects the ability to measure the muon energy as discussed in chapter 7.

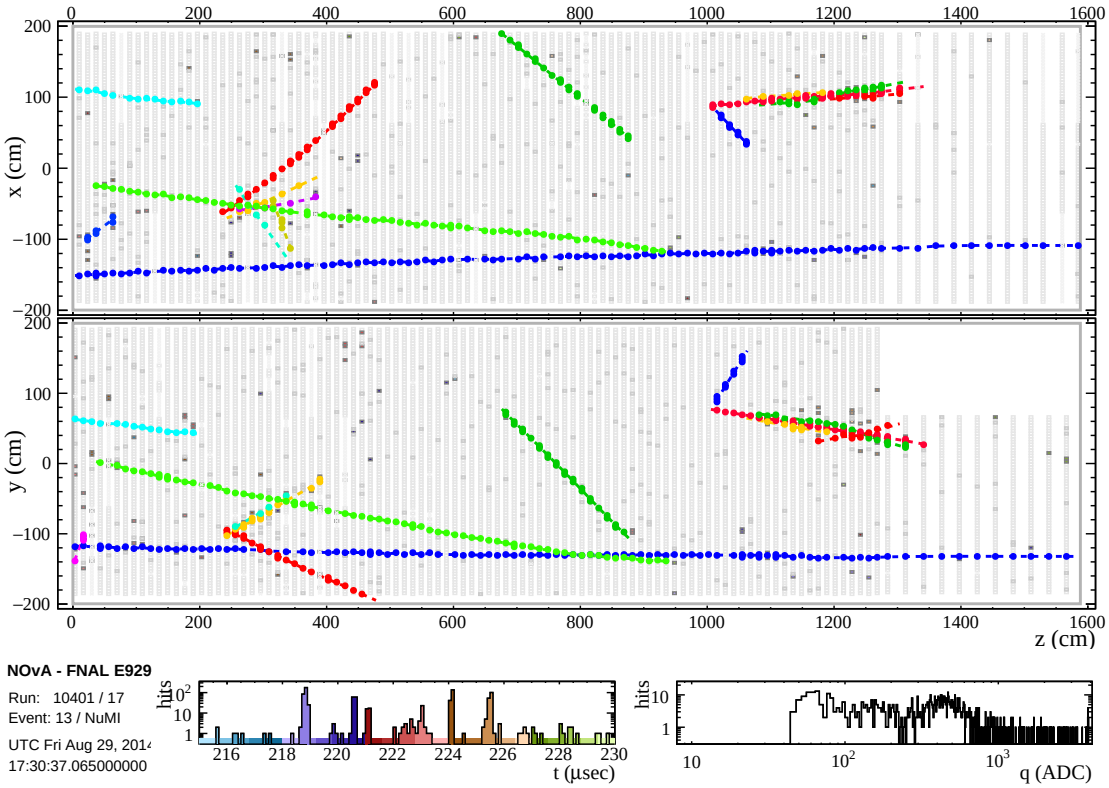

Figure 5.6: Reconstructed tracks in a typical trigger window in simulated near detector data. Tracks are indicated by color with hits from the same slice being drawn in the same color. The track fitted trajectory is drawn as a dashed line.

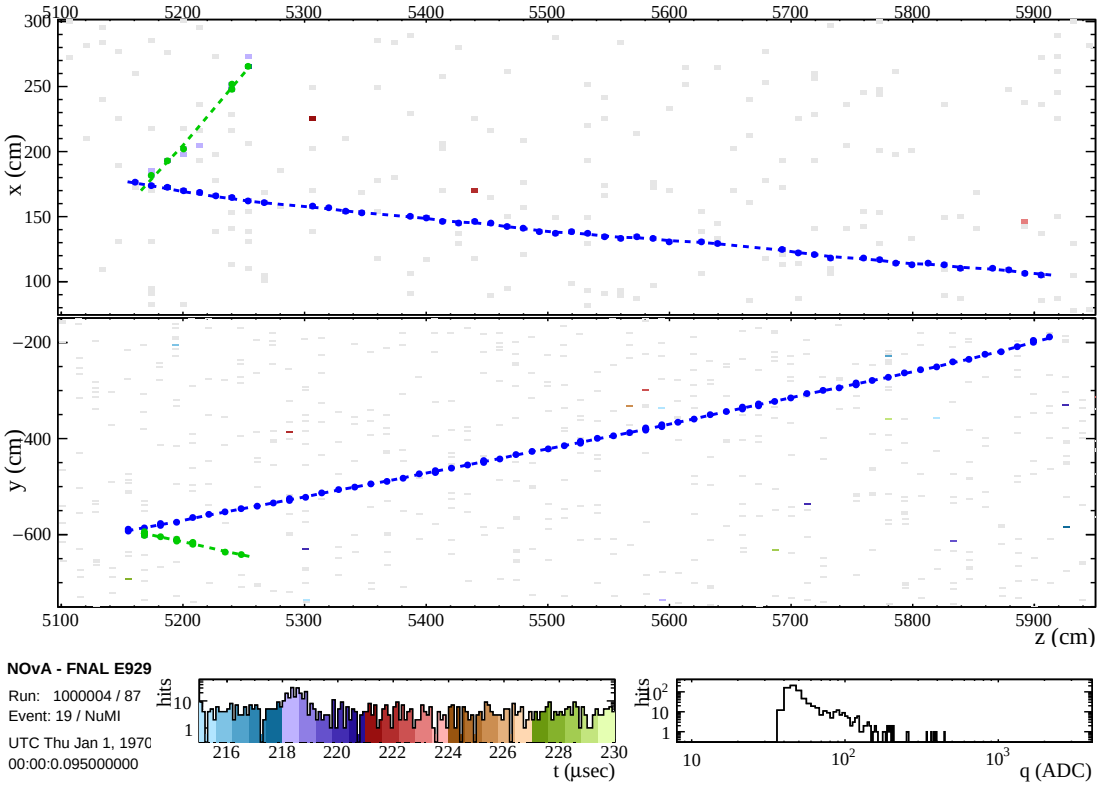

Figure 5.7: Reconstructed tracks in a typical trigger window in simulated far detector data. Tracks are indicated by color with hits from the same slice being drawn in the same color. The track fitted trajectory is drawn as a dashed line.

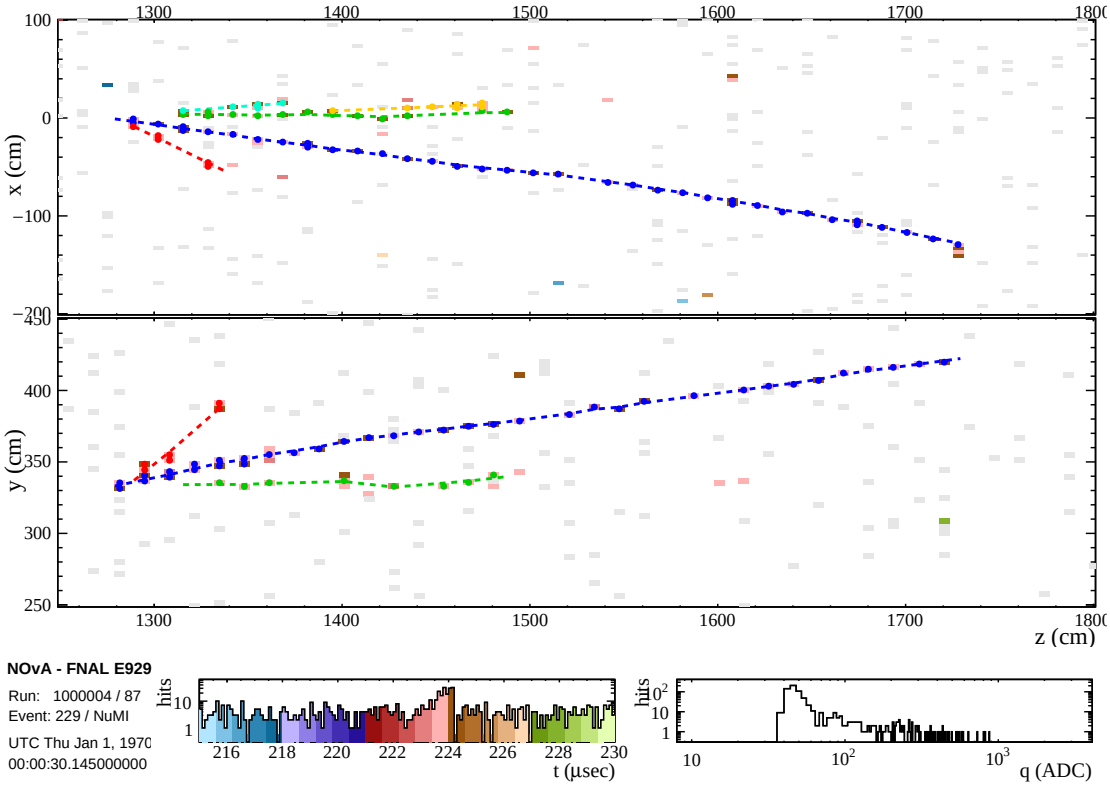

Figure 5.8: Reconstructed tracks in a typical trigger window in simulated far detector data. Tracks are indicated by color with hits from the same slice being drawn in the same color. The track fitted trajectory is drawn as a dashed line.

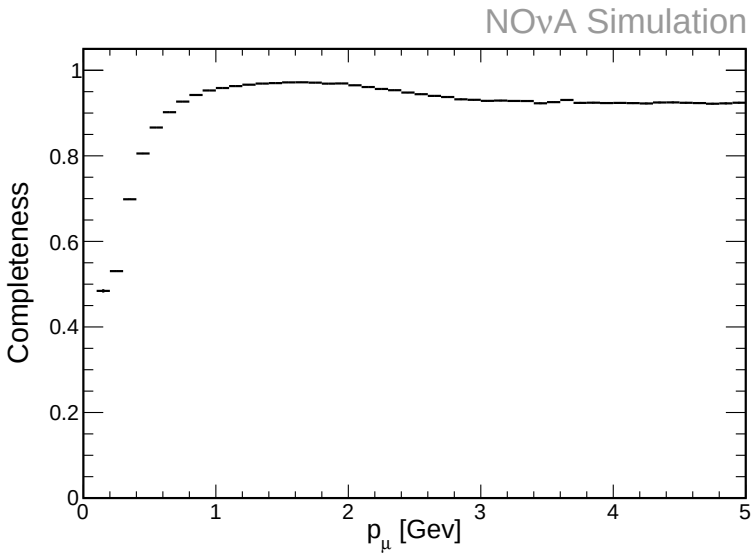

Figure 5.9: Muon track completeness as a function of the initial muon momentum in far detector simulated ν_μ CC interactions.

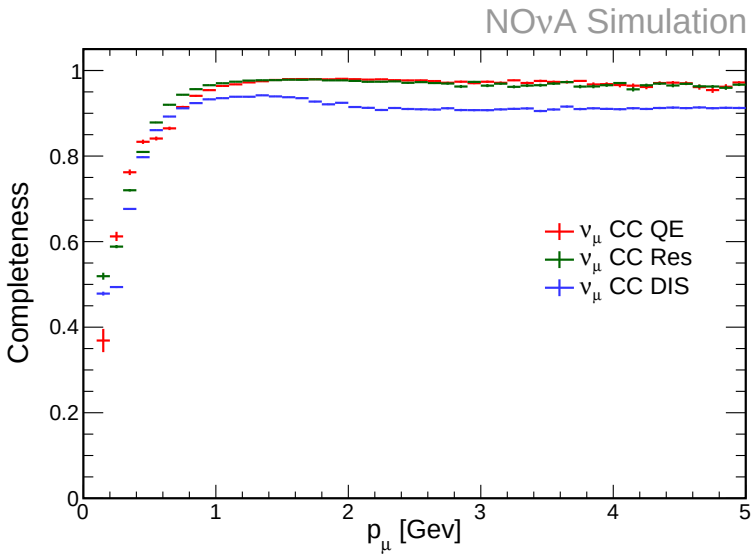

Figure 5.10: Muon track completeness as a function of the initial muon momentum in different interaction types in far detector simulated ν_μ CC interactions.

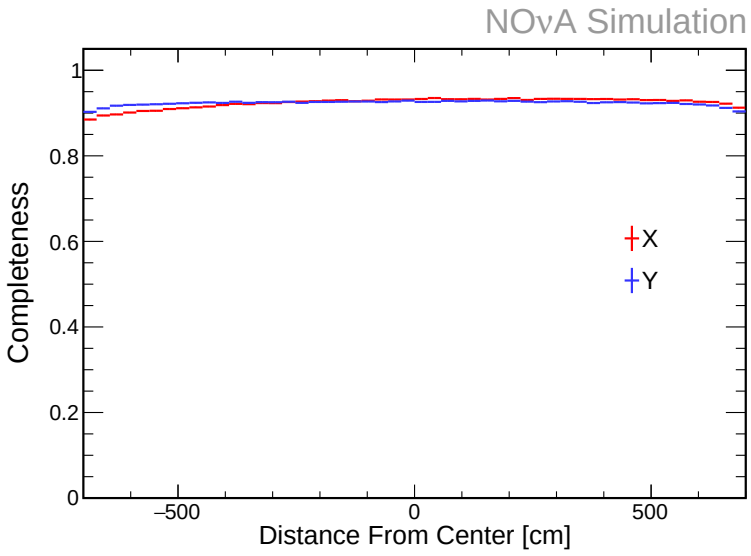

Figure 5.11: Muon track completeness as a function of the initial position of the muon in far detector simulated ν_μ CC interactions.

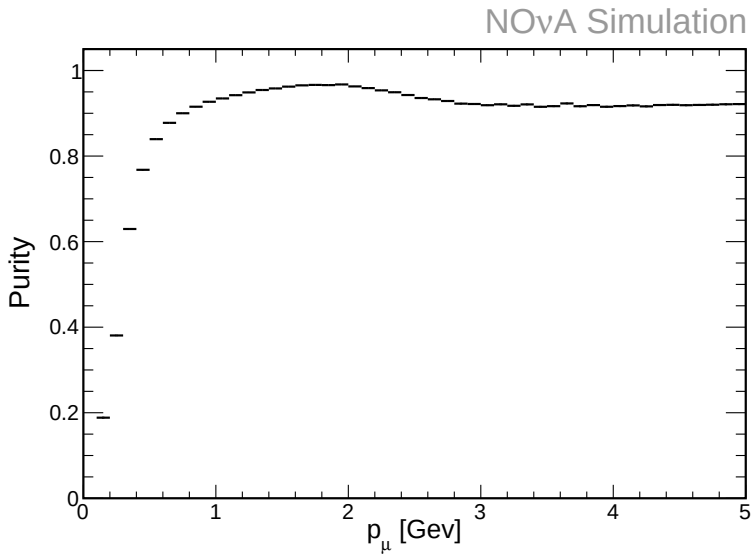

Figure 5.12: Muon track purity as a function of the initial muon momentum in far detector simulated ν_μ CC interactions.

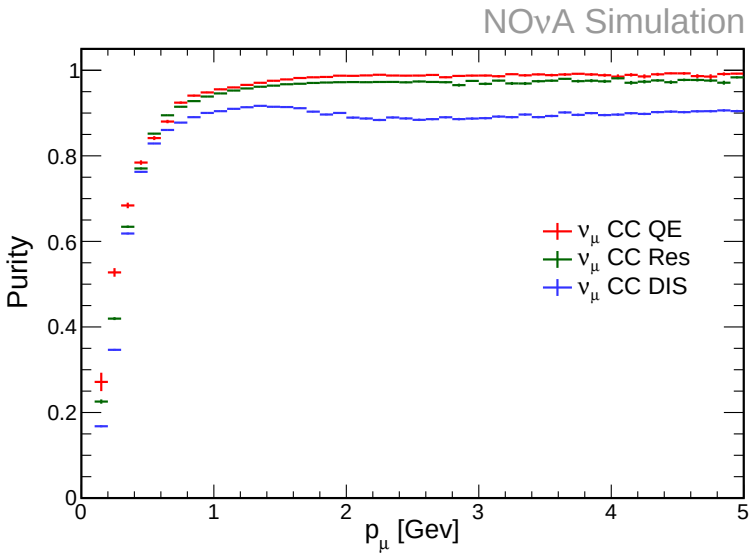

Figure 5.13: Muon track purity as a function of the initial muon momentum in different interaction types in far detector simulated ν_μ CC interactions.

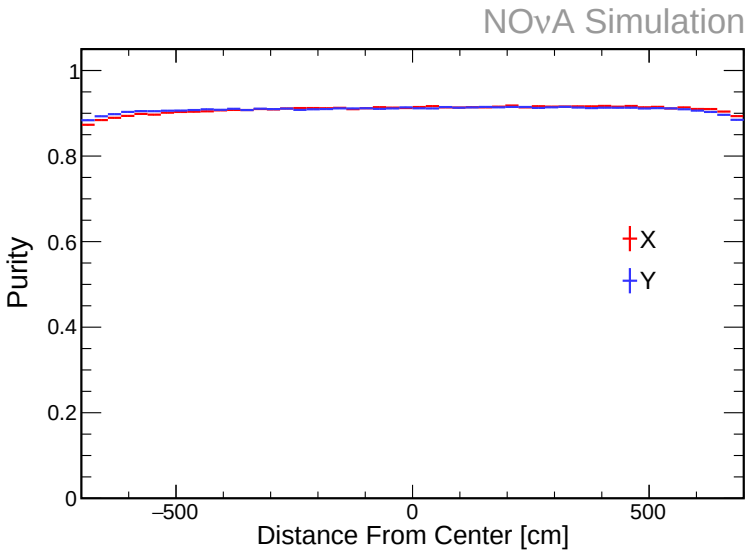

Figure 5.14: Muon track purity as a function of the initial position of the muon in far detector simulated ν_μ CC interactions.

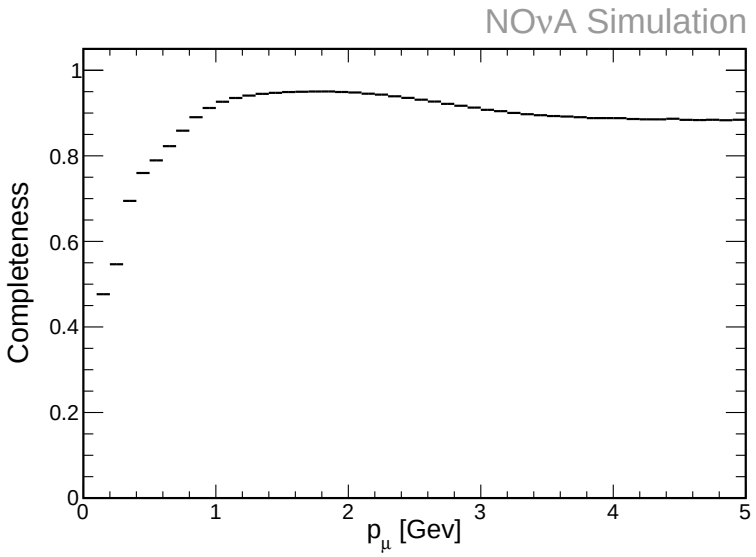

Figure 5.15: Muon track completeness as a function of the initial muon momentum in near detector simulated ν_μ CC interactions.

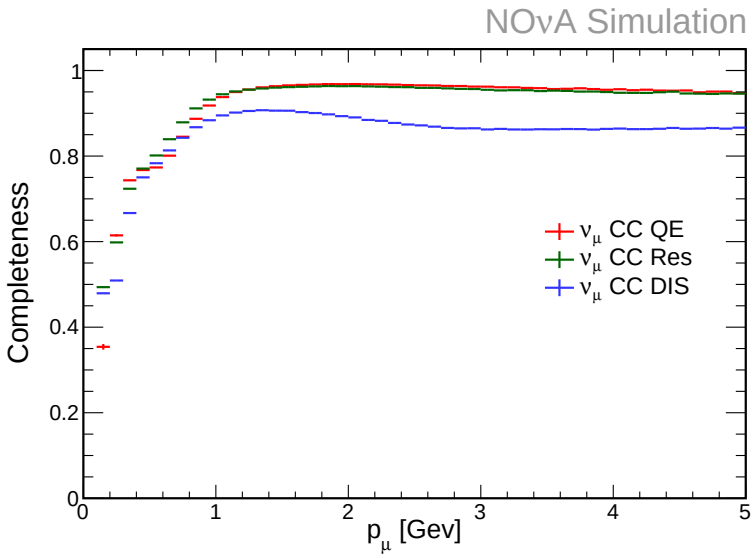

Figure 5.16: Muon track completeness as a function of the initial muon momentum in different interaction types in near detector simulated ν_μ CC interactions.

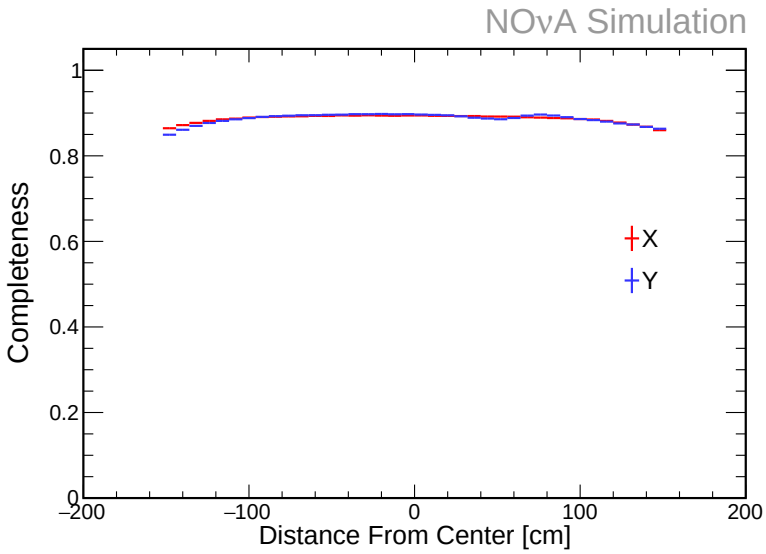

Figure 5.17: Muon track completeness as a function of the initial position of the muon in near detector simulated ν_μ CC interactions.

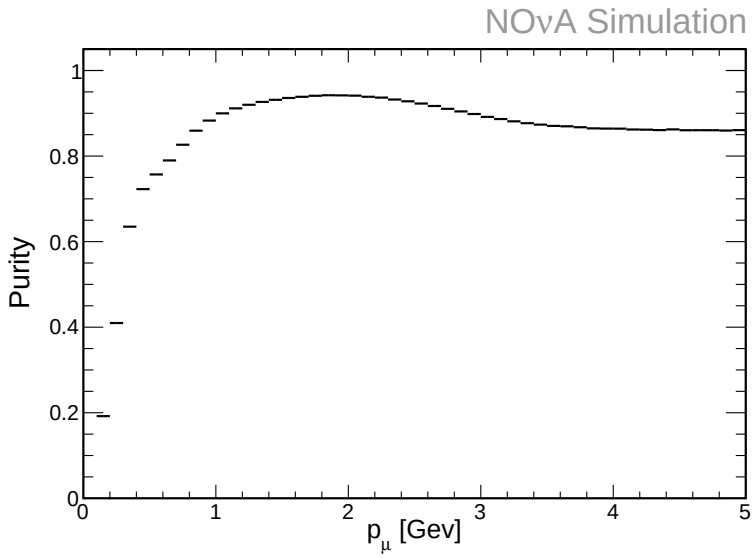

Figure 5.18: Muon track purity as a function of the initial muon momentum in near detector simulated ν_μ CC interactions.

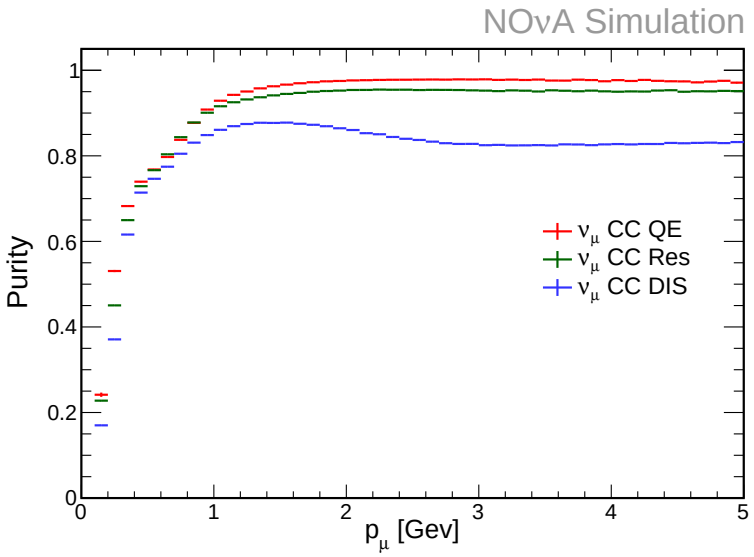

Figure 5.19: Muon track purity as a function of the initial muon momentum in different interaction types in near detector simulated ν_μ CC interactions.

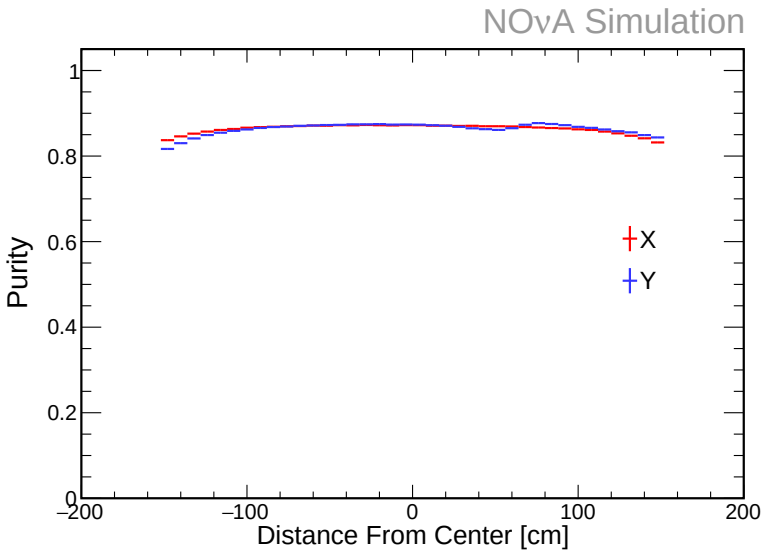

Figure 5.20: Muon track purity as a function of the initial position of the muon in near detector simulated ν_μ CC interactions.

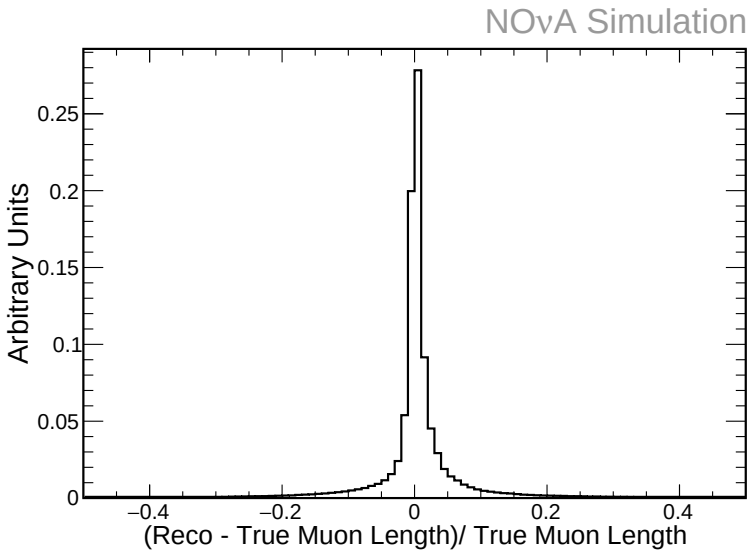

Figure 5.21: Resolution of reconstructed track length of muons in far detector simulated ν_μ CC interactions.

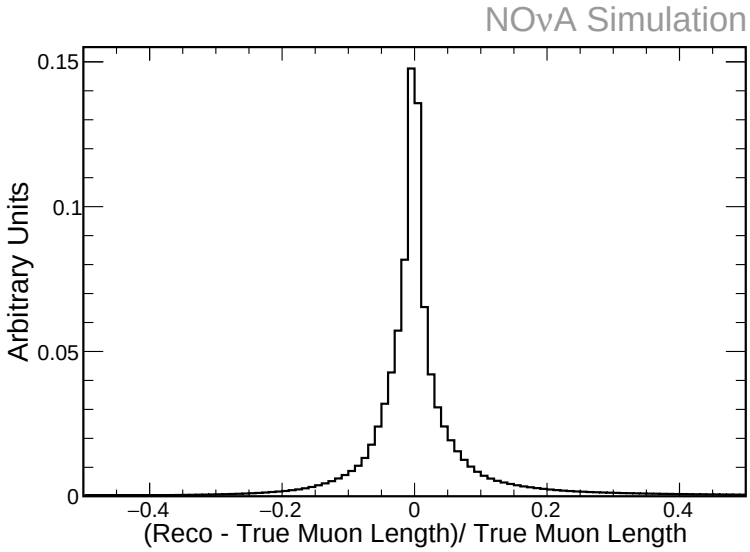

Figure 5.22: Resolution of reconstructed track length of muons in near detector simulated ν_μ CC interactions.

5.3 Calibration

Calibration determines the energy deposition in cells based on the amount of light that is measured in a hit and the hit position. The calibration procedure accomplishes this in two steps: a relative and an absolute energy scaling[58]. One step that expresses the response registered in an APD in comparable units no matter where in the detector it occurs and one step that provides a scaling to absolute energy units. The relative scaling is the first step of the calibration. It corrects for variations in response among different cells and for variations along the length of the fiber in the same cell so that all hits can be compared on equal footing across different regions of the detector. The absolute scaling is performed after the relative calibration is complete. It provides a scale factor so that energy depositions can be described in meaningful units, i.e. GeV. Because the relative calibration occurs before the absolute calibration, the absolute is a value that is independent of the cell or position within the cell.

The relative calibration relies on cosmic ray muons that pass through the entire detector. From these cosmic rays the response divided by path length, PE/cm, is determined in tricells in the reconstructed track. A tricell is a cell in which hits on a track exist on the two cells adjacent to it in the same plane, see figure 5.23. The track reconstruction used for calibration relies on a different algorithm than what is described above. Instead it uses the CosmicTrack algorithm which assumes a single straight line fit to all of the hits in the slice and rejects hits that are not consistent with that fit[59]. The tricell criteria allows for the path length of the track through the cell to be accurately determined. The mean tricell response is plotted as a function of the distance from the center of the cell along the fiber, W, and a fit to an exponential form is performed for each cell in the detector. An example cell in the far detector is shown in figure 5.24. The fit is then used to correct the mean response along W for each cell. Figures 5.25 and 5.26 show the comparison of the corrected response compared to true energy deposition before and after the relative calibration in the x and y view cells in simulated cosmic rays.

The absolute calibration also relies on cosmic ray muons, but uses muons that stop in the detector instead of passing through the entire detector. Stopping muons are used as the energy can be estimated accurately from the Bethe-Bloch formula. Stopping

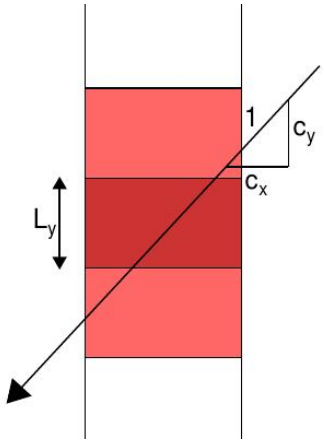

Figure 5.23: Diagram of tricell criteria.

muons are identified from requiring the reconstructed track end to be away from the detector edges and the presence of a Michel electron at the end of the track. Using the Bethe-Bloch formula and the composition of the NOνA scintillator the expected dE/dx of a minimum ionizing particle is 1.79 MeV/cm. The absolute calibration procedure measures the relatively corrected detector response in tricell hits as a function of the distance from the end of the track shown in figures 5.27 and 5.28 for far detector data and simulation. An average response from a window between 100 and 200 cm from the end of the track, the range at which the stopping muons are minimum ionizing in the detector, is calculated. From this average response the absolute energy factor is calculated as the factor that takes the relative corrected scale, measured in arbitrary units called PEcorr/cm, to a physical energy scale measured in GeV/cm. Figure 5.29 shows the relative detector response before absolute calibration in the track window used for absolute calibration in far detector simulation and data. Figure 5.29 shows the absolute detector response in the track window used for absolute calibration in far detector simulation and data.

Both the relative and absolute calibrations are done independently for the data using minimum biasing data taken outside of the beam window in random triggers and for the simulation using a cosmic ray simulation. Additionally both the far and near detector are calibrated independently.

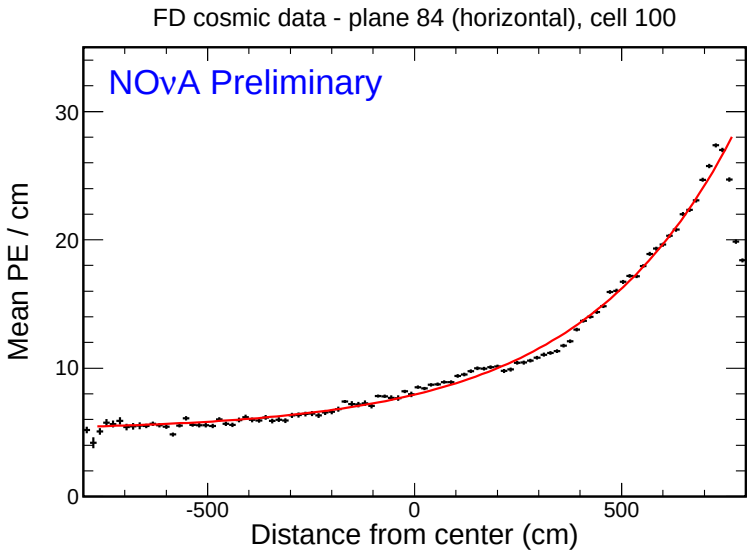

Figure 5.24: Cell response as function distance from the center of the cell for and example far detector cell.

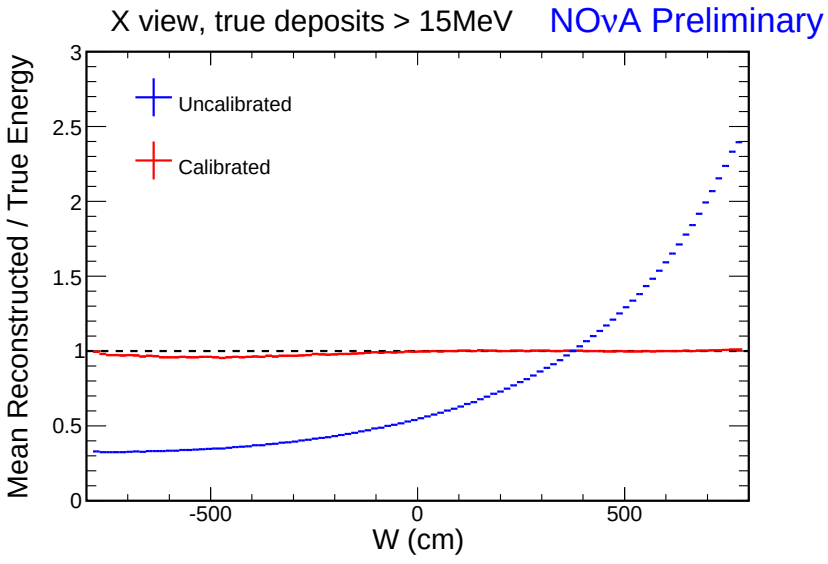

Figure 5.25: Cell response before and after calibration in the x view.

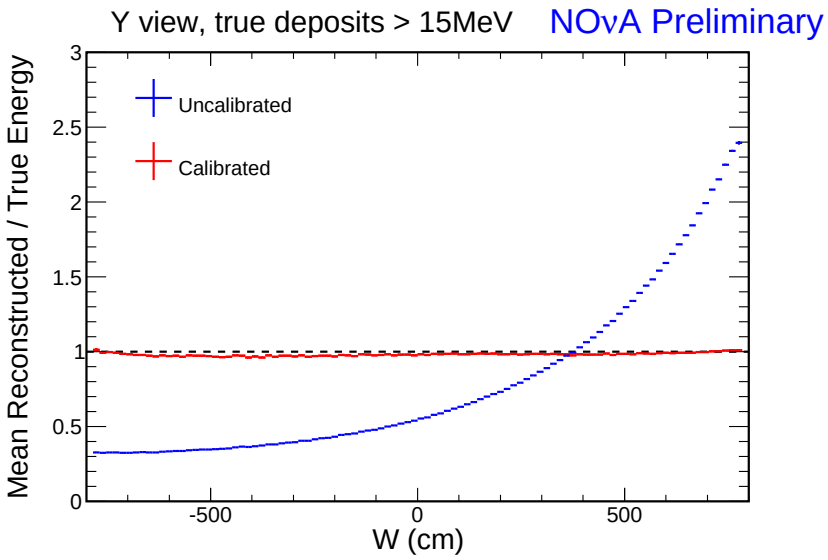

Figure 5.26: Cell response before and after calibration in the y view.

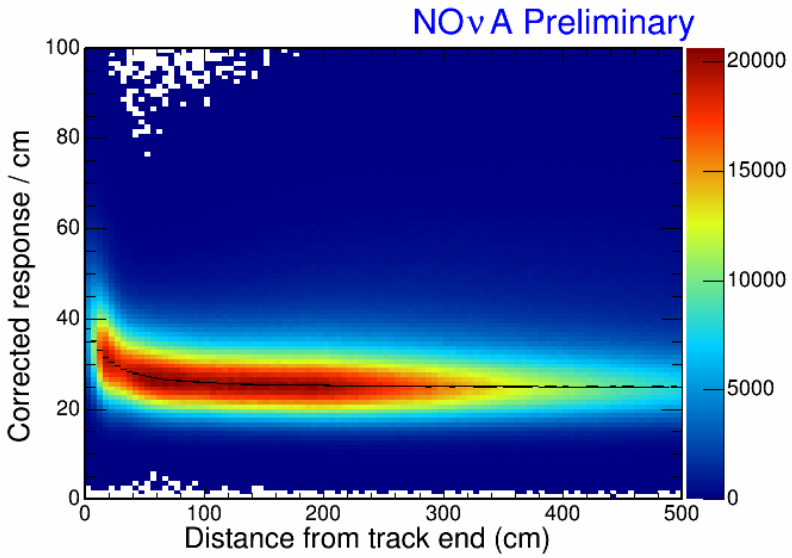

Figure 5.27: Corrected detector response as a function of distance from the track end in far detector data.

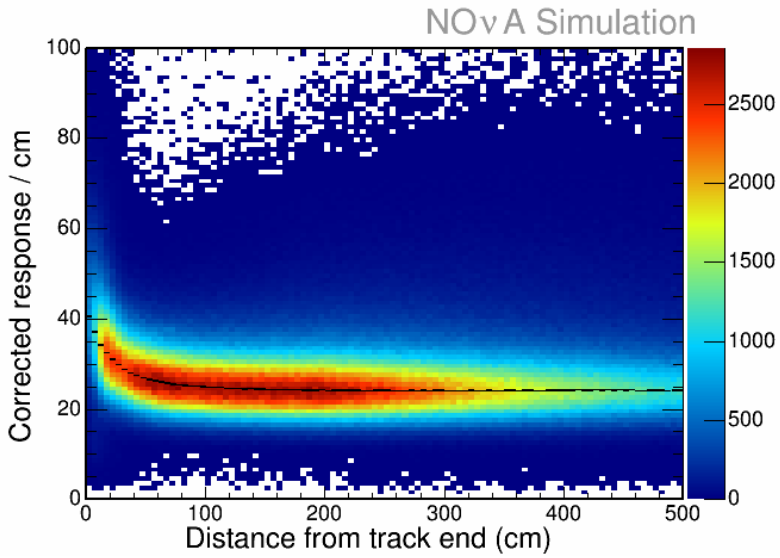

Figure 5.28: Corrected detector response as a function of distance from the track end in far detector simulation.

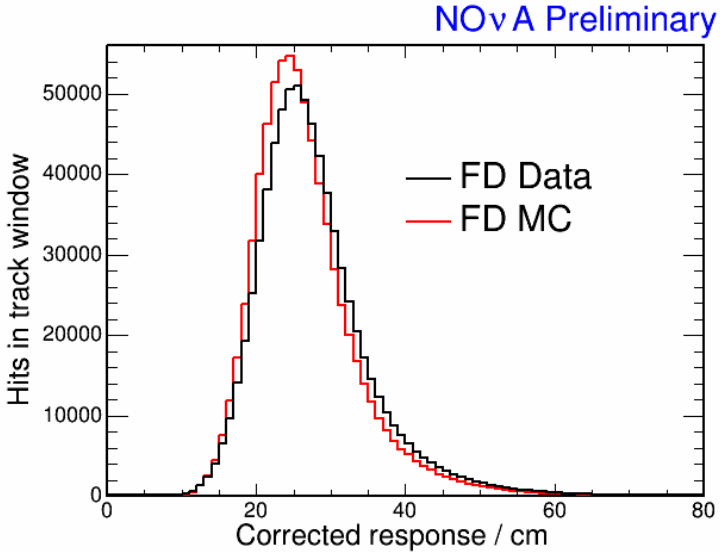

Figure 5.29: Corrected detector response as a function of distance from the track end in far detector data.

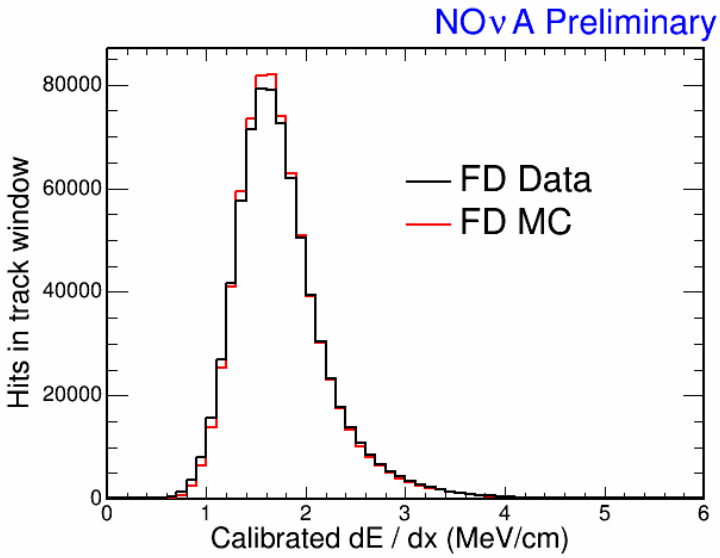

Figure 5.30: Corrected detector response as a function of distance from the track end in far detector simulation.

Chapter 6

ν_μ CC Selection

This chapter presents the **Re**constructed **M**uon **Id**entification (ReMId) particle identification (PID) algorithm. The primary goal of this PID is to discriminate between muon tracks coming from ν_μ charged current (CC) interactions and background tracks that originate from CC and neutral current (NC) interactions.

6.1 Features of Signal and Background

The signal for the ν_μ disappearance analysis consists of muon neutrinos that interact through a CC process. These interactions produce a muon in the final state. Observation of the muon in these events provides a handle for detecting ν_μ CC events. Besides interaction classification, identifying the muon specifically in a ν_μ CC event informs energy estimators of the leptonic and hadronic components of the interactions. Figures 6.1-6.6 show simulated event topologies of muons from neutrino interactions as well as the backgrounds resulting from non-ν_μ CC interactions in the NOνA Far Detector.

The majority of the background comes from NC interactions where one of the particles produced is a $\pi^\pm$. In these events, the $\pi^\pm$ has features similar to muons in ν_μ CC events. Figure 6.1 shows an example QE CC interaction producing a muon and proton in the final state. Figure 6.2 gives an example NC event with similar topology to figure 6.1 where the π^- in the final state can be misidentified as a muon. Figure 6.3 shows a typical DIS CC event in which a final state muon is produced along with hadronic activity. Figure 6.4 shows a NC event that has similar characteristics to the DIS CC

events. About 10% of the ν_μ CC events result in the final state muon of shorter length than other final state products, as in figures 6.1 and 6.5. For these events being able to correctly pick out which track is the muon, without simply assuming it is the longest track, is important for identifying the event as a ν_μ CC event.

Finally, the easiest background neutrino event to reject comes from ν_e CC interactions, seen in figure 6.6. These result in a final state electron which typically leaves a electromagnetic shower which is easily distinguished from muons in ν_μ CC events.

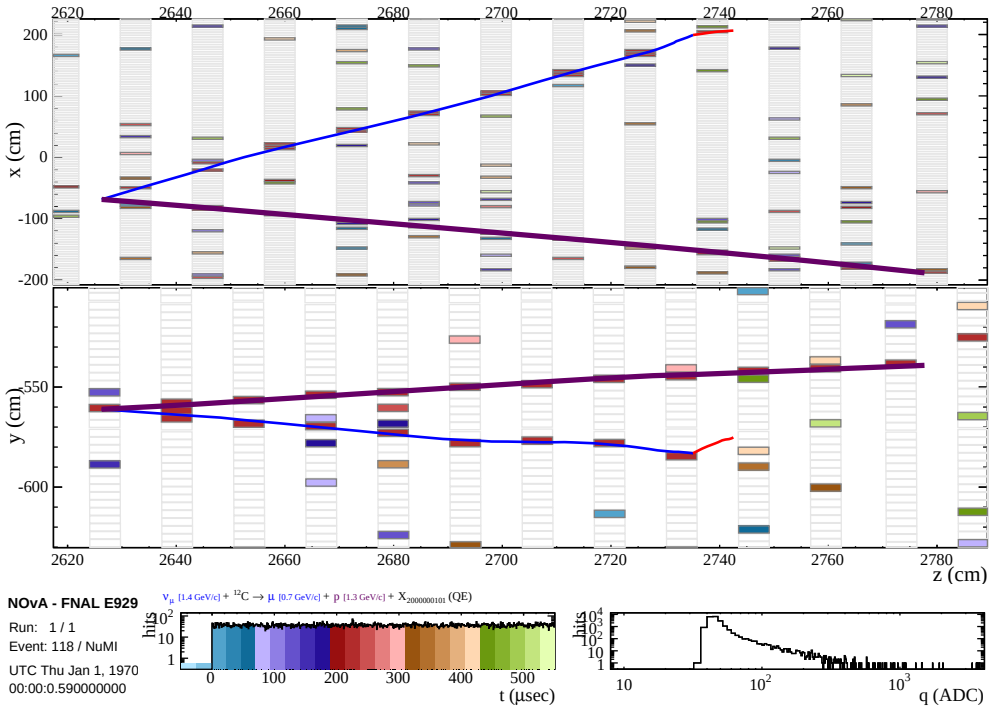

Figure 6.1: Example event display of an ν_μ CC quasi-elastic interaction resulting in a muon and proton in the final state. The muon is represented by the blue line and the proton by the purple.

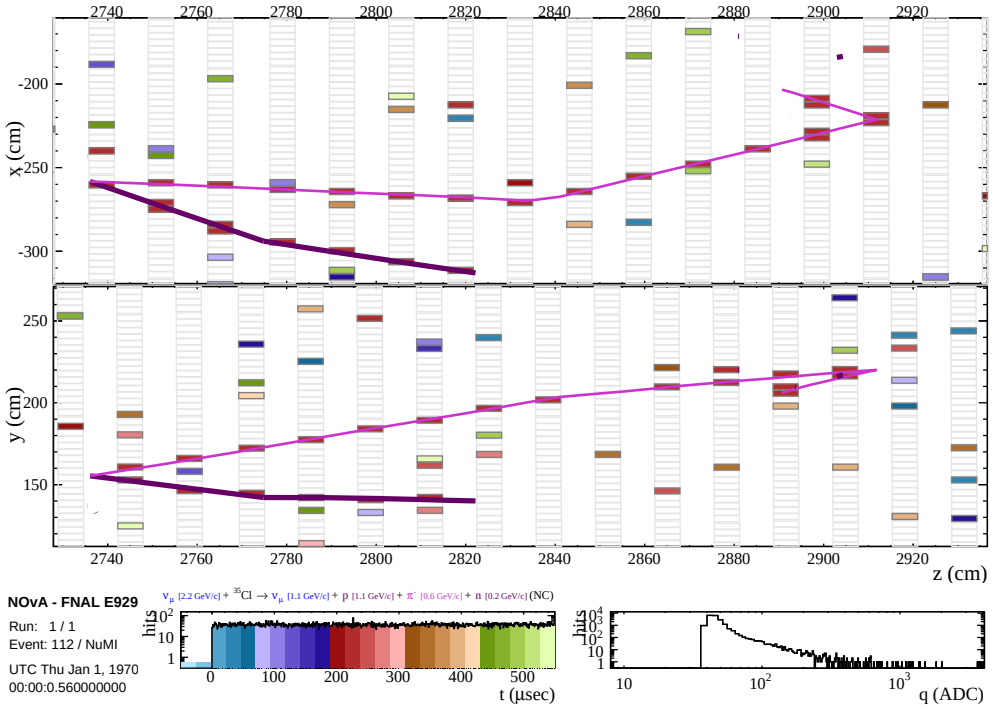

Figure 6.2: Example event display of an NC interaction with a similar topology to a ν_μ CC QE interaction. This event creates a proton, shown in purple, and π^-, shown in magenta, in the final state.

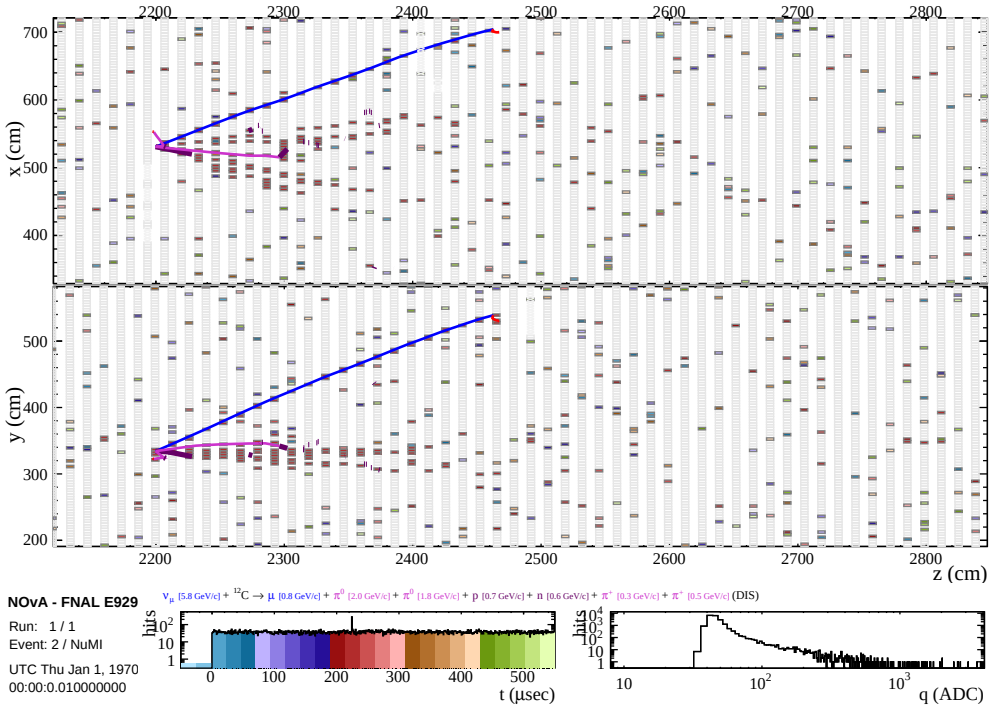

Figure 6.3: Example event display of a typical ν_μ CC deep inelastic interaction with a visible muon track and visible hadronic activity. This interaction results in a muon in, shown in blue, along with a hadronic shower.

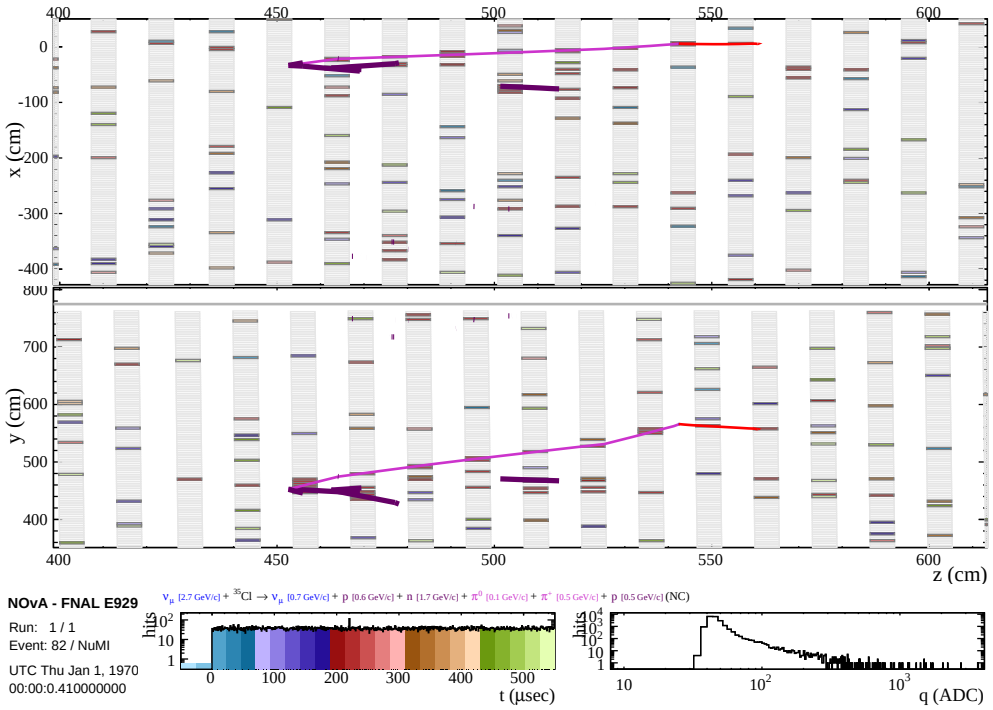

Figure 6.4: Example event display of an NC interaction with a charged pion track, shown in magenta, extending out from hadronic activity.

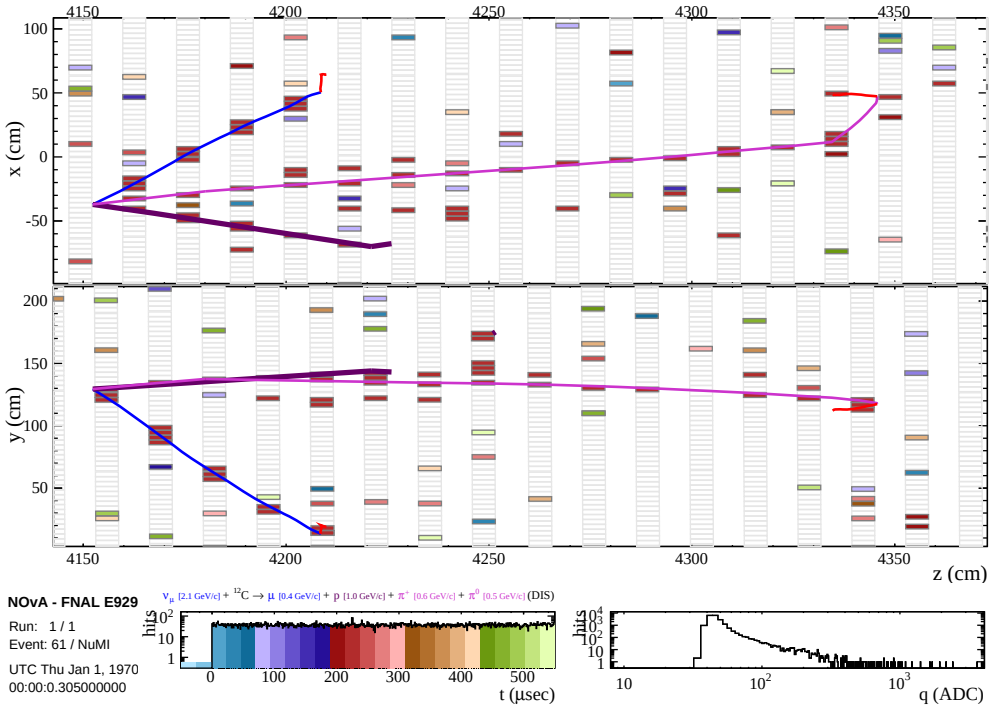

Figure 6.5: Example event display of an ν_μ CC deep inelastic interaction. Note the final state charged pion, shown in magenta, is longer than the final state muon, shown in blue, in this interaction.

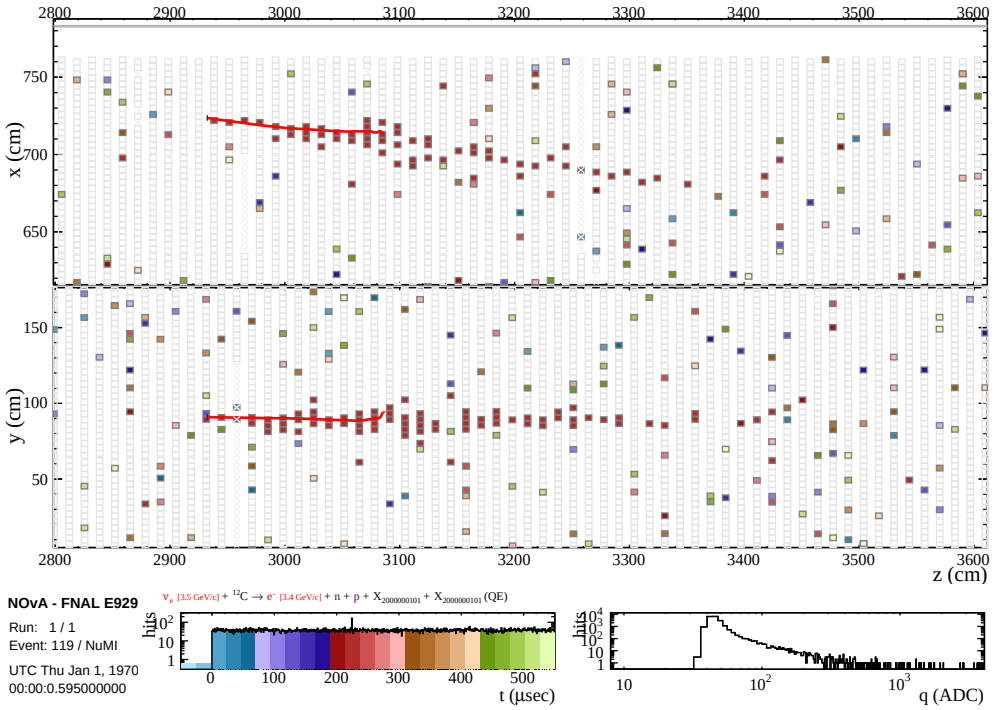

Figure 6.6: Example event display of an ν_e interaction resulting in an electromagnetic shower from the final state electron, shown in red.

6.1.1 Muon Identification Variables

ReMId uses four variables to classify the ν_μ CC muon likeness of the a reconstructed track: $\frac{dE}{dx}$ log-likelihood (LL), scattering LL, track length, and non-hadronic plane fraction. These variables characterize the behavior of muons in the NOνA detectors, which tend to be minimum ionizing particles leaving long tracks in the detector.

$\frac{dE}{dx}$ Log-Likelihood

Muons in the NOνA detectors lose a regular $\frac{dE}{dx}$ as a function of energy following the Bethe-Bloch equation. Charged pions, on the other hand, lose energy not only through Bethe-Bloch processes, but also through hadronic scattering. In the detectors, the interaction length for a charged pion is 82 cm[60]. Using the $\frac{dE}{dx}$ shape information makes it possible to distinguish particles from each other.

The $\frac{dE}{dx}$ is determined at each plane by summing the total calibrated visible energy associated with the reconstructed track in the plane and dividing by the total path length in active material that the track goes through in that plane. The $\frac{dE}{dx}$ measurement is performed on a plane level, instead of a cell by cell level, in order to avoid potential problems with the calculation of active path length that might result from reconstruction or alignment uncertainties.

To characterize the $\frac{dE}{dx}$, the LL that a particle of type i created the energy deposition profile of the track is defined as:

$$LL_i^E = \frac{1}{N_{Plane}} \sum_j P_j^i. \tag{6.1}$$

The $\frac{dE}{dx}$ is measured at plane j and the probability of the particle of type i to have the measured $\frac{dE}{dx}$, P_j^i, is calculated as a function of the distance from the track end from a sample histogram. Finally the number of planes in which the $\frac{dE}{dx}$ is measured, N_{Plane}, normalizes the LL among tracks of different lengths.

Figure 6.7 is an example distribution showing the probability of a muon depositing the measured $\frac{dE}{dx}$ at a distance from the end of the track of 500 cm. For each plane that is counted in the LL, the distance to the end of the track is calculated using the position of the track at the center of the plane; the probability is found using a distribution like figure 6.7 for the calculated distance from the end of the track. Figure 6.8 shows the

distribution of measured $\frac{dE}{dx}$ values as a function of distance from the end of the track under the muon assumption. Projections of figure 6.8 give the probability distributions used in the LL.

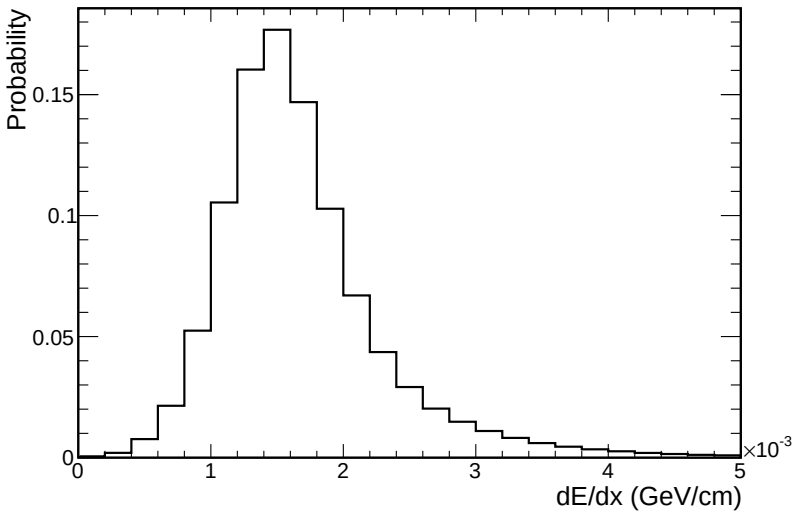

Figure 6.7: Probability distribution of muon $\frac{dE}{dx}$ at a distance of 500 cm from the end of the track.

The planes that go into the sum in Equation 6.1 are any plane in which the track has deposited energy and does not have energy contamination from vertex activity overlapping with the reconstructed track. The planes with energy contamination are determined from an algorithm designed to look for excess energy. This algorithm starts from the beginning of the track and looks for a drop in the $\frac{dE}{dx}$ per plane to a level consistent with a MIP independently in each view[61]. The energy deposition in planes with contamination will be inconsistent with any single particle type hypothesis and are removed from consideration of the LL calculation.

The difference between the $\frac{dE}{dx}$ LL under the charged pion assumption from the $\frac{dE}{dx}$ LL under the muon particle assumption, $LL^E_\mu - LL^E_{\pi^\pm}$, forms the final $\frac{dE}{dx}$ LL variable used as an input into ReMId. This difference is taken because the muon most closely resembles the charged pion in it's energy deposition shape and the difference gives a

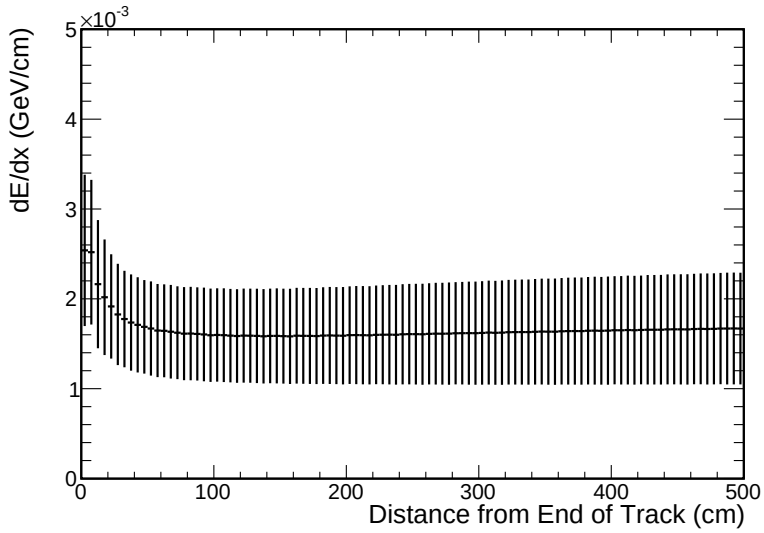

Figure 6.8: Profile of distribution of muon $\frac{dE}{dx}$ as a function of the distance from the end of the reconstructed track. The error bars show the RMS of the distribution.

measure of the likelihood the track is a muon compared to a charged pion. Figures 6.9 and 6.10 show the differences between the muon and charged pion $\frac{dE}{dx}$.

Scattering Log-Likelihood

The scattering LL variable works similarly to the $\frac{dE}{dx}$ LL variable except it looks at the scatter of the reconstructed track as a function of the distance from the end of the track. The NOνA detectors are not magnetized so any curvature in reconstructed tracks is due to scattering. Muons passing through the detector get most of their curvature from small angle multiple scattering with occasional hard scatters due to Coulomb scattering. Charged pions undergo the same Coulomb scattering, but have additional scattering from hadronic interactions. Figures 6.1 and 6.3 show typical multiple scattering muons. Figure 6.2 and 6.4 show examples of charged pion large angle scattering due to hadronic interactions.

To characterize the scattering of the reconstructed track, the scattering LL is defined

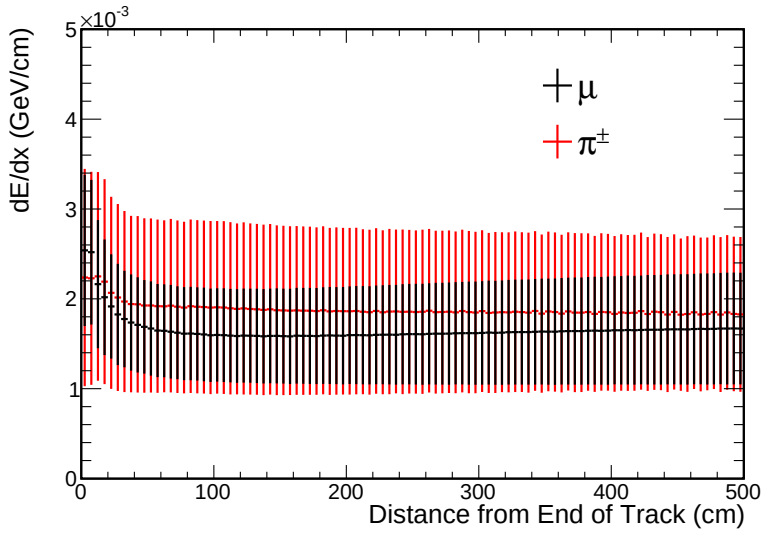

Figure 6.9: Profile of distributions of $\frac{dE}{dx}$ as a function of the distance from the end of the reconstructed track under the muon and charged pion particle assumptions. The error bars show the RMS of the distribution.

as

$$LL_i^{scat} = \frac{1}{N_{scat}} \sum_j P_j^i \tag{6.2}$$

where P_j^i is the probability, as a function of the distance from the end of the track, of the particle of type i to have a measured scatter at position j. Again a factor is applied to normalize the LL among tracks of different lengths.

The amount of scattering is measured as:

$$s = \frac{\theta^2}{d} \tag{6.3}$$

where θ is the scattering angle and d is the distance from the last scatter. This is a convenient metric for measuring scattering because for multiple scattering s will be a function of the energy of the particle which can be related to the distance from the end of the track [62]. The scattering measurements are made at every trajectory point on the track, except for the start and end point, by taking the difference of the track direction coming into and out of the trajectory point to determine the scattering angle

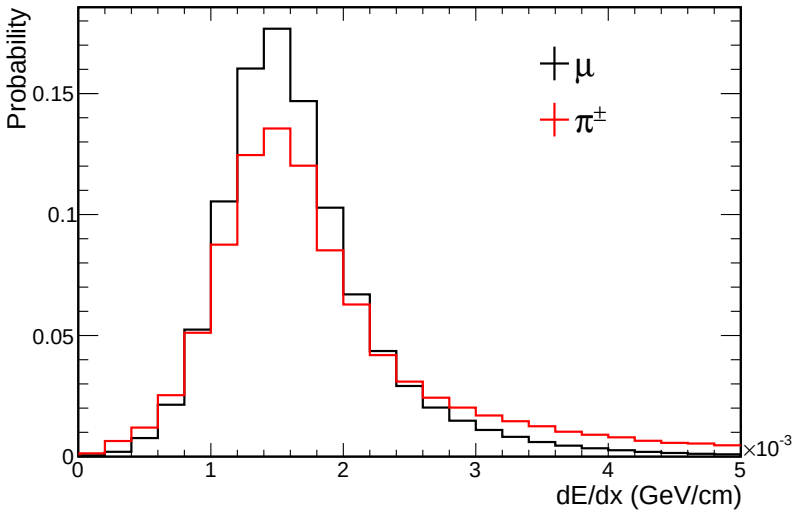

Figure 6.10: Probability distributions of $\frac{dE}{dx}$ at a distance of 500 cm from the end of the track under the muon and charged pion particle assumptions.

and the distance from the last trajectory point on the track to determine the distance from the last scatter.

Figure 6.11 shows the distribution of measured scattering values as a function of distance from the end of the track under the muon and charged pion assumptions. Figure 6.12 shows a projection of the sample distribution at a distance of 500 cm from the end of the track. From projections similar to Figure 6.12, the probabilities entering Equation 6.2 are calculated at all measurement points. The difference between the scattering LL under the charged pion assumption from the muon particle assumption, $LL_{\mu}^{scat} - LL_{\pi^{\pm}}^{scat}$, is the final scattering variable input into ReMId.

Track Length

The track length of the reconstructed track is input into ReMId. Hadronic showers produce many short reconstructed tracks. The total track length of the reconstructed track provides discrimination between tracks originating from hadronic showers and muons.

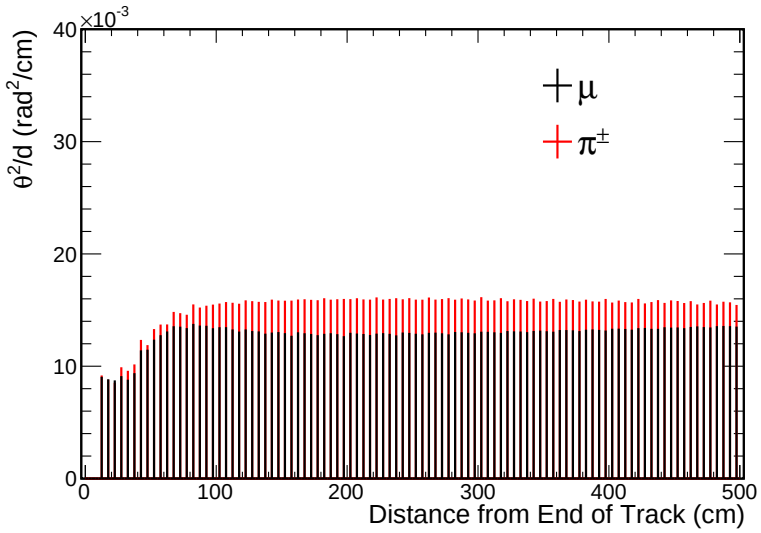

Figure 6.11: Profile of distributions of scattering as a function of the distance from the end of the reconstructed track. The data points are located at the peak of the distribution, 0, and the error bars show the RMS of the distribution from 0.

Non-hadronic Plane Fraction

The $\frac{dE}{dx}$ LL variable is calculated on a limited number of planes in the track due to energy contamination of the track. By excluding the planes with contamination, the $\frac{dE}{dx}$ LL variable more accurately represents the individual particle hypothesis; however, information about the hadronic energy deposition of the track is lost. Muons have very little hadronic contamination; it only results from imperfect separation of hadronic energy of the ν_μ CC event during track reconstruction. To recover the information about non-minimum ionizing energy loss, the fraction of planes used in the $\frac{dE}{dx}$ LL out of the total number of planes in the track with energy deposition, called the non-hadronic plane fraction, is input into ReMId.

Sample Histogram Generation

The sample histograms used in the LL variable calculations were generated from 5 million spills of simulated events. From these events, muon tracks from the ν_μ CC

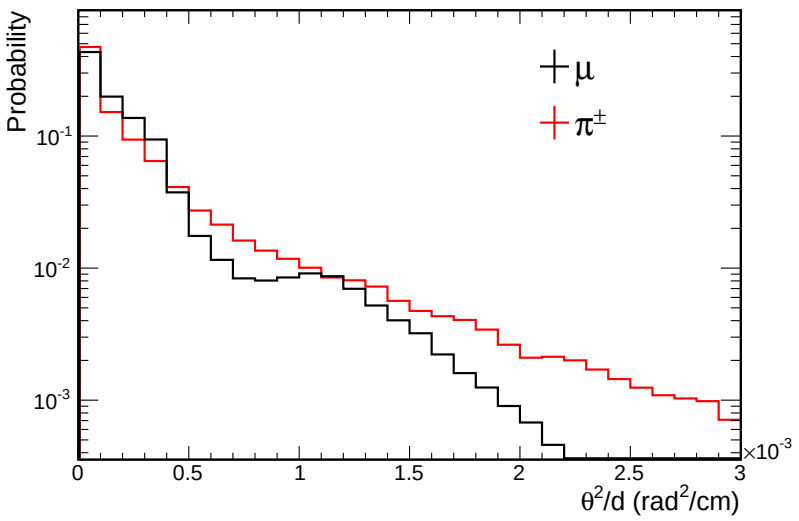

Figure 6.12: Probability distributions of scattering at a distance of 500 cm from the end of the track.

events are used to generate the expected $\frac{dE}{dx}$ and scattering samples, where as the pion sample come from charged pion tracks in the NC events. The reconstructed tracks used to create the histograms are required to be contained within the detector by having both the start and stop points at least 50 cm away from the detector edges. Tracks are matched to particles by assigning a reconstructed track to a true particle based on the particle type that is most pure based on the hits contained in the track.

6.2 Multivariate Analysis

6.2.1 k-Nearest Neighbour Classifier

ReMId uses a k-Nearest Neighbour (kNN) classifier to determine an overall PID value to characterize a track's likeness to a muon coming from a ν_μ CC event. The kNN method is implemented as part of the standard ROOT TMVA package[63]. The kNN algorithm works by comparing an input event to training events consisting of signal and background events in a multidimensional parameter space to classify how signal-like the input event is[64].

The determination of how signal like an event comes from finding the

$$k = k_S + k_B \tag{6.4}$$

nearest training events to the input event, where k_S is the number of signal events and k_B is the number of background events in the training sample. The closeness of the input event to the training events is calculated from the multidimensional Euclidean distance:

$$R = \left(\sum_{i=1}^{n_{var}} |x_i - y_i|^2 \right)^{\frac{1}{2}} \tag{6.5}$$

where n_{var} is the number of input parameters used, x_i is the value of the i^{th} variable of the input event and y_i is the value of the i^{th} variable of the training sample event it is being compared to. From the number of signal events in the k closest events the probability that the input event is signal-like is:

$$P_S = \frac{k_S}{k_S + k_B} = \frac{k_S}{k}. \tag{6.6}$$

ReMId uses the four variables described in sections 6.1.1-6.1.1 as inputs to the kNN algorithm with $k = 80$. The PID value of a reconstructed track is set as P_S. The PID value is limited in range between 0 and 1, where values close to 1 indicate high probability of being a muon and values close to 0 indicate very low muon likeness. The value of k was chosen as the lowest value that maximized the figure of merit (FOM), within the error of the statistics in the training sample. Where the FOM is calculated as:

$$FOM = \frac{S}{\sqrt{S+B}} \tag{6.7}$$

where S is the number of signal events and B is the number of background events.

6.2.2 Training

The ReMId training sample consists of simulated CC and NC events in the far detector. The training shown here uses an independent sample of 5 million spills. From these spills, cuts are applied for containment so that start and stop of the training sample track is at least 50 cm away from the detector edge. The signal training sample is made up of the track most representative of the muon in each CC event. The background training sample is made up of the track that most closely mimics a muon found in each NC event. If a track is matched to a final state charged pion, this is chosen as the most muon-like track in the NC event. Otherwise, if no charged pion is present, the most muon-like track is chosen as the longest reconstructed track in the NC event. Equal number of background and signal tracks are used in the training. After containment cuts, this resulted in 900,000 training tracks for each the signal and background populations. Distributions of the variables described in Sections 6.1.1-6.1.1 are shown in Figures 6.13-6.16. No oscillation were assumed in the training process as to not bias the PID to oscillation dependent performance.

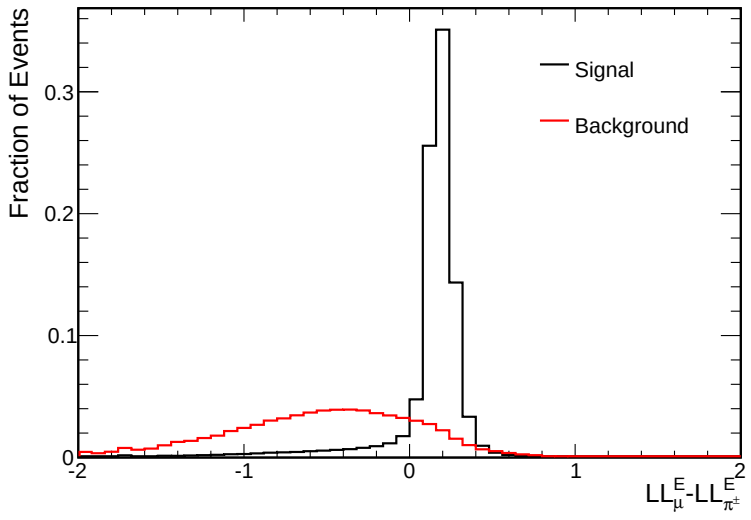

Figure 6.13: Distribution of the $\frac{dE}{dx}$ LL variable in kNN training sample.

Figure 6.17 shows the resulting PID distribution on a training and testing sample

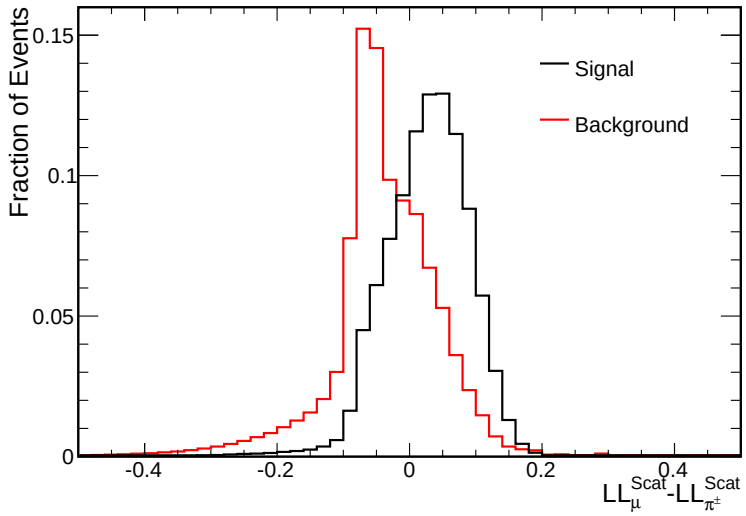

Figure 6.14: Distribution of the scattering LL variable in kNN training sample.

verifying that the kNN was not over-trained. The efficiency, purity, and FOM are plotted as a function of the PID cut value in Figure 6.18. As a result of the training it was determined that the selection efficiency would be 85% with a purity of 92 % at the cut value with highest FOM assuming equal number of signal and background events.

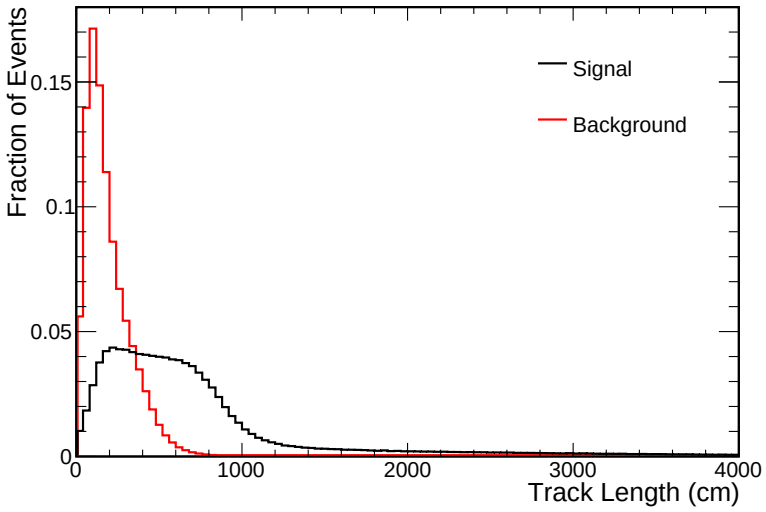

Figure 6.15: Distribution the track length variable in kNN training sample.

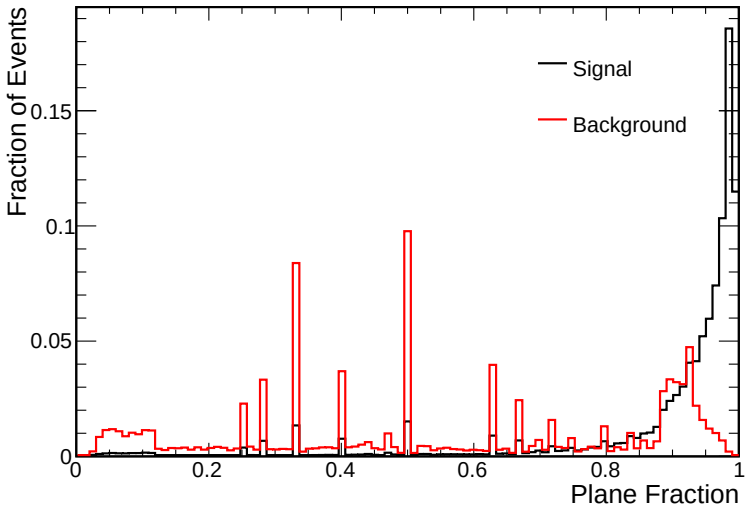

Figure 6.16: Distribution of the plane fraction variable in kNN training sample. Note the spiked behavior of the distribution coming from the discrete nature of the number of planes crossed and number of planes with $\frac{dE}{dx}$ measurements

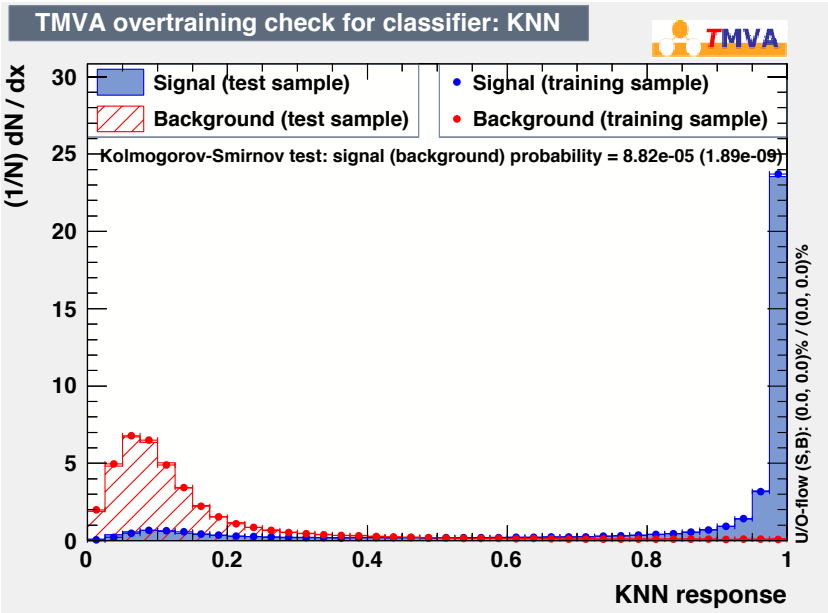

Figure 6.17: Overtraining test of PID output distributions of signal and background events.

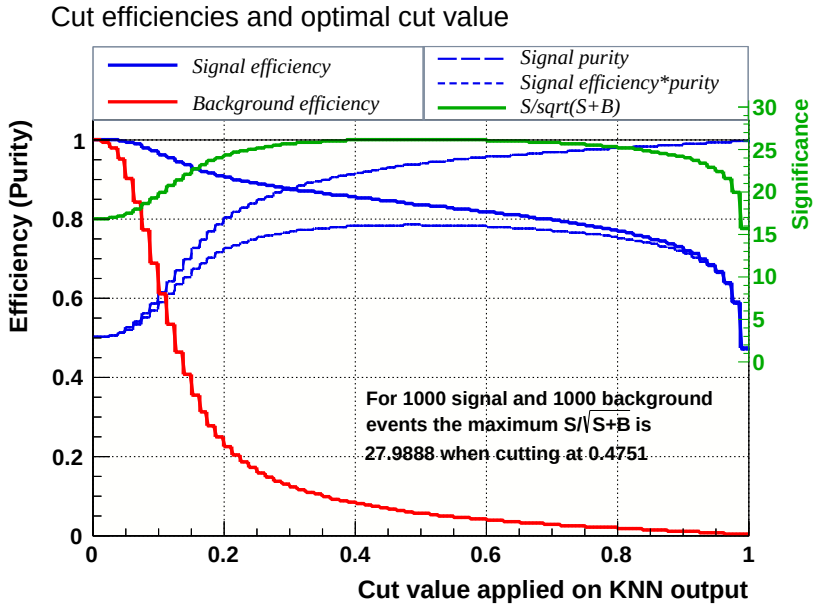

Figure 6.18: Training sample efficiencies, purities, and FOM in a testing sample as a function of PID cut value.

6.3 Performance

Figure 6.19 shows the PID distribution from the highest PID valued track for each slice determined by the ReMId algorithm in independent simulated far detector neutrino data, normalized to 3.37×10^{20} protons on target. Additionally figures 6.20-6.23 show the input variables to ReMId for the highest PID valued track in the slice. These distributions assume the standard oscillations parameters listed in table 2.1. The distributions are an independent sample from the training sample and show the expected distribution of signal and background events in the far detector data. The interactions entering these plots pass the containment cuts discussed in chapter 8 which ensure that the neutrino interaction is contained within the detector. The PID distribution shows the ability to separate ν_μ CC events from neutrino background events from the presence of a muon alone. The efficiency and purity at which the ν_μ CC events can be identified as a function of PID cut value are shown in figures 6.24 and 6.25. Where at a given PID cut value all events with that or higher PID value are accepted and those with lower PID values are rejected. For a PID value of 0.70 the ν_μ CC selection efficiency is 81% and the purity is 98%. The rejection efficiency of non-ν_μ CC events is 95%.

Efficiency and purity give general insight as to the performance of the PID, but were not used in determining the value at which to cut for accepting and rejecting events as ν_μ CC. Additionally traditional FOM metrics such as the number of signal events divided by the square root of the total number of events selected can be misleading in choosing a cut value for the ν_μ disappearance measurement. The issue arises in that the observation of disappearance inherently involves a region of energy in which the lack of signal ν_μ CC events are missing. This region is important for the measurement of the oscillation parameters, but an optimization to a standard FOM could choose cuts that would remove region of interest as it would not penalize the FOM. Instead of optimizing a cut value to an FOM value, optimization was done to determine the best cut value at which the value of θ_{23} could be determined under various assumptions of the true value of θ_{23} [65]. This study resulted in an optimal PID cut of 0.70 which is applied as part of event selection.

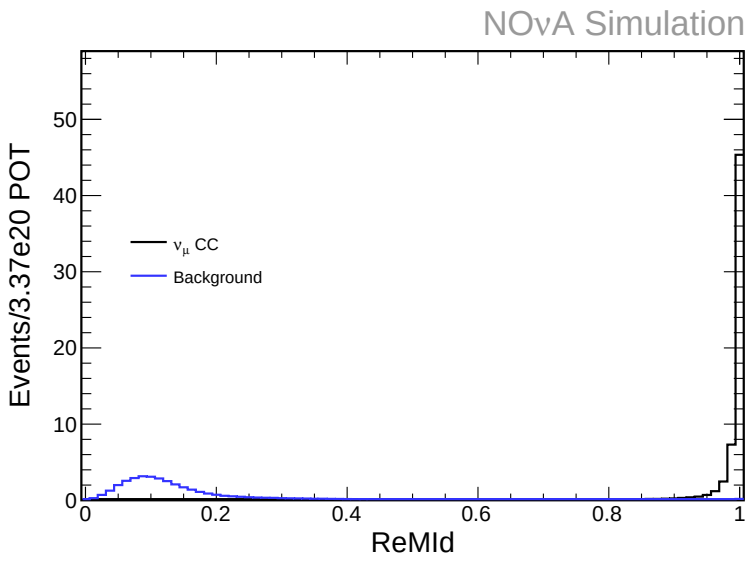

Figure 6.19: PID distribution of signal and background events in simulated far detector neutrino interactions.

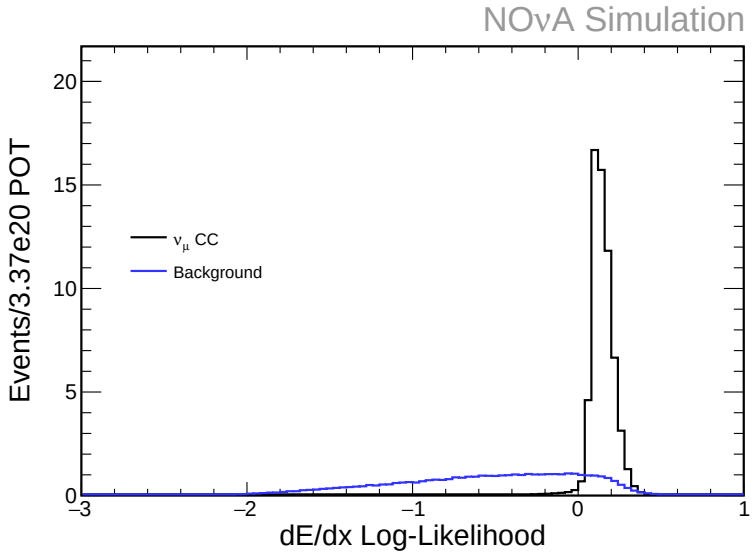

Figure 6.20: Distribution of PID input variable, $\frac{dE}{dx}$ LL, of signal and background events in simulated far detector neutrino interactions.

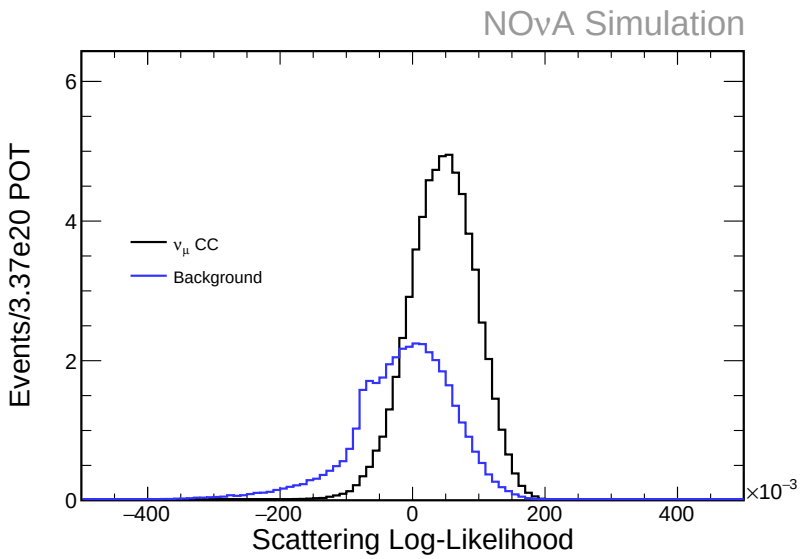

Figure 6.21: Distribution of PID input variable, scattering LL, of signal and background events in simulated far detector neutrino interactions

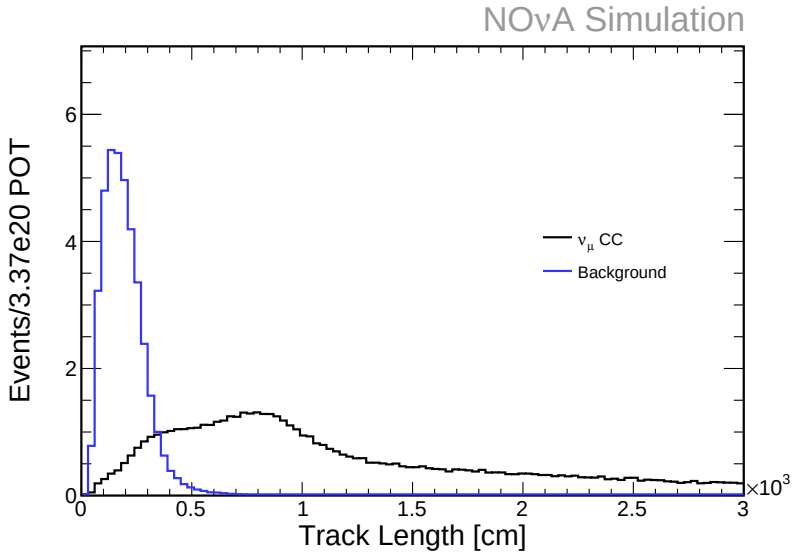

Figure 6.22: Distribution of PID input variable, track length, of signal and background events in simulated far detector neutrino interactions

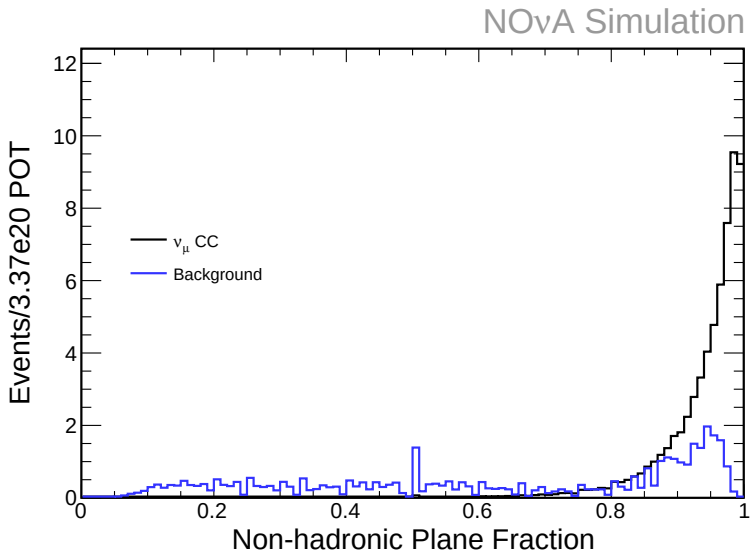

Figure 6.23: Distribution of PID input variable, non-hadronic plane fraction, of signal and background events in simulated far detector neutrino interactions

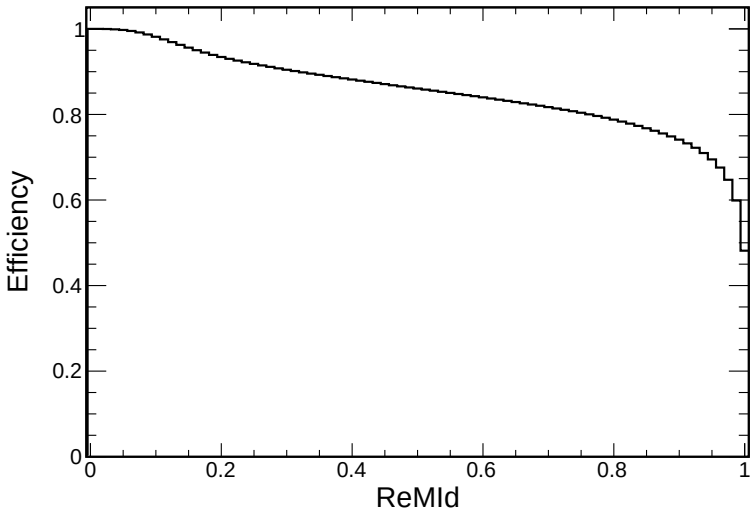

Figure 6.24: ν_μ CC selection efficiency as a function of PID cut value.

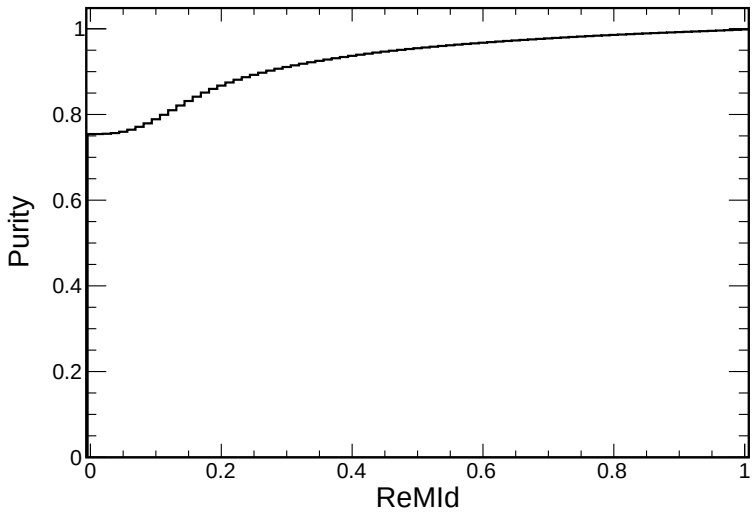

Figure 6.25: ν_μ CC selection purity as a function of PID cut value.

Chapter 7

Energy Estimation and Event Separation

The measurement of oscillation parameters from the disappearance of ν_μ is performed from a fit to the energy spectrum of the observed events. Accurate energy estimation leads to precise determination of the location of the oscillation minimum and the magnitude of the minimum increasing the power of the fit. The first section of this chapter describes how energy estimation is performed for the ν_μ analysis. The second section of this chapter describes how the energy estimation and event topology of ν_μ charged current (CC) events is used to separate the ν_μ CC sample into two subsamples, quasielastic (QE) and non-quasielastic (NonQE), which allows for the identification of a high energy resolution QE sample.

7.1 Energy Estimation

The energy estimation of ν_μ CC events is performed by splitting the interaction into the muon and hadronic systems [66]. The muon system is determined by the ReMId algorithm and the hadronic system is determined to be everything else in the slice except the muon. Additionally any overlapping hadronic energy on the identified muon track is grouped with the hadronic system. The energy from the final state muonic and hadronic systems are determined separately and the total neutrino energy is then the sum of the energy from these two components.

The muon energy is constructed from the track length of the reconstructed track that is identified as the most muon like in a slice from the ReMId algorithm. The algorithm relies on the $\frac{dE}{dx}$ of the track following the Bethe-Bloch curve as a function of the distance from the end of the track. By integrating over the path, the total kinetic energy lost by the muon can be determined and the initial energy can be found as a function of the total range of the particle. The muon energy estimation uses a linear spline to approximate the integral of the Bethe-Bloch equation to convert the track length to the energy with a total of four splines used. Using more than four linear segments was shown to not significantly improve the resolution in muon energy. The slopes, offset, and knots in the spline sections are found by fitting the peak of true muon energy distribution as a function of reconstructed track length of the most muon like track, as determined by ReMId, in simulated ν_μ CC events in the far detector. The correlation between track length and true muon energy is shown in figure 7.1 along with the resulting fit drawn as well. The resulting muon fractional energy resolution in the far detector is 3.2% shown in figure 7.2. The near detector uses the same fit from track length to estimate the neutrino energy with a modification to account for the muon catcher. Since the muon catcher has planes of steel interleaved with the active planes it does not follow the same relation between track length and energy as the active region. In order to account for this a linear fit is performed to determine a conversion between track length in the muon catcher to equivalent active track length. The equivalent active track length is then used instead of the actual reconstructed track length in the near detector.

The hadronic energy is determined using a fit procedure similar to the muon energy fit, except that the fit is performed on the calorimetric energy instead of track length. A spline fit is used to fit the reconstructed visible hadronic energy from the residual energy in the ν_μ CC interaction. The residual energy is determined from subtracting the reconstructed muon energy determined as described above from the true neutrino energy in the event. The hadronic energy fit also uses a linear spline function with four segments with the fit determining the slopes, offsets, and knots in the spline sections. Additionally the fit is performed for QE and NonQE interactions separately with the the interaction types separated by using the truth information in the simulation. Figures 7.3 show the fit of the reconstructed hadronic energy to the residual energy and figure

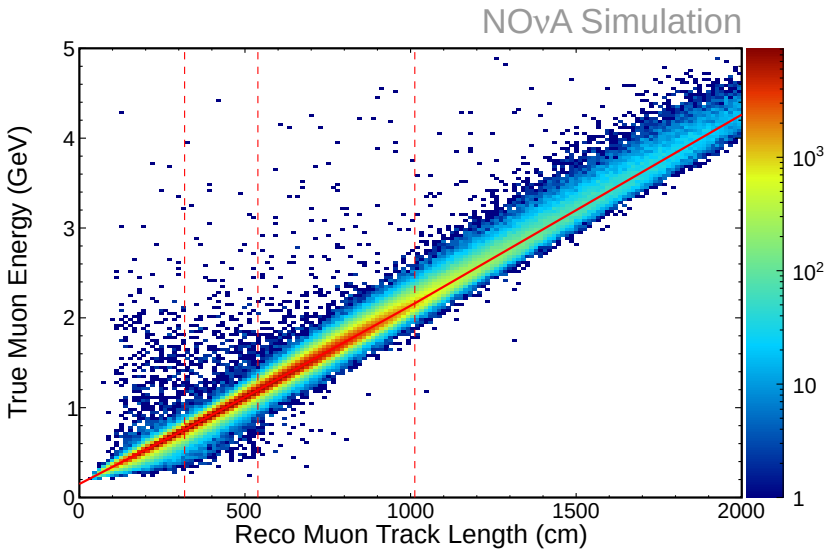

Figure 7.1: Muon energy fit.

7.4 shows the fractional energy resolution of the hadronic energy.

The resulting neutrino energy for the resolution for both QE and NonQE events is shown in figures 7.5 and 7.6. Even though the hadronic energy in a NonQE interaction can only be determined to 13%, the total neutrino energy resolution is better, 6%, because the muon generally dominates the energy.

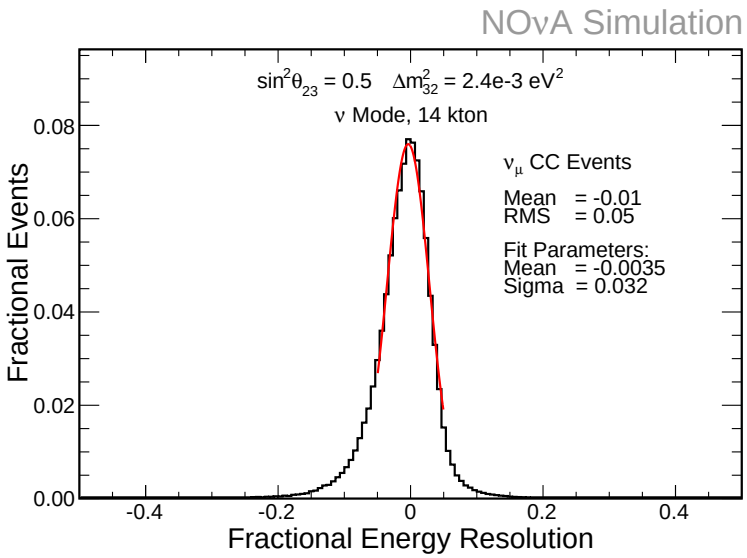

Figure 7.2: Muon energy fractional resolution.

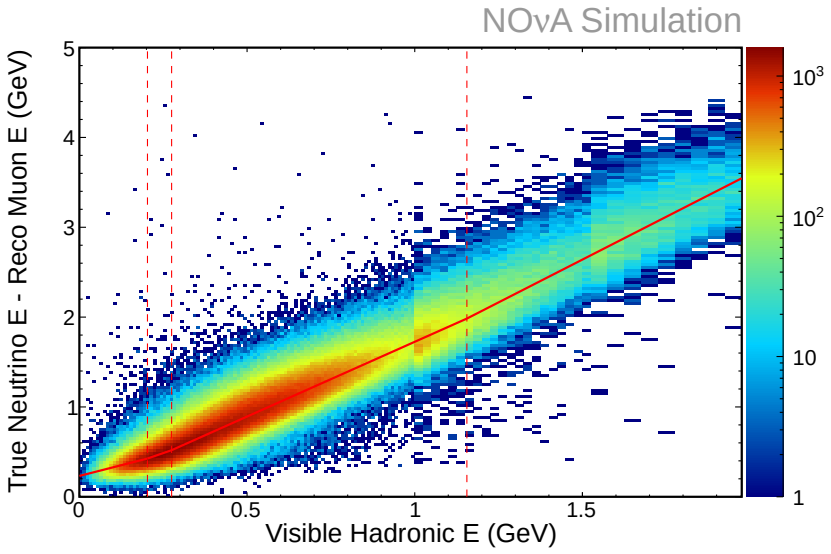

Figure 7.3: Hadronic energy fit for NonQE interaction types.

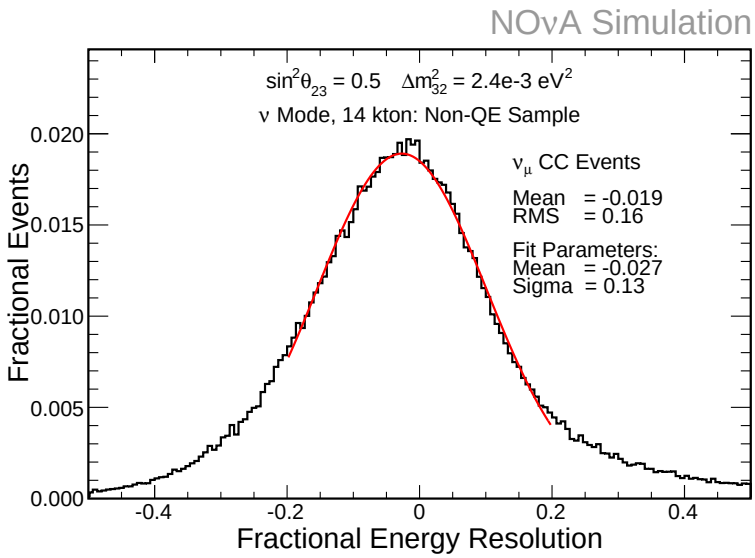

Figure 7.4: Hadronic energy fractional resolution for NonQE interaction types.

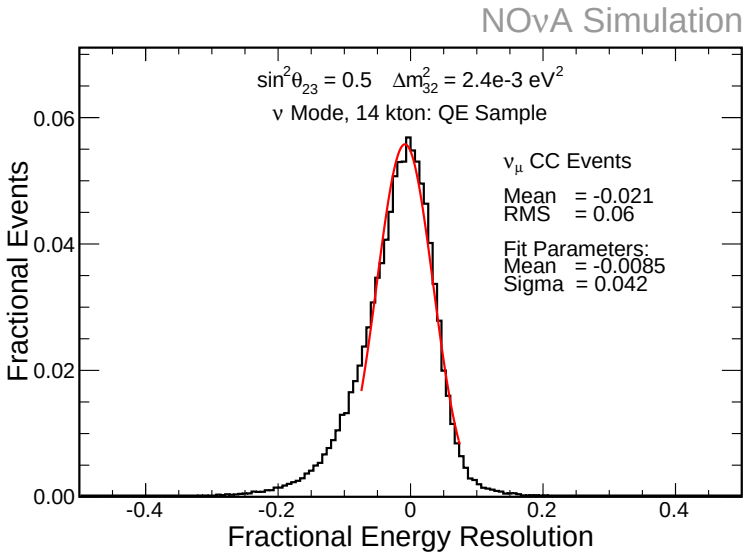

Figure 7.5: Fractional neutrino energy resolution for QE interactions.

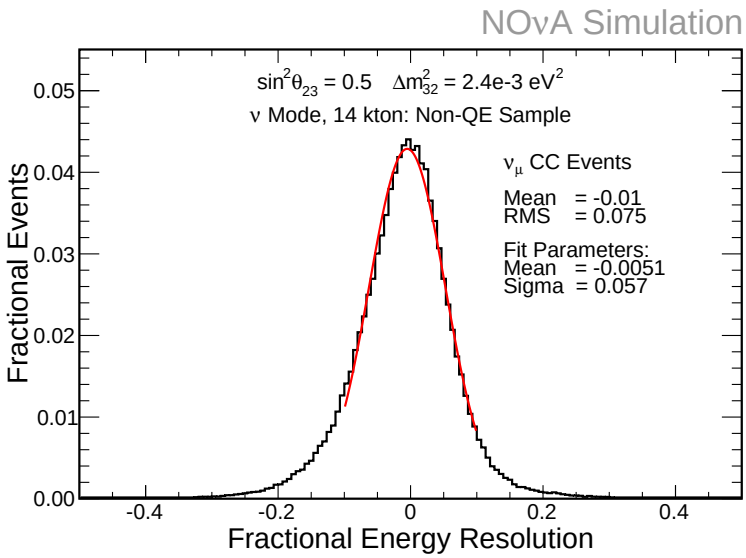

Figure 7.6: Fractional neutrino energy resolution for NonQE interactions.

7.2 Event Separation

This section presents the **Q**uasi**e**lastic **P**article **Id**entification (QePId) algorithm. The primary goal of QePId is to discriminate ν_μ charged current (CC) quasielastic (QE) interactions from other ν_μ CC interaction types. Identifying QE events allows for use of higher resolution energy estimators to be applied in both the QE and NonQE subsamples, making the combined sample measurement of the parameters in the ν_μ disappearance analysis more precise [67].

7.2.1 Features of ν_μ CC QE Events and Backgrounds

ν_μ CC QE interactions result in a final state muon and proton. Figures 7.7 and 7.8 show typical topologies of QE events in the NOνA Far Detector. Other interaction types, like DIS or RES interactions, produce final state particles besides a muon and proton. These often show up as additional visible prongs or hadronic showers in the events as seen in figures 7.9 and 7.10. When these other interaction types result in a one or two track topology, sometimes the extra final state particles can not be disentangled from each other or do not deposit visible energy. They then can mimic QE events.

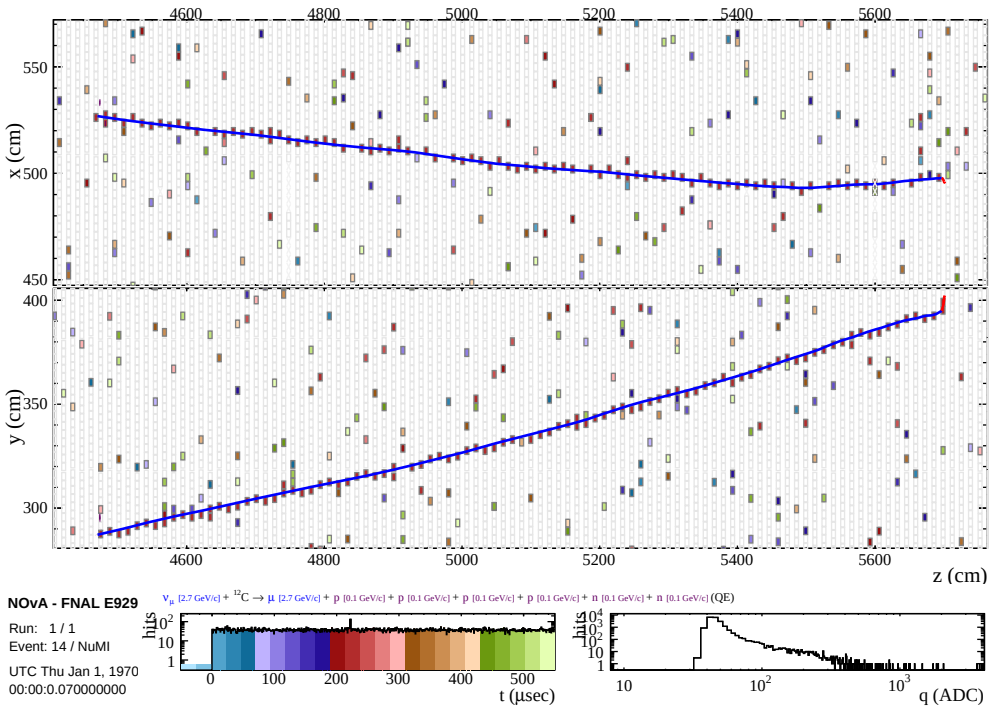

Figure 7.7: Example event display of an ν_μ CC QE interaction with only a visible muon in the final state.

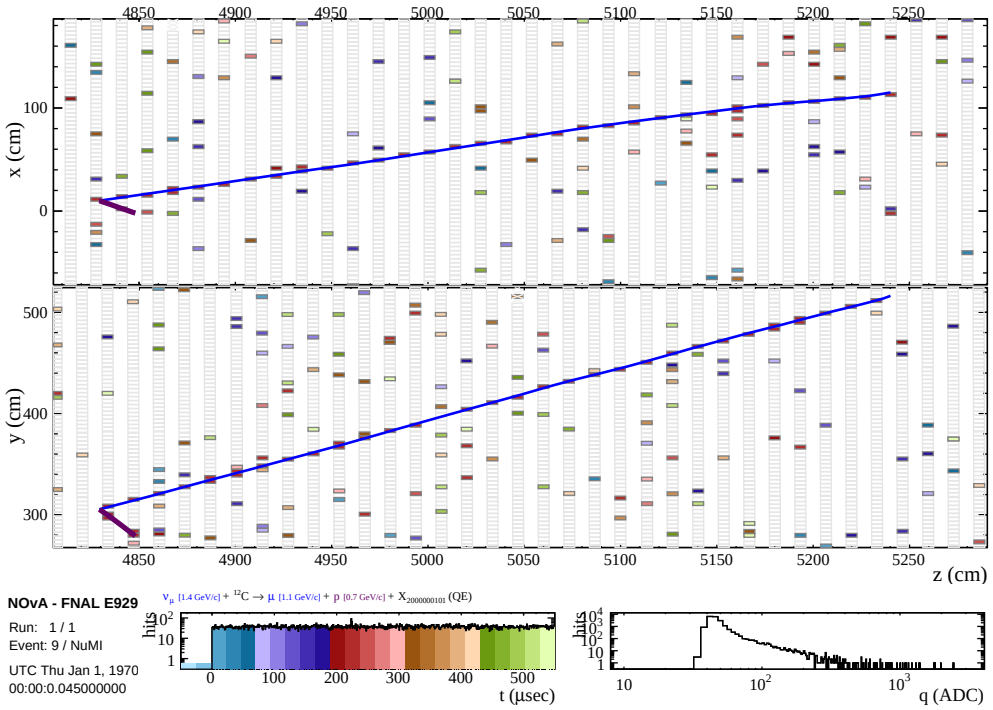

Figure 7.8: Example event display of an ν_μ CC QE interaction with a visible muon and proton in the final state.

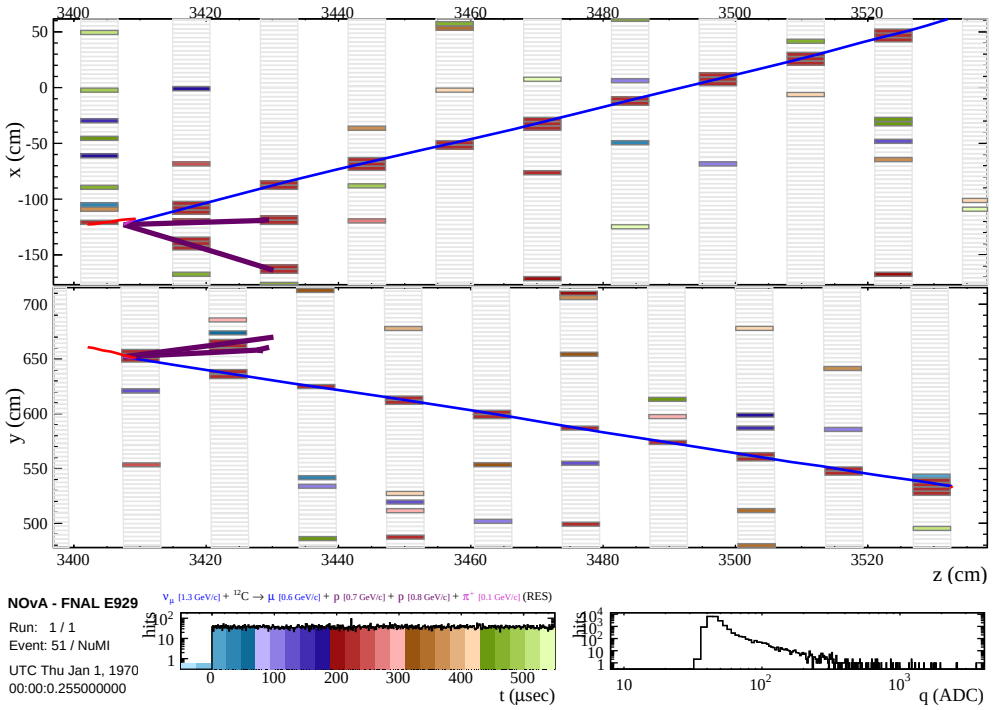

Figure 7.9: Example event display of a typical ν_μ CC resonance interaction with a visible muon track and multiple proton prongs.

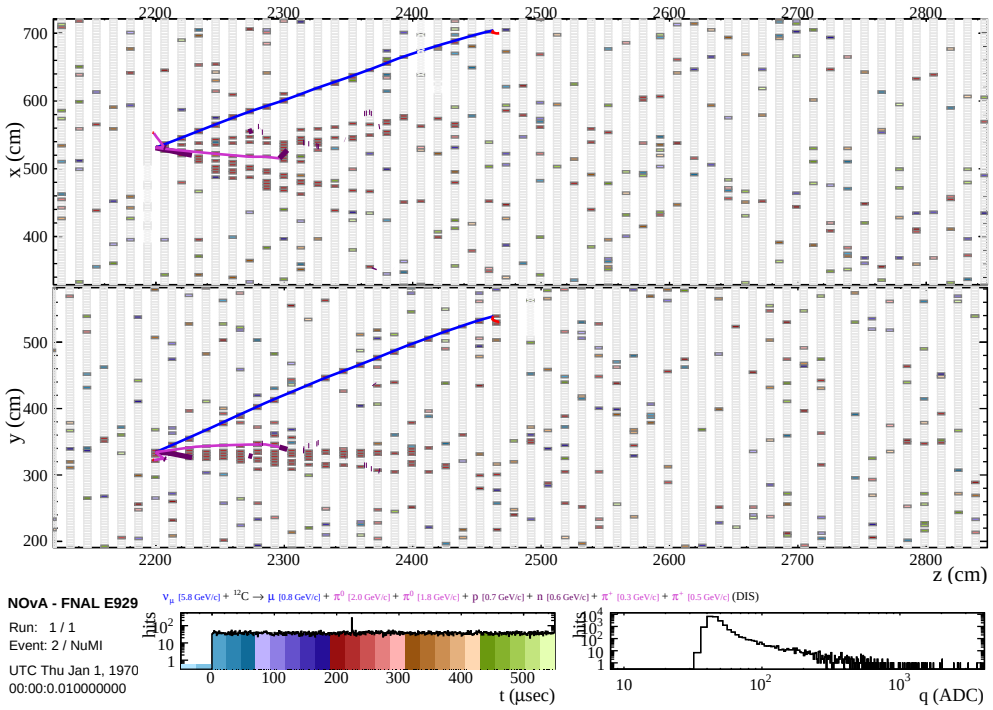

Figure 7.10: Example event display of a typical ν_μ CC deep inelastic interaction with a visible muon track and visible hadronic activity.

7.2.2 QE Variables

The QePId algorithm is designed to pick out QE events after ν_μ CC event identification has taken place so that it deals with a nearly pure sample of ν_μ CC events. Additionally, because QE events result in a final state muon and proton, QePId only tries to identify QE events from slices with only one or two reconstructed tracks. 92% of all QE events have one or two reconstructed three dimensional tracks [68]. QePId uses three (four) variables to classify the ν_μ CC QE likeness of the reconstructed slices with one (two) reconstructed tracks in them. The variables used are the off-track energy, fractional QE energy difference, fractional energy difference z-test, and $\frac{dE}{dx}$ ratio. The following sections motivate how these variables characterize ν_μ CC QE interactions in the NOνA detectors.

Off-Track Energy

QE interactions do not deposit energy unassociated with the final state muon and proton, whereas other interaction types have the ability to deposit additional energy due to the additional final state particles. The off-track energy variable is the ratio of energy not associated with any reconstructed track to the sum of all the energy on reconstructed tracks in a slice. Figures 7.11 and 7.12 show the distribution of off-track energy in QE and NonQE events in the one and two track samples.

Fractional Energy Difference

The ν_μ CC energy estimator has two methods for determining the neutrino energy in QE interactions. The standard estimate described in the above section uses a fit to muon and hadronic energy components of the interaction, $TrkQEE$. Another energy estimate uses the two-body kinematics and known final state hadron mass of a QE interaction in the standard QE energy formula, $AngleQEE$ defined in equation 7.1. For NonQE interactions the final state hadron mass is greater than QE interactions.

$$AngleQEE' = \frac{2M_n' - \left(M_n'^{\,2} + M_\mu^2 + M_p^2\right)}{2\left(M_n' - E_\mu + \sqrt{E_\mu^2 - M_\mu^2}\cos\theta\right)} \tag{7.1}$$

M'_n is the neutron mass less the nuclear binding energy. For QE interactions these two energy estimations should be consistent with each other. This energy estimate gives a lower energy resolution than the fit to muon and hadronic components making it less than ideal for the energy estimation; however, it still provides an additional constraint on QE interactions. The energy difference variable is the ratio of the subtraction of the $AngleQEE$ energy from the $TrkQEE$ energy to the $TrkQEE$ energy.

$$\text{QE Energy Difference} = \frac{|TrkQEE - AngleQEE|}{TrkQEE} \tag{7.2}$$

Figures 7.13 and 7.14 show the distribution of fractional energy difference in QE and NonQE events in the one and two track samples.

Fractional Energy Difference Z-test

For some QE interactions, the $AngleQEE$ energy estimation can have large uncertainties due to reconstruction uncertainties and Fermi motion of the target nucleon within the nucleus. These uncertainties make it possible for the event to look like a NonQE event in the energy difference variable. In order to identify these events better, a z-test variable of the difference of the $AngleQEE$ energy from the $TrkQEE$ energy divided by the uncertainty in the $AngleQEE$:

$$\text{Energy Difference Z-test} = \frac{|TrkQEE - AngleQEE|}{\sigma_{AngleQEE}}. \tag{7.3}$$

is used. The uncertainty on the energy, $AngleQEE$, is defined as:

$$\sigma^2_{AngleQEE} = AngleQEE^2 \left(\frac{\sigma_x^2 + AngleQEE^2 \sigma_y^2}{\left(2M'_n E_\mu - \left(M'^2_n + M_\mu^2 - M_p^2\right)\right)^2} \right) \tag{7.4}$$

$$\sigma_x^2 = 4\left(M_n^2 + M_b^2\right)\sigma^2_{E_\mu} + 4\left(M_n^2 + E_\mu^2 + \frac{1}{2}M_b^2\right)\sigma^2_{M_b} \tag{7.5}$$

$$\sigma_y^2 = 4\sigma^2_{M_b} + 4\sigma^2_{E_\mu} + 4\left(\frac{E_\mu^2 \cos^2\theta \sigma^2_{E_\mu}}{2p_\mu^2} + p_\mu^2 \sigma^2_{\cos\theta}\right) \tag{7.6}$$

where σ_{E_μ} is the uncertainty in the track energy estimation and $\sigma_{\cos\theta}$ is the uncertainty in the track direction. Figures 7.15 and 7.16 show the distribution of fractional energy difference in QE and NonQE events in the one and two track samples.

$\frac{dE}{dx}$ Ratio

Slices that have a second reconstructed track have more handles for determining if they are a QE event. In two track QE events, one track should be from a muon and one track should be from a proton. To measure the energy deposition profile of the second, non-muon track, the ratio of the average $\frac{dE}{dx}$ of the non-muon track to the average $\frac{dE}{dx}$ of the muon track is taken. The muon track is taken as the track with the highest ReMID value.

$$\frac{dE}{dx} \text{ Ratio} = \frac{\frac{dE}{dx}_{non-muon}}{\frac{dE}{dx}_{muon}} \tag{7.7}$$

Figures 7.17 show the distribution of $\frac{dE}{dx}$ ratio in QE and NonQE events in the two track sample.

7.2.3 Multivariate Analysis

k-Nearest Neighbour Classifier

Simlarly to ReMId, QePId uses a kNN classifier to determine an overall PID value to characterize a slice's likeness to a ν_μ CC QE event. QePId uses the four variables described in Sections 7.2.2-7.2.2 as inputs to the kNN algorithm with $k = 50$. The PID value is limited in range between 0 and 1 where values close to 1 indicate high probability of being a QE event and values close to 0 indicate a very low QE event likeness. The value of k was chosen as the lowest value that maximized the FOM, within the error of the statistics in the training sample.

Training

The QePId training sample consists of simulated events in the far detector. From these spills, cuts are applied for containment so that the start and stop of the training sample, most muon-like track is at least 50 cm away from the detector edge. Additionally, a requirement is made that the ReMId value of the track with the highest ReMId value is greater than 0.70. This creates a sample of ν_μ CC events likely to be present in the ν_μ disappearance analysis sample. The signal training sample is made of events that pass these cuts and by truth are labeled as a QE interaction. Any events passing the cuts that are not a QE interaction, by truth, make up the background training sample. Both

the signal and background samples are further split into the one and two track samples, which are trained separately. Both track samples use 50,000 signal and background sample events. The input variable distributions, described in Sections 7.2.2-7.2.2, are shown in Figures 7.11-7.17 for the one and two track samples.

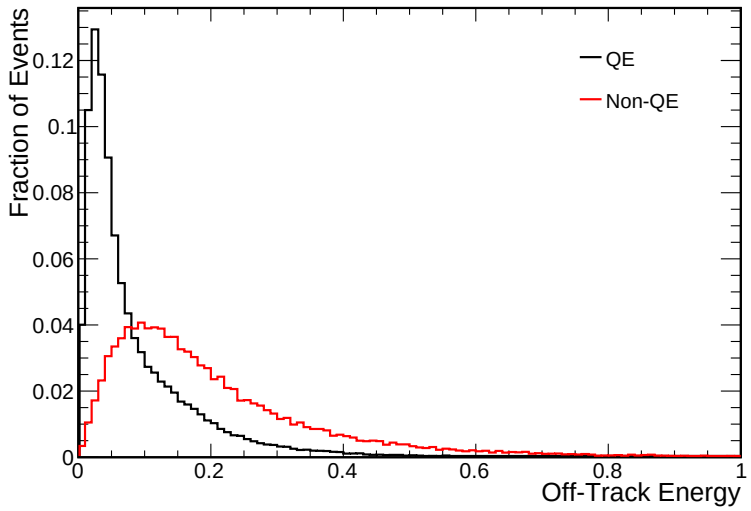

Figure 7.11: Distribution of the off track energy in the one track kNN training sample.

Figures 7.18 and 7.19 show the resulting PID distributions on a training and testing sample, verifying that the kNN was not over-trained. The efficiency, purity, and FOM are plotted as a function of the PID cut value in Figures 7.20 and 7.21. Note that this should not be used for determining the optimal cut value for the ν_μ disappearance analysis as the maximum sensitivity to the oscillation channel occurs where the signal disappears due to oscillations.

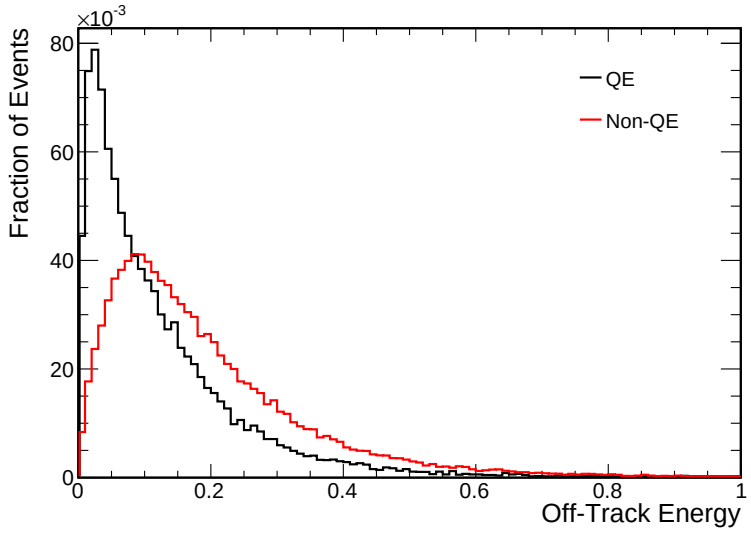

Figure 7.12: Distribution of the off track energy in the two track kNN training sample.

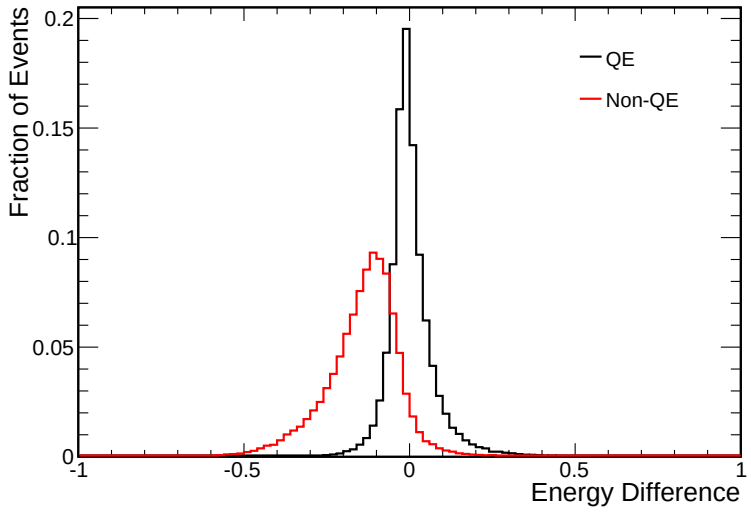

Figure 7.13: Distribution of the fractional energy difference variable in the one track kNN training sample.

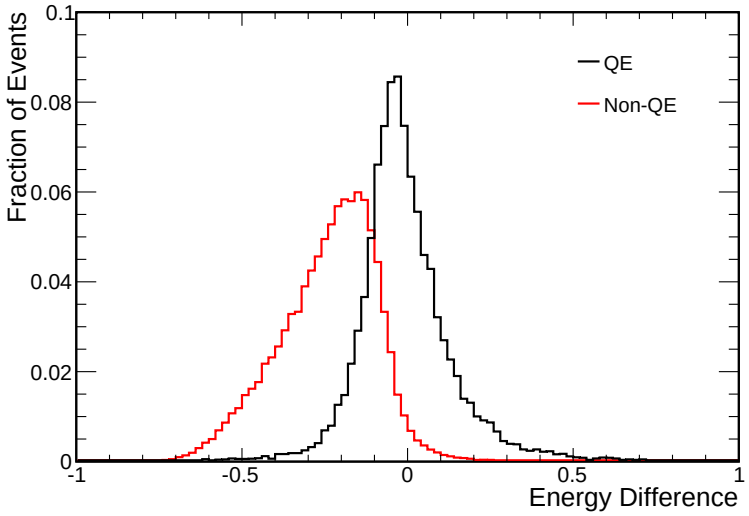

Figure 7.14: Distribution of the fractional energy difference variable in the two track kNN training sample.

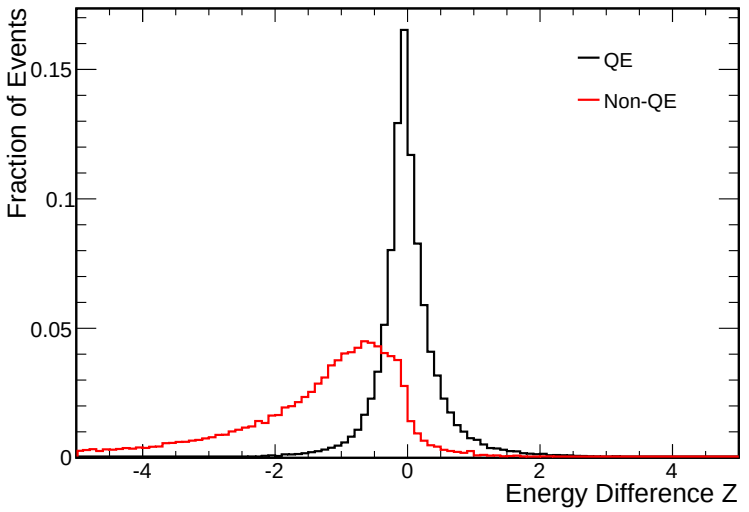

Figure 7.15: Distribution of the fractional energy difference z-test variable in the one track kNN training sample.

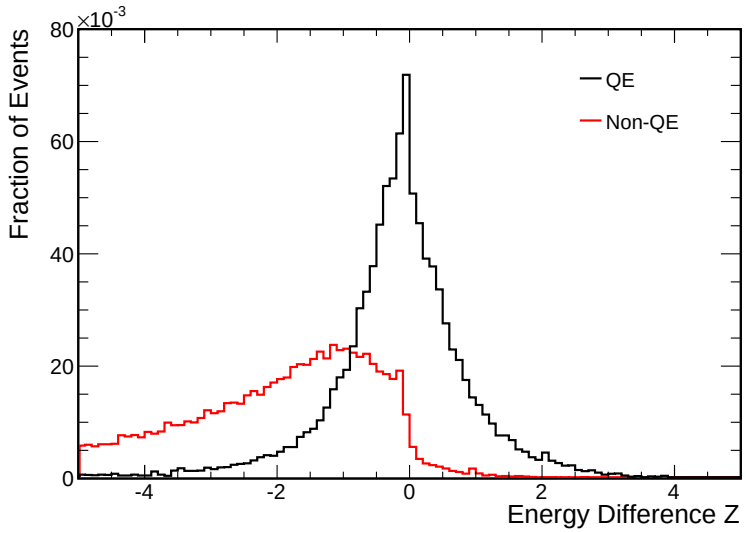

Figure 7.16: Distribution of the fractional energy difference z-test variable in the two track kNN training sample.

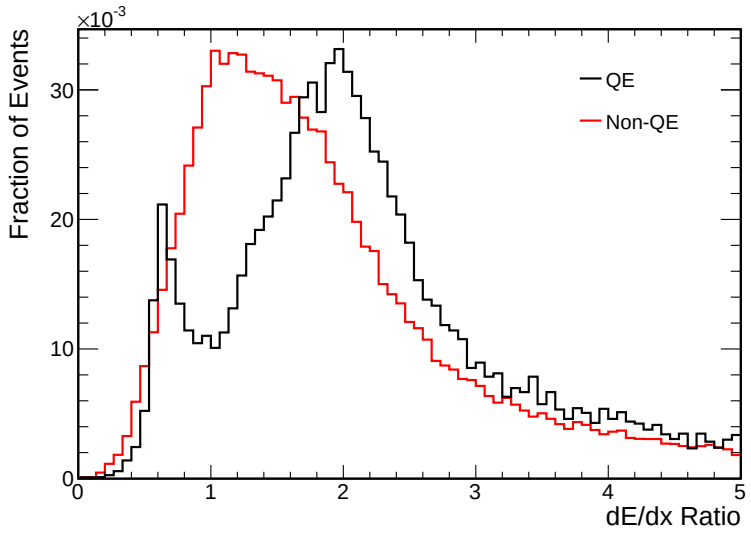

Figure 7.17: Distribution of the $\frac{dE}{dx}$ ratio variable in the two track kNN training sample.

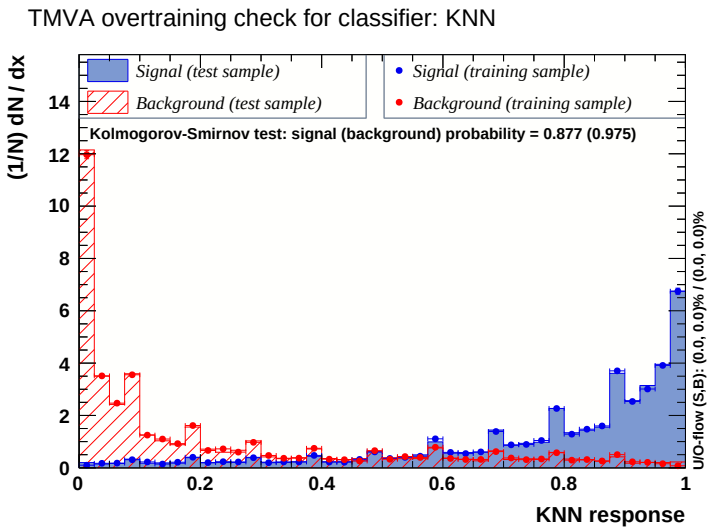

Figure 7.18: Training and testing sample PID output distributions of signal and background in the one track sample. Note spikes in the distributions are from the default binning in the TMVA training algorithm.

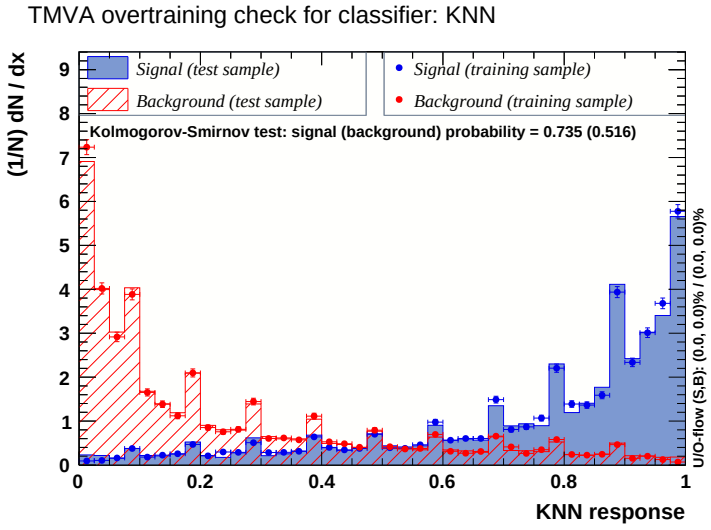

Figure 7.19: Training and testing sample PID output distributions of signal and background in the two track sample. Note spikes in the distributions are from the default binning in the TMVA training algorithm.

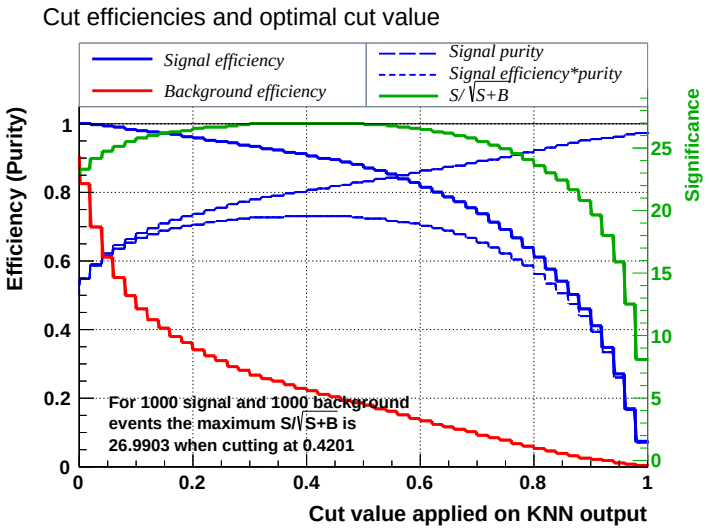

Figure 7.20: Sample efficiencies, purities, and FOM as a function of PID cut value of a testing sample in the one track sample.

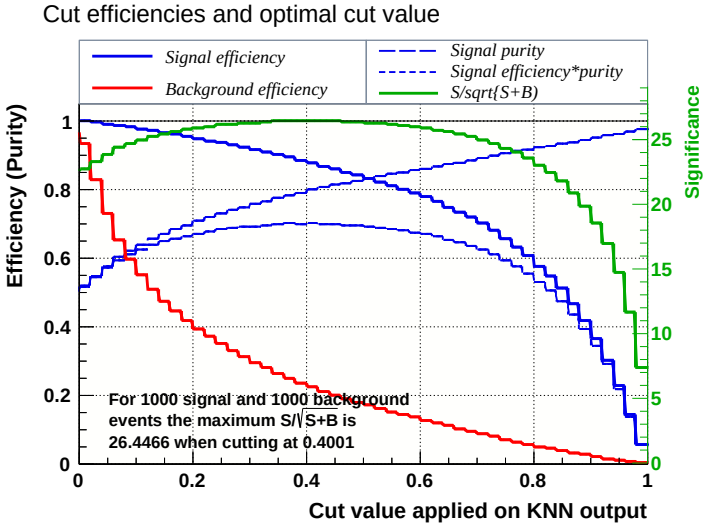

Figure 7.21: Sample efficiencies, purities, and FOM as a function of PID cut value of a testing sample in the two track sample.

7.2.4 Performance

Figure 7.22 and 7.23 shows the PID distribution from the highest PID valued track for each slice determined by the QePId algorithm in an independent simulated far detector neutrino data, normalized to 3.37×10^{20} protons on target and separated into the one and two track samples. Additionally figures 7.24-7.30 show the input variables to QePId for each slice passing a ReMId cut of 0.70 classifying it as a ν_μ CC interaction. These distributions assume the standard oscillations parameters listed in table 2.1. The distributions are an independent sample from the training sample and show the expected distribution of signal and background events in the far detector data. The interactions entering these plots pass the containment cuts discussed in chapter 8 which ensure that the neutrino interaction is contained within the detector. The PID distribution shows the ability to separate ν_μ CC QE events from NonQE events and other neutrino backgrounds present in the overall ν_μ CC sample. The PID cut values for the one and two track sample were chosen in the same process of optimizing the ν_μ CC PID cut value to the best measurement of θ_{23}. This resulted in optimal cut values of 0.45 for the one track sample and 0.40 for the two track sample which are applied as part of event classification. This suggests that the efficiency of finding QE events with good energy resolution outweighs the negative impact of misidentifying NonQE events as QE events.

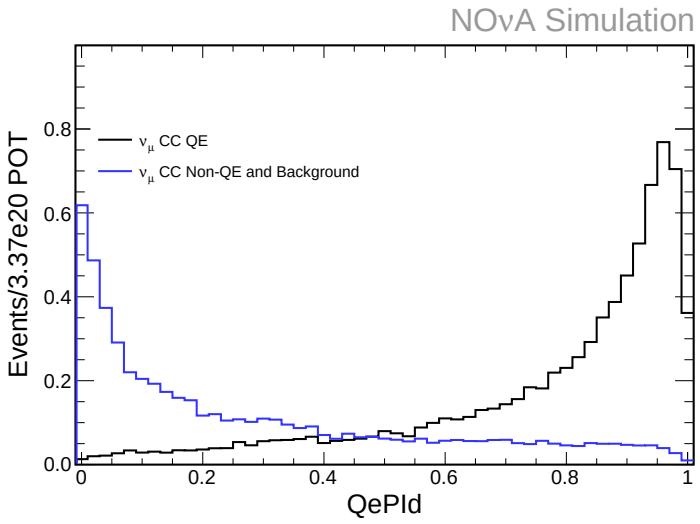

Figure 7.22: PID distribution of signal and background events in the one track sample.

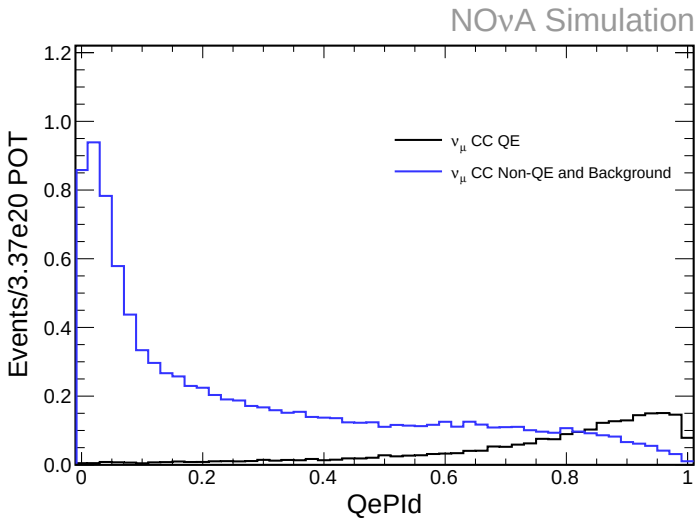

Figure 7.23: PID distribution of signal and background events in the two track sample.

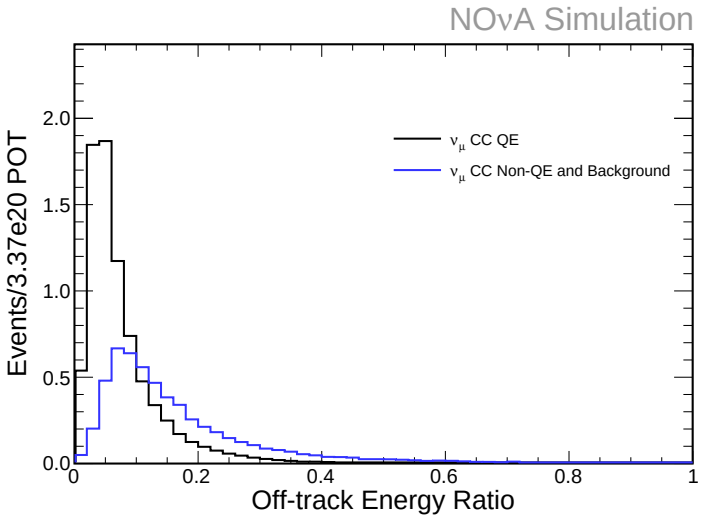

Figure 7.24: Distribution of PID input variable, off-track energy, of signal and background events in simulated far detector neutrino interactions in the one track sample.

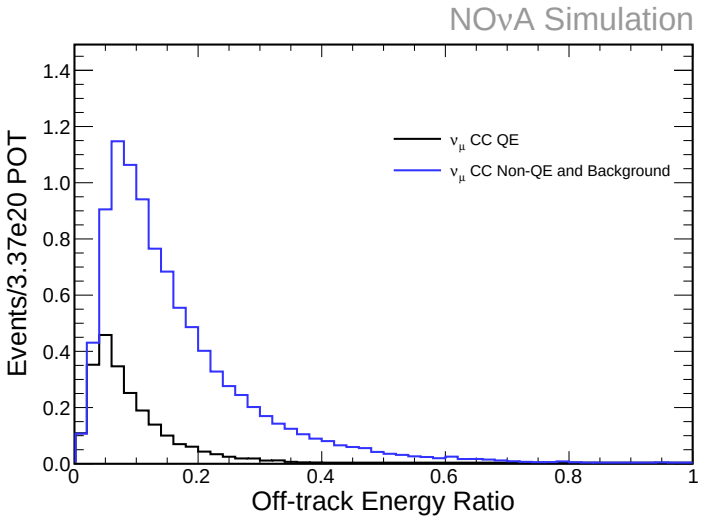

Figure 7.25: Distribution of PID input variable, off-track energy, of signal and background events in simulated far detector neutrino interactions in the two track sample.

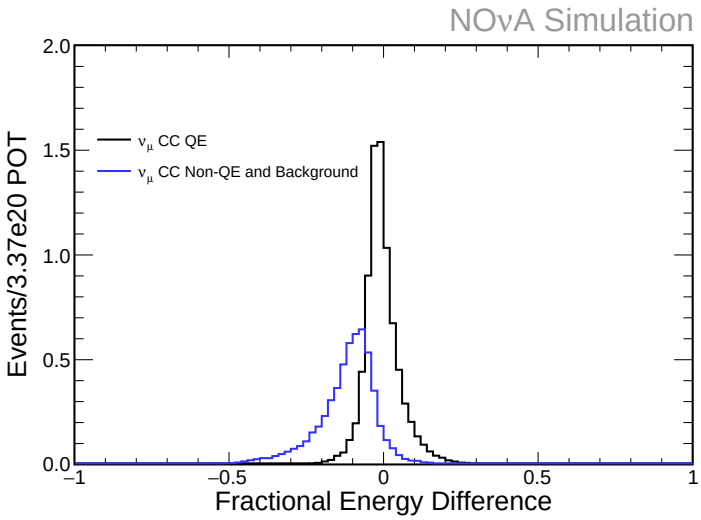

Figure 7.26: Distribution of PID input variable, fractional energy difference, of signal and background events in simulated far detector neutrino interactions in the one track sample.

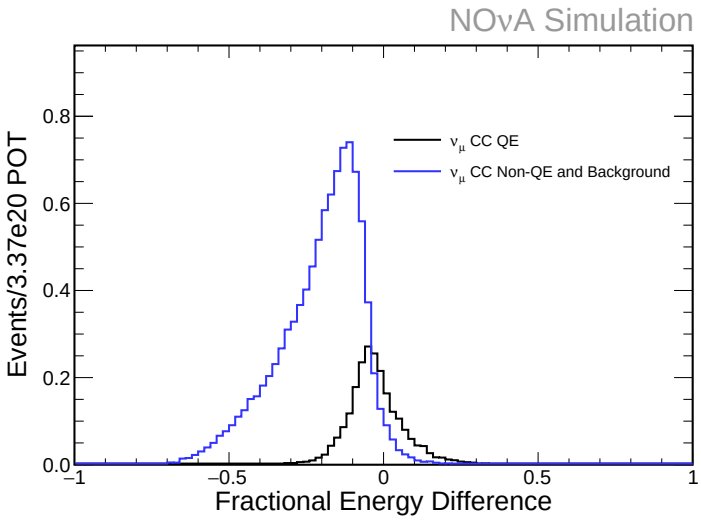

Figure 7.27: Distribution of PID input variable, fractional energy difference, of signal and background events in simulated far detector neutrino interactions in the two track sample.

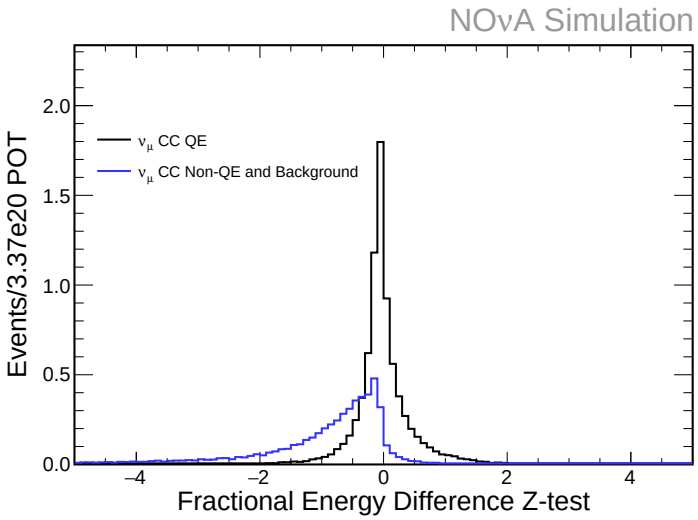

Figure 7.28: Distribution of PID input variable, fractional energy difference Z-test, of signal and background events in simulated far detector neutrino interactions in the one track sample.

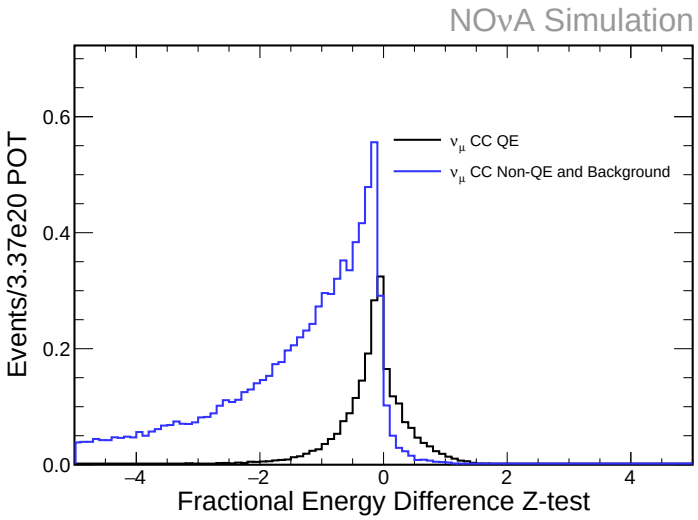

Figure 7.29: Distribution of PID input variable, fractional energy difference Z-test, of signal and background events in simulated far detector neutrino interactions in the two track sample.

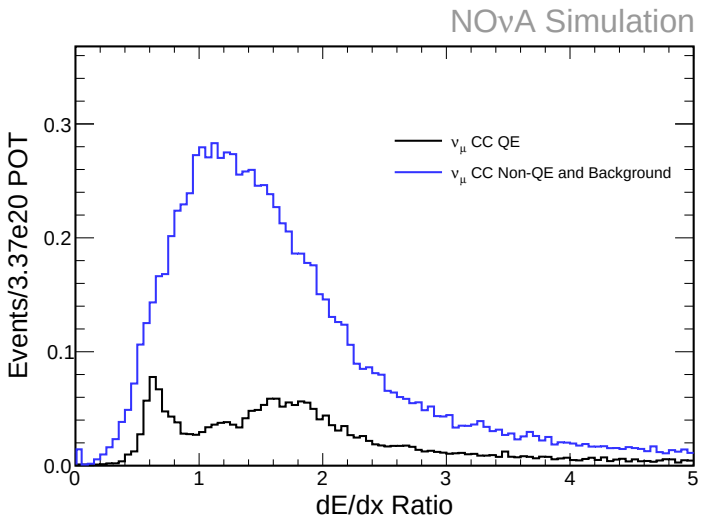

Figure 7.30: Distribution of PID input variable, $\frac{dE}{dx}$ Ratio, of signal and background events in simulated far detector neutrino interactions in the two track sample.

Chapter 8

Cosmic Rejection

Cosmic ray background in the far detector is the largest background to this analysis with the detector seeing a cosmic ray rate of 160 kHz. Additionally because most cosmic ray particles that make it to the surface of the Earth are muons, they can be easily misidentified as single track muons coming from a ν_μ charged current (CC) interaction. This chapter discusses the techniques used to reject cosmic rays from the ν_μ CC signal. In the process of separating cosmic rays from ν_μ CC interactions, two populations of ν_μ CC interactions with different constraints for cosmic rejection are identified. This first population is the fully contained ν_μ CC events in which both the interaction vertex and particles emerging from the interaction are contained in the detector. The contained sample and the cosmic rejection cuts needed to identify this sample are discussed in section 8.1. The second population is the escaping ν_μ CC events in which the vertex of the interaction is contained in the detector, but the final state muon is allowed to leave the detector. The escaping population and its associated cosmic rejection are discussed in the section 8.2.

In general the information that separates a ν_μ CC interaction from a cosmic ray entering the detector is the directionality of the energy in the slice, the position of the energy in the detector, and time of the interaction occurring within a beam spill. A ν_μ CC interaction tends to have its momentum aligned with the beam axis and, neglecting selection inefficiencies near the detector edges, the interactions tend to be uniformly distributed throughout the volume. Conversely, cosmic ray activity tends be directed downwards in the detector and the activity tends to concentrate near detector edges.

Figure 8.1 diagrams the basic differences in position and directionality of cosmic rays and ν_μ CC interactions. This analysis uses a set of cuts based on this information to reject cosmic rays and define contained and escaping populations.

The variables used in this analysis for cosmic rejection were determined from testing a large set of potentially useful variables. The variables and the cuts applied to them were tuned in two rounds. First an initial tuning based on the FOM of the ratio of the number of signal events selected to the square root of the number of signal and cosmic ray background events selected by ReMId as ν_μ CC-like. After this initial cut tuning, variables were fine tuned by varying around the initial tuned cut values to determine the optimal cut values for the variables considered. Where the optimal cuts were determined from the cuts and variables that resulted in the best measurement of the oscillation parameters. The computational requirements of the large data set used for this tuning and the combinatorics of all the variables and cut values made a one step tuning on the best measurement of the oscillation parameters infeasible. At each stage of the tuning if a variable was not found to have any power to separate signal from cosmic ray background it was removed. The resulting subset of variables used and the cuts applied to those variables are described in the following sections. For all plots comparing the expected ν_μ CC signal and the cosmic ray background, the ν_μ CC signal is taken from simulation of neutrino interactions in the far detector and the cosmic ray background is taken from real far detector data taken out of time with the beam spills. The far detector data is scaled down to the expected amount of cosmic background in the beam spill window by normalizing to the equivalent live time needed to achieve the approximate POT used in this analysis.

8.1 Contained Population

The contained sample is defined by having the neutrino interaction vertex within the detector with all the visible particles from the interaction ranging out within the detector volume. This sample has the best ability to be identified as a ν_μ CC interaction and have properly reconstructed neutrino energy because all of the information about the interaction is contained within the detector. Additionally they are the easiest to separate from cosmic ray background because most cosmic rays will deposit some energy near

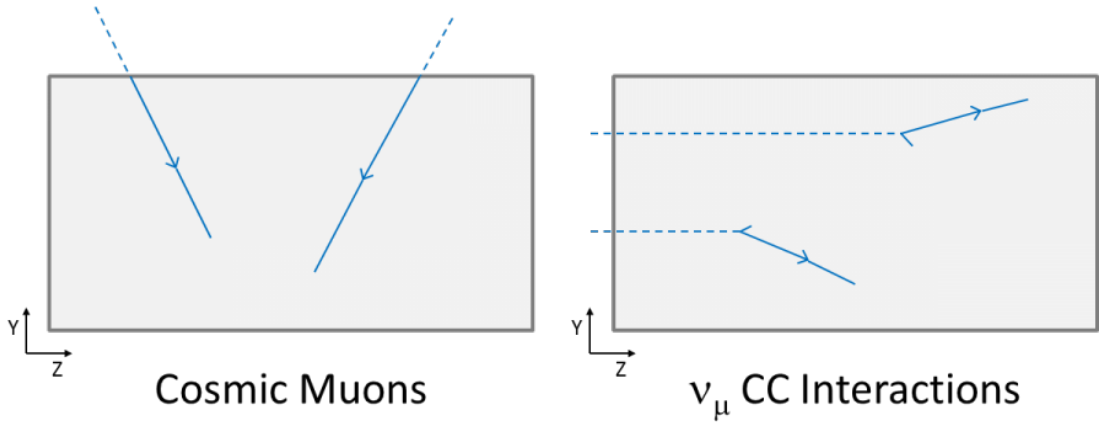

Figure 8.1: Diagram of basic topology of cosmic rays and ν_μ CC interactions. Dashed lines indicate particles that are not visible. For cosmic rays this is where the particle is outside of the detector. For ν_μ CC interactions this is representing the initial state neutrino

the edge of the detector where it enters the detector volume. There are cases where this is not true due to the presence of cosmic ray traveling through a large amount of PVC before hitting active material, detector inefficiencies, or the cosmic ray activity originating from a neutral particle. The contained sample cuts use a combination of positional, momentum, and angular cuts to separate cosmic background. Additionally a data quality cut is applied to reject electronic ringing, a pathological electronic failure mode, that can be induced by cosmic rays. A slice must pass all of the cuts in order for it to be considered as part of the contained sample.

The directionality of the track, as determined by the KalmanTrack algorithm described in chapter 5, is set by assuming that the track is beam directed. This assigns the start of the track as the side with the lowest z position, most upstream of the beam, and the end of the track as side with the highest z position, most downstream position. This assumption is true ∼100% of the time for muons from ν_μ CC interactions. However, for cosmic rays the particle direction is ∼100% downwards, unless the particle scatters in the material around the detector or originates from an neutrino that has traveled through the earth. Figure 8.2 diagrams the directionality assumptions for cosmic rays and ν_μ CC interactions. Because of these directionality assumptions two

populations are defined, positive and negative. The positive population is defined as having the most muon like track directed in the positive y direction at the start of the track and the negative population is defined as anything not in the positive population. Figure 8.3 illustrates the populations and figure 8.4 shows the distribution of the initial y direction of the most muon like track in ν_μ CC interactions and cosmic ray background. The reason for this distinction is that for the negative population the track direction assumption is correct for both the case of ν_μ CC interaction and cosmic rays where as in the positive population the assumption is correct for the ν_μ CC interactions and incorrect for cosmic rays. More explicitly, for the negative population the cosmic ray is expected to be entering the detector at the track start where as for the positive population the cosmic ray is expected to be entering from the track end. All the cuts to separate signal from cosmic ray background are defined for each the negative and positive samples independently.

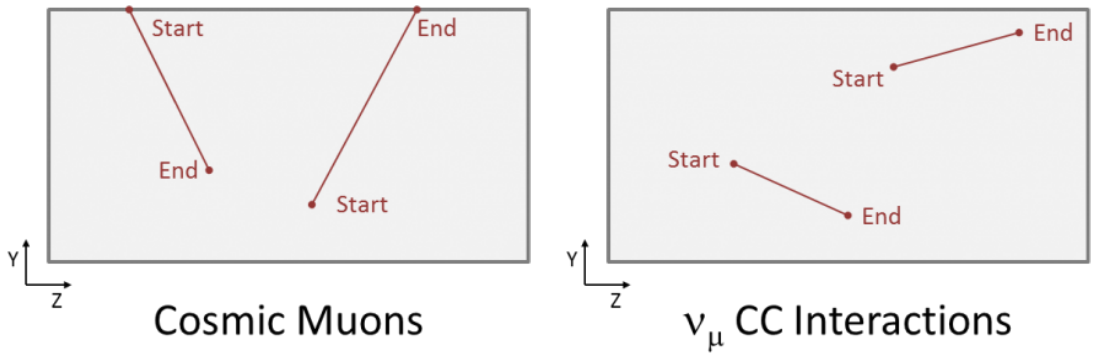

Figure 8.2: Diagram of start and stop point of muon like tracks in cosmic rays and ν_μ CC interactions from figure 8.1.

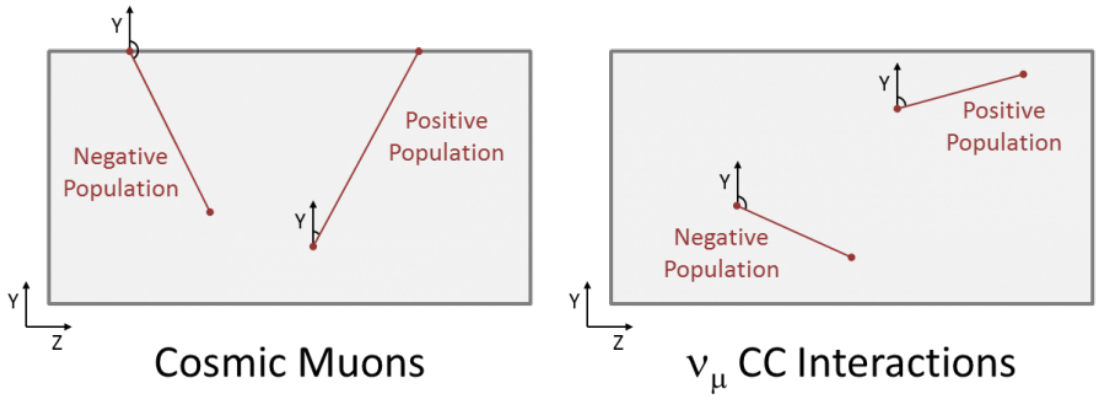

Figure 8.3: Diagram of positive and negative populations in cosmic rays and ν_μ CC interactions from figure 8.1.

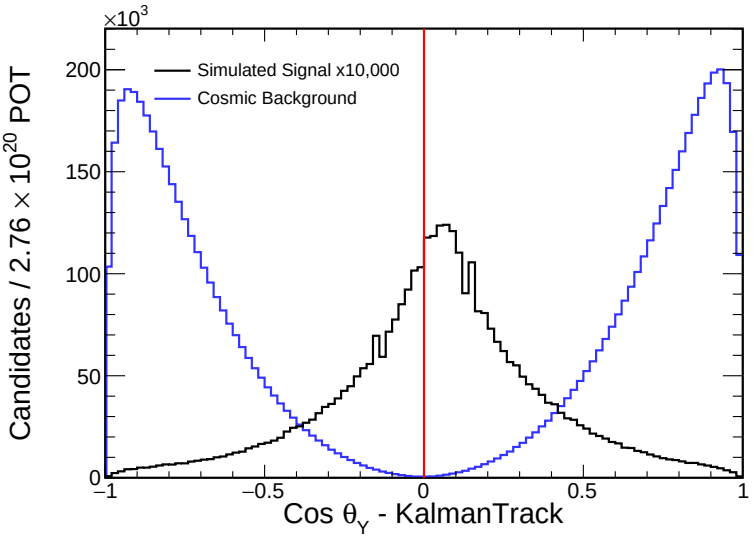

Figure 8.4: Positive and negative populations for cosmic rays and ν_μ CC interactions.

Positional Cuts

Positional cuts ensure that all the reconstructed tracks in a slice are well inside the detector volume. For the contained population both the start point of the tracks, interaction vertex, and the end points of track must be contained within the detector. They are applied to the most muon like track and all the rest of the tracks in the slice separately. More stringent cuts are applied to the identified muon track as it is generally more well known than the hadronic tracks in a ν_μ CC interaction.

The identified muon track in the negative population must pass the following positional cuts for it to be considered contained:

- | Start x position | $<$ 740 cm
- Start y position $>$ -750 cm
- Start y position $<$ 650 cm
- Start z position $>$ 40 cm from the front face of the first instrumented plane in the detector configuration
- | End x position | $<$ 740 cm
- End y position $>$ -750 cm
- End y position $<$ 725 cm
- End z position $>$ 20 cm from the back face of the last instrumented plane in the detector configuration

The identified muon track in the positive population must pass the following positional cuts to be considered contained:

- | Start x position | $<$ 740 cm
- Start y position $>$ -750 cm
- Start y position $<$ 725 cm
- Start z position $>$ 20 cm from the front face of the first instrumented plane in the detector configuration

- | End x position | < 740 cm
- End y position > -750 cm
- End y position < 650 cm
- End z position > 40 cm from the back face of the last instrumented plane in the detector configuration

The start and end y and z positional cuts are swapped in the negative and positive populations to reflect the difference in the direction assumption in cosmic rays between the two samples. Figures 8.5-8.28 show the distribution of start and end positions of cosmic ray data and simulated neutrino events with all other cosmic rejection cuts applied except the above positional cuts for the negative and positive populations. The red line in the figures represents the border defined by the cuts.

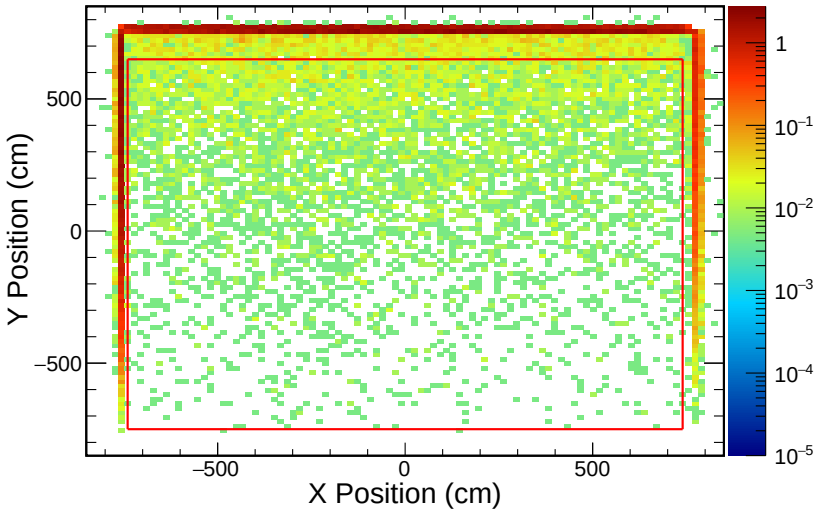

Figure 8.5: Negative population track start x and y position distribution in cosmic ray data.

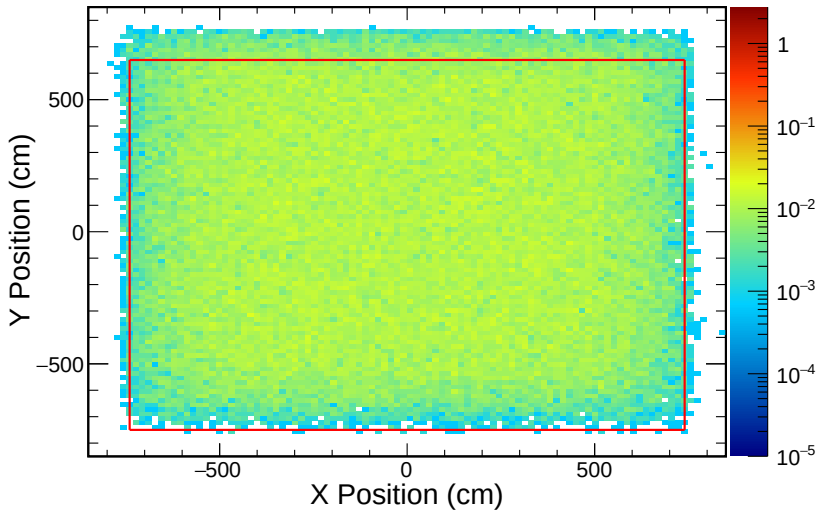

Figure 8.6: Negative population track start x and y position distribution in simulated neutrino data.

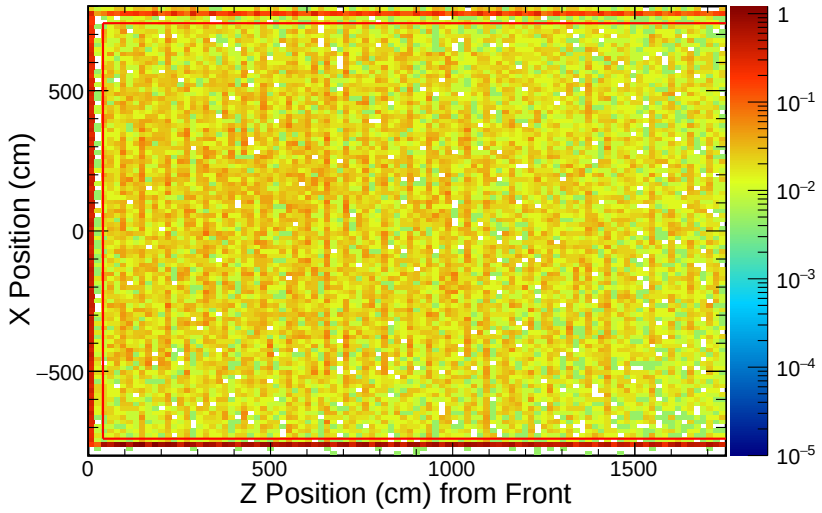

Figure 8.7: Negative population track start x and z position distribution in cosmic ray data.

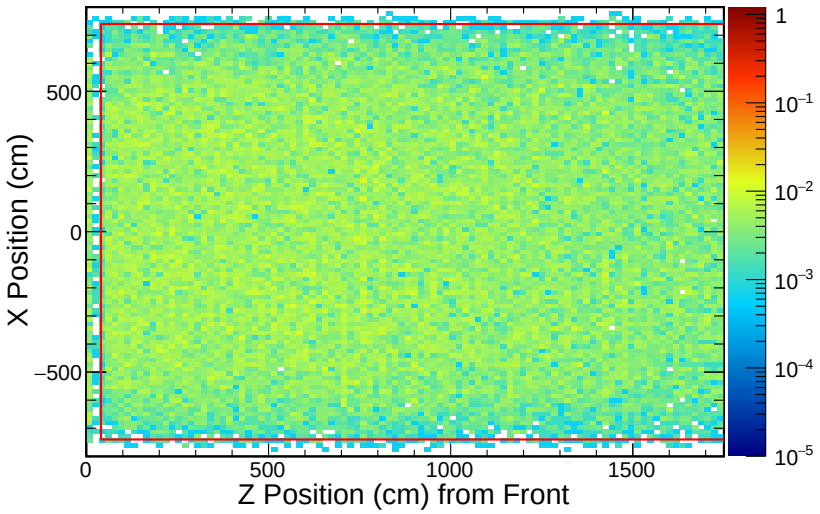

Figure 8.8: Negative population track start x and z position distribution in simulated neutrino data.

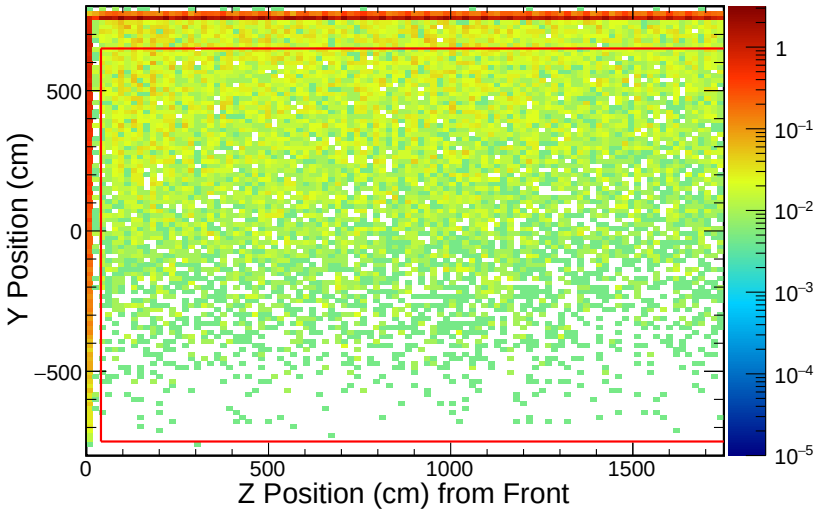

Figure 8.9: Negative population track start y and z position distribution in cosmic ray data.

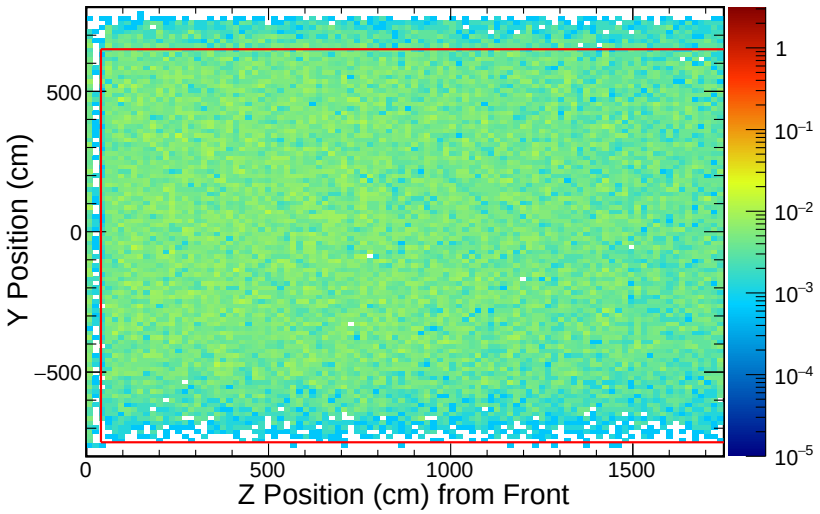

Figure 8.10: Negative population track start y and z position distribution in simulated neutrino data.

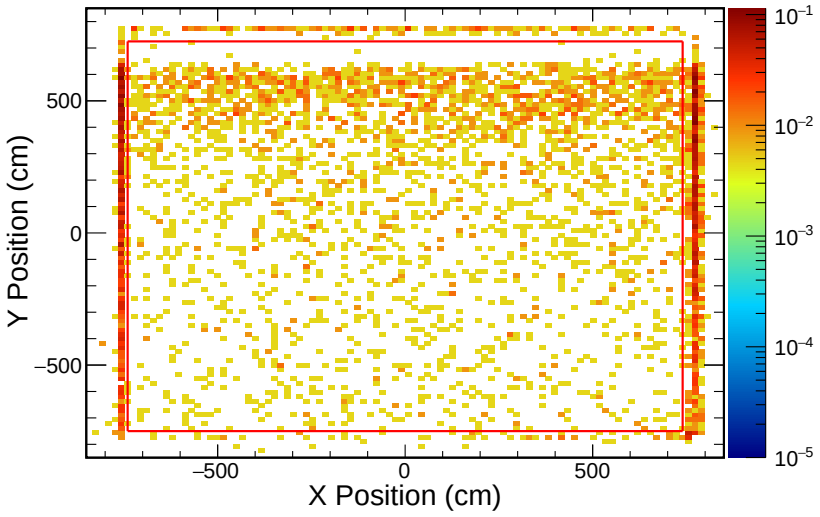

Figure 8.11: Negative population track end x and y position distribution in cosmic ray data.

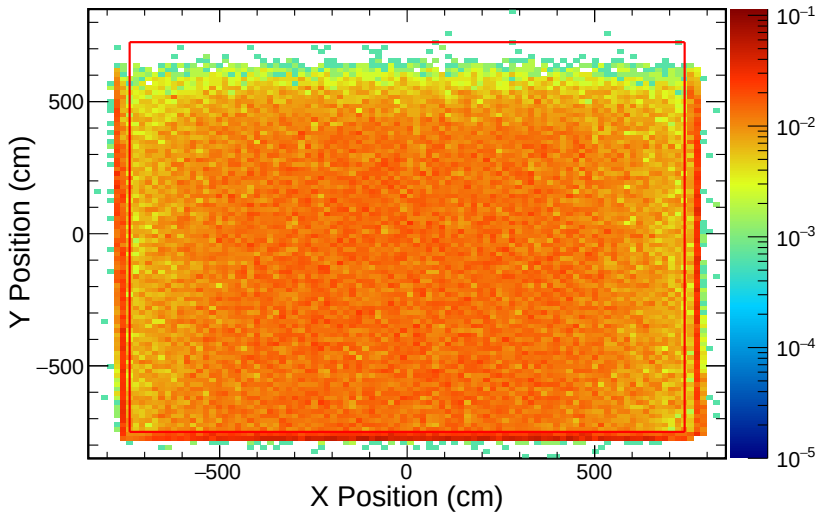

Figure 8.12: Negative population track end x and y position distribution in simulated neutrino data.

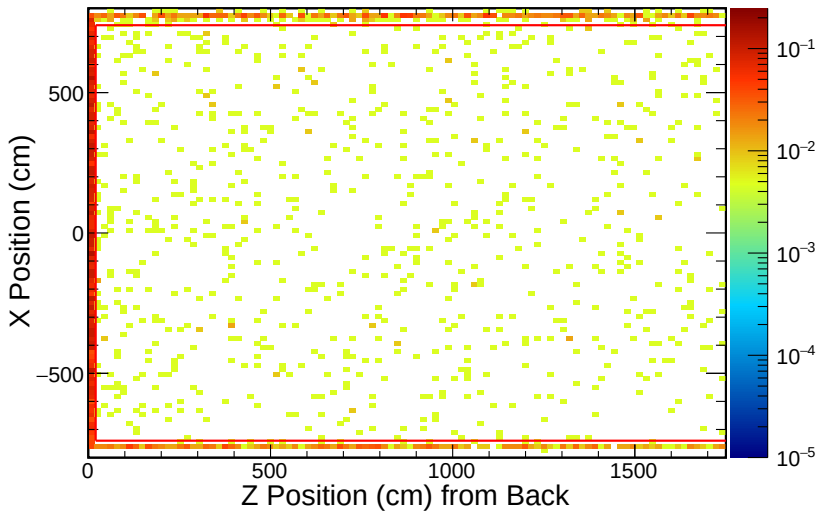

Figure 8.13: Negative population track end x and z position distribution in cosmic ray data.

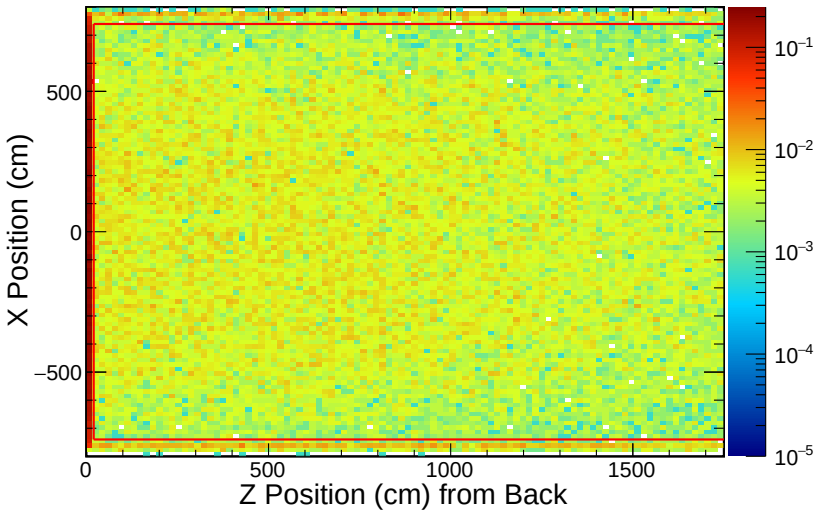

Figure 8.14: Negative population track end x and z position distribution in simulated neutrino data.

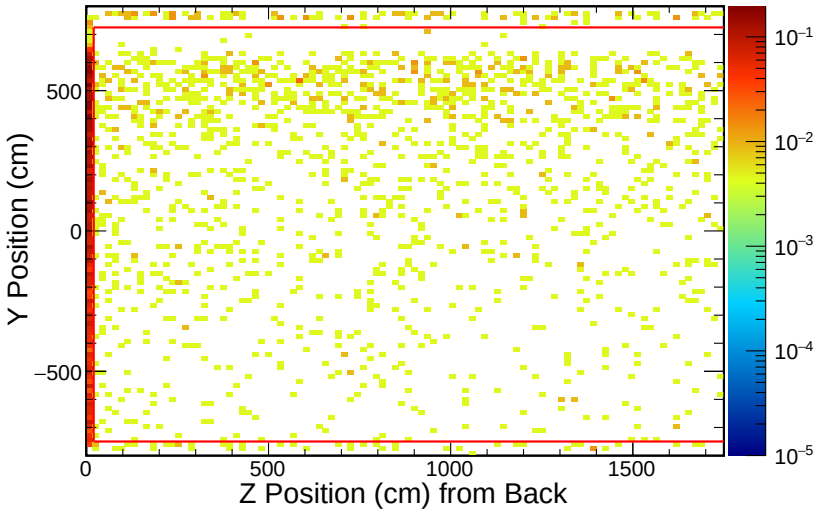

Figure 8.15: Negative population track end y and z position distribution in cosmic ray data.

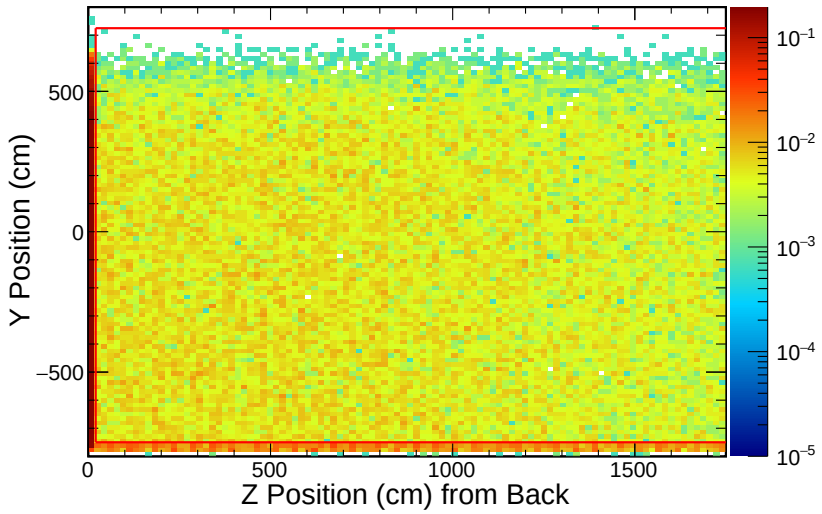

Figure 8.16: Negative population track end y and z position distribution in simulated neutrino data.

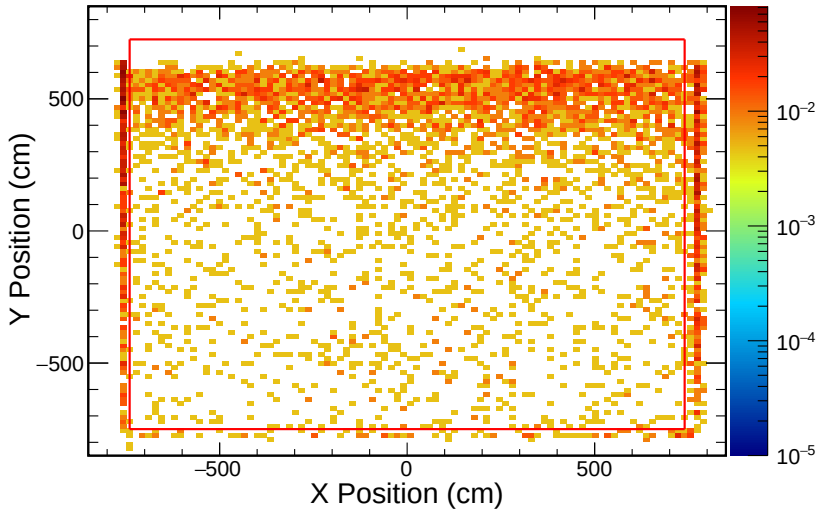

Figure 8.17: Positive population track start x and y position distribution in cosmic ray data.

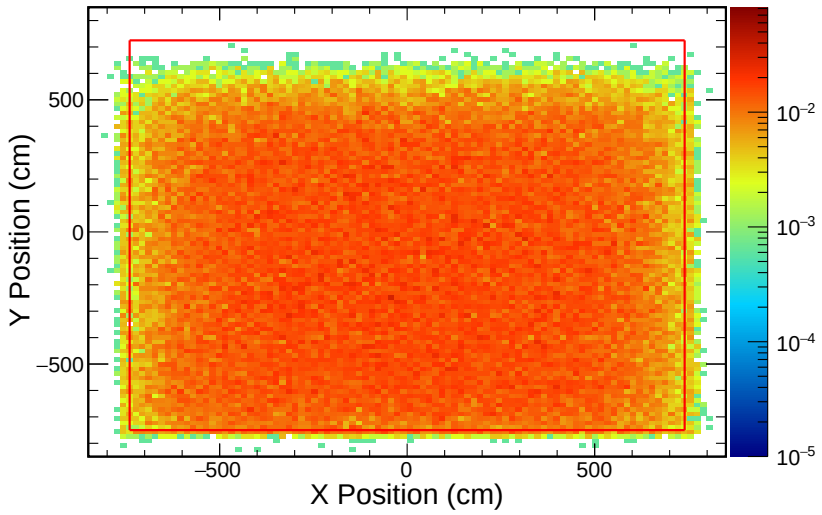

Figure 8.18: Positive population track start x and y position distribution in simulated neutrino data.

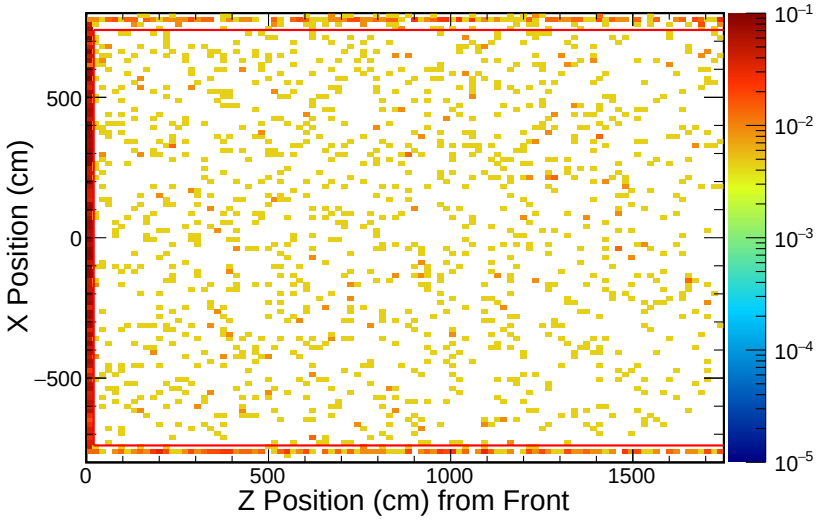

Figure 8.19: Positive population track start x and z position distribution in cosmic ray data.

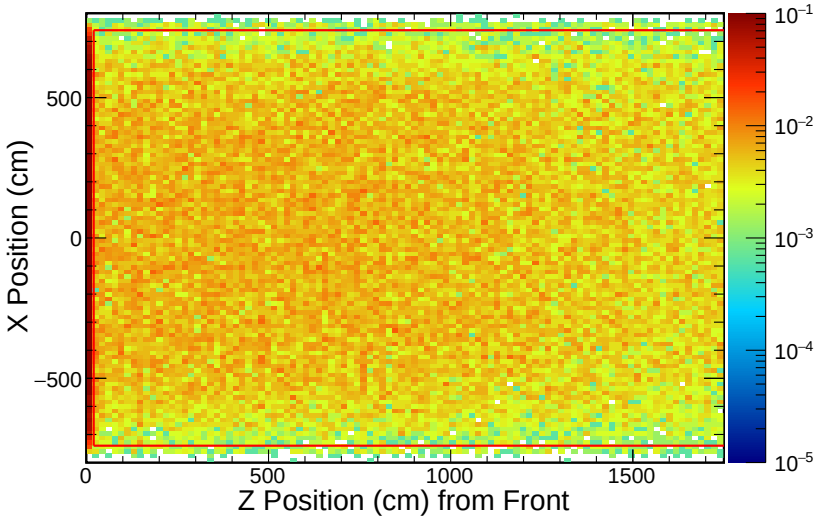

Figure 8.20: Positive population track start x and z position distribution in simulated neutrino data.

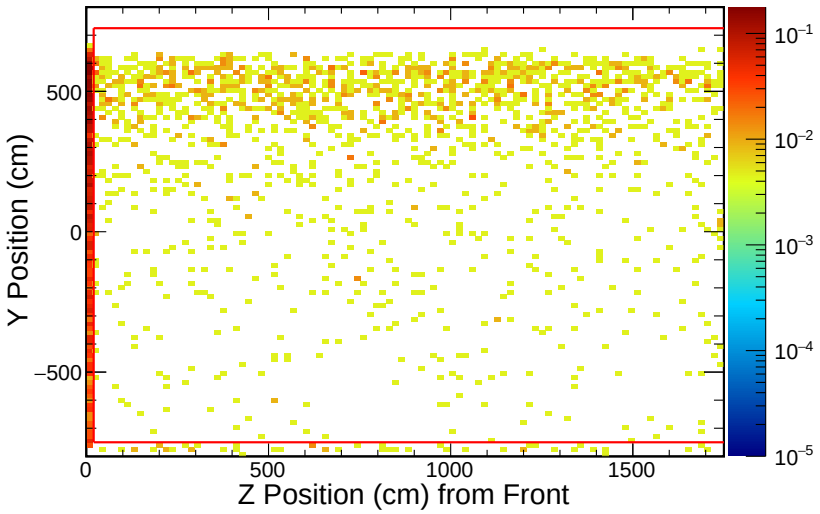

Figure 8.21: Positive population track start y and z position distribution in cosmic ray data.

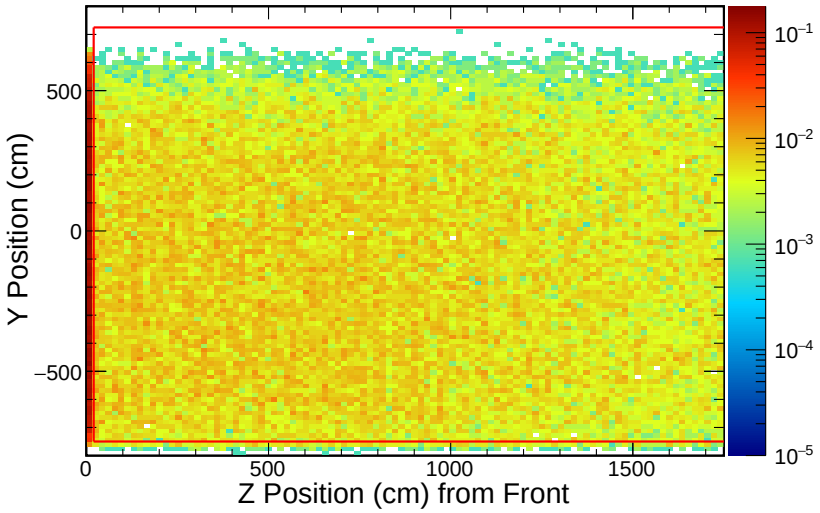

Figure 8.22: Positive population track start y and z position distribution in simulated neutrino data.

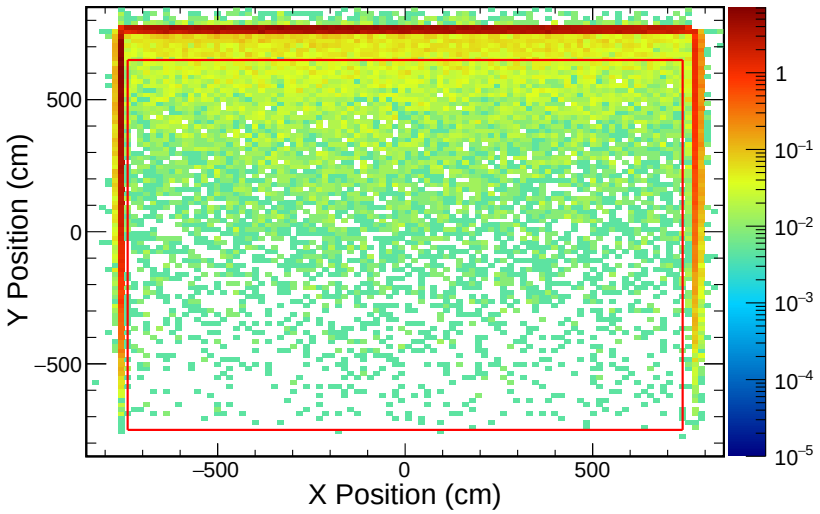

Figure 8.23: Positive population track end x and y position distribution in cosmic ray data.

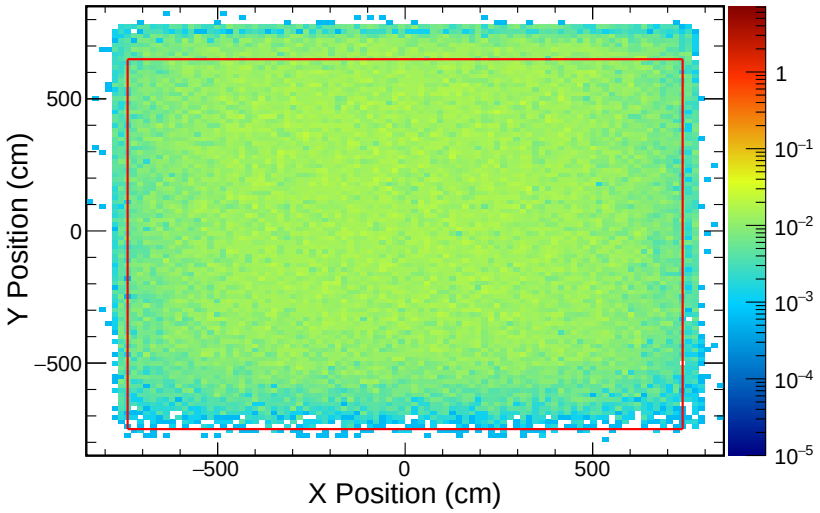

Figure 8.24: Positive population track end x and y position distribution in simulated neutrino data.

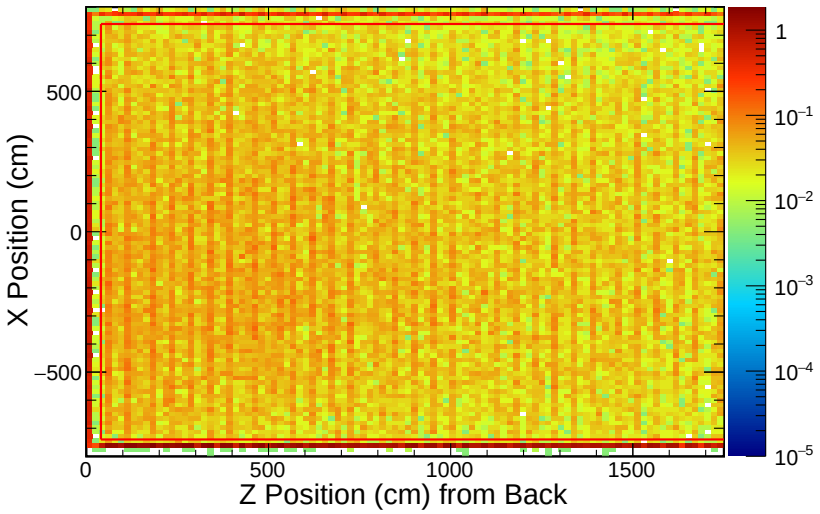

Figure 8.25: Positive population track end x and z position distribution in cosmic ray data.

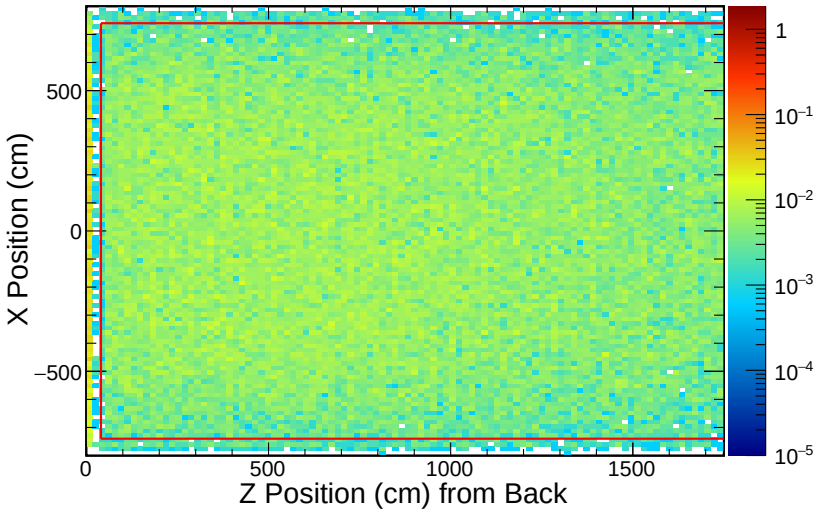

Figure 8.26: Positive population track end x and z position distribution in simulated neutrino data.

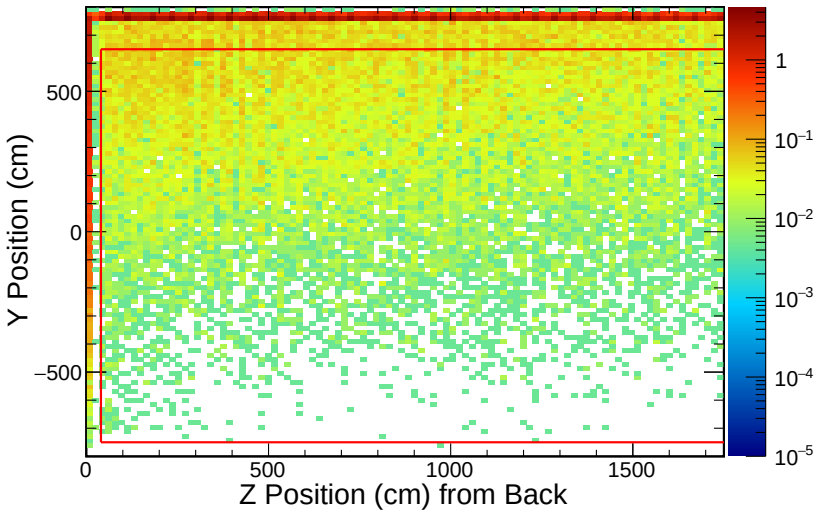

Figure 8.27: Positive population track end y and z position distribution in cosmic ray data.

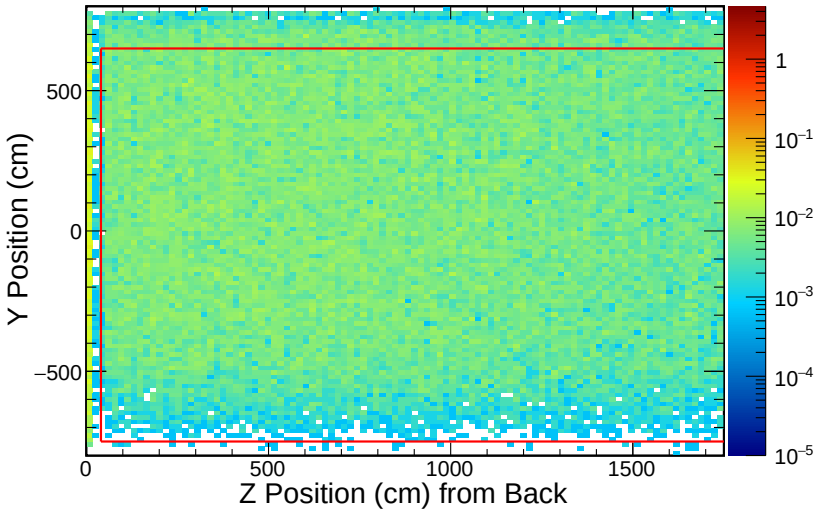

Figure 8.28: Positive population track end y and z position distribution in simulated neutrino data.

All tracks not identified as the muon track in both the negative and positive population must pass the following positional cuts for the event to be considered contained:

- | Start x position | < 740 cm
- Start y position > -750 cm
- Start y position < 725 cm
- Start z position > 20 cm from edge front face of the first instrumented plane in the detector configuration
- | End x position | < 740 cm
- End y position > -750 cm
- End y position < 725 cm
- End z position > 20 cm from edge back face of the last instrumented plane in the detector configuration

Figure 8.29 shows the distribution of all non-muon tracks that are contained and not contained in both negative and positive populations when all containment cuts are applied.

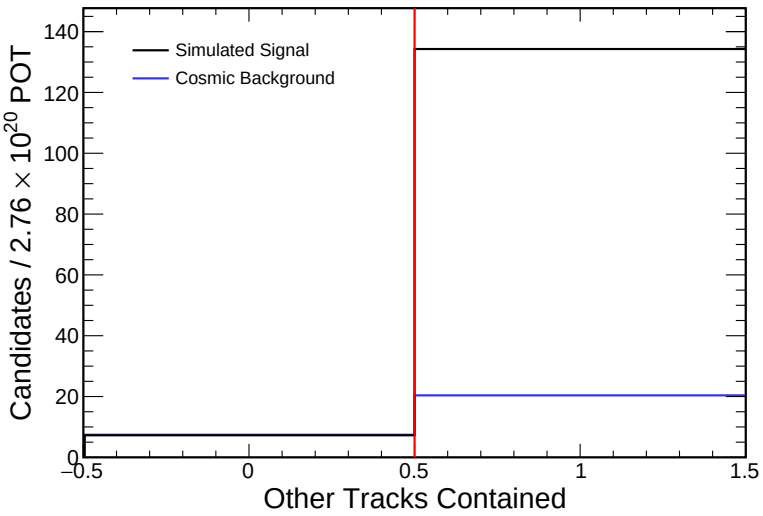

Figure 8.29: Distribution of events with all non-muon tracks passing and failing containment cuts in the negative and positive populations in cosmic ray data and simulated neutrino data.

Directional Cuts

Directional cuts are applied to select events that are generally aligned with the beam. In order to determine how inline with the beam an event is the fraction of momentum transverse to the beam line in the slice is calculated. The slice momentum is calculated using the calorimetric energy of the slice with the direction coming from the dot product between the beam line direction and the vector formed from the event vertex to the energy weighted average position of the slice. This approximation assumes that all particles are relativistic in order to determine the direction of the momentum in the absence of identification of the particles that make up the hadronic system in the interaction. For neutrino events there should be very little total momentum transverse to the beam and any nonzero values represent invisible particle in the detector, fermi motion of the target nuclei and the imperfection of assuming completely relativistic motion. Figures 8.30 and 8.31 show the distribution of transverse momentum in both the negative and positive populations, respectively, with all other cosmic rejection cuts applied. In both populations the transverse momentum has to be less than 0.65.

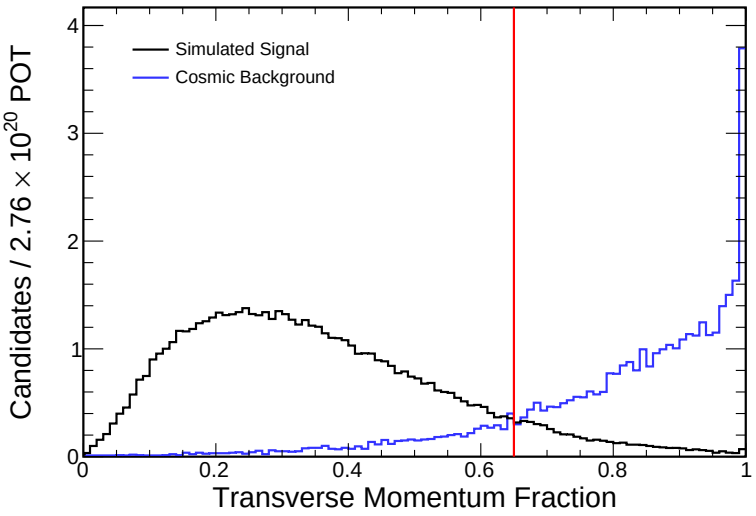

Figure 8.30: Distribution of fractional transverse momentum in the negative population of cosmic ray data and simulated neutrino data.

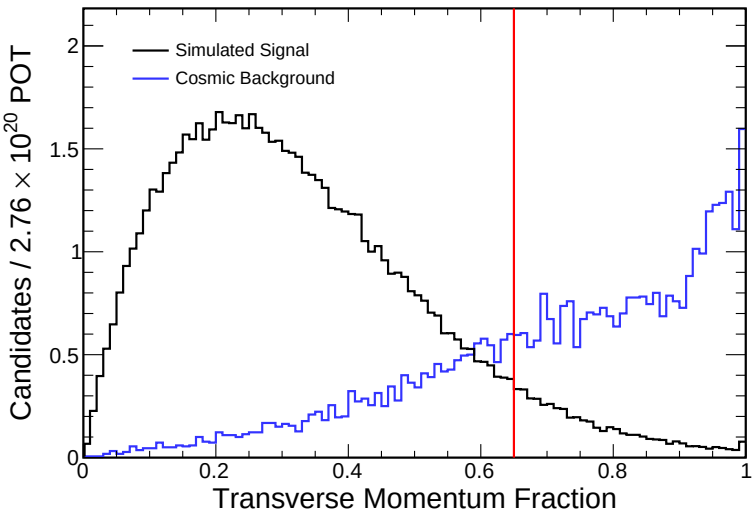

Figure 8.31: Distribution of fractional transverse momentum in the positive population of cosmic ray data and simulated neutrino data.

Combination Cuts

The final cuts defining the contained sample and separating it from cosmic background use the correlation of the angle of the muon track and its projected distance to the edge of the detector. For tracks with very steep angles it is more probable for them to travel further distances into the detector before depositing visible energy than shallow angled tracks. This is because steep angle tracks are able to travel large distances in the PVC of the detector compared to shallow angle tracks. A correlated dog-leg cut between the projected distance to the closest detector wall from the highest y positioned end of the track and the angle of the track with respect to the beam is used. The cut and distributions of cosmic data and simulated neutrino signal are shown in figures 8.32-8.35 for the negative and positive populations. Everything inside the red line to the left of the plot is rejected.

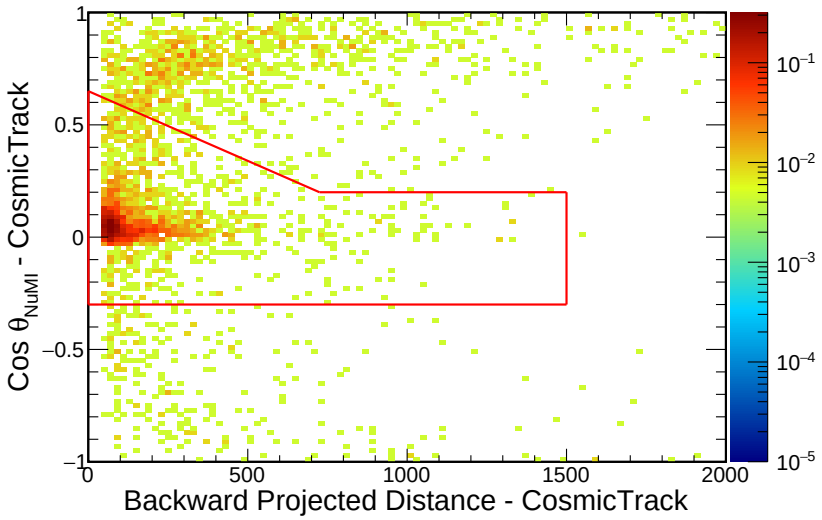

Figure 8.32: Distribution of distance to detector edge and track angle in the negative population of cosmic ray data.

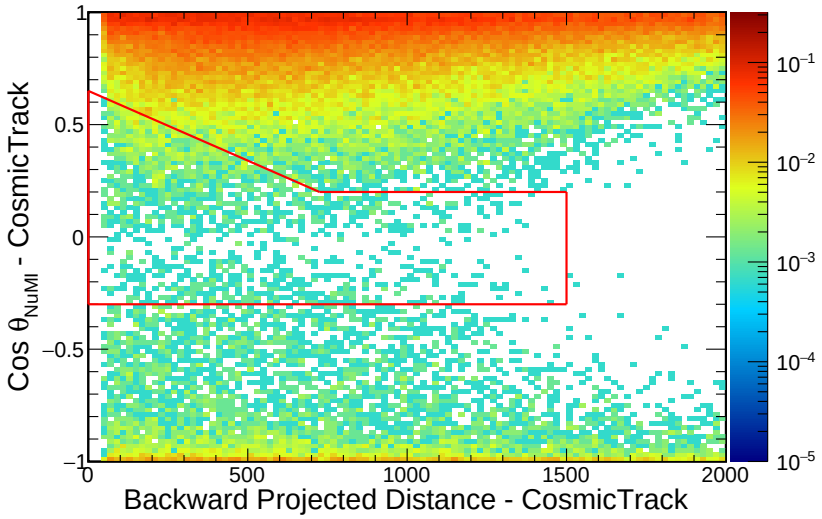

Figure 8.33: Distribution of distance to detector edge and track angle in the negative population of simulated neutrino data.

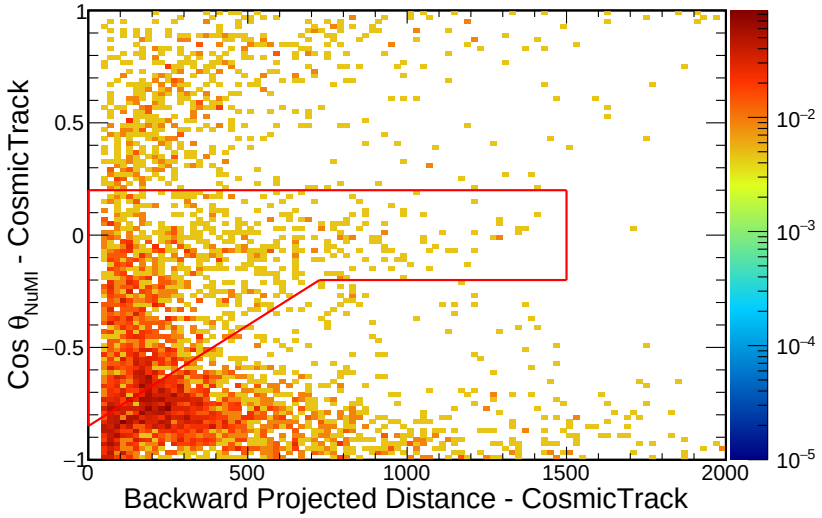

Figure 8.34: Distribution of distance to detector edge and track angle in the positive population of cosmic ray data.

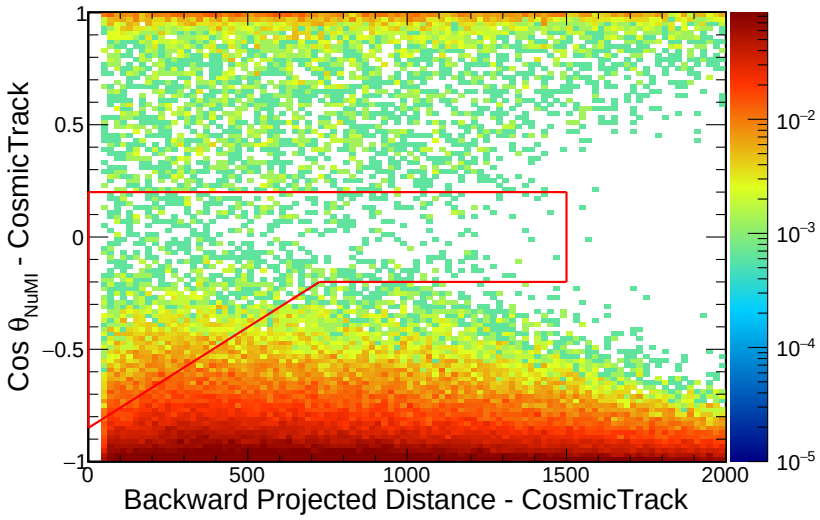

Figure 8.35: Distribution of distance to detector edge and track angle in the positive population of simulated neutrino data.

Data Quality

When high energy depositions in an APD of in the near or far detector occur, it creates a negative image charge on near by pixels of the same APD at the level of 1.86% of the total charge on the APD[69]. These image charges can induce a significant dip in the trace and when the channel recovers it can trigger a hit. These events are referred to as flashers because they can appear to make a whole APD "flash" as shown in figure 8.36. Because the channels have to recover before they trigger a hit, the hits associated with these flashers typically occur $\sim$10 μs after the instigating cosmic ray hit and they are often grouped in slices that do not include the original cosmic ray. This makes the slice appear contained and can fake a ν_μ CC topology. This topology is identified by a high number of hits in the same plane. A metric that takes the ratio of the total number of hits in the slice to the total number of planes crossed by the muon track is used to identify them[70]. A cut is set so that anything greater than 8 is determined to be a flasher and disregarded. The distribution of the metric is shown in figure 8.37.

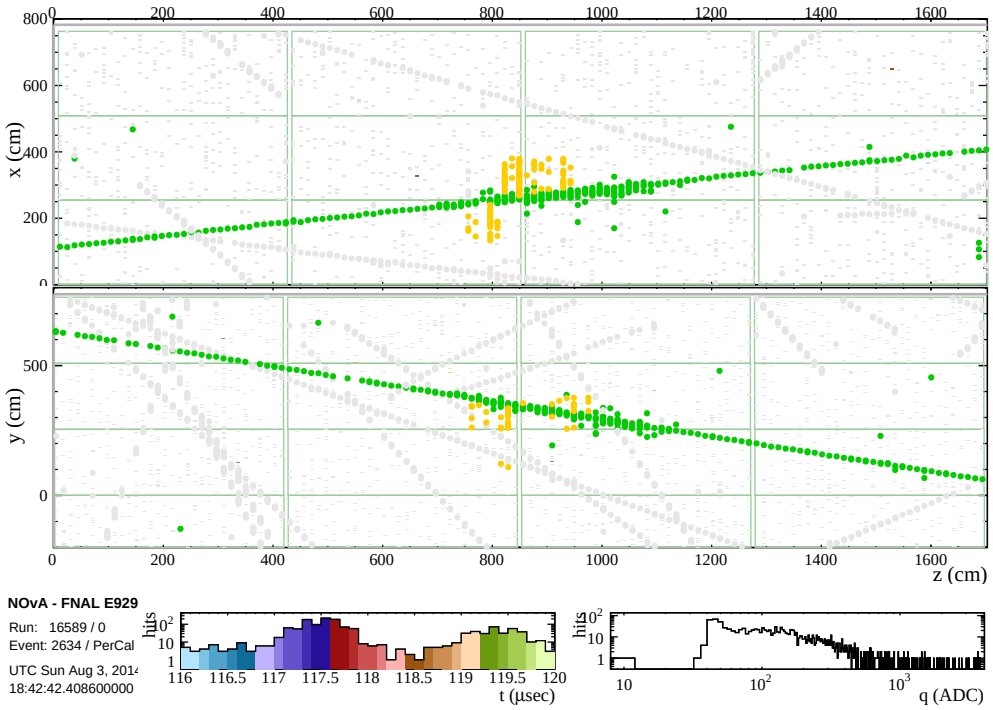

Figure 8.36: Event display of an example flasher in the far detector. The instigating cosmic ray slice is drawn in green with the contained flasher slice drawn in yellow.

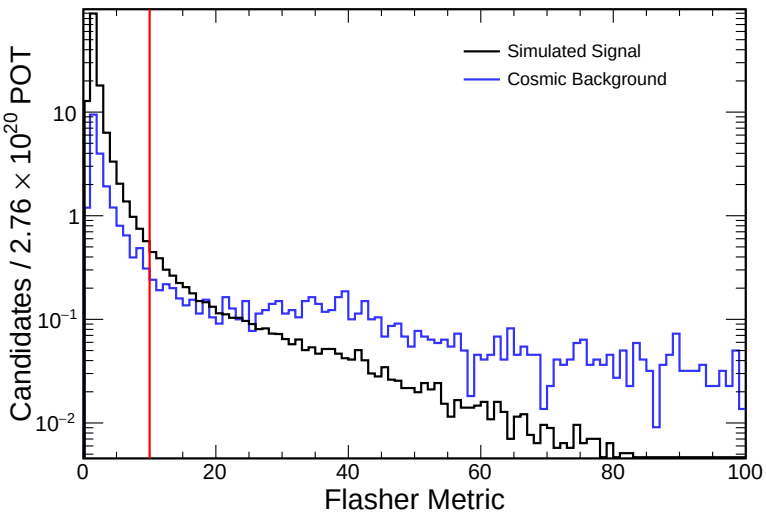

Figure 8.37: Distribution of flasher metric for the cosmic ray and simulated neutrino data.

8.2 Escaping Population

The escaping sample is defined by having the neutrino interaction vertex within the detector with at least one visible particle from the interaction not considered contained within the detector fiducial volume. Since the muon typically travels the farthest distance of all the particles it is often the particle that leaves the fiducial volume of the detector. This sample does not have as much information available as the contained sample making it harder to identify ν_μ CC interactions and also difficult to correctly reconstruct the neutrino energy. Furthermore cosmic ray rejection is challenging because a muon created from a ν_μ CC interaction and leaving the detector looks topologically similar to cosmic ray muon entering the detector and stopping within the detector volume. In order to overcome this challenge, more stringent cuts are used to reject cosmic ray background than in the contained sample. In general the escaping population cuts follows a similar classification procedure as the contained sample by making positions, momentum, and angular cuts to separate out cosmic background. Also the sample is again split into positive and negative samples for the same reasons as the contained sample. Additionally for escaping events only the positive sample will be more easily confused with the cosmic background as the side of the track that is not contained is the same side that is expected to be the entry location of a cosmic ray. Separation of the positive and negative samples allows for tighter cuts to be applied to the positive sample compared to the negative sample to compensate for this. One important difference in the escaping population cuts is the use of hadronic energy to separate ν_μ CC interactions and cosmic rays which will be discussed further below. A slice must not be considered contained and must pass all of the cuts in order for it to be considered as part of the escaping sample.

Positional Cuts

Positional cuts ensure that interaction vertex, start of the muon track, is inside the detector volume. Because of the escaping nature of the sample no positional cuts are applied to the end of the tracks. The cuts are applied to only the most muon like track. Cuts that specifically ensured containment of the non-muon tracks in the slice did not show improvement in the samples overall sensitivity to the oscillation parameters and

are not used.

The identified muon track in the negative population must pass the following positional cuts for it to be considered in the escaping sample:

- | Start x position | < 740 cm
- Start y position > -750 cm
- Start y position < 650 cm
- Start z position > 50 cm from the front face of the first instrumented plane in the detector configuration
- Projected distance from the start of the track to the nearest detector face > 50 cm

The identified muon track in the positive population must pass the following positional cuts to be considered in the escaping sample:

- | Start x position | < 740 cm
- Start y position > -750 cm
- Start y position < 725 cm
- Start z position > 70 cm from the front face of the first instrumented plane in the detector configuration
- Projected distance from the start of the track to the nearest detector face > 50 cm

Figures 8.38-8.51 show distributions of the above variables with all other cosmic rejection cuts applied for the escaping sample.

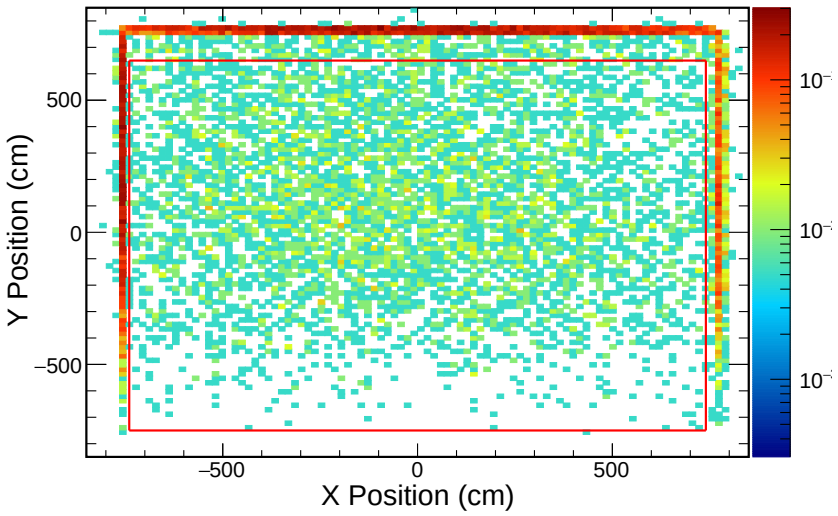

Figure 8.38: Negative population muon track start x and y position distribution in cosmic ray data.

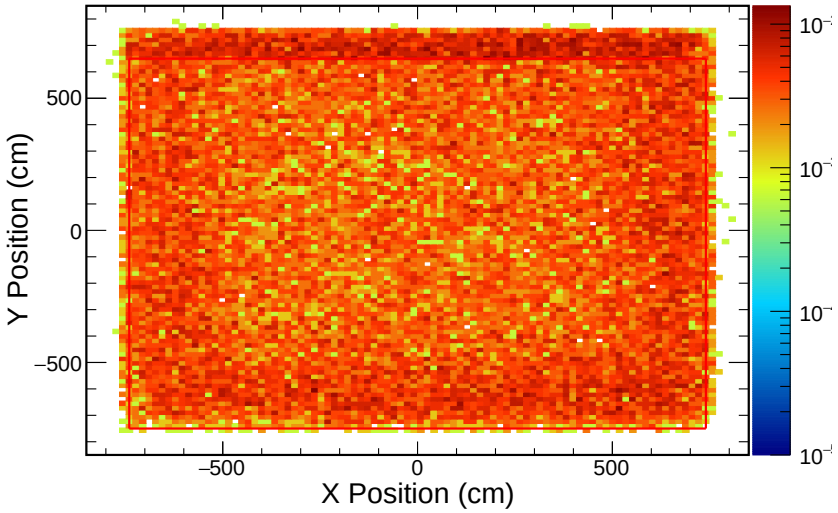

Figure 8.39: Negative population muon track start x and y position distribution in simulated neutrino data.

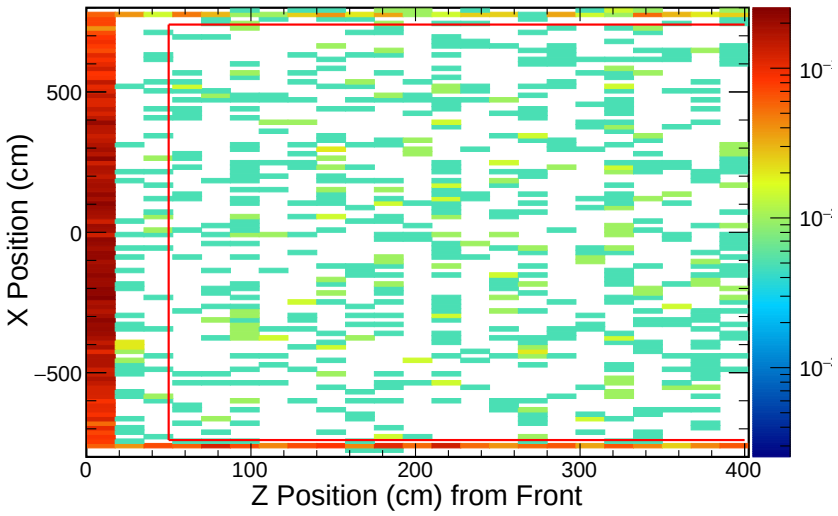

Figure 8.40: Negative population muon track start x and z position distribution in cosmic ray data.

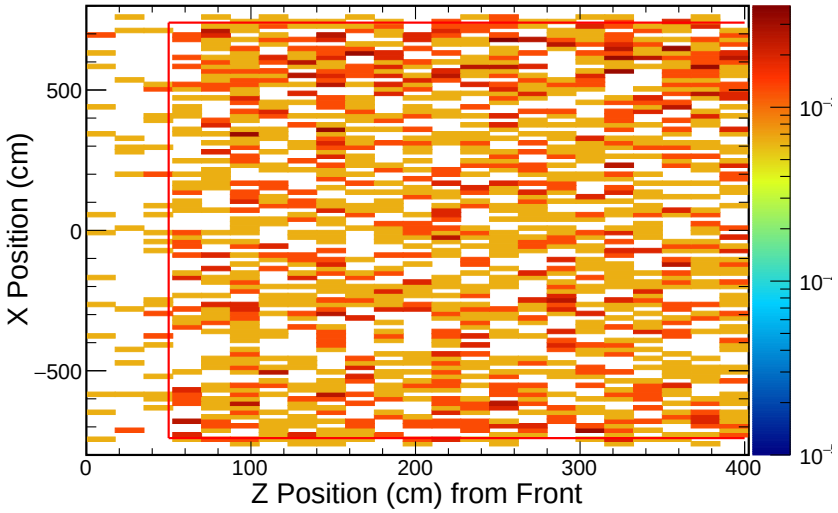

Figure 8.41: Negative population muon track start x and z position distribution in simulated neutrino data.

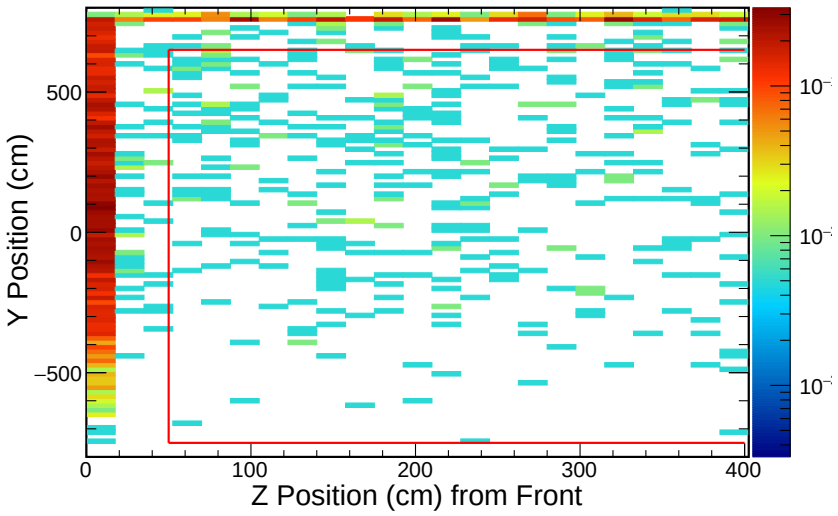

Figure 8.42: Negative population muon track start y and z position distribution in cosmic ray data.

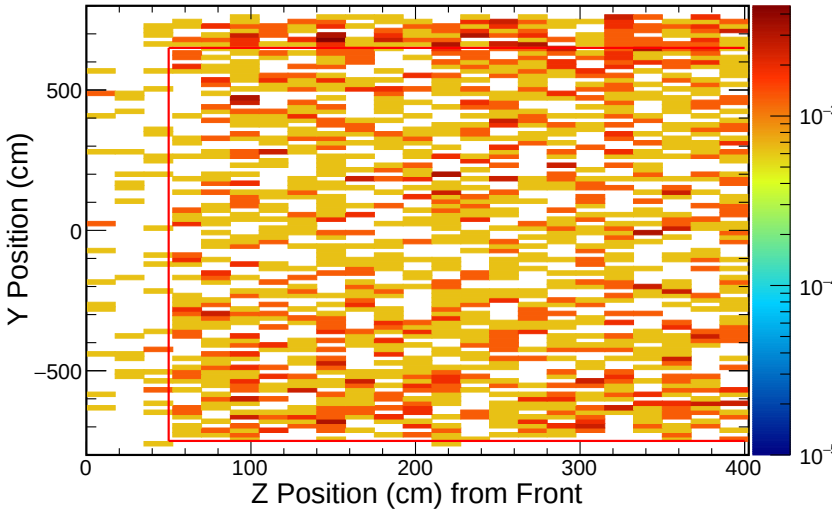

Figure 8.43: Negative population muon track start y and z position distribution in simulated neutrino data.

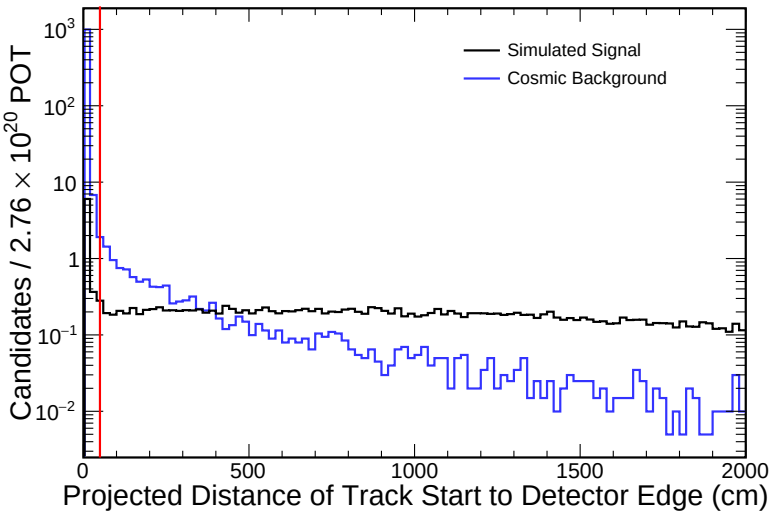

Figure 8.44: Distribution of distance from the muon track start to the detector edge in the negative population of cosmic ray and simulated neutrino data.

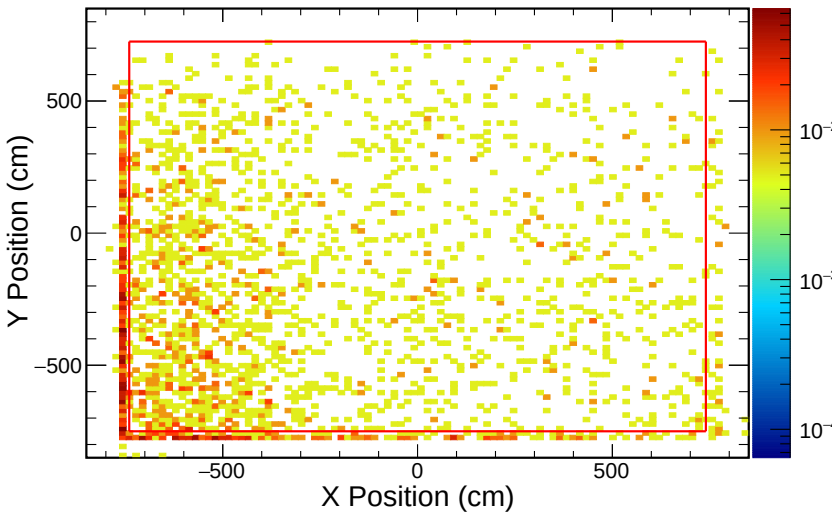

Figure 8.45: Positive population muon track start x and y position distribution in cosmic ray data.

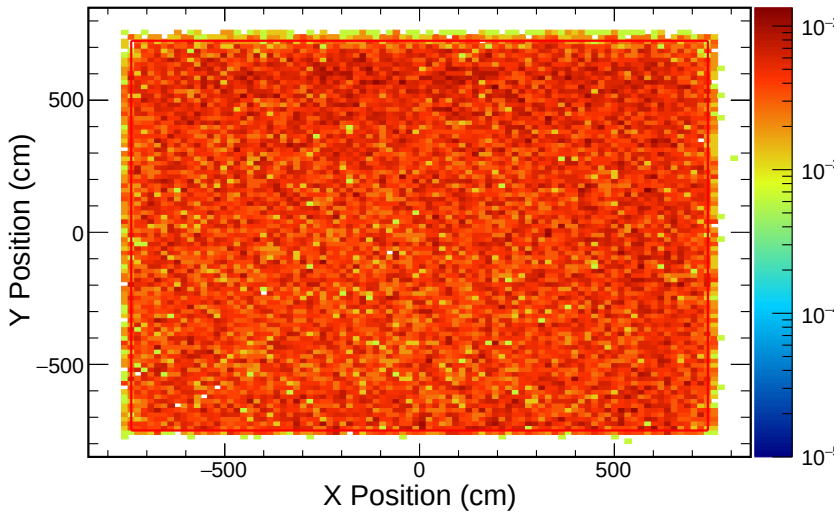

Figure 8.46: Positive population muon track start x and y position distribution in simulated neutrino data.

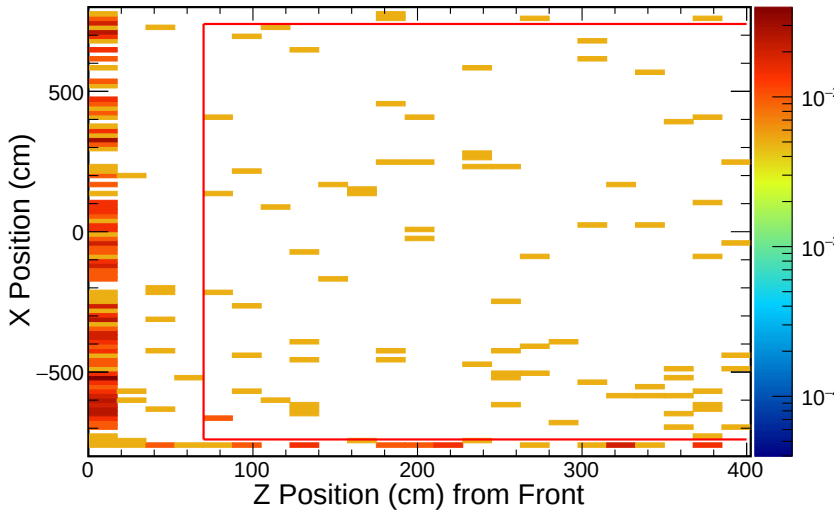

Figure 8.47: Positive population muon track start x and z position distribution in cosmic ray data.

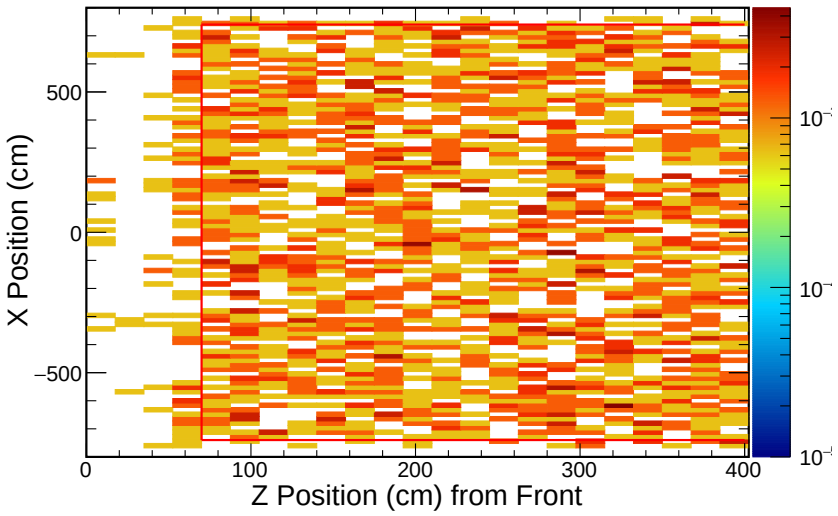

Figure 8.48: Positive population muon track start x and z position distribution in simulated neutrino data.

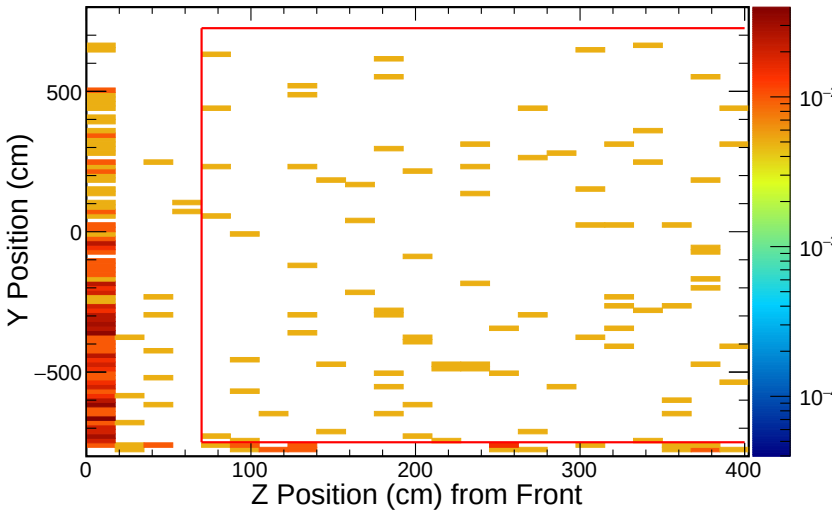

Figure 8.49: Positive population muon track start y and z position distribution in cosmic ray data.

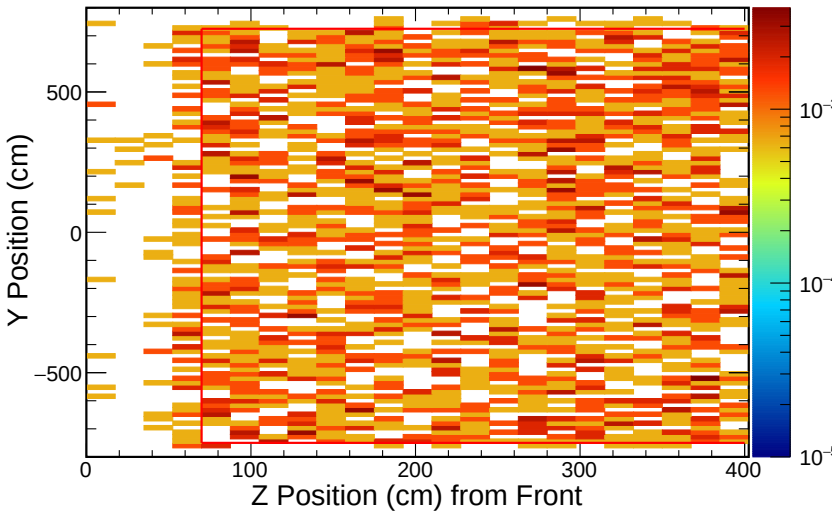

Figure 8.50: Positive population muon track start y and z position distribution in simulated neutrino data.

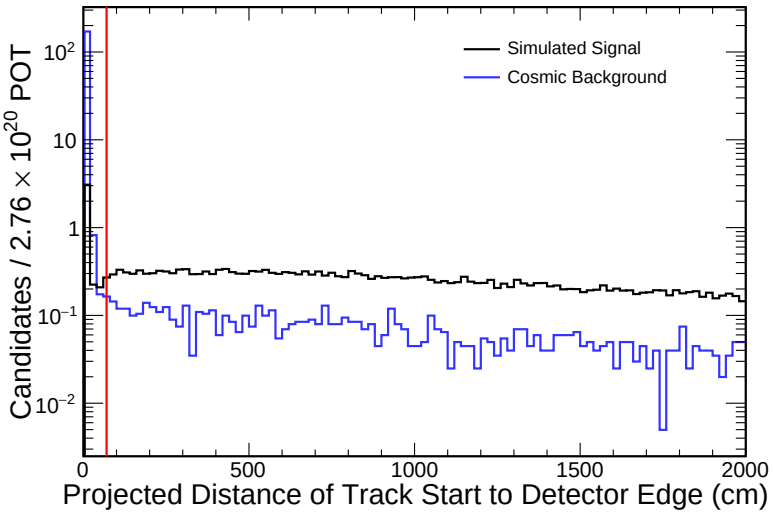

Figure 8.51: Distribution of distance from the muon track start to the detector edge in the positive population of cosmic ray and simulated neutrino data.

Directional Cuts

Directional cuts are applied to select events that are generally aligned with the beam. Similarly to the contained sample, a cut on the fractional transverse momentum is used. However, for the escaping sample the transverse momentum is a worse approximation than the contained sample because of the missing energy from the escaping particles is not accounted for. In addition to the fractional transverse momentum cuts, cuts on the direction of the muon track in the slice are employed.

Events in the negative sample must pass the following cuts in fractional transverse momentum of the slice and the direction of the muon track relative to the beam direction:

- Fractional Transverse Momentum < 0.40
- $\cos\theta_{NuMI} > 0.70$

Events in the positive sample must pass the following cuts in fractional transverse momentum of the slice and the direction of the muon track relative to the zenith:

- Fractional Transverse Momentum < 0.35
- $\cos\theta_Y$ - KalmanTrack < 0.35
- $\cos\theta_Y$ - CosmicTrack $>$ -0.3

Distributions of these variables with all other cosmic rejection cuts applied for the escaping sample are shown in figures 8.52-8.56.

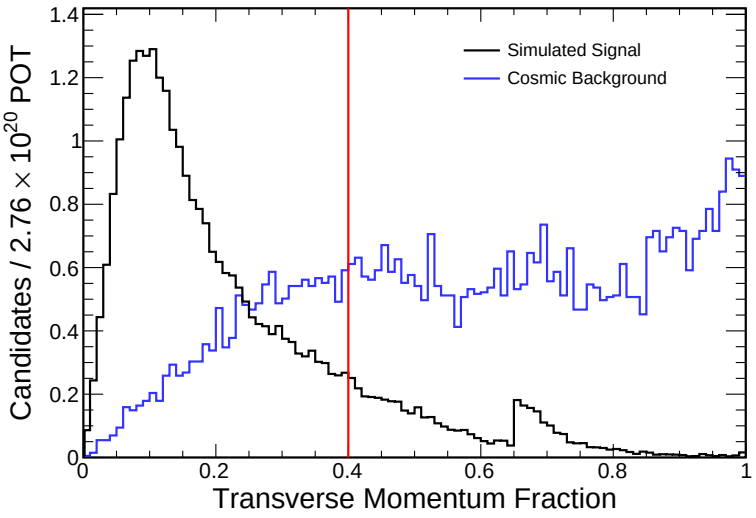

Figure 8.52: Distribution of fractional transverse momentum in the negative population of cosmic ray data and simulated neutrino data.

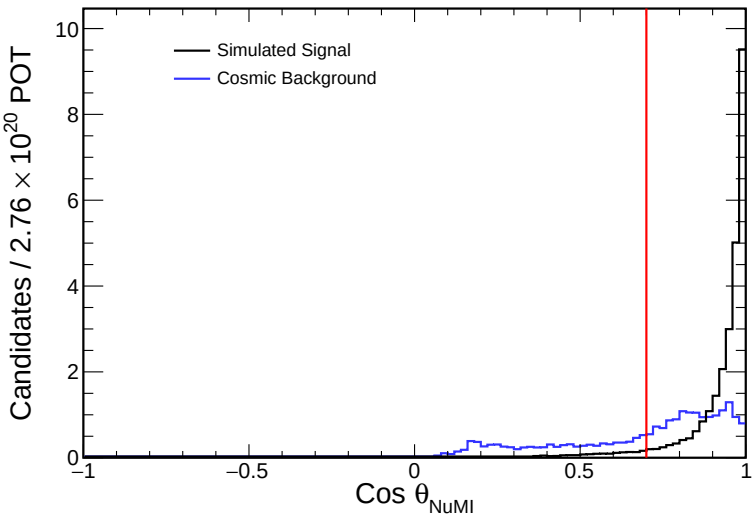

Figure 8.53: Distribution of direction of the muon track start relative to the beam direction negative population of cosmic ray and simulated neutrino data.

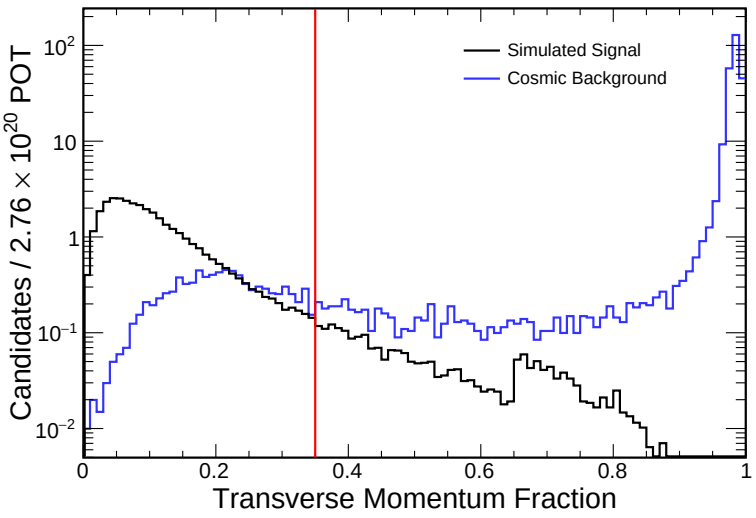

Figure 8.54: Distribution of fractional transverse momentum in the positive population of cosmic ray data and simulated neutrino data.

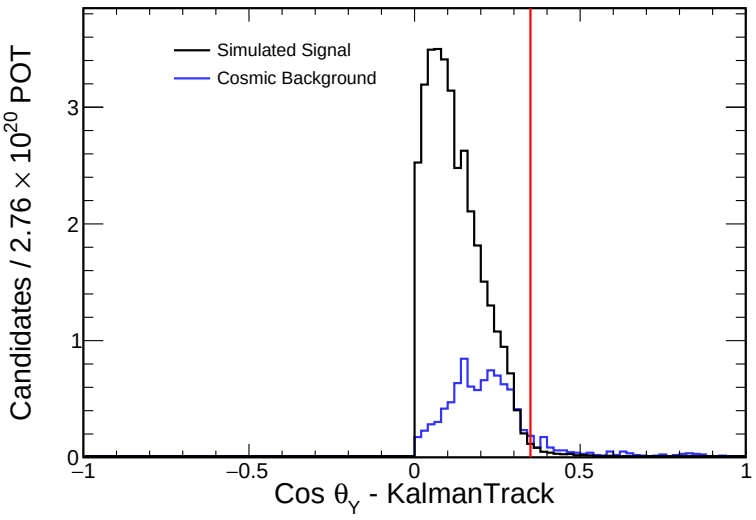

Figure 8.55: Distribution of direction of the muon track start relative to the y direction using the KalmanTrack reconstruction in the positive population of cosmic ray and simulated neutrino data.

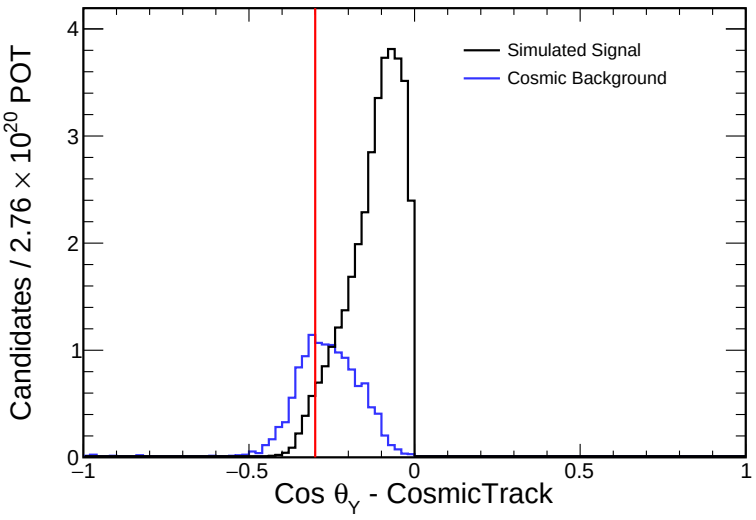

Figure 8.56: Distribution of direction of the muon track start relative to the y direction using the CosmicTrack reconstruction in the positive population of cosmic ray and simulated neutrino data.

Energy Cuts

The final cuts that define the escaping population are on the hadronic energy in the slice. This is a unique cut compared to the contained sample. It is utilized because one way to tell an entering cosmic ray muon apart from an exiting ν_μ CC interaction muon is that ν_μ CC interactions generally generate some visible hadronic energy where as the cosmic ray muon leaves $\sim$0 hadronic energy in the detector. Events in the negative sample, shown in figure 8.57, must have at least 0.20 GeV hadronic energy in the slice. Events in the positive population must have at least 0.30 GeV hadronic energy in the slice with at least 0.075 GeV of the energy overlapping with the muon track. In the positive population the requirement on overlapping energy with the track ensures that the energy determined to be hadronic energy by the energy estimation algorithms is near the vertex of the interaction. The positive population distributions of hadronic energy and overlapping hadronic energy with all other cosmic rejection cuts applied are shown in figures 8.58 and 8.59

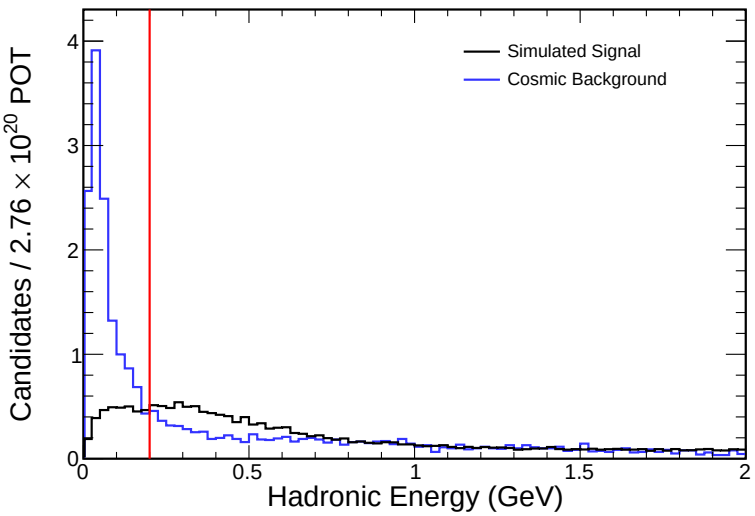

Figure 8.57: Distribution of hadronic energy in the negative population of cosmic ray and simulated neutrino data.

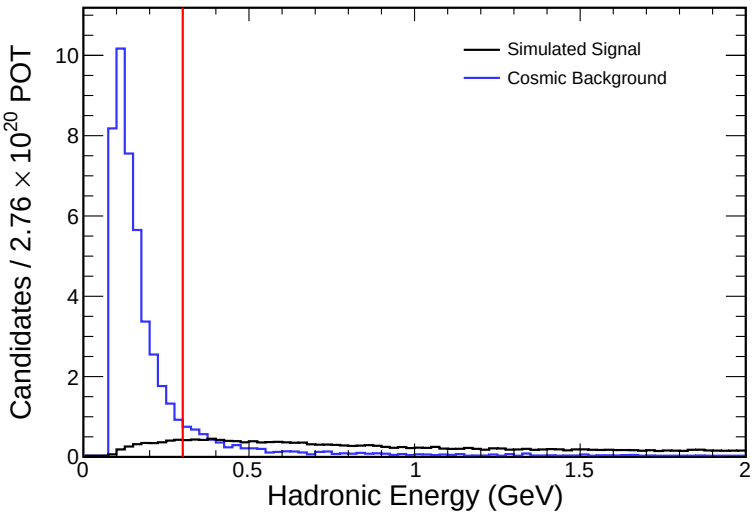

Figure 8.58: Distribution of hadronic energy in the positive population of cosmic ray and simulated neutrino data.

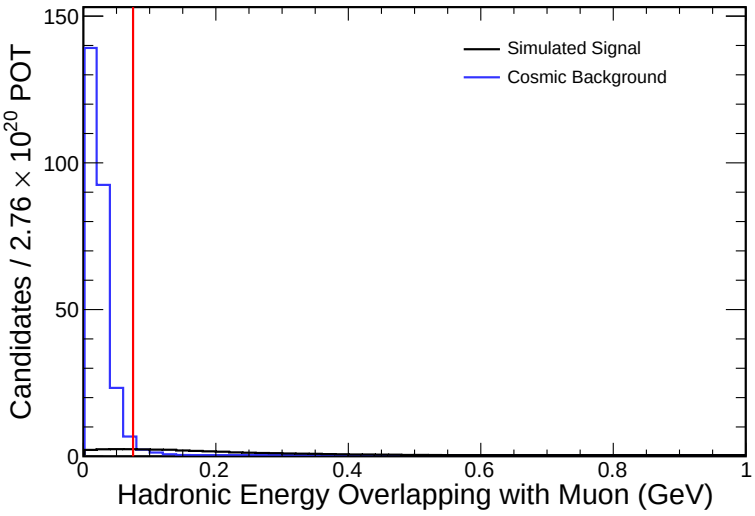

Figure 8.59: Distribution of hadronic energy overlapping with the muon track in the positive population of cosmic ray and simulated neutrino data.

Data Quality

Similarly to the contained population case flashers can create a background to the ν_μ CC sample in the escaping case as well. In the case of the escaping sample the background comes about if the flasher is in the same slice with a stopping cosmic ray muon. A cut at 8 in the flasher metric is again used to remove this background. The distribution for the escaping sample is shown in figure 8.60.

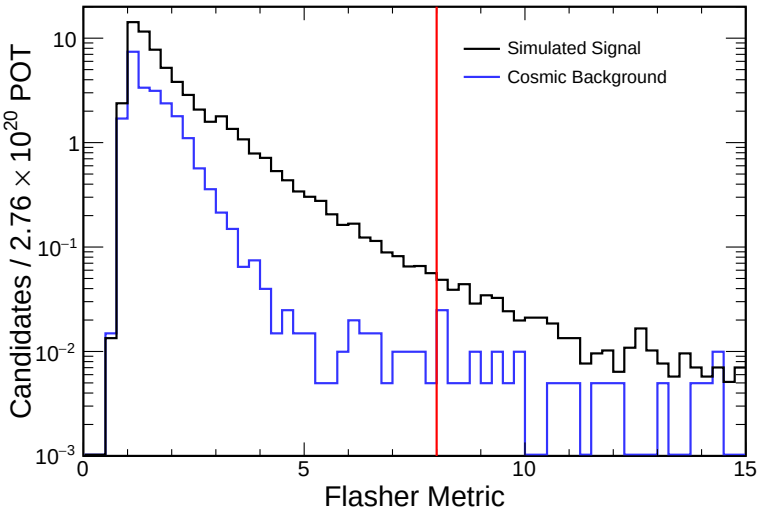

Figure 8.60: Distribution of flasher metric for the cosmic ray and simulated neutrino data.

Chapter 9

Event Selection

Events in each detector are selected to maximize the sensitivity of measuring the oscillation parameters governing ν_μ disappearance. Event selection generally falls into three sets of categories: requiring the detector is recording quality NuMI spill data, background rejection, and classification into sub-samples. The first category, data quality, ensures that the data used is of sufficiently good quality for oscillation physics analysis. The second category is optimized to eliminate non-ν_μ CC like events while keeping ν_μ CC events. The third category classifies the events passing data quality and background rejection into samples with different topological characteristics. The selections used for background rejection and signal selection as well as sub-sample classification were determined to optimize the measurement of the oscillation parameters as described in previous chapters. This analysis blinded the in-beam spill far detector data to remove any bias in algorithm design and event selection and all optimization of event selection in the far detector was based on simulated data. The near detector data was not blinded so the analysis methods and event selection could be checked against the simulation without biasing the results of measuring oscillation parameters. These near detector event selection cross checks are presented in section 9.2.1.

9.1 Data Quality

Data quality cuts are applied to ensure both that the beam is operating in a mode to produce a flux of neutrinos in the near and far detector consistent with the design and

the detectors are operating in a mode in which they sufficiently collect neutrino data. The beam quality is ensured through the following cuts applied to each beam spill[71]:

- Spill time recorded by NOνA matched that of Fermilab Accelerator Division records within 0.5 s
- At least 2×10^{12} POT in the spill
- -202 kA < Horn Current < -198 kA
- 0.02 mm < Beam Position at the Target (horizontal and vertical dimensions) < 2.0 mm
- 0.57 mm < Beam Width at the Target (horizontal and vertical dimensions) < 1.58 mm

The detector data quality is ensured through the following cuts applied to each subrun in the near detector[72]:

- Timestamp of first event < timestamp of last event
- Timestamp of first and last events later than January 1st, 2013
- Number of NuMI triggers > 1000
- Fraction of empty spills < 3%
- 217 μs $\leq$ Start of Beam Peak $\leq$ 219 μs
- 227 μs $\leq$ Start of Beam Peak $\leq$ 229 μs
- 12 Hz < Median rate of hits with ADC values consistent with the minimum ionizing particles < 20 Hz
- Number of good diblocks = 4
- Fraction of reconstructed two dimensional tracks < 15%
- 3.5< Number of slices per trigger window < 5.5

In particular the cuts on the rate of ADC hits and the number of slices per trigger window remove subruns in which the detector is overly noisy or quiet. This checks that the FEB gains and thresholds are correctly set during the subrun. The following cuts are applied to each spill in the near detector[73]:

- No DCMs are missing from the readout
- Fraction of hits in DCMs in the top most position on the detector side $< 45\%$

The second spill level cut removes events in which there was excess electronic noise from the detector hall lights being on. The following cuts are applied to each subrun in the far detector[72]:

- Number of non-empty triggers > 0
- Timestamp of first event $<$ timestamp of last event
- Timestamp of first and last events later than January 1st, 2013
- Subrun live time > 1.0 s
- 13 Hz $<$ Median rate of hits with ADC values consistent with the minimum ionizing particles $<$ 23 Hz
- Number of consecutive good diblocks > 1
- Fraction of reconstructed two dimensional tracks $< 15\%$
- $1.2 <$ Number of slices per trigger window per 10^4 pixels < 3.2
- Master TDU is in sync with GPS

and to each of the spills in the far detector[74]

- At least 4 consecutive diblocks
- No DCMs are missing from the readout
- No DCMs report in an error state
- DCM edge metric > 0.2

In particular the last cut ensures that DCMs are time synchronized with each other.

9.2 Near Detector Selection

Events in the near detector are selected to pass the data quality cuts described in section 9.1 as well as the ReMId cut to select ν_μ CC events described in chapter 6. Additionally events must pass the following containment cut:

- All hits in the slice must be > 2 cells away from a detector edge
- All hits in a slice must be > 3 planes from the front of the detector and < 3 planes from the back of the detector
- The z position of the start of the muon track < 1150 cm
- The z position of the end of the muon track < 1275 cm
- Y position at the beginning of the muon catcher < 55 cm for muon tracks that enter the muon catcher
- Projected number of cells between start of muon track and detector edge > 8
- Projected number of cells between end of muon track and detector edge > 5
- Hadronic energy in the muon catcher < 30 MeV

The selected events are classified as QE or NonQE events based on the QePId cut described in chapter 7 resulting in two event samples in the near detector referred to as QE and NonQE. The energy of each sample is determined by the QE energy estimator and NonQE energy estimator described in chapter 7, respectively. Only events with less than 10 GeV of energy in the near detector are used in this analysis.

9.2.1 Data-Simulation Comparisons

This analysis relies heavily on the use of simulation. The simulation was tuned to the data as described in chapter 4 but that tuning does not guarantee that the simulation accurately models the data through all facets of the reconstruction and event selection used in this analysis. In order to check the validity of the simulation and the behavior of the algorithms and selections used in this analysis the near detector in beam spill data was compared to the simulated neutrino events. The near detector simulation

models multiple beam neutrino interaction per spill and assumes a beam power of 250 kW. The interactions include both those that originate inside the detector as well as those that originate outside the detector in the surrounding rock. There is no cosmic ray background in the near detector simulation because rate is so low compared to the neutrino interaction rate.

Figures 9.1-9.22 show the agreement of the data and simulation for events that pass the near detector containment and data quality cuts. Figures 9.1-9.10 show the agreement of slices that pass containment cuts. These figures agree in both overall shape and normalization with some small disagreements in the extents of the slice near the detector edges and overall normalization agreeing to 2%. These small shape discrepancies can result from a difference in the noise in the simulation compared to the data. Figures 9.11-9.22 show agreement of the most muon like track in contained slices. These again show good agreement between data and simulation with the same normalization difference as seen in the overall slice distributions. The largest shape difference is seen in figure 9.11 which shows the data with longer tracks than the simulation on average.

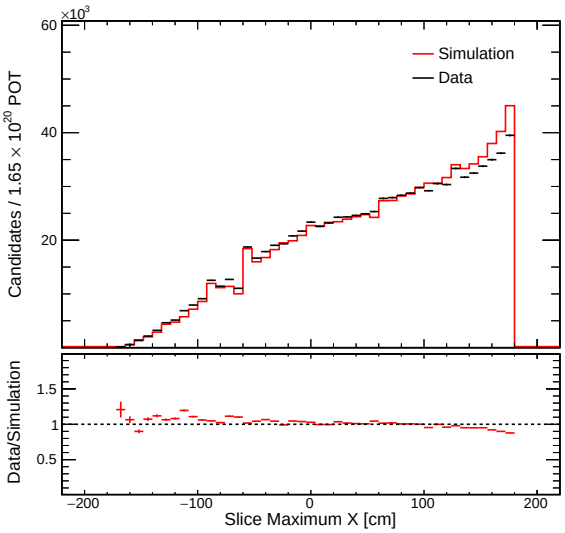

Figure 9.1: Maximum position in the x direction of any hits in a contained slice.

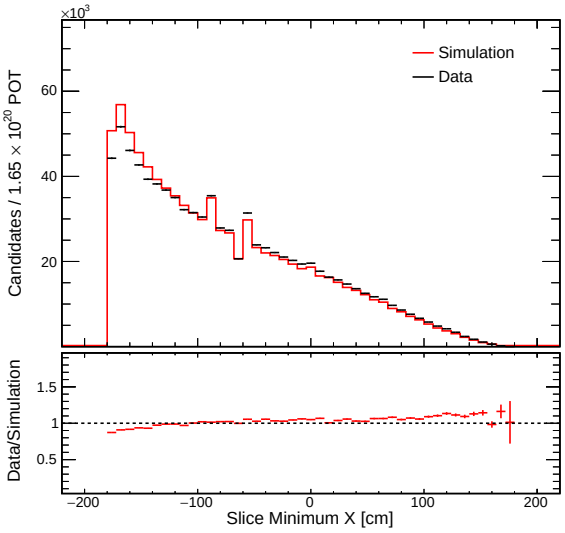

Figure 9.2: Minimum position in the x direction of any hits in a contained slice.

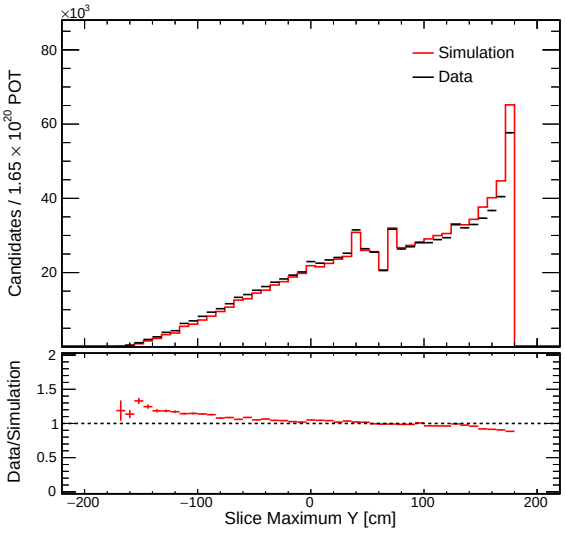

Figure 9.3: Maximum position in the y direction of any hits in a contained slice.

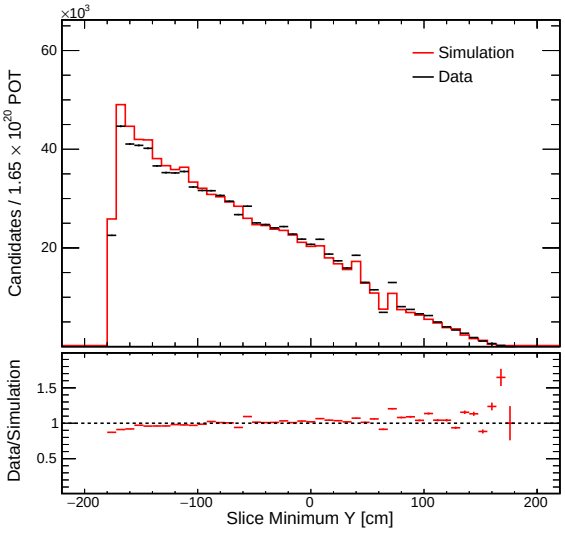

Figure 9.4: Minimum position in the y direction of any hits in a contained slice.

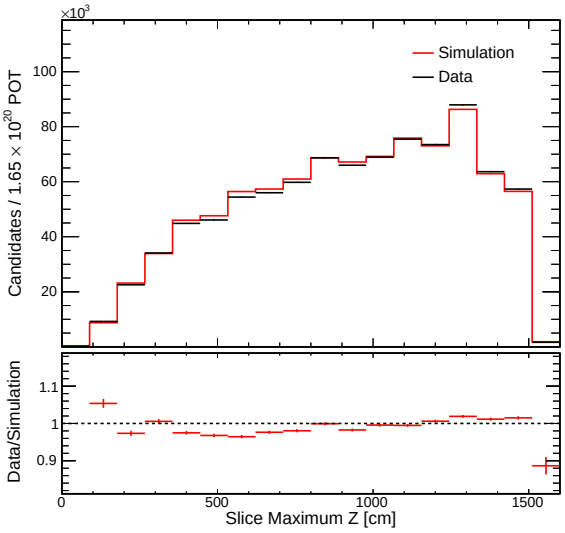

Figure 9.5: Maximum position in the z direction of any hits in a contained slice.

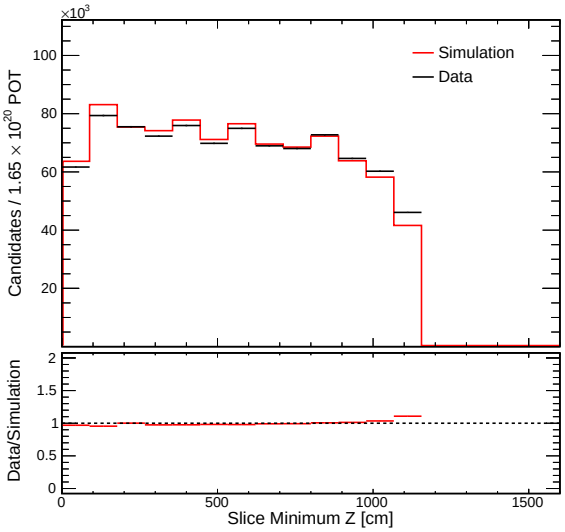

Figure 9.6: Minimum position in the z direction of any hits in a contained slice.

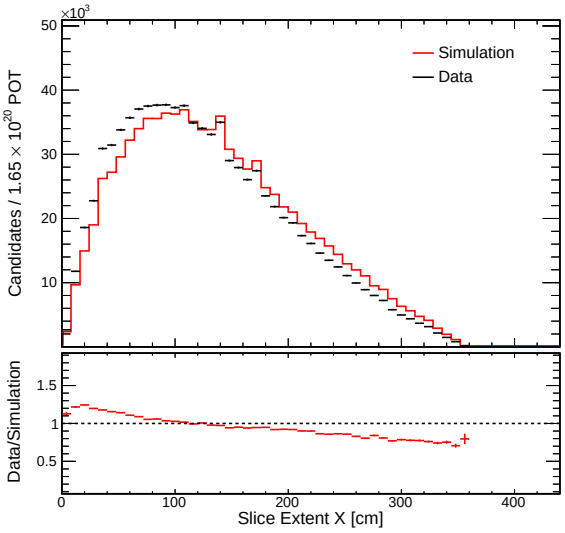

Figure 9.7: Extent of hits of in a slice in the x direction in contained slices.

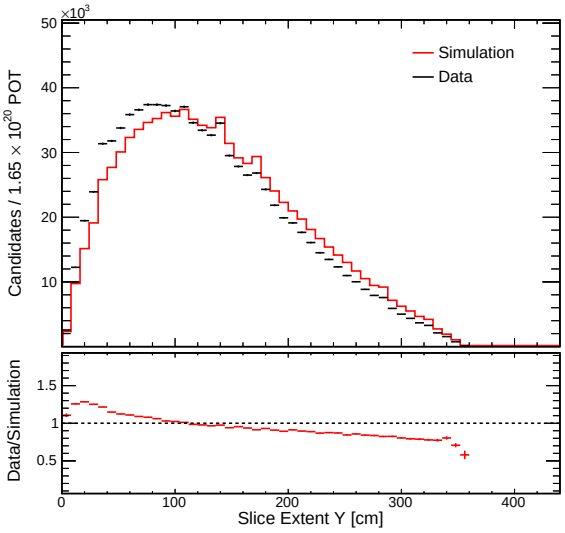

Figure 9.8: Extent of hits of in a slice in the y direction in contained slices.

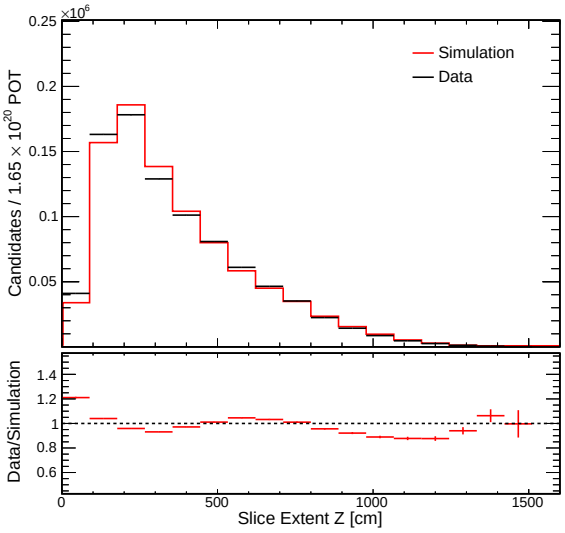

Figure 9.9: Extent of hits of in a slice in the z direction in contained slices.

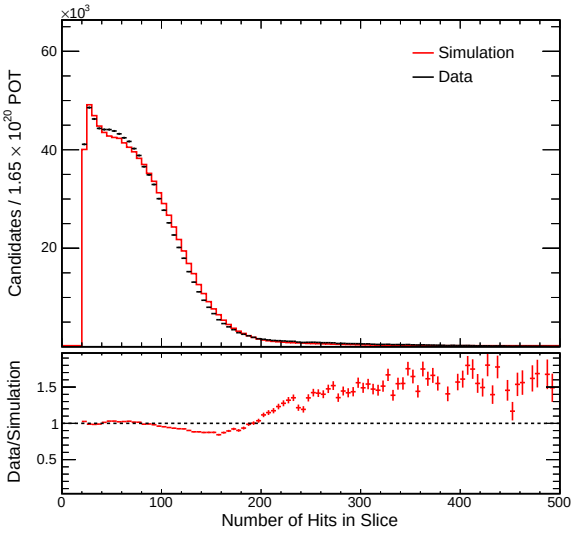

Figure 9.10: Number of hits in contained slices.

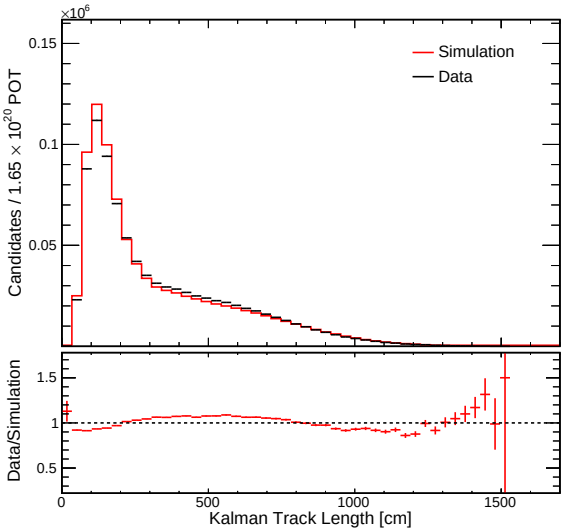

Figure 9.11: Length of the most muon like track in contained slices.

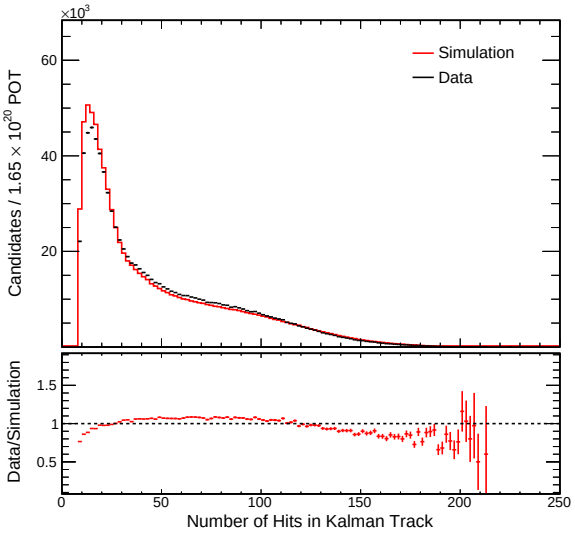

Figure 9.12: Number of hits in the most muon like track in contained slices.

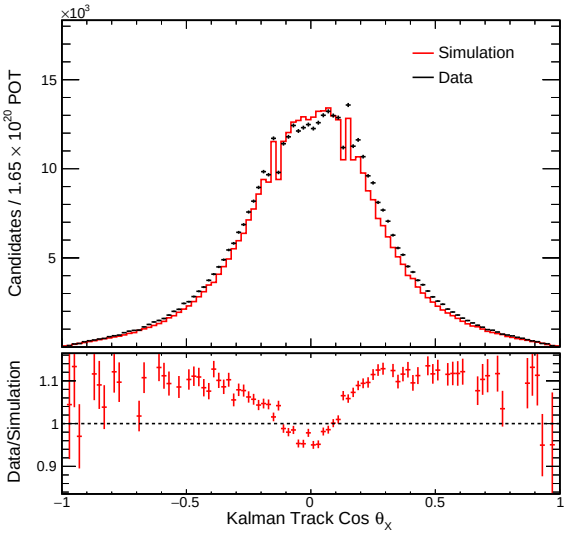

Figure 9.13: Track direction with respect to the x direction in the most muon like track in contained slices.

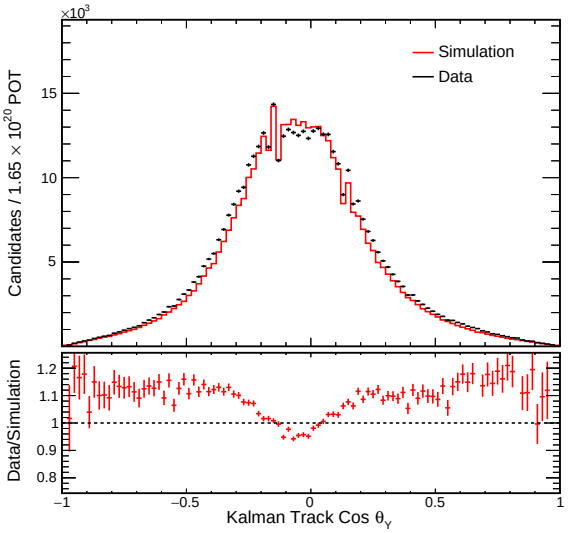

Figure 9.14: Track direction with respect to the y direction in the most muon like track in contained slices.

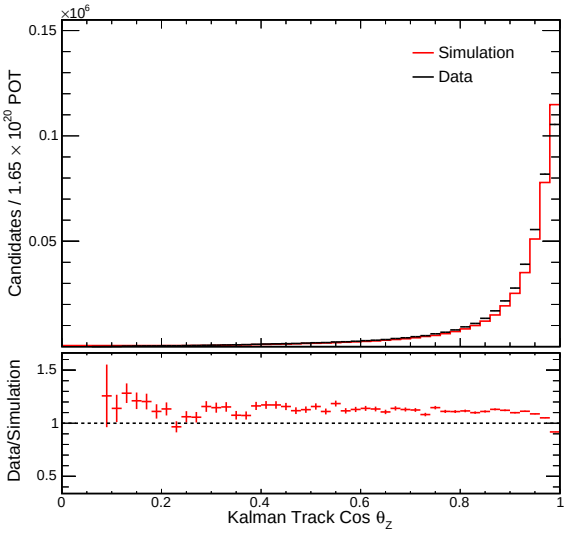

Figure 9.15: Track direction with respect to the z direction in the most muon like track in contained slices.

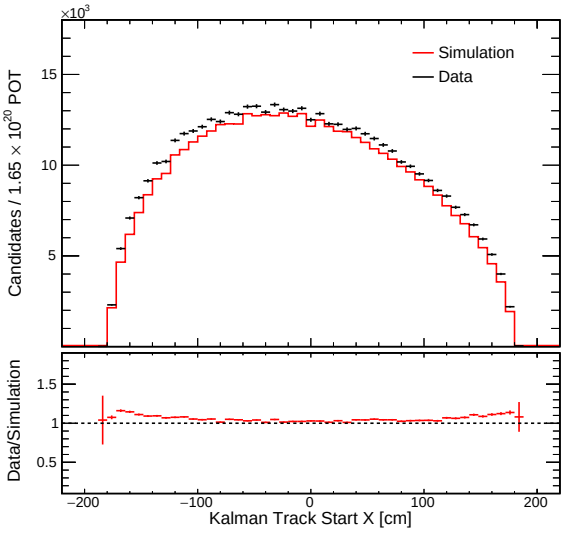

Figure 9.16: Track start x position in the most muon like track in contained slices.

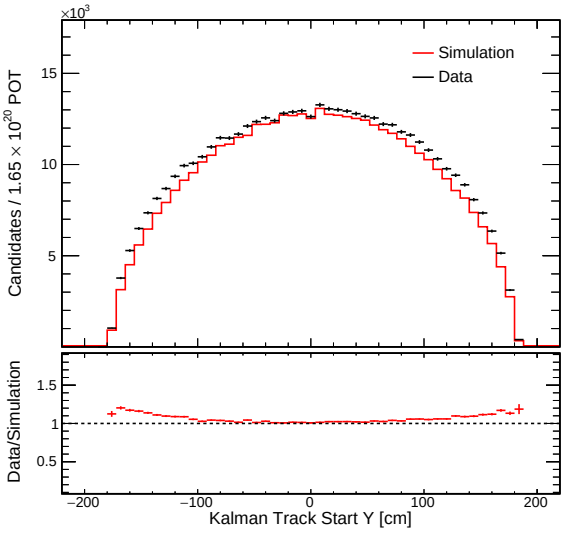

Figure 9.17: Track start y position in the most muon like track in contained slices.

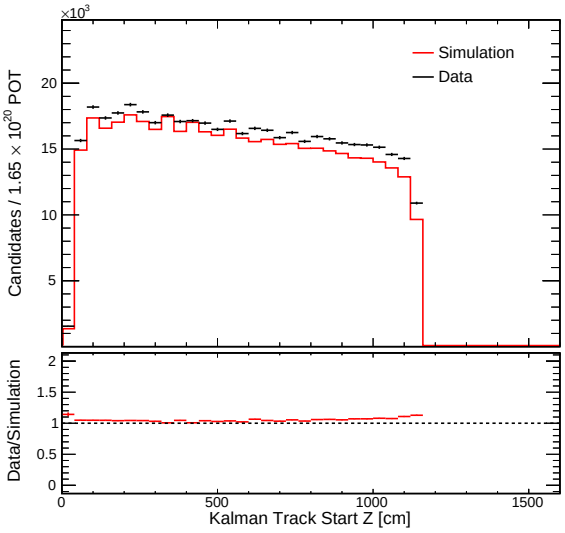

Figure 9.18: Track start z position in the most muon like track in contained slices.

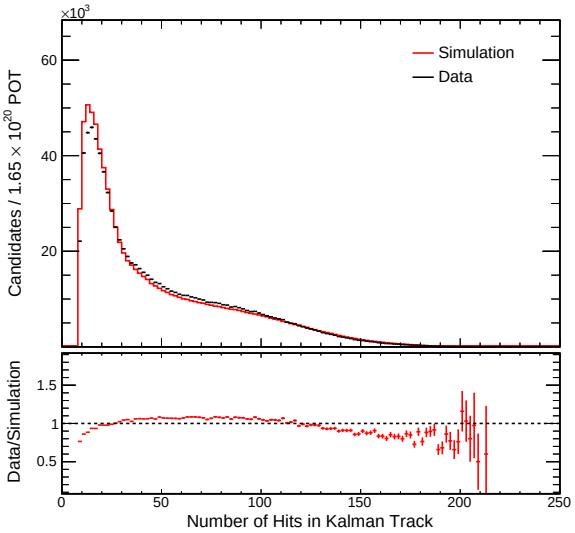

Figure 9.19: Number of hits in the most muon like track in contained slices.

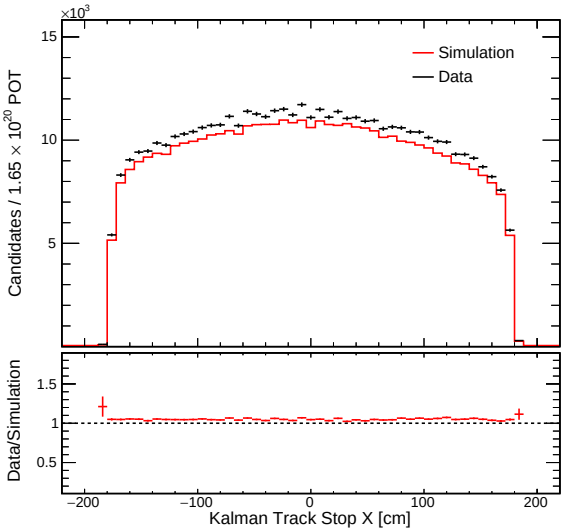

Figure 9.20: Track end x position in the most muon like track in contained slices.

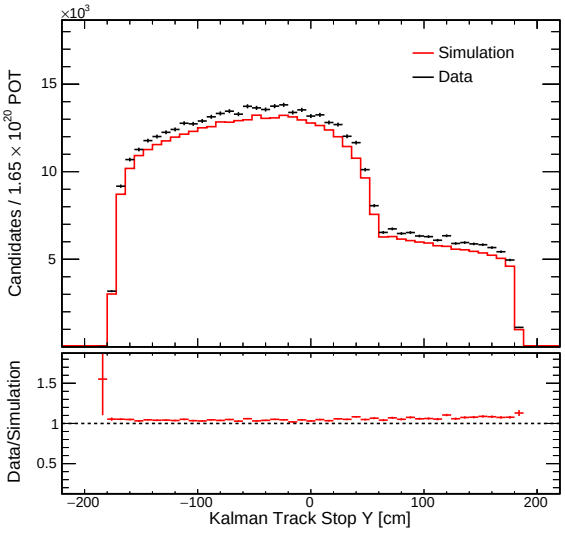

Figure 9.21: Track end y position in the most muon like track in contained slices.

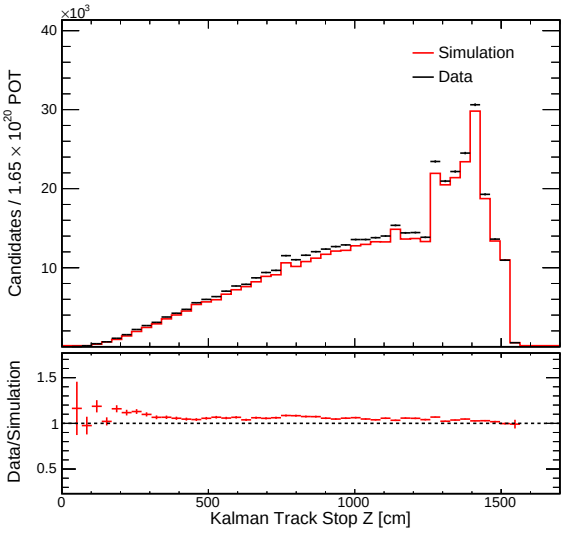

Figure 9.22: Track end z position in the most muon like track in contained slices.

Figures 9.23-9.26 show the agreement of the data and simulation for ReMId selection of ν_μ CC events for slices that are contained and pass data quality. Again these distribution agree well with the same overall normalization difference. There are shape differences seen all figures indicating the data shows more ν_μ CC like events than the simulation. This is seen in the figure 9.23 as a slight excess of data events near 1.0 and lack of data events below 0.2 compared to the simulation.

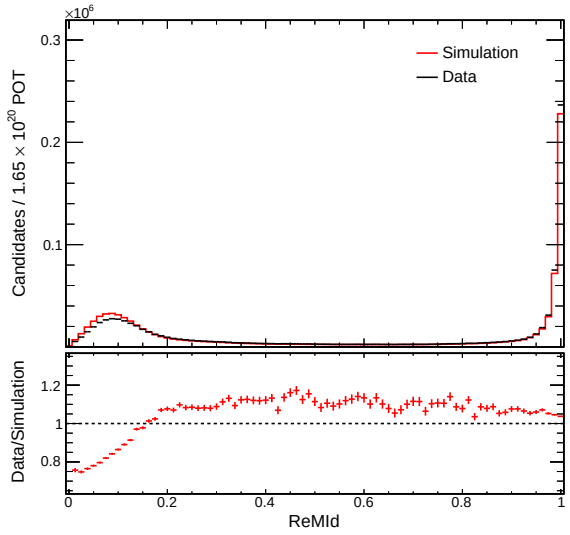

Figure 9.23: ReMId distribution in contained slices.

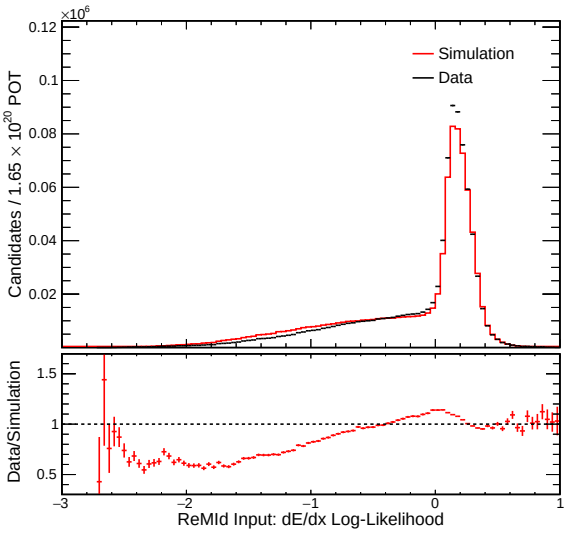

Figure 9.24: ReMId $\frac{dE}{dx}$ LL distribution in contained slices.

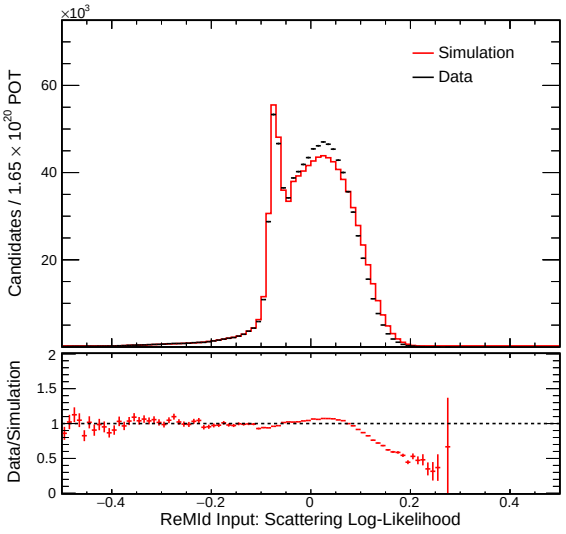

Figure 9.25: ReMId scattering LL distribution in contained slices.

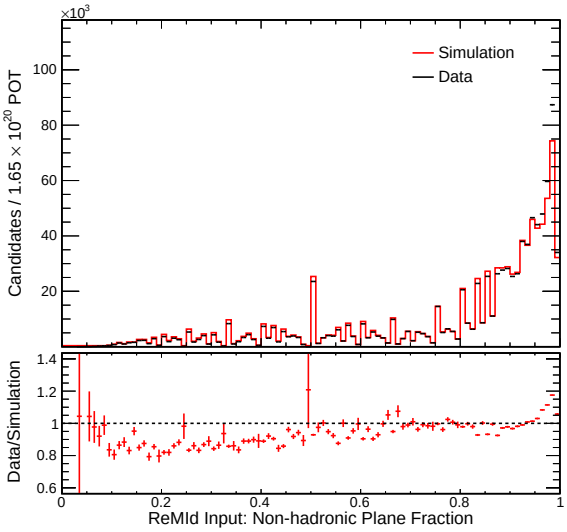

Figure 9.26: ReMId non-hadronic plane fraction distribution in contained slices.

For slices passing the ReMId ν_μ CC selection, figures 9.27-9.32 show the agreement of the data and simulation. In particular the largest discrepancy between data and simulation occurs for the comparison of hadronic energy and number of hadronic hits seen in figures 9.29-9.31 even though figure 9.32 shows agreement in the average visible hadronic energy in each hadronic hit. This discrepancy is discussed further in chapter 11.

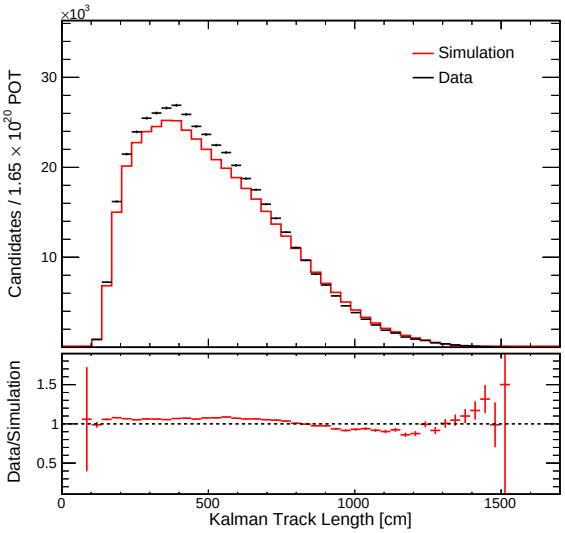

Figure 9.27: Track length of muon track in contained slices passing ν_μ CC selection.

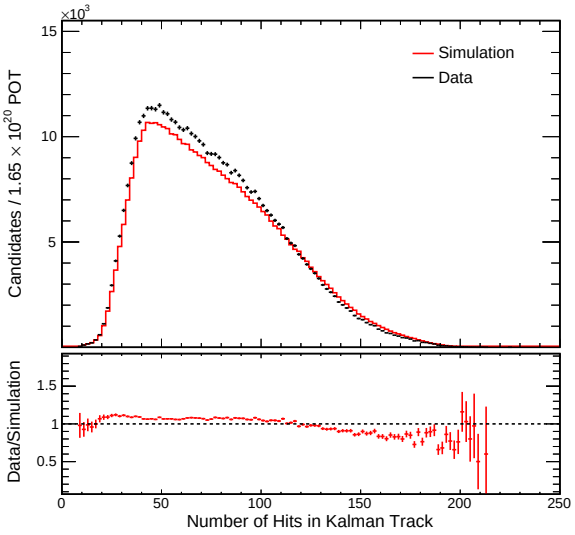

Figure 9.28: Number of hits in the muon track in contained slices passing ν_μ CC selection.

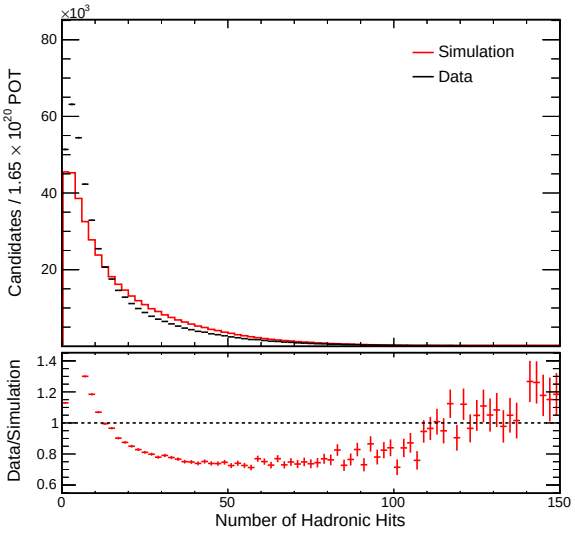

Figure 9.29: Number of hadronic hits in contained slices passing ν_μ CC selection.

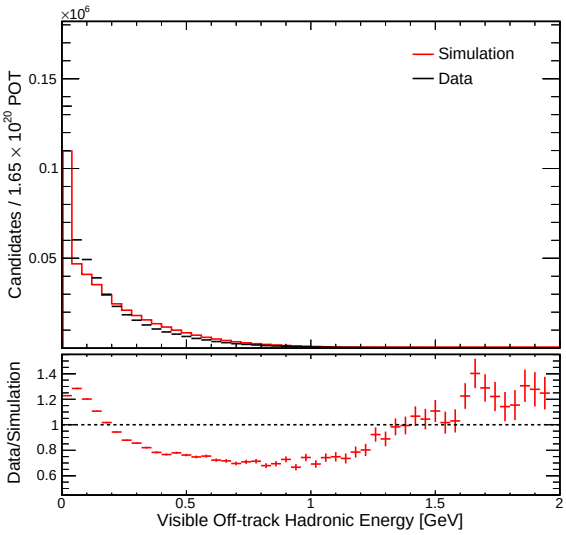

Figure 9.30: Hadronic energy not overlapping with the muon track in contained slices passing ν_μ CC selection.

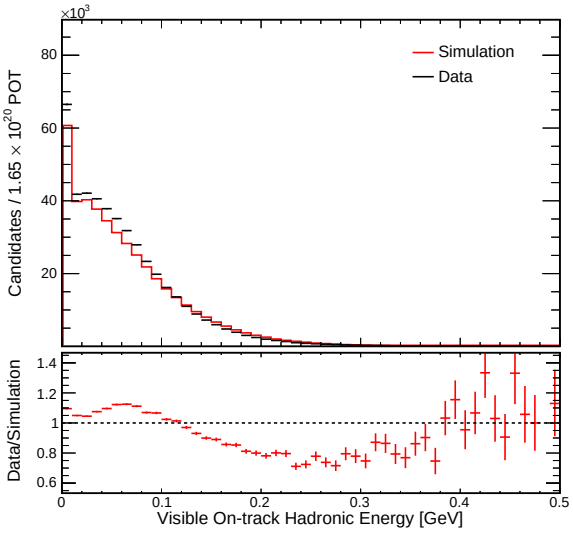

Figure 9.31: Hadronic energy overlapping with the muon track in contained slices passing ν_μ CC selection.

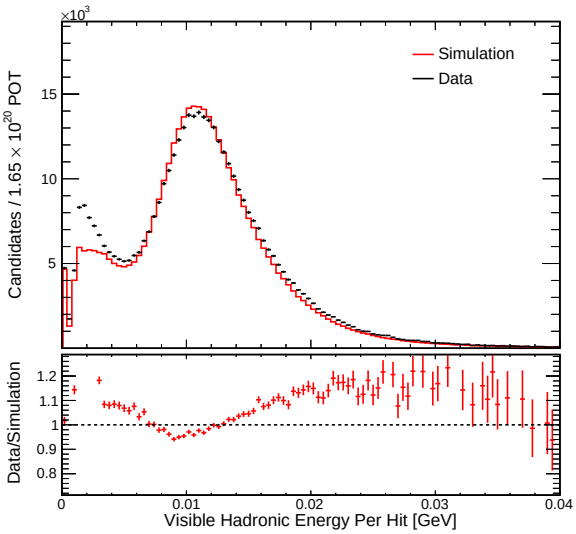

Figure 9.32: Average visible hadronic energy per hadronic hit in contained slices passing ν_μ CC selection.

Figures 9.33 and 9.34 show the agreement of the energy spectra of the QE and NonQE events. Where figures 9.35-9.43 show the agreement of the data and simulation for QePId selection of QE and NonQE events for slices that are contained, pass data quality, and are selected as ν_μ CC events. The disagreement seen in the hadronic system of the events in the near detector also shows in the energy spectrum of the events and the QePId classification as well.

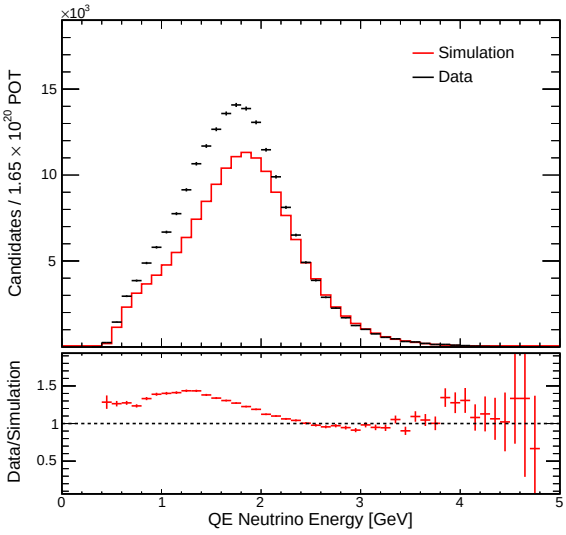

Figure 9.33: Energy spectrum of QE selected events.

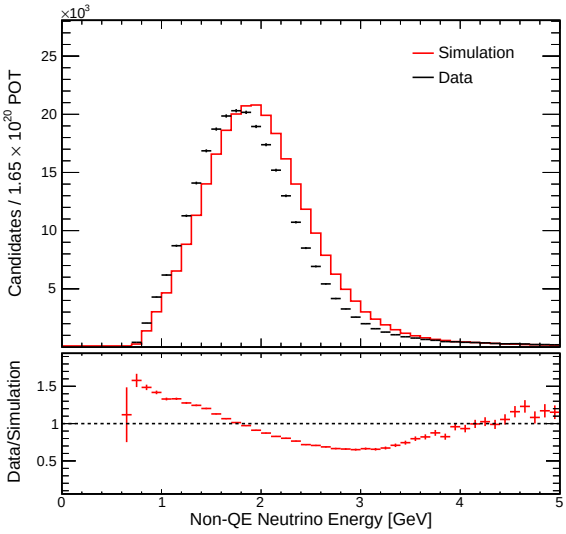

Figure 9.34: Energy spectrum of NonQE selected events.

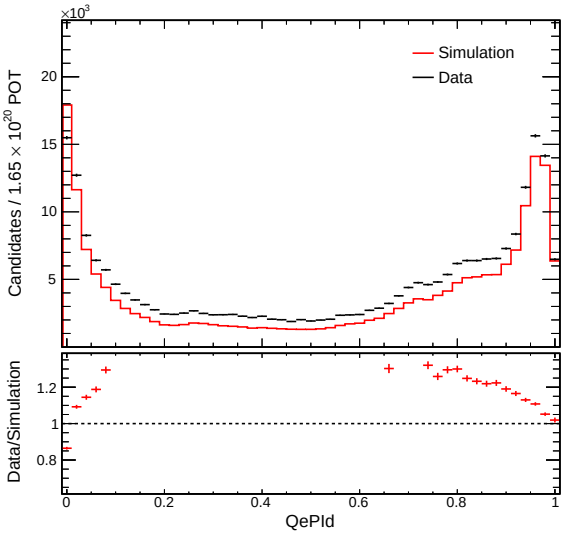

Figure 9.35: QePID distribution in contained slices passing ν_μ CC selection with one reconstructed track.

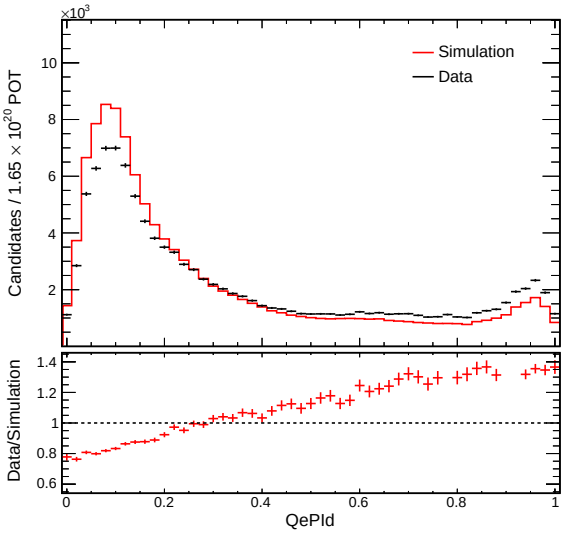

Figure 9.36: QePID distribution in contained slices passing ν_μ CC selection with two reconstructed track.

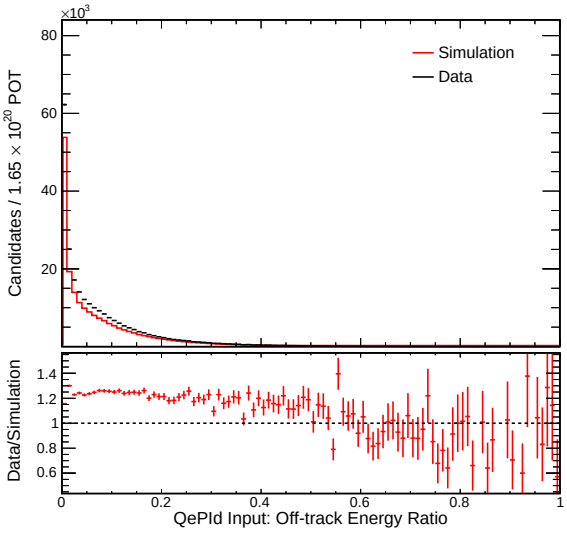

Figure 9.37: Off-track energy ratio distribution in contained slices passing ν_μ CC selection with one reconstructed track.

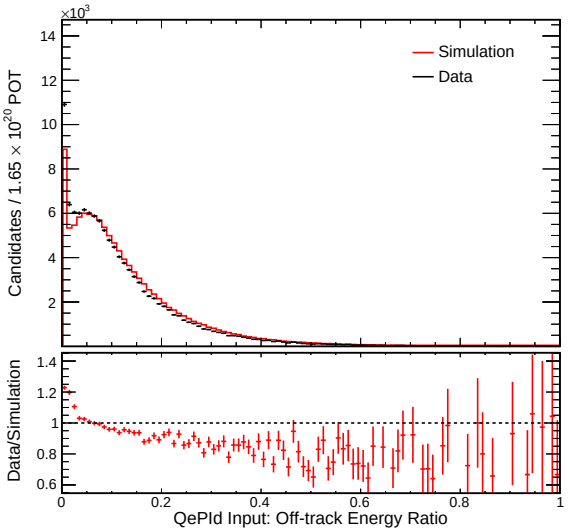

Figure 9.38: Off-track energy ratio distribution in contained slices passing ν_μ CC selection with two reconstructed track.

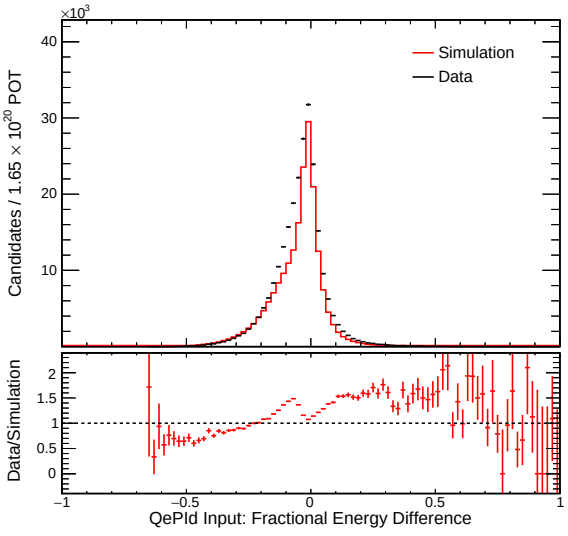

Figure 9.39: Fractional energy difference distribution in contained slices passing ν_μ CC selection with one reconstructed track.

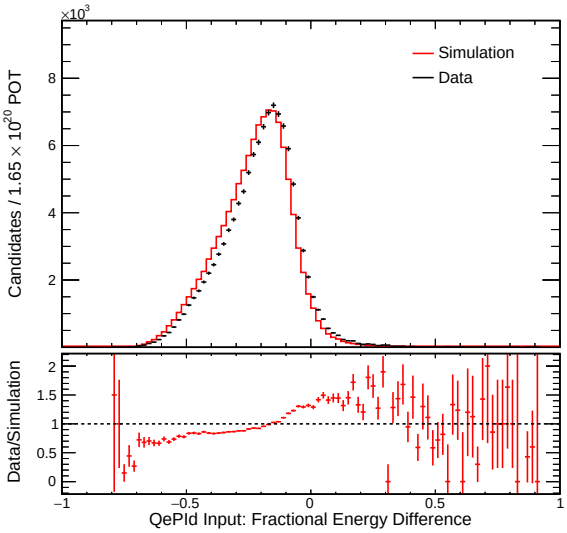

Figure 9.40: Fractional energy difference distribution in contained slices passing ν_μ CC selection with two reconstructed track.

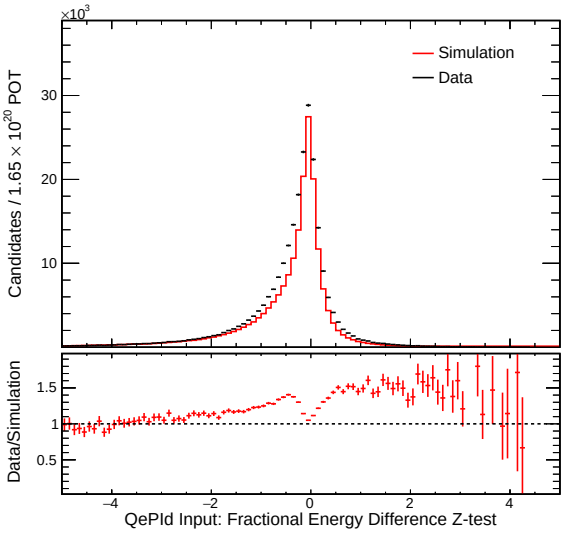

Figure 9.41: Fractional energy difference z-test distribution in contained slices passing ν_μ CC selection with one reconstructed track.

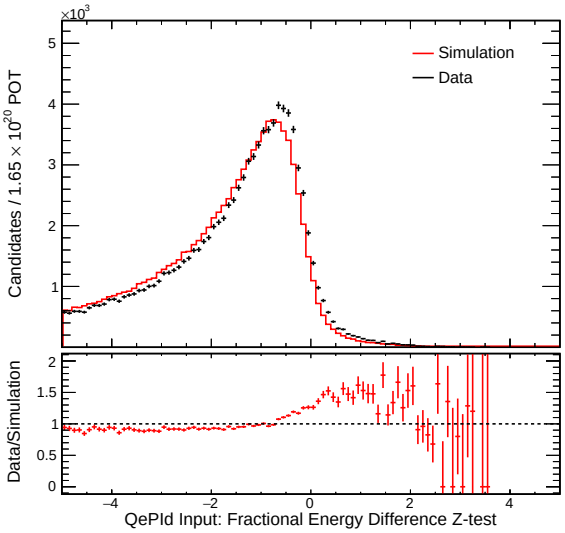

Figure 9.42: Fractional energy difference z-test distribution in contained slices passing ν_μ CC selection with two reconstructed track.

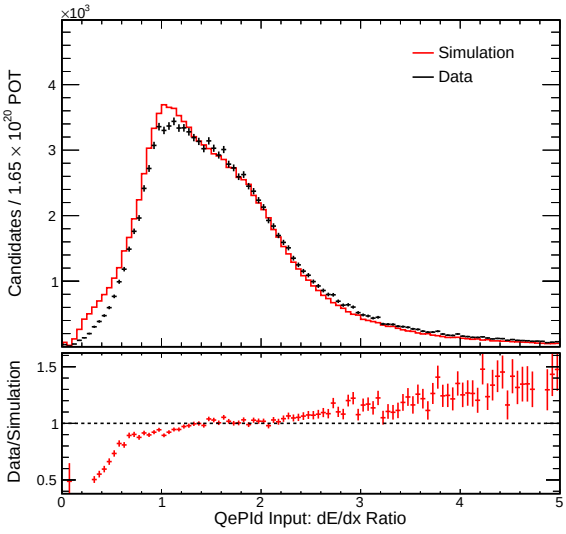

Figure 9.43: $\frac{dE}{dx}$ ratio distribution in contained slices passing ν_μ CC selection with two reconstructed track.

9.3 Far Detector Selection

Events in the far detector are selected to pass the data quality cuts described in section 9.1 as well as the ReMId cut to select ν_μ CC events described in chapter 6. Additionally events must fall within the beam spill window. For pre-shutdown data this is between 218.125 μs and 230.125 μs or between 282.125 μs and 294.125 μs. For post-shutdown data the beam spill window is only between 218.125 μs and 230.125 μs. Events must also pass the contained population cosmic rejection cuts or fail the contained population cosmic rejection cuts and pass the escaping population cosmic rejection cuts described in chapter 8. Further the events passing the contained population cosmic rejection cuts are further classified as QE or NonQE events based on the QePId cut described in chapter 7. This results in three event samples in the far detector: the contained QE sample, the contained NonQE sample, and the escaping sample referred to as QE, NonQE, and escaping. The energy of each sample is determined by the QE energy estimator, NonQE energy estimator, and the NonQE energy estimator described in 7, respectively. The escaping sample relies on the NonQE energy estimator as the basis of energy estimation because the cuts required to make it into this sample result in $\sim$0 of ν_μ CC QE interactions. The lack of ν_μ CC QE interactions in the escaping sample is mainly a result of the requirement on hadronic energy in the interaction. Only events with less than 10 GeV of visible energy in the far detector are used in this analysis.

9.3.1 Cosmic Background Subtraction

In the far detector the selected cosmic ray background can be measured in data that is taken asynchronous to the beam spills. This data comes in two forms, calibration data that is taken from separate trigger windows to NuMI spills and out of beam spill data within the same trigger window as the NuMI spills. From this data an estimate of the cosmic background in the beam spill window can be made. This is done through a fit to the out of time data from the calibration data to obtain the shape of the energy spectrum of the cosmic background for each of the three sample in the far detector separately. Both the QE and NonQE sample are fit to a Landau function with a constant baseline. The escaping sample was fit to a piecewise continuous function with the low energy side described by a quadratic function and the high energy side a constant baseline.

The joint between the quadratic and constant baseline was determined by the fit. The overall normalization of the cosmic background was taken from the out of beam spill data within the NuMI trigger windows. Figures 9.44-9.46 show the selected cosmic background data as well as the fit. This background is accounted for in the fit for the ν_μ disappearance oscillation parameters.

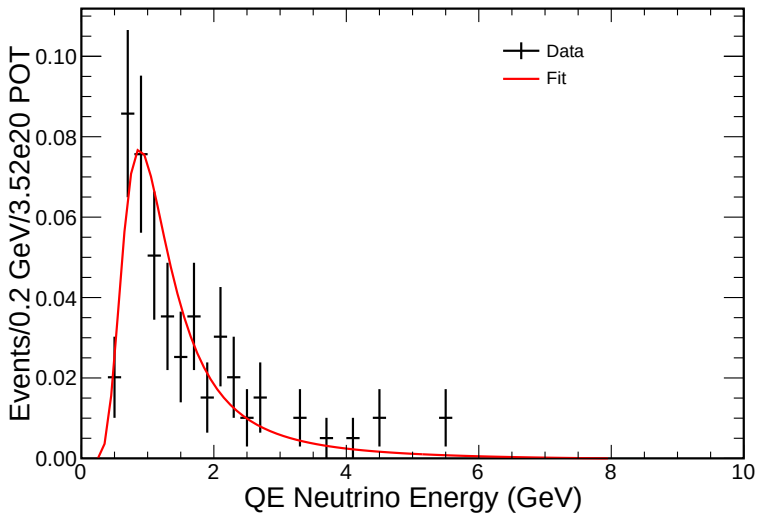

Figure 9.44: Energy spectrum of selected cosmic background events in data along with the fit and background estimate in the QE sample. The background estimate is taken from the fit and shows the expected background event count in each energy bin used in the analysis.

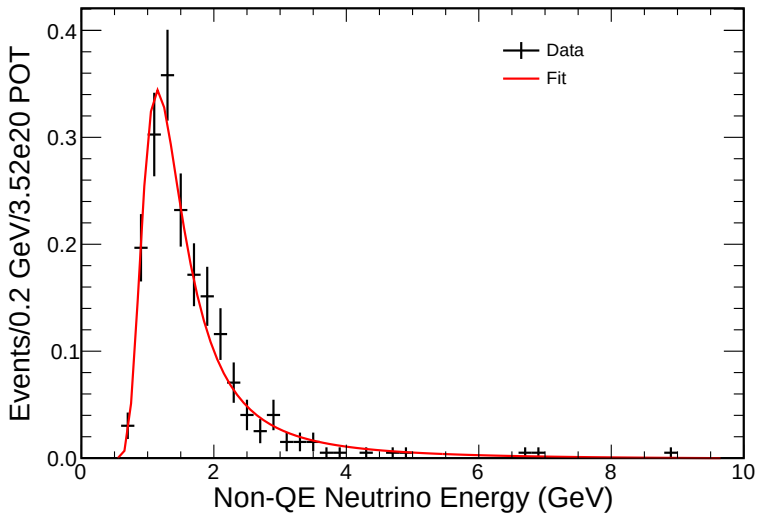

Figure 9.45: Energy spectrum of selected cosmic background events in data along with the fit and background estimate in the NonQE sample. The background estimate is taken from the fit and shows the expected background event count in each energy bin used in the analysis.

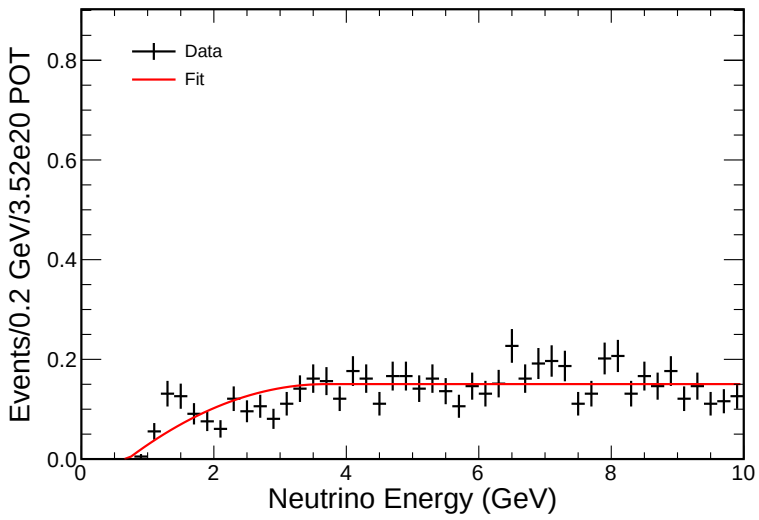

Figure 9.46: Energy spectrum of selected cosmic background events in data along with the fit and background estimate in the escaping sample. The background estimate is taken from the fit and shows the expected background event count in each energy bin used in the analysis. Note the expected background has variable binning making it appear to diverge at high energies.

Chapter 10

Far Detector Prediction

This oscillation analysis compares the measured far detector spectrum of selected events to the predicted far detector spectrum to determine the oscillations parameters. This chapter describes the process of determining the predicted far detector spectrum.

This analysis uses the selected events at the near detector to determine a prediction for the events at the far detector[75]. In particular the prediction is the number of far detector events, $F_S^{Pred}(B_j)$, in the reconstructed variable B with bins j for the selection criteria S in the far detector. In a far detector only experiment the prediction of the events at the far detector would be completely reliant on the modeling of the beam flux and detector response in simulation. By using two functionally identical detectors the goal is to cancel many of the systematic effects from the potential mismodelling of any of the components in the beam flux and detector response through an extrapolation process. The topic of systematics and cancellation between near and far detector is presented in chapter 11. The extrapolation does not provide the prediction of $F_S^{Pred}(B_j)$, directly, but instead $F_{\alpha\to\beta,S}^{Pred}\left(E_i^T, B_j\right)$ which is the number of far detector events with true energy E^T in bin i in the reconstructed variable B with bins j for the selection criteria S in the far detector resulting from oscillation of neutrinos of flavor α in the near detector to flavor β in the far detector. The full prediction $F_S^{Pred}(B_j)$ is related to $F_{\alpha\to\beta,S}^{Pred}\left(E_i^T, B_j\right)$ through

$$F_S^{Pred}(B_j) = \sum_{\alpha\to\beta}\sum_i F_{\alpha\to\beta,S}^{Pred}\left(E_i^T, B_j\right) P_{\alpha\to\beta}\left(E_i^T\right) \tag{10.1}$$

where $P_{\alpha\to\beta}\left(E_i^T\right)$ is the probability that neutrino flavor α oscillates to flavor β at

true energy E_i^T. $P_{\alpha\to\beta}\left(E_i^T\right)$ is governed by the oscillation parameters and is what is fit for when the full prediction $F_S^{Pred}\left(B_j\right)$ is compared to the data. Fitting will be discussed in chapter 12 and the rest of this chapter will focus on the determination of $F_{\alpha\to\beta,S}^{Pred}\left(E_i^T, B_j\right)$ through extrapolation. Additionally, because oscillations do not effect NC interactions the notation α and β refer to only CC interactions with state α and β and the NC interactions are handled through an additional $NC \to NC$ channel. The determination of $F_{\alpha\to\beta,S}^{Pred}\left(E_i^T, B_j\right)$ is handled differently for major and minor signals and backgrounds. For this analysis the major signals are from the $\mu \to \mu$ and $\bar{\mu} \to \bar{\mu}$ oscillation and the major background is from $NC \to NC$ channel. The rest of the oscillation channels are considered to be minor.

The expected event rates of the minor backgrounds in the near detector data are not able to provide sufficient statistics to be reliably extrapolated. For this case $F_{\alpha\to\beta,S}^{Pred}\left(E_i^T, B_j\right)$ is set to the simulated only prediction. This does not make use of the advantages of the two detector experiment to predict the far detector flux; however, because of the low selection rate of these backgrounds, any misestimation of the far detector prediction from the backgrounds has negligible effect on the resulting measurement.

The major signals and background are predicted in the far detector through the steps of determining the components of the channels measured in the near detector data, relating the estimated energy of the components to the true energy spectrum in the near detector, determining the flux at the far detector given the measured flux at the near detector. In particular these tasks account for imperfect signal selection, imperfect energy estimation, and predicting the far detector flux given the geometrical and selection differences between the near and far detectors. These tasks are accomplished through the procedure:

1. The number of near detector data selected events N^{Data} is measured in bins of reconstructed energy B_k as $N^{Data}\left(B_k\right)$

2. The near detector data is decomposed in each bin B_k into the different major channels α by the proportions of that channel in the simulation out of the total selected resulting in $N_\alpha^{Data}\left(B_k\right)$

3. Unfold the decomposed data in each bin B_k into true energy to get a prediction $N^{Pred}\left(E_i^T\right)$ of the true events in channel α at true energy E_i^T. The unfolding

is done through the ratio of number of near detector events in the simulation in channel α with true energy E_i^T in bin B_k, $N_\alpha^{Sim}\left(E_i^T, B_k\right)$ to the total number of near detector events in the simulation in channel α in bin B_k, $N_\alpha^{Sim}\left(B_k\right)$:

$$N^{Pred}\left(E_i^T\right) = \sum_k N_\alpha^{Data}\left(B_k\right) \frac{N_\alpha^{Sim}\left(E_i^T, B_k\right)}{N_\alpha^{Sim}\left(B_k\right)} \tag{10.2}$$

4. Predict the number of far detector events in channel β at true energy E_i^T in bins B_j, $F_{\alpha\to\beta,S}^{Pred}\left(E_i^T, B_j\right)$, from the predicted number of near detector events of channel α at true energy E_i^T, $N^{Pred}\left(E_i^T\right)$ by multiplying by the ratio of the simulated number of events in the far detector at true energy E_i^T in bin B_j, $F_\beta^{Sim}\left(E_i^T, B_j\right)$, to the number of simulated near detector events in channel α at true energy E_i^T, $N_\alpha^{Sim}\left(E_i^T\right)$:

$$F_{\alpha\to\beta,S}^{Pred}\left(E_i^T, B_j\right) = N^{Pred}\left(E_i^T\right) \frac{F_\beta^{Sim}\left(E_i^T, B_j\right)}{N_\alpha^{Sim}\left(E_i^T\right)} \tag{10.3}$$

Both steps 2 and 4 make use of the ratio of simulated events in a given bin of either a reconstructed variable or true energy. For the cases with no events in those bins and the denominator of the ratios are zero, the extrapolation procedure of not reweighing which results in taking the simulated prediction in that particular bin. Furthermore the ratio in step 4 relates the far and near detector flux and selection together. In the ideal two detector experiment the use of the ratio would cancel all the uncertainties in the beam flux, cross sections, and detector response modeling. However given the differences in the beam flux seen at the near and far detectors, i.e. the near detector sees a line source of neutrinos and the far detector effectively sees a point source, and the differences in the actual detectors themselves these differences do not completely cancel. The true energy binning in the above is chosen so that each bin is given approximately equal sensitivity to the oscillations.

The near detector selected QE and NonQE samples are used independently for the prediction of the QE and NonQE events at the far detector with each near detector sample going through the above procedure to predict the far detector spectrum. Because the escaping sample makes no distinction between QE and NonQE the sum of the QE and NonQE samples are extrapolated to determine a far detector prediction. The

escaping sample at the far detector contains event topologies that are not in the near detector samples used for extrapolation. For these events the pure simulation prediction is used. This results in larger systematic errors discussed in chapter 11 due to beam uncertainties that do not cancel from the extrapolation process. However, the events that can be extrapolated remove most of the uncertainty in the oscillation region and the remaining uncertainties are tolerable in the analysis.

The proportion of the major signal and background components used for decomposition of the near detector events is shown for the QE and NonQE samples in figures 10.1 and 10.2

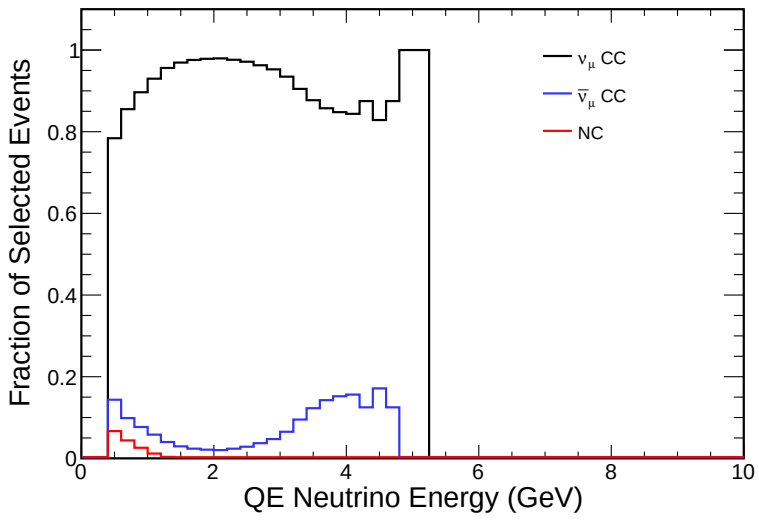

Figure 10.1: Proportion of selected QE events in each of the three major signals and backgrounds.

Figures 10.3-10.8 show the extrapolation process for the decomposed ν_μ channel for the NonQE sample. The full extrapolation of all major channels for the NonQE and QE samples is shown in appendix A. In particular figure 10.3 shows the decomposed ν_μ NonQE events selected in the near detector data and simulation, also referred to as Monte-Carlo (MC). Figure 10.4 shows the mapping between the reconstructed energy of the selected neutrino events to the true energy as determined by the simulation used

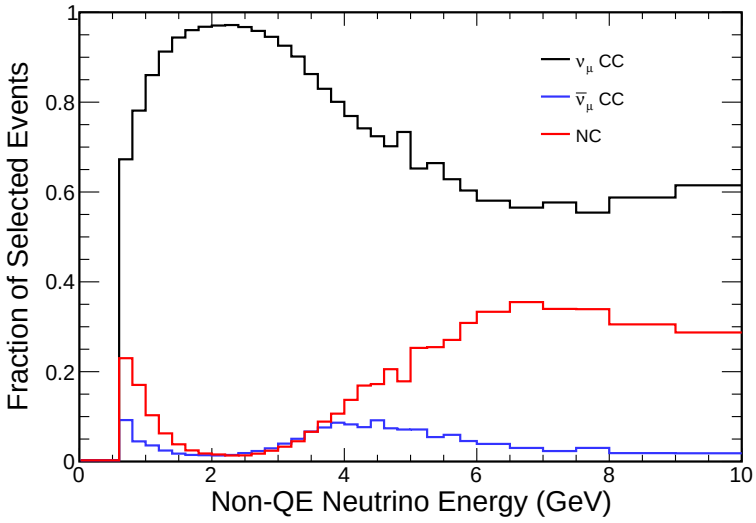

Figure 10.2: Proportion of selected NonQE events in each of the three major signals and backgrounds.

in step 3 in the extrapolation procedure which results in a true energy spectrum of near detector events shown in figure 10.5. The true energy spectrum of selected events in the far detector found in step 4 of the extrapolation is shown in figure 10.6. Finally the spectrum of predicted far detector events is mapped to reconstructed energy using the mapping shown in figure 10.7 which results in the predicted far detector spectrum for the NonQE events in figure 10.8. The total predicted spectrum for the three samples, NonQE, QE, and escaping are shown in figures 10.8 -10.10. These show the predicted unoscillated expected neutrino spectrums in all three samples with all backgrounds except for cosmic ray background included.

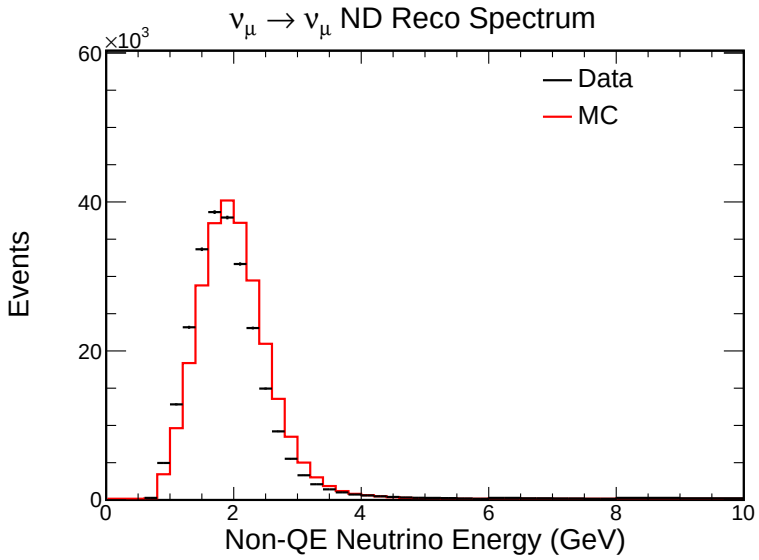

Figure 10.3: Selected NonQE events in near detector data and simulation.

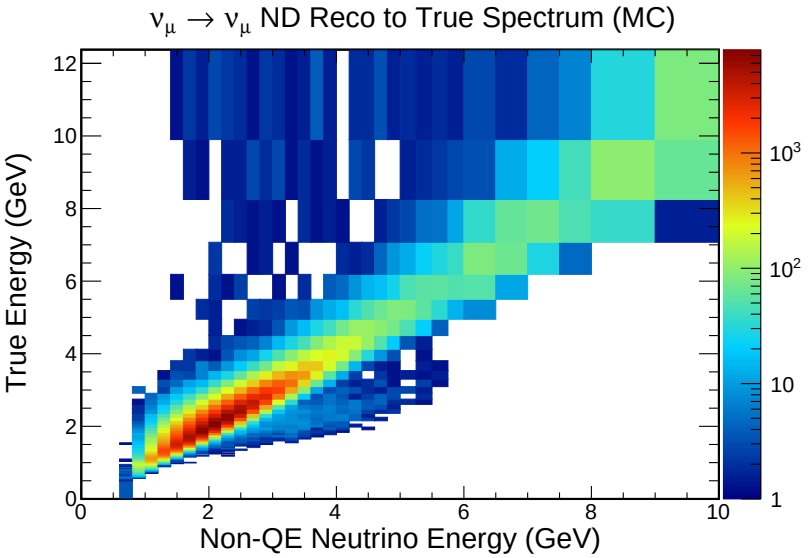

Figure 10.4: Mapping of between reconstructed and true energy of selected NonQE events in near detector.

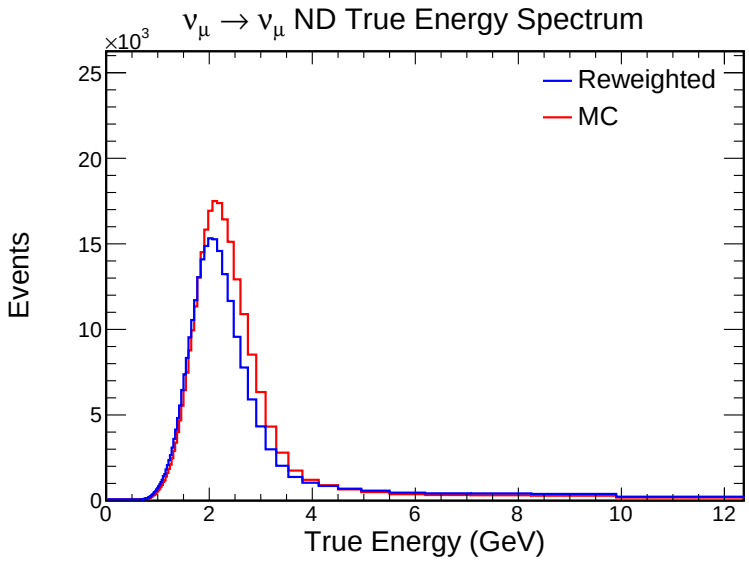

Figure 10.5: True energy spectra of selected NonQE events in near detector data and simulation. The reweighed spectrum is determined by the data selected events and the simulation spectrum is determined from the base simulation of near detector events.

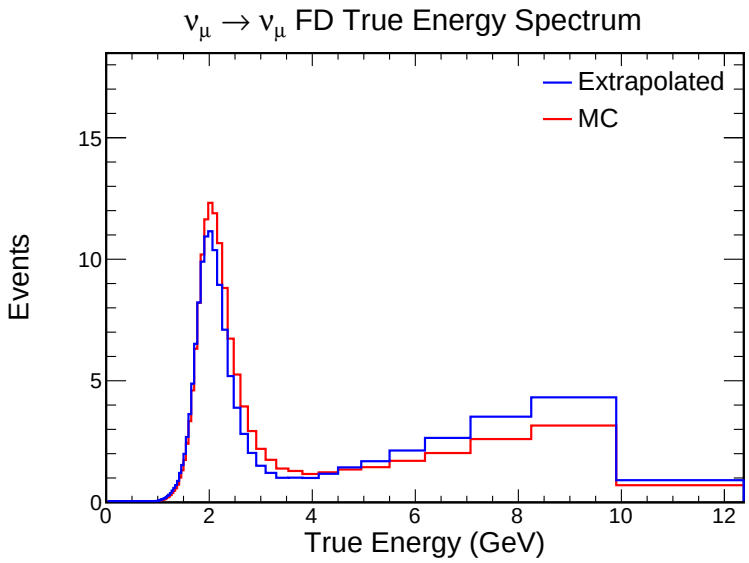

Figure 10.6: True energy spectra of selected NonQE events in far detector data and simulation. The extrapolated spectrum comes from extrapolated data events in the near detector and the simulation is from the base simulation of far detector events.

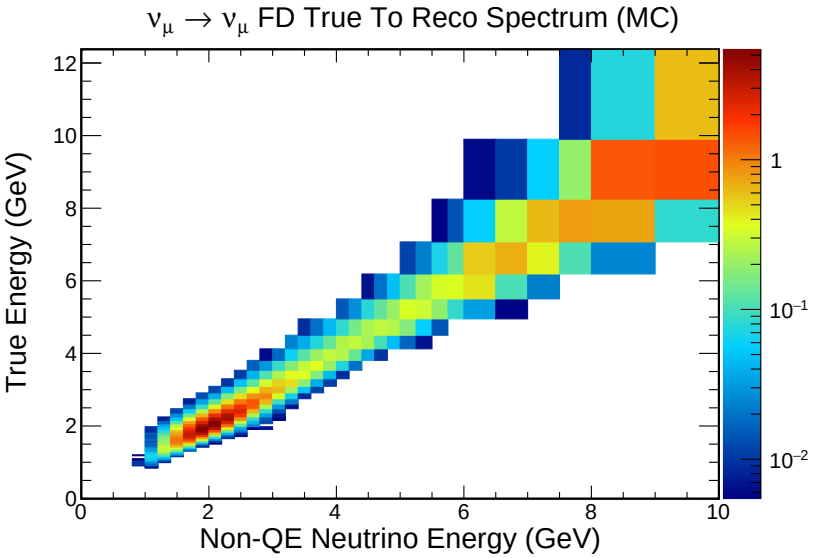

Figure 10.7: Mapping of between reconstructed and true energy of selected NonQE events in far detector.

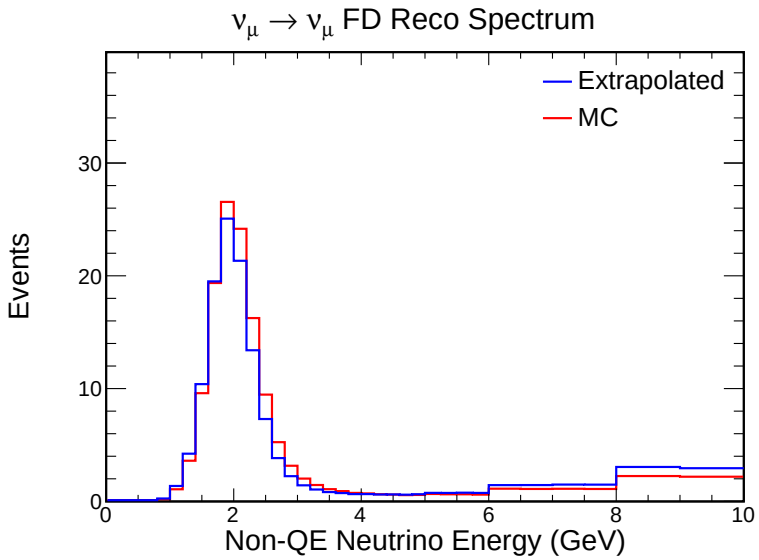

Figure 10.8: Reconstructed energy spectra of selected NonQE events in far detector data and simulation. The extrapolated spectrum comes from extrapolated data events in the near detector and the simulation is from the base simulation of far detector events.

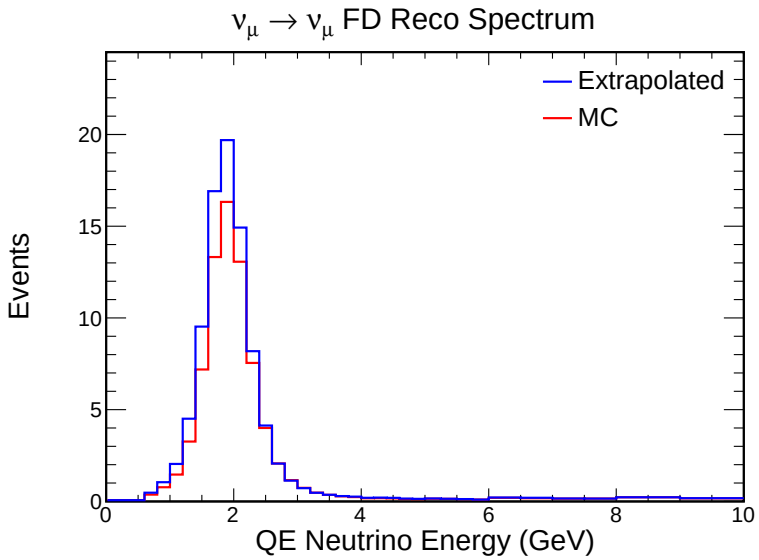

Figure 10.9: Reconstructed energy spectra of selected QE events in far detector data and simulation. The extrapolated spectrum comes from extrapolated data events in the near detector and the simulation is from the base simulation of far detector events.

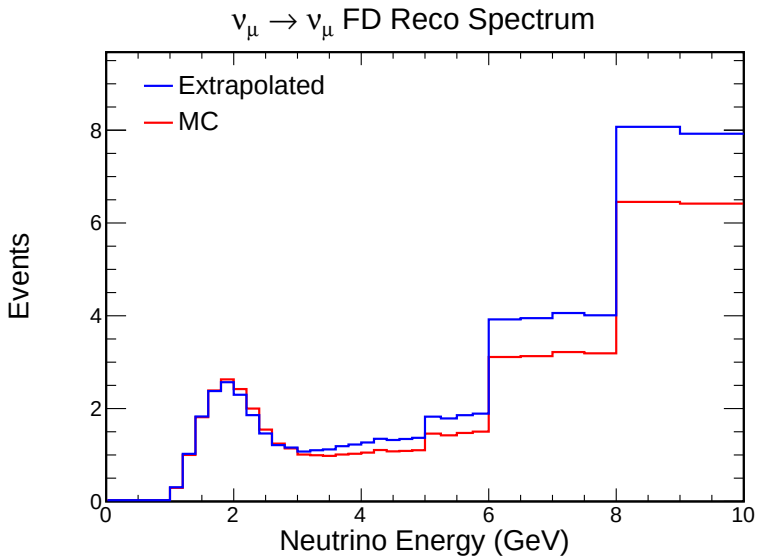

Figure 10.10: Reconstructed energy spectra of selected escaping events in far detector data and simulation. The extrapolated spectrum comes from extrapolated data events in the near detector and the simulation is from the base simulation of far detector events.

Chapter 11

Systematics

This analysis suffers from systematic uncertainty due to mis-modeling of neutrino interactions, mis-modeling of the beam, mis-modeling of the detector responses, and uncertainty in the analysis methods. Although the systematic uncertainty does not dominate, it does have an impact on the result. By design, to a large extent, many of the systematic uncertainties are reduced by using two detectors. This chapter describes the sources and determination of systematic uncertainty. The analysis fitting method described in chapter 12 incorporates the systematics described here into the determination of the oscillation parameters. For each of the systematic uncertainties used in this analysis plots showing the uncertainty in the near detector, far detector without using extrapolation from the near detector, and the far detector with extrapolation are shown for the NonQE sample only, except were noted. For the full plots of systematic uncertainty of the QE and escaping samples see appendix B.

11.1 Beam

The uncertainties in the beam are largely due to uncertainties in the hadronic cross-sections and misalignments of the horns and beam position on the target. The goal of the two detector experiment is to have these uncertainties cancel as much as possible due to the ratios used in the extrapolation process described in chapter 10. However, the two detectors see different energy spectrums and have different acceptances due to the detector size and positioning. In particular the near detector will not be able to

provide information about some of the high energy events in the escaping population in the far detector so that the full beam uncertainty applies to some portion of the events in the far detector. The event selection described was chosen to minimize that case to acceptable levels. In order to evaluate the uncertainties from the beam were broken up into two categories, hadronic production uncertainties and beam transport uncertainties.

The hadronic production uncertainty arise from the uncertainty in the initial creation of particles from collisions of the proton beam with the graphite target. The error due to the hadronic production uncertainties was evaluated as the difference between the data coming from the NA49 experiment and the simulation used for hadronic production. NA49 was a fixed target experiment designed to measure hadronic processes in fine detail. It used two large time projection chamber detectors to measure hadronic shower development and an additional two smaller detectors to measure the behavior near the interaction vertex. [76]. The difference between the NA49 data and simulation is determined as function of neutrino energy and signifies the impact on the analysis by using different parameterizations of the hadronic production.

The beam transport uncertainties arise from the uncertainties of the focusing of the charged mesons produced in the target collisions. These uncertainties are generated from the imperfect knowledge of the horn and beam positions relative to the target and any uncertainties in the current running through the horn. The total uncertainty as a function of neutrino energy is determined by applying the following shifts to the simulation and determining the shift in neutrino energy from the nominal spectrum [77].

1. Beam position $\pm$ 0.5 mm in both horizontal and vertical directions relative to the target center

2. Beam spot size $\pm$ 0.2 mm in both horizontal and vertical directions.

3. Target position 2 mm closer to the beam

4. Horn current $\pm$ 1 kA

5. Horn surface magnetic field modeled as an exponential instead of a linear distribution

6. Position of both the first and second horns ± 2 mm in both the horizontal and vertical directions

For ease of computation all of the independent beam systematics described above where combined in a total beam systematic. This was done by summing in quadrature the absolute maximum of the the ± shifts from each systematic in each bin of neutrino energy. Figure 11.1 show systematic uncertainty in the analysis from the beam. As noted previously, the escaping sample suffers from having less cancelation in the beam uncertainty than the nonQE and QE samples. This contributes to the beam being the largest uncertainty in the escaping sample as seen in figure 11.2

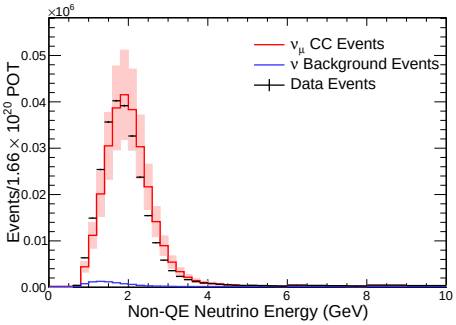

(a) Near Detector

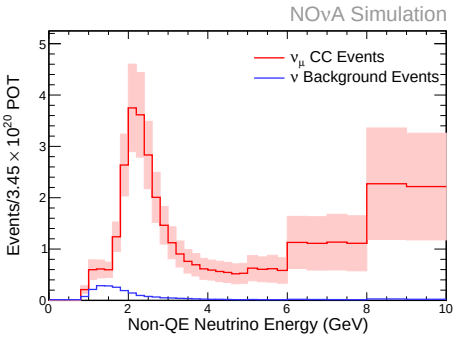

(b) Far Detector without Extrapolation

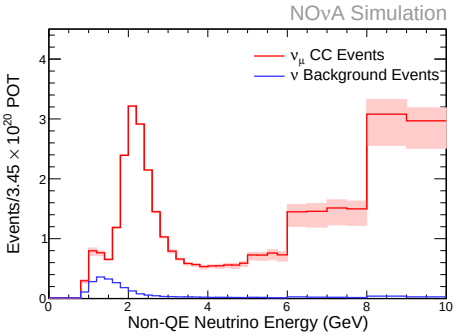

(c) Far Detector with Extrapolation

Figure 11.1: Reconstructed energy of selected events in the nonQE sample with the systematic error band from beam uncertainties. All selected simulated events are shown in red with the a red systematic error band. The contribution to the selected events from background in the simulation is shown in blue. For the near detector the data is drawn in black with statistical error bars. For the far detector the oscillation parameters listed in table 2.1 are assumed.

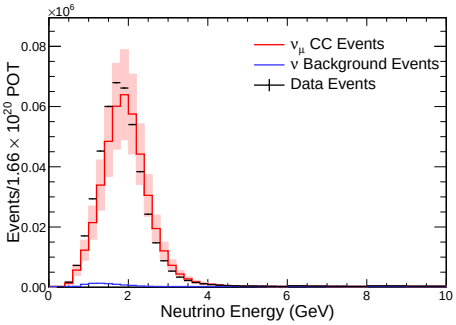

(a) Near Detector

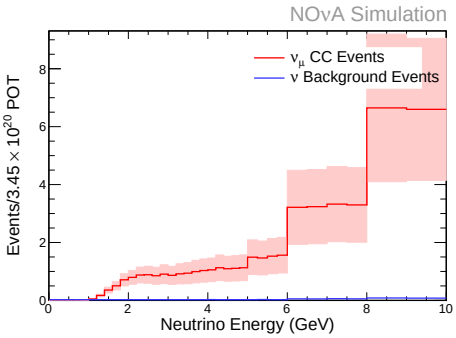

(b) Far Detector without Extrapolation

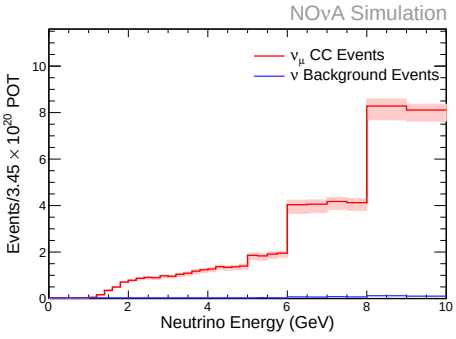

(c) Far Detector with Extrapolation

Figure 11.2: Reconstructed energy of selected events in the escaping sample with the systematic error band from beam uncertainties. All selected simulated events are shown in red with the a red systematic error band. The contribution to the selected events from background in the simulation is shown in blue. For the near detector the data is drawn in black with statistical error bars. For the far detector the oscillation parameters listed in table 2.1 are assumed.

11.2 Neutrino Interactions

This analysis relies on GENIE for the simulation of neutrino interactions in the near and far detectors as described in chapter 4. GENIE uses physical models as well as data from neutrino cross-section experiments to determine the interaction cross-sections of neutrinos and the modeling of the hadronization of the final state particles leaving the interaction. Unfortunately neutrino cross-sections are not that well known which leads to a large uncertainty in their modeling. Similarly to the beam, the goal of a two detector experiment is to have these uncertainties cancel. Again similarly to the beam due to the differences in the near and far detector they do not completely cancel. The systematic uncertainty due to the cross sections and final state interaction modeling is handled through reweighting events in the simulation by shifting the parameters in GENIE that are used to determine the cross-sections and interaction modeling within the uncertainty. In total there are 44 parameters in GENIE. The nominal and uncertianty of the parameters were determined from the GENIE users manual [78] It is not computationally feasible to treat each of these parameters individually within the fitting procedure of this analysis. Instead the 6 parameters producing the largest effects on the selected event spectrums are treated individually and all other parameters where grouped into one small systematic uncertainty [79]. The impact of these uncertainties are discussed below.

11.2.1 Large GENIE uncertainties

The six largest uncertainties in the neutrino interaction modeling and there uncertainties are the following:

1. CC QE M_A $\pm^{+25\%}_{-15\%}$
2. CC RES M_A $\pm 20\%$
3. CC RES M_V $\pm 10\%$
4. NC RES M_A $\pm 20\%$
5. NC RES M_V $\pm 10\%$
6. NC elastic M_A $\pm 25\%$

Figures 11.3-11.8 show the individual systematic uncertainties due to the above six parameters.

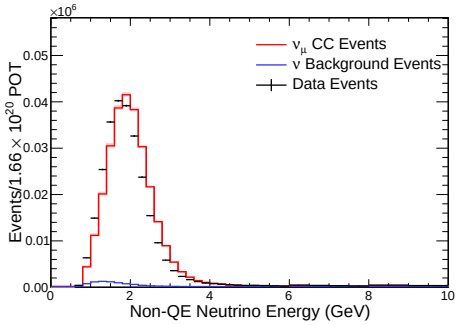

(a) Near Detector

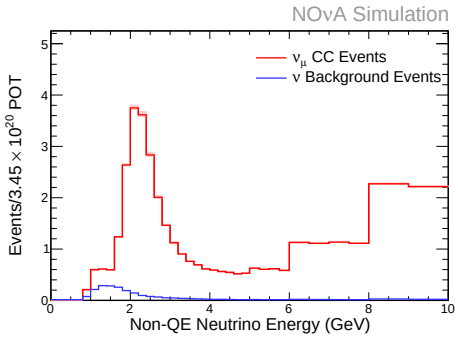

(b) Far Detector without Extrapolation

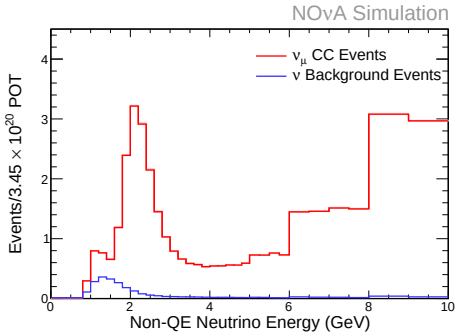

(c) Far Detector with Extrapolation

Figure 11.3: Reconstructed energy of selected events in the nonQE sample with the systematic error band from M_A CC QE. All selected simulated events are shown in red with the a red systematic error band. The contribution to the selected events from background in the simulation is shown in blue. For the near detector the data is drawn in black with statistical error bars. For the far detector the oscillation parameters listed in table 2.1 are assumed.

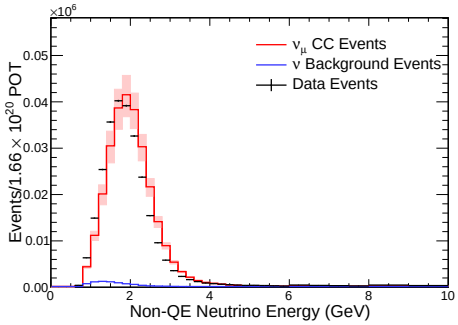

(a) Near Detector

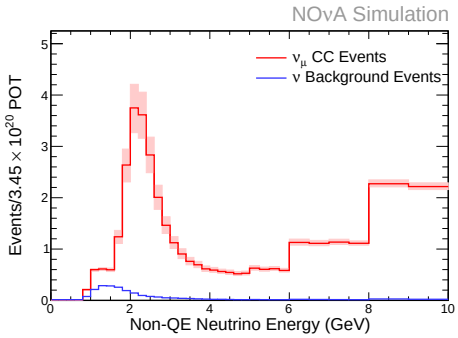

(b) Far Detector without Extrapolation

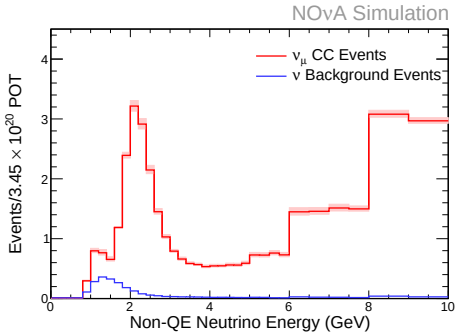

(c) Far Detector with Extrapolation

Figure 11.4: Reconstructed energy of selected events in the nonQE sample with the systematic error band from M_A CC RES. All selected simulated events are shown in red with the a red systematic error band. The contribution to the selected events from background in the simulation is shown in blue. For the near detector the data is drawn in black with statistical error bars. For the far detector the oscillation parameters listed in table 2.1 are assumed.

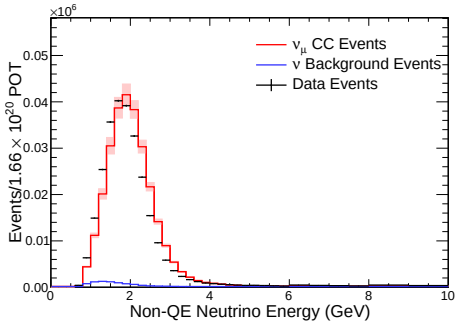

(a) Near Detector

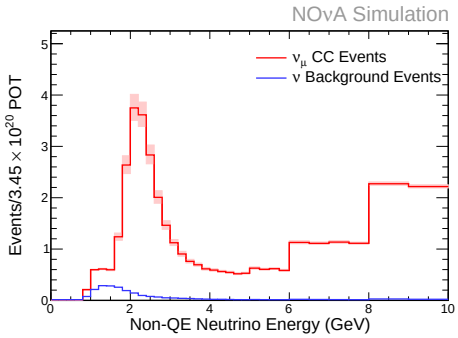

(b) Far Detector without Extrapolation

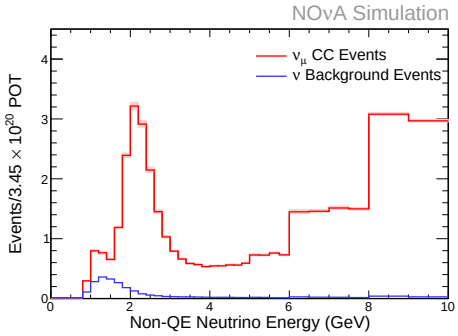

(c) Far Detector with Extrapolation

Figure 11.5: Reconstructed energy of selected events in the nonQE sample with the systematic error band from M_v CC RES. All selected simulated events are shown in red with the a red systematic error band. The contribution to the selected events from background in the simulation is shown in blue. For the near detector the data is drawn in black with statistical error bars. For the far detector the oscillation parameters listed in table 2.1 are assumed.

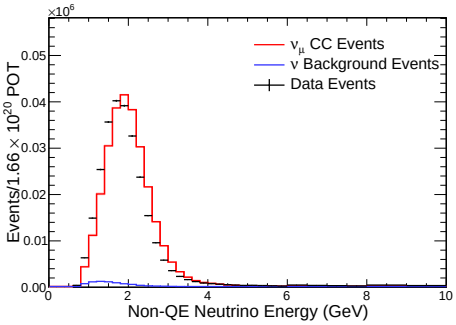

(a) Near Detector

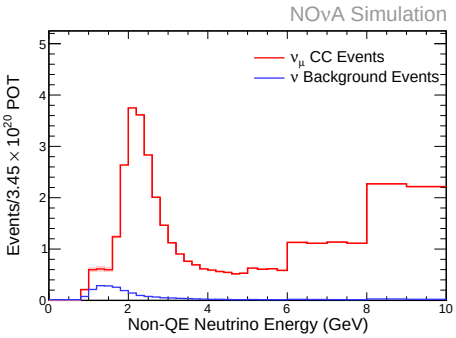

(b) Far Detector without Extrapolation

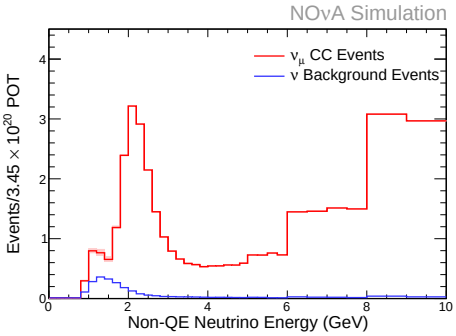

(c) Far Detector with Extrapolation

Figure 11.6: Reconstructed energy of selected events in the nonQE sample with the systematic error band from M_A NC RES. All selected simulated events are shown in red with the a red systematic error band. The contribution to the selected events from background in the simulation is shown in blue. For the near detector the data is drawn in black with statistical error bars. For the far detector the oscillation parameters listed in table 2.1 are assumed.

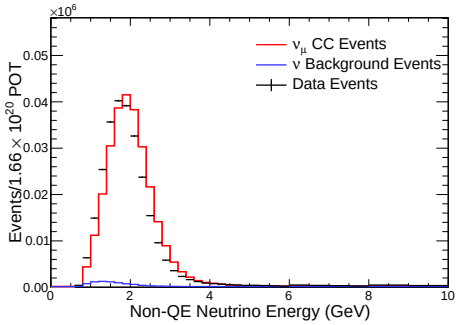

(a) Near Detector

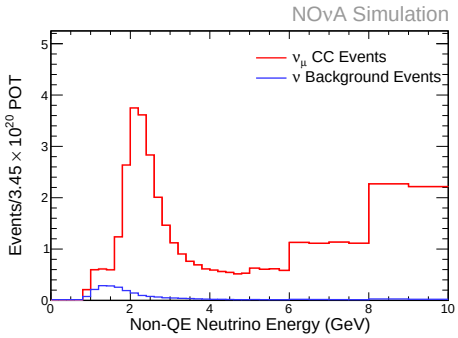

(b) Far Detector without Extrapolation

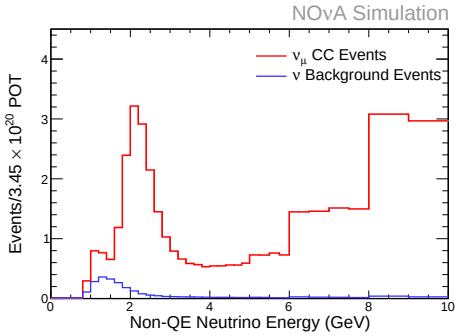

(c) Far Detector with Extrapolation

Figure 11.7: Reconstructed energy of selected events in the nonQE sample with the systematic error band from M_v NC RES. All selected simulated events are shown in red with the a red systematic error band. The contribution to the selected events from background in the simulation is shown in blue. For the near detector the data is drawn in black with statistical error bars. For the far detector the oscillation parameters listed in table 2.1 are assumed.

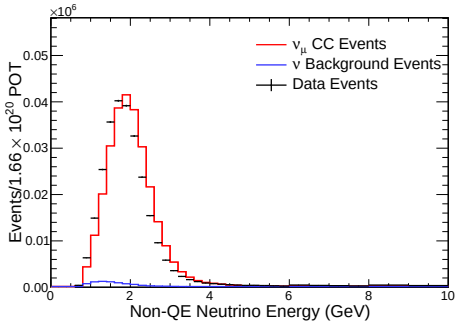

(a) Near Detector

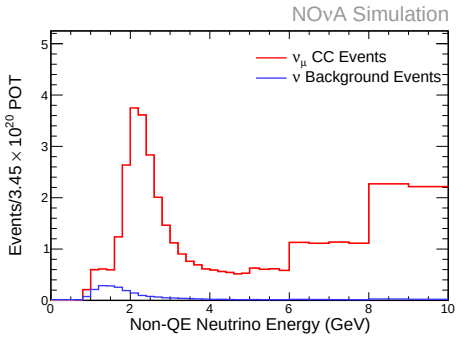

(b) Far Detector without Extrapolation

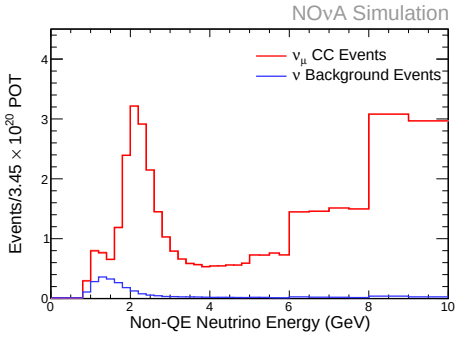

(c) Far Detector with Extrapolation

Figure 11.8: Reconstructed energy of selected events in the nonQE sample with the systematic error band from M_A NC elastic. All selected simulated events are shown in red with the a red systematic error band. The contribution to the selected events from background in the simulation is shown in blue. For the near detector the data is drawn in black with statistical error bars. For the far detector the oscillation parameters listed in table 2.1 are assumed.

11.2.2 Small GENIE uncertainties

The remaining neutrino interaction uncertainties were combined into one systematic uncertainty using the same method was used to combine the beam uncertainties. The shifts that make up the total uncertainty are:

1. NC elastic strange axial form factor η $\pm 30\%$
2. CC QE Pauli suppression $\pm 35\%$
3. BBA05 or Dipole CC QE vector form factor
4. CC and NC M_A $\pm 50\%$
5. Nuclear size parameter controlling pion absorption in Rein-Sehgal model $\pm 10\%$
6. Non-resonance background in νp CC 1π reactions $\pm 50\%$
7. Non-resonance background in νp CC 2π reactions $\pm 50\%$
8. Non-resonance background in νn CC 1π reactions $\pm 50\%$
9. Non-resonance background in νn CC 2π reactions $\pm 50\%$
10. Non-resonance background in νp NC 1π reactions $\pm 50\%$
11. Non-resonance background in νp NC 2π reactions $\pm 50\%$
12. Non-resonance background in νn NC 1π reactions $\pm 50\%$
13. Non-resonance background in νn NC 2π reactions $\pm 50\%$
14. A_{HT} higher-twist parameter in Bodek-Yang model scaling variable ξ $\pm 25\%$
15. B_{HT} higher-twist parameter in Bodek-Yang model scaling variable ξ $\pm 25\%$
16. C_{V1u} u valence GRV98 PDF correction parameter in Bodek-Yang model $\pm 30\%$
17. C_{V2u} u valence GRV98 PDF correction parameter in Bodek-Yang model $\pm 40\%$
18. Inclusive CC DIS cross-section normalization factor

19. $\frac{\bar{\nu}}{\nu}$ CC ratio
20. DIS nuclear modification (shadowing, anti-shadowing, EMC)
21. Pion transverse momentum for $N\pi$ states in AGKY
22. Pion Feynman x for $N\pi$ states in AGKY
23. Hadron formation zone ±50%
24. Isotropic or Rein-Sehgal pion angular distribution in $\Delta \to N\pi$
25. Branching ratio for radiative resonance decays ±50%
26. Branching ratio for single η resonance decays ±50%
27. Nucleon mean free path ±20%
28. Nucleon charge exchange probability ±50%
29. Nucleon elastic reaction probability ±30%
30. Nucleon inelastic reaction probability ±40%
31. Nucleon absorption probability ±20%
32. Nucleon-pion production probability ±20%
33. Pion mean free path ±20%
34. Pion charge exchange probability ±50%
35. Pion elastic reaction probability ±10%
36. Pion inelastic reaction probability ±40%
37. Pion absorption probability ±20%
38. Pion-pion production probability ±20%

The total uncertainty from these shifts is shown in figure 11.9.

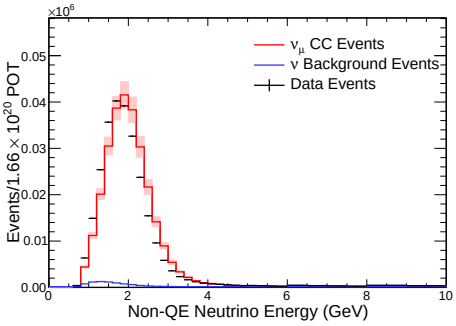

(a) Near Detector

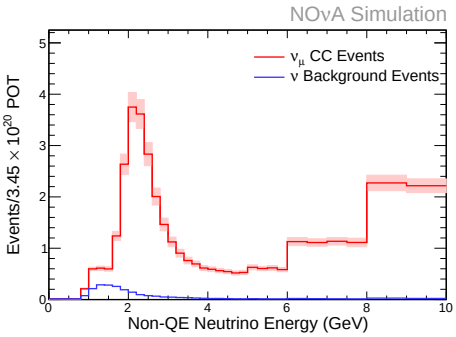

(b) Far Detector without Extrapolation

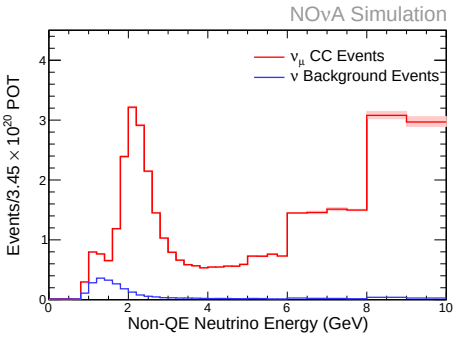

(c) Far Detector with Extrapolation

Figure 11.9: Reconstructed energy of selected events in the nonQE sample with the systematic error band from the small GENIE uncertainties. All selected simulated events are shown in red with the a red systematic error band. The contribution to the selected events from background in the simulation is shown in blue. For the near detector the data is drawn in black with statistical error bars. For the far detector the oscillation parameters listed in table 2.1 are assumed.

11.3 Detector Mass

Uncertainty in the normalization of the number of events in the detector comes in two forms, absolute and relative. The absolute normalization is common to both the near and far detectors where as the relative uncertainty accounts for the differences in event counts between the two detectors. Normalization uncertainties are dominated by the mass uncertainty in the fiducial volume of the detector and the mass modeling in the simulated detector. The total uncertainty from these shifts is shown in figure 11.10.

11.3.1 Absolute Normalization

The mass uncertainty of the constructed detectors was found to be 0.7% from the uncertainty of the mass of the basic components that make up the detector: PVC, scintillator, glue, and fiber[80]. Additionally there is a 0.82% uncertainty introduced from the difference between the simulated mass of the detectors compared to the as built detector[81]. Adding these uncertainties together in quadrature results in a total uncertainty of 1.08% in the absolute number of selected events in both the near and far detector. The total uncertainty from these shifts is shown in figure 11.11.

11.3.2 Relative Normalization

In addition to the mass difference mis-modeling between the as built and simulated detector mass, there is an additional difference between the simulated far and near detector mass. This difference arises from a 0.6 mm difference in the extrusion widths used in the far and near detectors and results in a 0.5% uncertainty in the number of selected events in one detector compared to the other[81].

11.3.3 Muon Energy Scale

The muon energy is determined from the length of the reconstructed muon track. Mis-modeling of the detector mass provides a potential source through which systematic uncertainty in the muon length and hence energy can arise. A study propagating this uncertainty through the entire analysis showed that this had negligible effects on the analysis [82] and is not considered in this analysis.

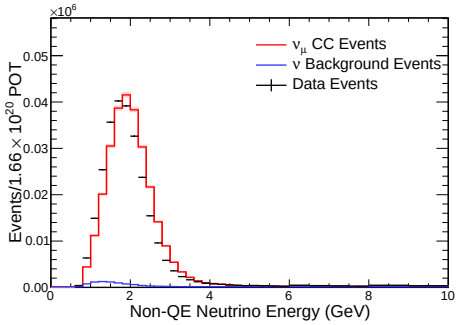

(a) Near Detector

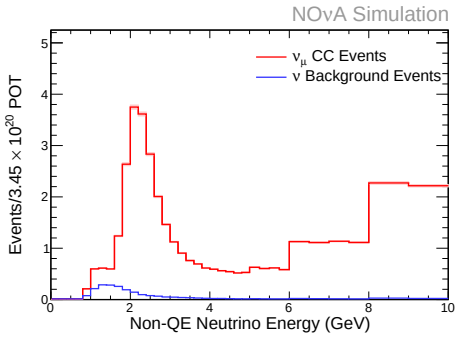

(b) Far Detector without Extrapolation

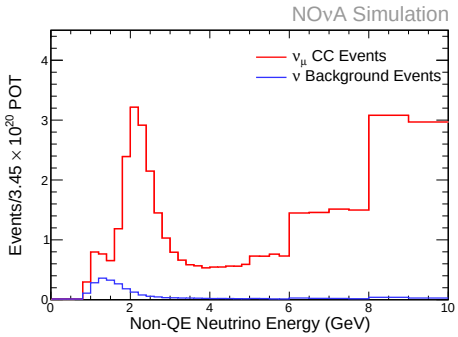

(c) Far Detector with Extrapolation

Figure 11.10: Reconstructed energy of selected events in the nonQE sample with the systematic error band from the absolute normalization uncertainty. All selected simulated events are shown in red with the a red systematic error band. The contribution to the selected events from background in the simulation is shown in blue. For the near detector the data is drawn in black with statistical error bars. For the far detector the oscillation parameters listed in table 2.1 are assumed.

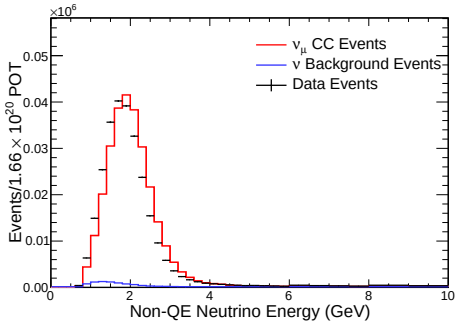

(a) Near Detector

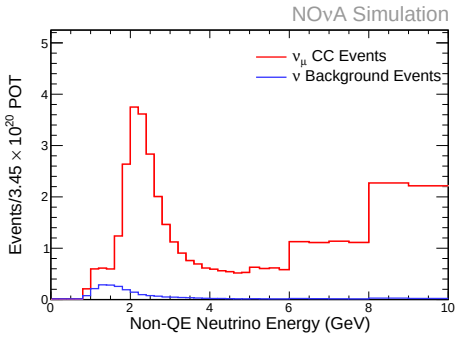

(b) Far Detector without Extrapolation

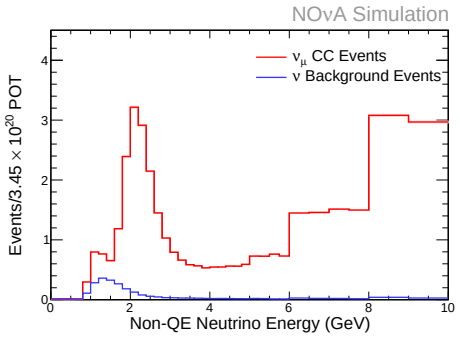

(c) Far Detector with Extrapolation

Figure 11.11: Reconstructed energy of selected events in the nonQE sample with the systematic error band from the relative normalization uncertainty. All selected simulated events are shown in red with the a red systematic error band. The contribution to the selected events from background in the simulation is shown in blue. For the near detector the data is drawn in black with statistical error bars. For the far detector the oscillation parameters listed in table 2.1 are assumed.

11.4 POT Accounting

Besides the uncertainties in the mass, uncertainties in the total number of POT can lead to normalization uncertainties. Additionally, because the datasets used in both near and far detector do not include only runs in which both the near and far detector are taking data, any time dependent uncertainties in the POT accounting could lead to a normalization uncertainty. The POT for this analysis was obtained from the fermilab accelerator division who record how many POT were delivered to the target in each beam spill. A study to examine the reliability of the POT recording procedure and its stability determined that the POT accounting was accurate to better than 0.5% and has been neglected [83].

11.5 Calibration

11.5.1 Absolute Energy Scale

The calibration procedure described in chapter 5 determines the absolute energy scale that converts the attenuation corrected light signal measured in the cells to an energy deposited in the scintillator of the cell. There exists uncertainty in how well the absolute energy scale determined by this procedure. Studies looking at sources with well known energy deposition profiles such as muons in the near detector from the neutrino interactions [84], the reconstructed π° mass in the near detector [85], and Michel electrons in the near and far detectors [86] show that a $\sim$5% uncertainty exists in the absolute energy scale determined by the detector calibration. Any uncertainty in the absolute energy scale could effect the performance of the ν_{μ} CC selection as well as the estimation of hadronic energy of selected events. The uncertainty on this analysis was determined by performing the analysis in simulated data with a shift in the absolute energy scale of $\pm$5% in both the near and far detector independently. The shifted samples were compared to the nominal simulation and the uncertainty was determined as a shift in the peak of the reconstructed energy and a normalization difference in the selected events in each bin of reconstructed energy. Figures 11.12 and 11.13 show the affect of the uncertainty in the near and far detectors respectively.

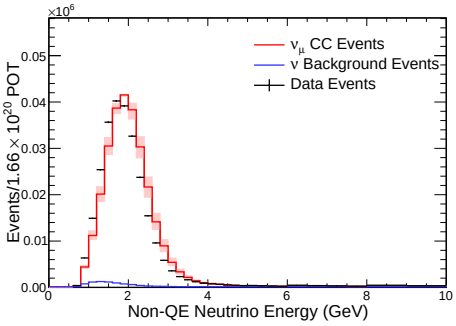

(a) Near Detector

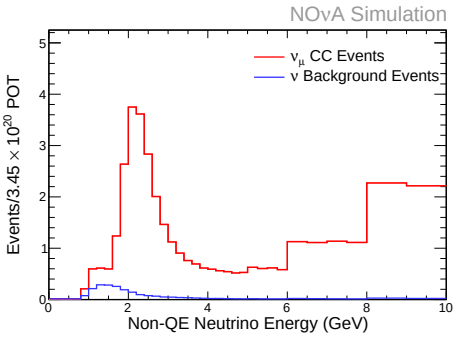

(b) Far Detector without Extrapolation

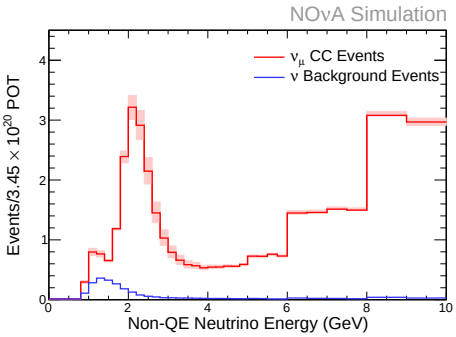

(c) Far Detector with Extrapolation

Figure 11.12: Reconstructed energy of selected events in the nonQE sample with the systematic error band from the absolute energy uncertainty in the near detector. All selected simulated events are shown in red with the a red systematic error band. The contribution to the selected events from background in the simulation is shown in blue. For the near detector the data is drawn in black with statistical error bars. For the far detector the oscillation parameters listed in table 2.1 are assumed.

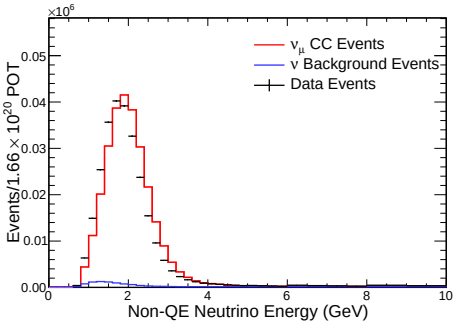

(a) Near Detector

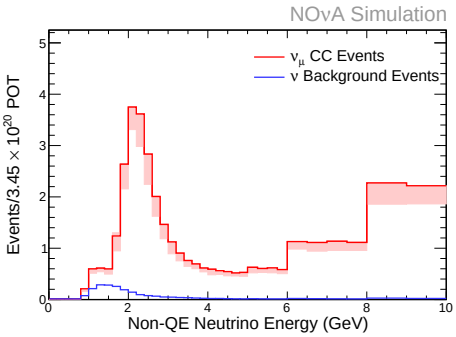

(b) Far Detector without Extrapolation

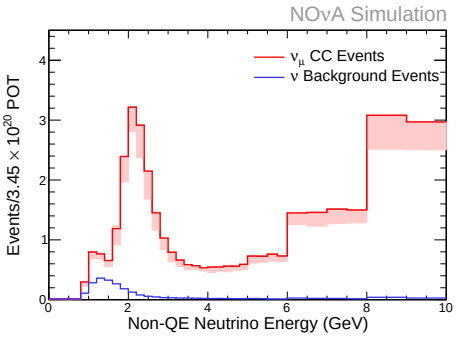

(c) Far Detector with Extrapolation

Figure 11.13: Reconstructed energy of selected events in the nonQE sample with the systematic error band from the absolute energy uncertainty in the far detector. All selected simulated events are shown in red with the a red systematic error band. The contribution to the selected events from background in the simulation is shown in blue. For the near detector the data is drawn in black with statistical error bars. For the far detector the oscillation parameters listed in table 2.1 are assumed.

11.5.2 Uniform Simulation Calibration

For ease of computation all of the horizontal cells and all of the vertical cells are modeled with the same response in the simulation. This is certainly not the case in the as built detector in which some cells will have higher of lower responses for the same deposited energy. This effect should be accounted for in the cell by cell calibration procedure. However to determine if a systematic uncertainty is introduced by this modeling a simulation was created in which the calibration was randomly shifted so that the width of the distribution of the calibrated energy among detector cells in the simulation matched that seen in data. The alternative simulation was compared to the nominal simulation and was determined to have no impact on the analysis [87].

11.5.3 Thresholds

The modeling of readout thresholds in the simulation effects the simulation calibration procedure and introduces a relationship between the calibrated energy and the distance along the cell length from the readout. Any mis-modeling of the thresholds could introduce a difference in the simulation and data. In the nominal simulation a difference of up to 20% in the calibrated energy at the far end of a cell in the far detector exists. In order to estimate the significance of this affect an alternative simulation was generated in which the calibrated detector response as a function of the distance from the readout was made to match the data was generated and compared to the nominal simulation. The difference seen was small compared to the overall calibration uncertainties in the near and far detectors and differences in reconstructed neutrino energies seen in the near detector and is not included in the total systematic error [87].

11.6 Alignment

The simulated detector geometry is based off of bulk measurements of the built detector. These measurements determine the average stagger and orientation of the planes relative between plane in the detector as well as the overall positioning of the detector. However, precise position information of each individual cell is not used. This can effect the outcome of the analysis as the ν_μ CC selection relies on scattering information along the

reconstructed track and the muon energy relies on the total length of the reconstructed track. In order to assess the systematic uncertainty due to the misalignment of the cells in the simulation compared to the real detector, an analysis was performed in which the simulation assumed a certain geometry in the generation of the neutrino interactions, but then used a shifted geometry for the reconstruction and analysis [88]. The shifted geometry was differed from the geometry used in the generation by the maximum deviations expected from the bulk measurements to the precise alignment positioning of cells in the detector. Comparing the analysis using the shifted geometry to an analysis using the same geometry as the interaction where generated in showed negligible differences.

11.7 Bad Channels

In the reconstruction procedure some channels are determined to be bad and the data from these channels are not used. A channel is determined to be bad if it records excessive noise, too little activity, or it can not be calibrated. These are indications that the channel is not behaving as expected and the results from the channel are unreliable. Bad channels are determined on a subrun by subrun basis from the cosmic trigger data and a mask is determined to remove suspect channels. On average less than 4% of all channels are found to be bad at any given time. This process of determining bad channels could affect the analysis. Its impact was determined by applying a random bad channel mask on simulation at the worst level of bad channels seen in the data and comparing the results to the nominal simulation. From this study it was determined that mis determination of bad channels has no impact on the analysis [89].

11.8 Hadronic Modeling

11.8.1 GEANT4 Particle Propagation

GEANT4 is used to model the propagation of particles through the NOνA detectors. Incorrectly modeling particle energy loss could result in systematic errors in the event selection and reconstructed energies. Systematic modeling errors are more likely to impact hadronic energy loss as electromagnetic energy loss processes are more accurately

modeled. GEANT4 configures the particle energy loss through a physics list which defines the models used for energy loss.

To determine the systematic effect from particle propagation errors simulations using several different physics lists were generated and compared to the near detector data [90]. The standard physics list used for the simulation is QGSP_BERT_HP. Three additional physics lists were used for comparison. The first, QGSP_BIC_HP, replaces the Bertini cascade process used in the nominal simulation for primary proton and neutron propagation below 10 GeV with the Binary cascade model. The second, QGSC_BERT, does not use the high precision neutron simulation used in the nominal simulation and used the chiral invariant phase space model instead of the G4Precompound model to simulate nuclei de-excitation. The third, FTF_BIC, does not use a high precision neutron model, replaces the Bertini cascade model with the Binary cascade model, and uses the FRITIOF description of string excitation and fragmentation to model high energy interactions of pions, kaons, protons, neutrons, and nuclei.

The result of changing the propagation models used by GEANT4 showed that the mean value of the peak of reconstructed neutrino energy in NonQE events shifts by 0.5% and the overall normalization of the selected events changes by 1%. These shifts account for only a small fraction of the discrepancies between the data and simulation seen in the near detector data. Instead a data-driven approach to the hadronic modeling systematic, described in section 11.8.3, is used to quantify the hadronic modeling systematic. The data-driven systematic also overlaps with the effects that would be encompassed by the particle propagation systematic described here so that systematic uncertainties in the modeling particle propagation are neglected.

11.8.2 Birks' Law

Charge particles traveling though liquid scintillator can quench the scintillator resulting in a nonlinear relationship between the energy loss of the particle and the light produced in the scintillator. This process is described by an empirical relationship known as Birks' Law which is parameterized by two constants, Birks' and Chou's constants, that are a property of the scintillator. These constants where measured in the NOνA scintillator and found to approximately four times larger than similar scintillator blends used by other experiments. In order to determine any systematic error induced by the incorrect

values of Birks' and Chou's constants used two alternative simulations with constants near other experiments measured for the constants. These alternative simulations were compared to the nominal simulation and a shift in the mean value of the peak of reconstructed neutrino energy in NonQE events shifts by 0.5% and the overall normalization of the selected events changes by 2% was observed [91]. Like the particle propagation systematic, the uncertainty from Birks' Law accounts for a negligible amount of the hadronic energy discrepancy and is double counted by a data driven systematic and is neglected.

11.8.3 Number of Hadronic Hits

Many investigations were undertaken to determine the source or sources of discrepancy between the number of hadronic hits seen in the data and simulation from both detector response and physics modeling uncertainties. However no one or combination of uncertainties results in accounting for even the majority of the discrepancy. Additionally the uncertainties induced were not able to both produce the shift in the reconstructed neutrino events and fix the discrepancy between the proportion of NonQE and QE events seen. Subsequently in order to account for the systematic uncertainty in hadronic modeling a data driven approach was taken.

The uncertainty in modeling of the hadronic system of the neutrino interactions is determined by the difference between data and simulation of the hadronic system of neutrino interactions in the near detector. This mis-modeling is evident in the difference in the number of hits produced by the hadronic system as seen in figure 9.29. The simulation shows a 30% increase in the number of hits coming from the hadronic system. The energy per hadronic hit is consistent between data and simulation, to within calibration uncertainties, as seen in figure 9.32. In order to estimate the systematic uncertainty induced because of the hadronic modeling of the a simulation was created in a random 30% of the hadronic hits in each reconstructed slice is removed. This simulation was compared to the nominal simulation and the uncertainty was determined as the shift in the peak of the reconstructed energy and a normalization difference in the selected events in each bin of reconstructed energy for each selection sample. Figures 11.14-11.18 show the distributions of reconstructed neutrino energy, number of hadronic hits, and event selection distributions for this simulation and show that this alternative

simulation covers the difference between the data and simulation seen in the nominal simulation. Appendix C show additional figures comparing the alternative simulation and the near detector data and show that this data driven simulation still accurately describes the features seen in near detector neutrino interactions.

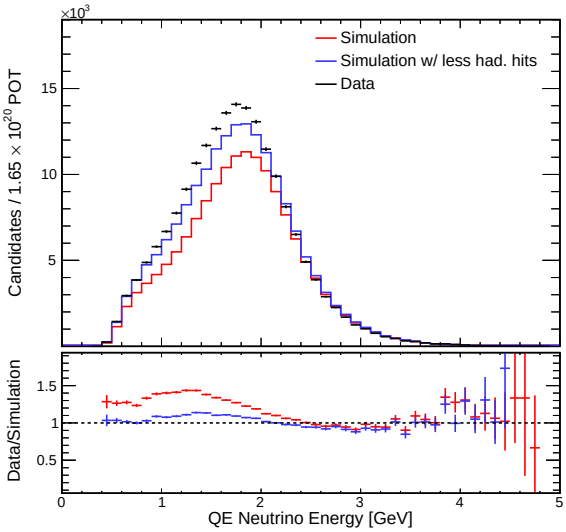

Figure 11.14: Energy spectrum of QE selected events.

The hadronic modeling uncertainty determined in this manner can not be attributed to a specific effect. This makes it impossible to determine if the effect would be the same in both the near and far detectors or could be a relative systematic error between them. As such this systematic is applied conservatively as a relative systematic between each detector and is determined as a shift in the peak of reconstructed neutrino energy and an energy dependent normalization scaling. While this method likely does not describe the precise mechanism in which the data differs in number of hadronic hits from the simulation it does model the effect of the discrepancy in the modeling independent of the cause. Figures 11.19 and 11.20 show the affect of the uncertainty in the near and far detectors respectively.

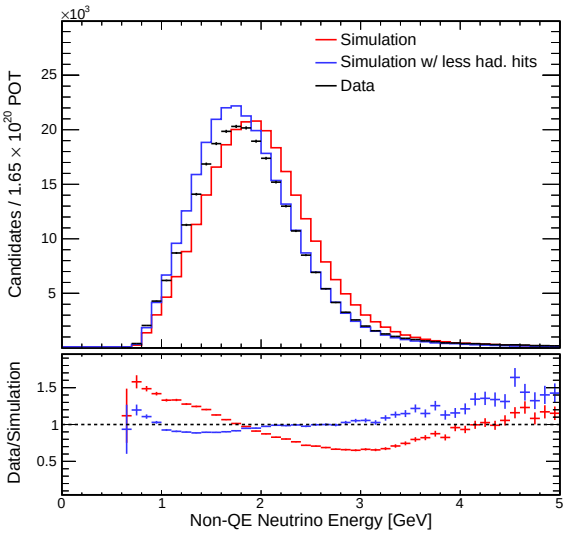

Figure 11.15: Energy spectrum of Non-QE selected events.

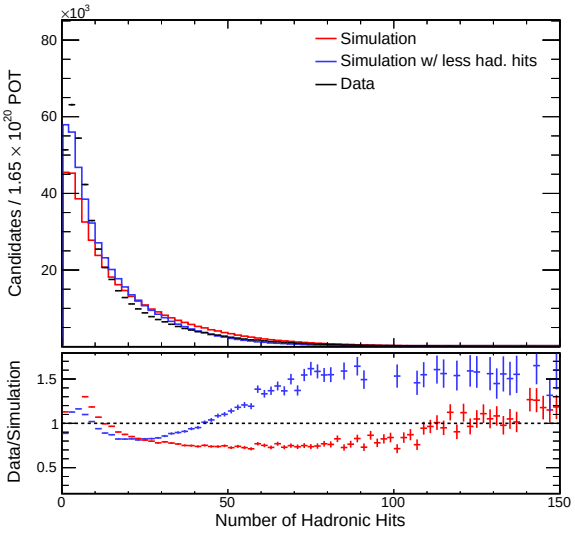

Figure 11.16: Number of hadronic hits in contained slices passing ν_μ CC selection.

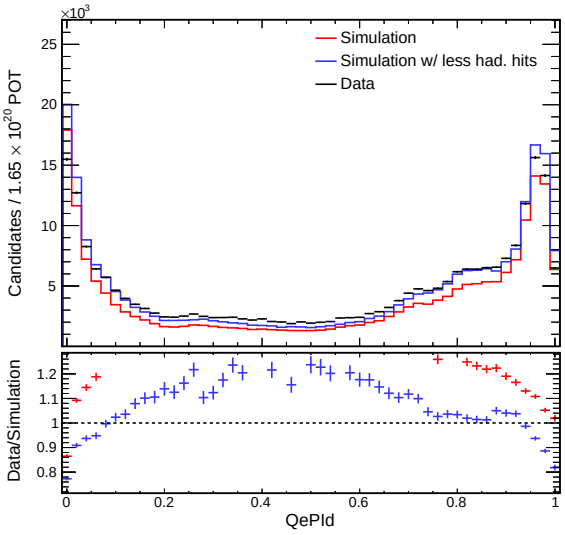

Figure 11.17: QePID distribution in contained slices passing ν_μ CC selection with one reconstructed track.

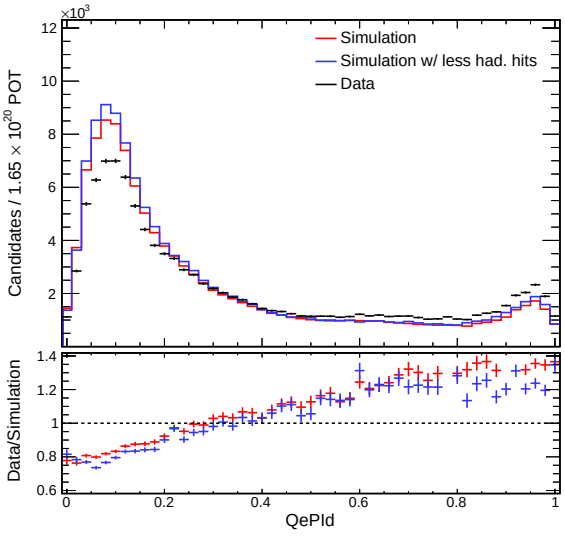

Figure 11.18: QePID distribution in contained slices passing ν_μ CC selection with two reconstructed track.

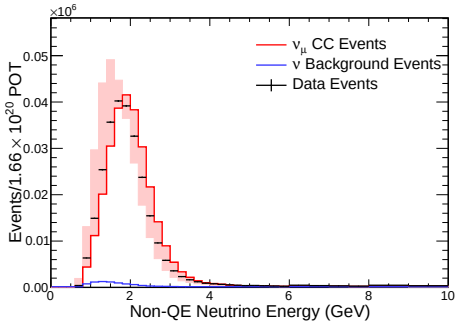

(a) Near Detector

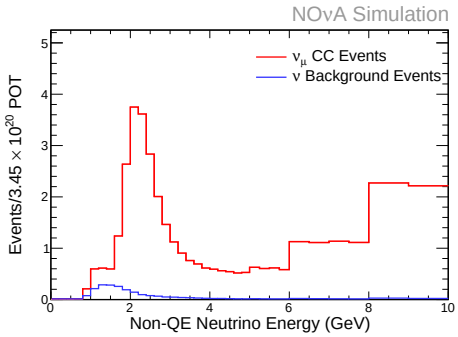

(b) Far Detector without Extrapolation

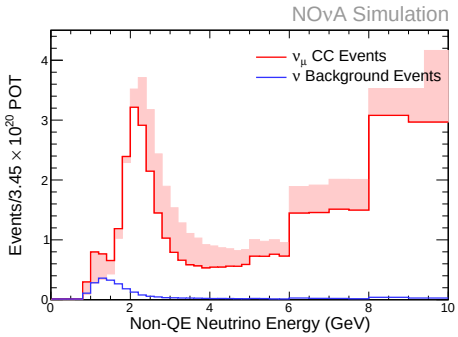

(c) Far Detector with Extrapolation

Figure 11.19: Reconstructed energy of selected events in the nonQE sample with the systematic error band from the hadronic modeling uncertainty in the near detector. All selected simulated events are shown in red with the a red systematic error band. The contribution to the selected events from background in the simulation is shown in blue. For the near detector the data is drawn in black with statistical error bars. For the far detector the oscillation parameters listed in table 2.1 are assumed.

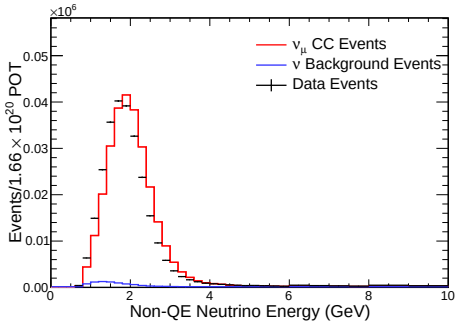

(a) Near Detector

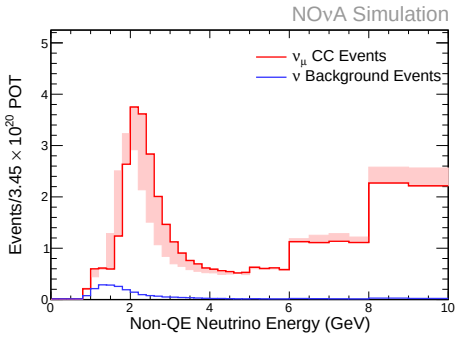

(b) Far Detector without Extrapolation

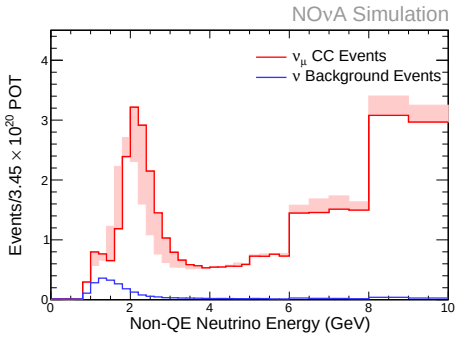

(c) Far Detector with Extrapolation

Figure 11.20: Reconstructed energy of selected events in the nonQE sample with the systematic error band from the hadronic modeling uncertainty in the far detector. All selected simulated events are shown in red with the a red systematic error band. The contribution to the selected events from background in the simulation is shown in blue. For the near detector the data is drawn in black with statistical error bars. For the far detector the oscillation parameters listed in table 2.1 are assumed.

11.9 Total Systematics

The total systematic error in the analysis is determined from contributions from the individual sources of error discussed in this chapter. The largest contributors to the systematic error are the hadronic modeling, absolute energy, and beam uncertainties. Figures 11.21-11.23 show the total systematic errors in the three samples used in this analysis.

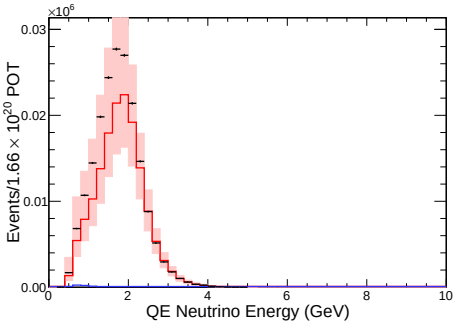

(a) Near Detector

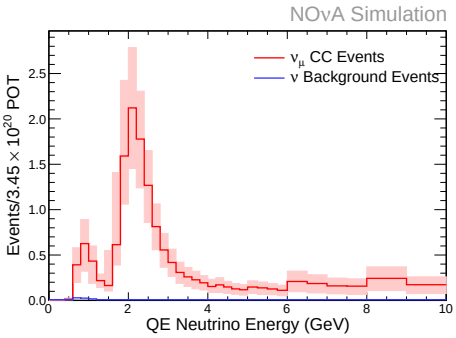

(b) Far Detector without Extrapolation

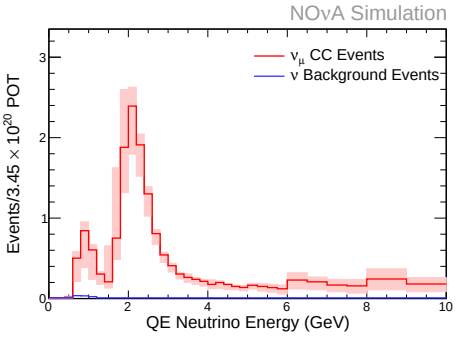

(c) Far Detector with Extrapolation

Figure 11.21: Reconstructed energy of selected events in the QE sample with the total systematic error band. All selected simulated events are shown in red with the a red systematic error band. The contribution to the selected events from background in the simulation is shown in blue. For the near detector the data is drawn in black with statistical error bars. For the far detector the oscillation parameters listed in table 2.1 are assumed.

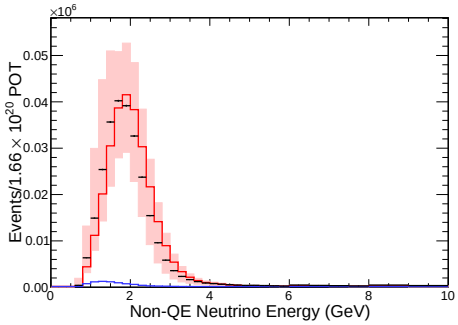

(a) Near Detector

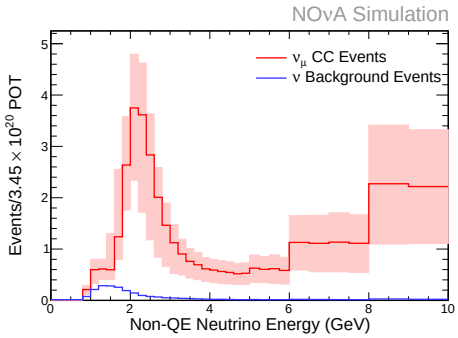

(b) Far Detector without Extrapolation

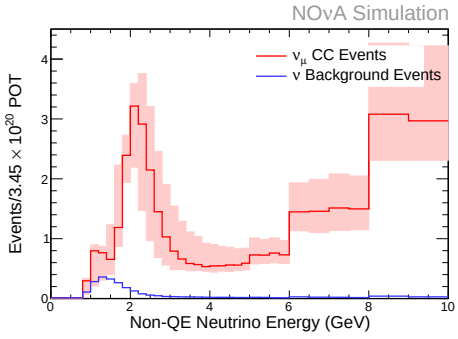

(c) Far Detector with Extrapolation

Figure 11.22: Reconstructed energy of selected events in the nonQE sample with the total systematic error band. All selected simulated events are shown in red with the a red systematic error band. The contribution to the selected events from background in the simulation is shown in blue. For the near detector the data is drawn in black with statistical error bars. For the far detector the oscillation parameters listed in table 2.1 are assumed.

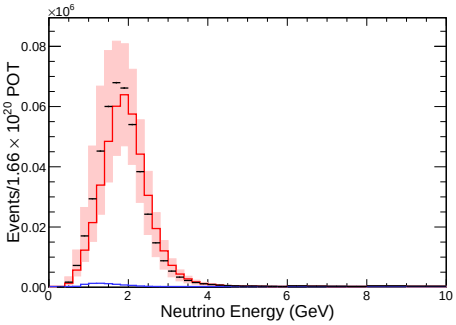

(a) Near Detector

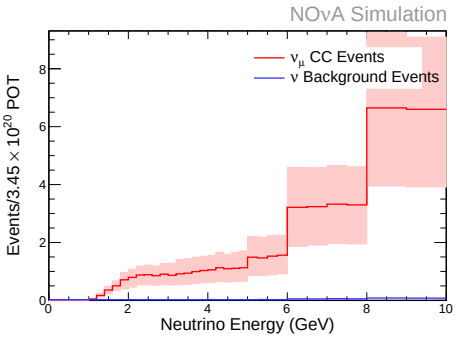

(b) Far Detector without Extrapolation

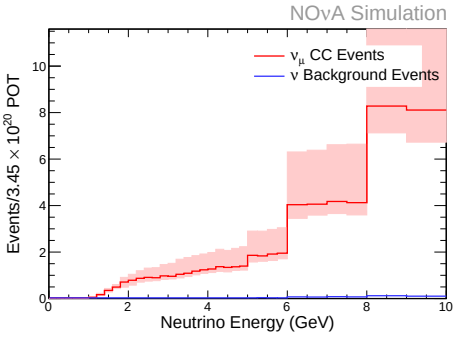

(c) Far Detector with Extrapolation

Figure 11.23: Reconstructed energy of selected events in the escaping sample with the total systematic error band. All selected simulated events are shown in red with the a red systematic error band. The contribution to the selected events from background in the simulation is shown in blue. For the near detector the data is drawn in black with statistical error bars. For the far detector the oscillation parameters listed in table 2.1 are assumed.

Chapter 12

Results

The previous chapters detail the procedure for determining a prediction and its associated errors of the signal and background expected in the ν_μ disappearance analysis. These predictions are summarized in table 12.1 under two oscillation scenarios, no oscillations and the oscillation parameters listed in table 2.1.

Table 12.1: Predicted event count in the far detector under the oscillation parameters listed in table 2.1, Osc., and with no oscillations, No Osc.

	QE		NonQE		Escaping	
	Osc.	No Osc.	Osc.	No Osc.	Osc.	No Osc.
Signal	16.0	92.7	35.4	136.5	57.8	72.7
Stat	$\pm^{5.1}_{3.9}$	$\pm^{9.6}_{9.6}$	$\pm^{6.4}_{6.2}$	$\pm^{11.7}_{11.7}$	$\pm^{7.6}_{7.6}$	$\pm^{8.5}_{8.5}$
Syst	$\pm^{3.9}_{3.8}$	$\pm^{54.6}_{54.6}$	$\pm^{15.8}_{15.8}$	$\pm^{79.1}_{79.1}$	$\pm^{33.4}_{33.4}$	$\pm^{39.3}_{39.3}$
Background	0.8	0.8	4.9	4.9	10.1	10.1
Stat	$\pm^{2.2}_{0.7}$	$\pm^{2.2}_{0.7}$	$\pm^{2.9}_{1.6}$	$\pm^{2.9}_{1.6}$	$\pm^{4.3}_{3.1}$	$\pm^{4.3}_{3.1}$
Syst	$\pm^{0.0}_{0.0}$	$\pm^{0.0}_{0.0}$	$\pm^{0.4}_{0.4}$	$\pm^{0.4}_{0.4}$	$\pm^{0.7}_{0.7}$	$\pm^{0.8}_{0.8}$
Total	16.8	93.5	40.3	141.4	67.9	82.8
Stat	$\pm^{5.2}_{4.1}$	$\pm^{9.7}_{9.7}$	$\pm^{6.4}_{6.3}$	$\pm^{11.9}_{11.9}$	$\pm^{8.2}_{8.2}$	$\pm^{9.1}_{9.1}$
Syst	$\pm^{3.8}_{3.8}$	$\pm^{54.6}_{54.6}$	$\pm^{16.2}_{16.2}$	$\pm^{79.5}_{79.5}$	$\pm^{34.1}_{34.1}$	$\pm^{40.1}_{40.1}$

This chapter presents the results of applying the described analysis to the first analysis data collected in the NOνA experiment. Section 12.1 details the events measured

in the far detector data and section 12.2 describes the ν_μ oscillation parameter measurement.

12.1 Far Detector Events

This analysis observes 23 events in the QE sample, 25 events in the NonQE sample, and 66 events in the escaping sample in the far detector data. The details of the specific run, subrun, event, slice, time in the event, PID value, and energy of the measured events of the three samples are listed in tables 12.2-12.4. Example events from each of the three samples are shown in figures 12.1-12.3.

Table 12.2: Selected events in the QE sample in the far detector.

Run	Subrun	Event	Slice	Time [μs]	ReMId	Energy [GeV]
15028	18	124609	37	219.6	1.00	3.91
16382	53	302896	25	226.7	1.00	1.79
16751	11	45215	41	224.5	1.00	2.21
16895	49	88217	19	285.4	1.00	3.55
17953	38	256887	29	228.3	0.98	2.59
18302	37	413485	32	218.1	0.98	1.19
18464	40	546039	24	221.3	1.00	1.98
18529	41	542995	30	222.8	1.00	8.79
18571	3	50129	27	226.1	1.00	1.94
18639	10	141206	43	220.5	0.98	3.36
18653	16	219065	36	227.0	0.97	2.31
18756	37	597960	22	226.1	1.00	2.26
18862	51	820267	37	227.7	0.95	0.88
18963	15	229864	37	221.4.	1.00	1.77
19018	28	413004	39	228.0	1.00	5.27
19054	26	383867	34	220.8	0.98	3.75
19332	16	221786	44	221.7	1.00	3.96
19347	3	50163	34	218.9	0.73	0.65
19350	46	664010	29	218.4	0.98	1.41
19420	38	561111	32	225.0	1.00	2.62
19422	22	334692	34	226.7	1.00	2.77
19425	61	903289	26	220.6	1.00	1.86
19468	30	512430	25	227.2	1.00	2.33

Table 12.3: Selected events in the NonQE sample in the far detector.

Run	Subrun	Event	Slice	Time [μs]	ReMId	Energy [GeV]
14828	38	192569	32	226.1	1.00	2.76
15085	0	1746	19	228.3	1.00	4.22
15679	16	142934	19	287.5	0.82	1.41
15974	14	88744	15	287.6	0.82	2.14
16315	4	17937	36	286.6	1.00	2.83
16450	17	93029	39	289.6	0.80	2.07
16453	33	178062	37	292.1	0.93	1.38
16675	54	249520	26	221.0	0.75	0.81
16730	25	101478	31	220.5	1.00	3.32
18342	47	609061	34	226.4	0.98	2.10
18401	2	35501	34	225.7	0.75	1.48
18417	43	582977	30	226.0	0.81	0.96
18572	19	255330	24	226.8	0.95	1.80
18791	48	765587	29	224.9	1.00	2.80
19004	22	318354	37	225.8	1.00	2.73
19058	39	568646	29	222.9	1.00	1.99
19084	62	908450	22	221.9	1.00	3.92
19107	52	756898	32	225.9	0.78	1.32
19154	45	663979	30	228.1	0.73	0.89
19296	35	482441	19	223.1	0.92	1.55
19327	18	248695	22	220.0	0.86	1.08
19356	11	156460	34	220.5	0.98	1.64
19423	1	20137	36	220.3	1.00	2.23
19476	6	110767	25	221.9	1.00	1.75
19485	61	1068905	32	228.6	0.78	2.16

Table 12.4: Selected events in the escaping sample in the far detector.

Run	Subrun	Event	Slice	Time [μs]	ReMId	Energy [GeV]
14632	1	13191	9	284.5	1.00	6.61
14728	29	156142	20	227.5	1.00	8.45
15007	5	40276	15	227.8	0.73	5.67
15054	9	63228	21	219.6	1.00	8.44
15109	54	388395	22	224.8	0.86	3.00
15229	32	230717	17	224.5	1.00	5.99
15236	57	391855	29	226.9	1.00	4.76
15251	5	37574	21	289.3	1.00	9.74
15344	36	51539	19	223.0	0.88	5.80
15452	26	68613	18	225.3	0.97	3.84
15699	36	350628	16	221.3	1.00	5.96
16259	25	95673	18	219.5	0.98	7.66
16270	8	34539	15	223.3	1.00	5.78
16325	24	104993	37	288.5	1.00	9.93
16459	24	103585	22	222.5	1.00	4.28
16736	39	158778	30	227.4	0.95	1.76
16747	33	133545	30	227.6	0.96	3.00
16871	15	62053	27	286.7	1.00	8.42
16938	8	41677	36	226.6	1.00	3.67
16967	43	148397	24	224.5	1.00	8.24
17938	33	217367	27	219.9	0.75	1.19
17949	7	47824	39	228.7	0.98	8.19
18015	54	349942	31	219.7	0.97	5.94
18129	6	41981	16	222.4	1.00	8.39
18130	18	121702	28	225.2	1.00	6.62
18247	15	165544	31	223.2	0.95	7.13
18258	30	323510	26	227.3	1.00	9.23
18271	18	199625	42	224.5	1.00	6.45
18283	32	356769	36	223.8	0.78	4.06
18322	5	58439	37	227.4	1.00	7.25
18335	2	33280	44	225.9	1.00	8.35
18345	61	781674	28	221.3	1.00	5.19
18395	26	333743	38	225.3	1.00	9.26
18418	54	735825	25	220.8	1.00	5.69
18585	19	256146	42	225.7	1.00	7.35

Continued on next page

Continued from previous page						
Run	Subrun	Event	Slice	Time [μs]	ReMId	Energy [GeV]
18591	33	439769	34	224.4	1.00	8.11
18592	7	101286	29	223.1	1.00	7.51
18595	34	449603	26	219.7	1.00	5.64
18655	35	464336	31	228.1	1.00	3.53
18817	51	806469	26	226.4	1.00	7.18
18931	29	449762	30	220.2	1.00	3.20
18977	42	635744	36	220.1	1.00	9.69
18988	59	862975	28	225.8	1.00	9.53
18996	10	146648	24	226.6	1.00	5.67
19051	42	609771	34	228.8	1.00	2.83
19067	45	647572	30	220.7	1.00	9.16
19083	22	323577	41	227.6	0.97	9.37
19123	42	630747	23	221.9	0.96	7.68
19207	46	670155	36	222.8	0.97	6.57
19248	36	516830	36	221.0	1.00	9.53
19249	35	489053	28	225.4	1.00	7.13
19271	41	585502	37	224.1	0.98	6.61
19279	37	533637	28	221.3	1.00	1.99
19305	49	686631	27	220.1	1.00	6.39
19306	0	11575	33	226.0	1.00	5.78
19317	49	706081	30	219.7	1.00	1.53
19334	61	821626	37	219.6	1.00	7.40
19366	3	49166	26	222.6	0.88	5.04
19422	48	725272	39	220.7	1.00	9.58
19429	12	192912	43	224.9	1.00	7.14
19481	61	1082472	25	227.8	1.00	4.74
19497	28	425031	37	228.0	0.98	3.12
19521	40	697929	34	224.5	1.00	2.83
19524	2	45559	36	220.5	1.00	8.98
19580	49	826536	33	222.1	1.00	6.08
19586	52	873001	50	222.0	1.00	7.35

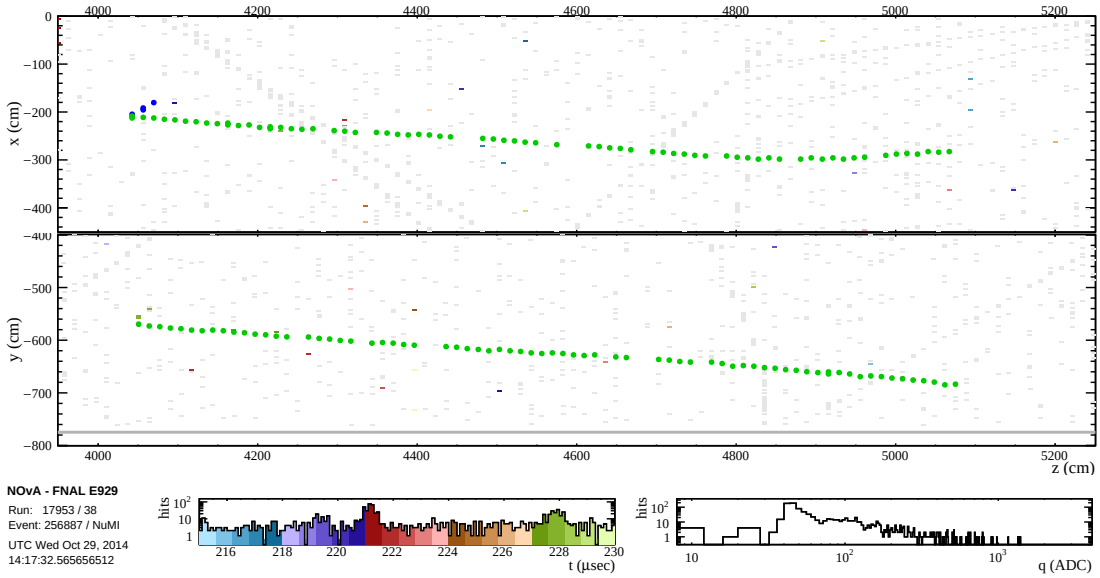

Figure 12.1: Event display of a selected QE event from run 17953 subrun 38 event 256887. Colored dots correspond to hits in reconstructed tracks. Hits in the readout not in the beam time window displayed are shown in gray. The display is zoomed in time and to the region of interest in the detector.

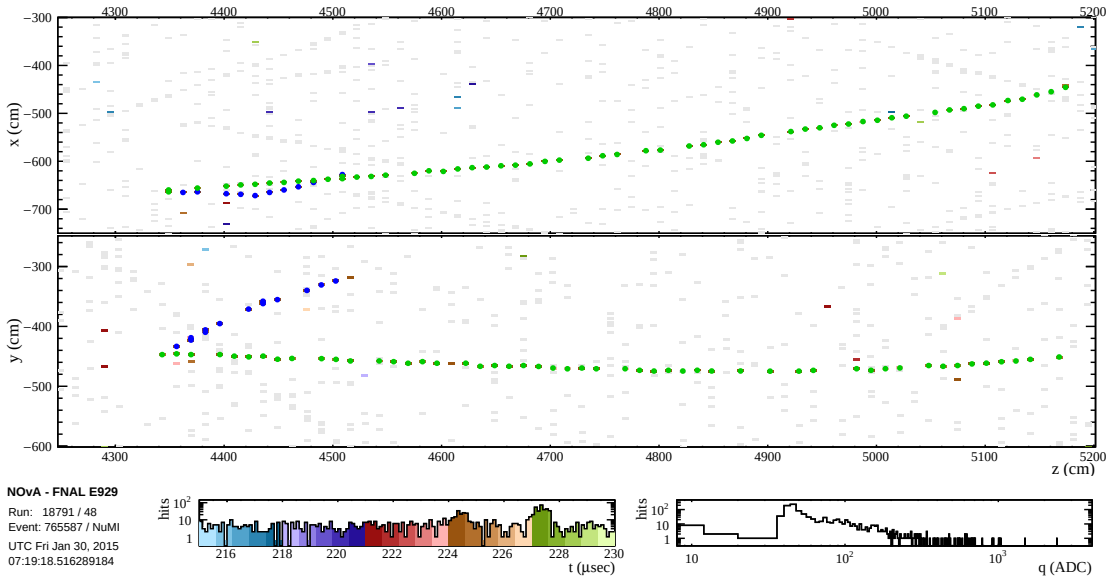

Figure 12.2: Event display of a selected NonQE event from run 18791 subrun 48 event 765587. Colored dots correspond to hits in reconstructed tracks. Hits in the readout not in the beam time window displayed are shown in gray. The display is zoomed in time and to the region of interest in the detector.

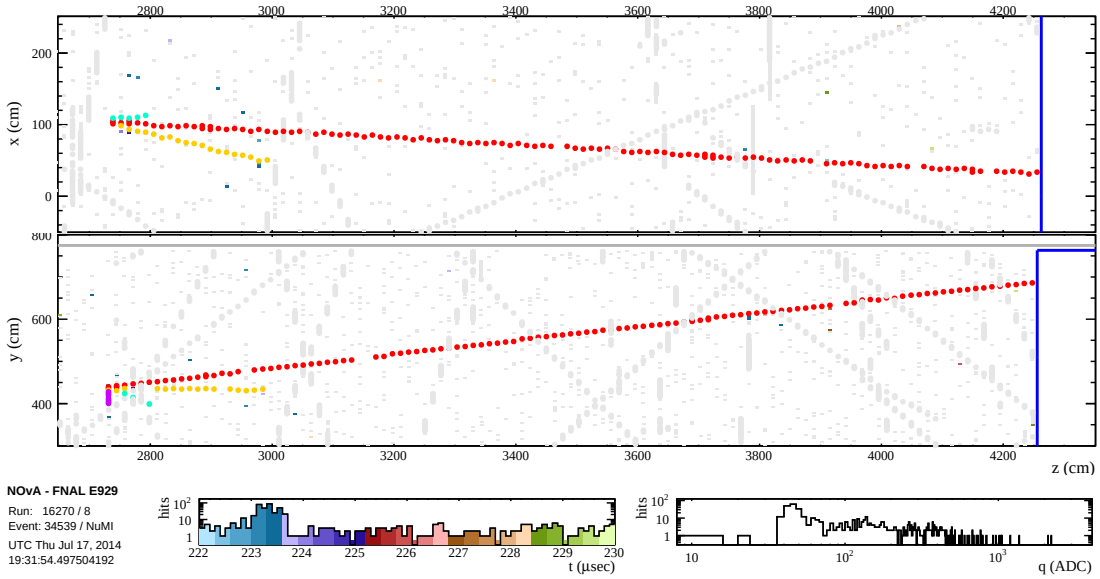

Figure 12.3: Event display of a selected escaping event from run 16270 subrun 8 event 34539. Colored dots correspond to hits in reconstructed tracks. Hits in the readout not in the beam time window displayed are shown in gray. The display is zoomed in time and to the region of interest in the detector. The blue line represents the end of the instrumented region of the detector.

Figures 12.4-12.42 compare the far detector data events to the expected results from the simulation for each of the three event samples used in this analysis. The simulation used for comparison uses the oscillation parameters listed in table 2.1 with the values $\sin^2\theta_{23} = 0.41$ and $\left|\Delta m^2_{32}\right| = 2.5 \times 10^{-3}$ eV^2 and is scaled down to the POT exposure seen in the far detector data. Figures 12.4-12.6 show the agreement of slice level variables, figures 12.7-12.30 show the agreement of tracking, and figures 12.31-12.42 show the agreement of PID and energy variables. For all distributions examined the data and simulation agree to the level of the statistical and systematic uncertainties present in the analysis.

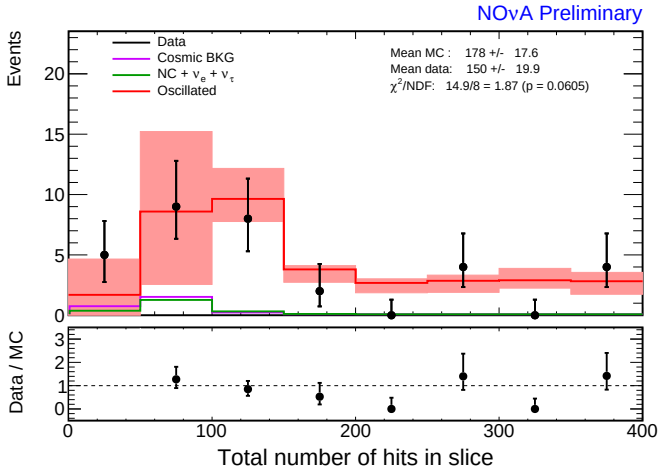

Figure 12.4: Total number of hits in the slice of selected non QE events in the far detector data. The prediction is drawn in red with the systematic errors shown in the error bands. The major sources of background are shown in magenta and green.

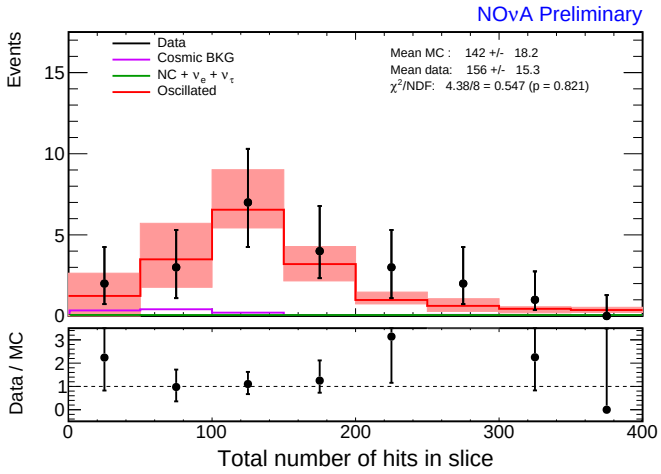

Figure 12.5: Total number of hits in the slice of selected QE events in the far detector data. The prediction is drawn in red with the systematic errors shown in the error bands. The major sources of background are shown in magenta and green.

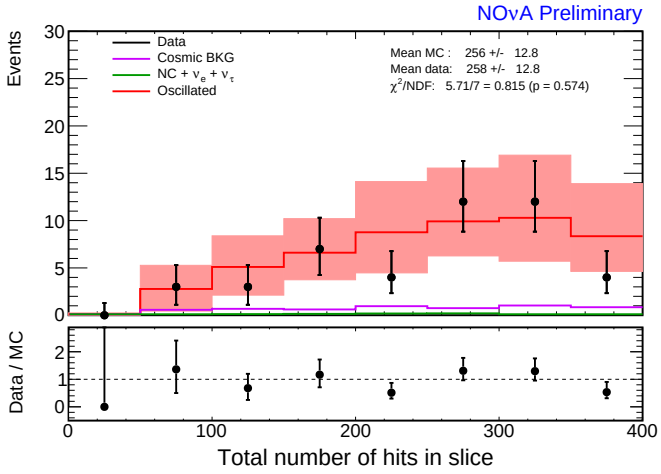

Figure 12.6: Total number of hits in the slice of selected escaping events in the far detector data. The prediction is drawn in red with the systematic errors shown in the error bands. The major sources of background are shown in magenta and green.

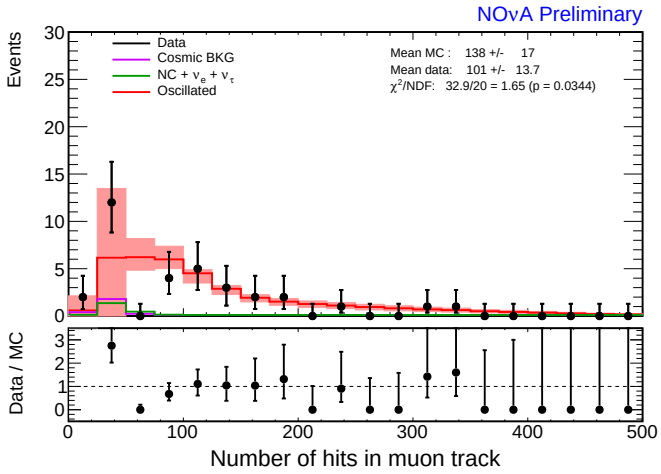

Figure 12.7: Total number of hits in the most muon like track in selected non QE events in the far detector data. The prediction is drawn in red with the systematic errors shown in the error bands. The major sources of background are shown in magenta and green.

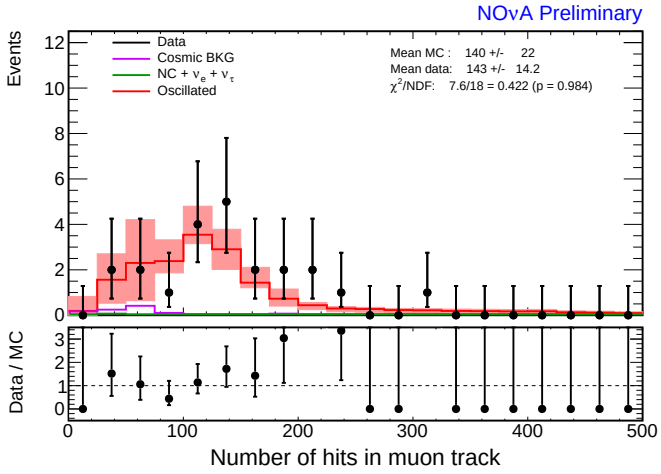

Figure 12.8: Total number of hits in the most muon like track in selected QE events in the far detector data. The prediction is drawn in red with the systematic errors shown in the error bands. The major sources of background are shown in magenta and green.

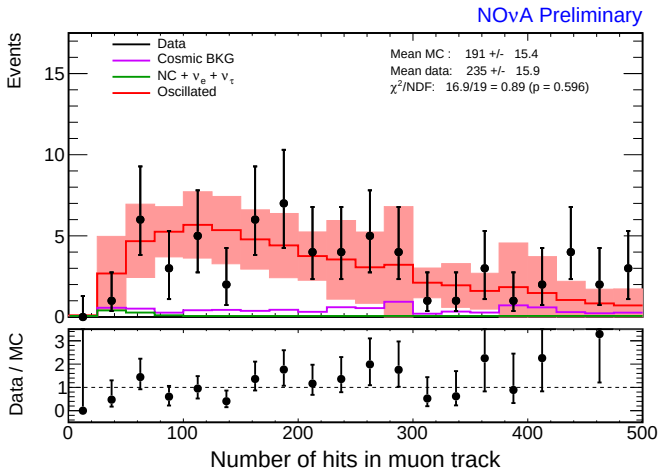

Figure 12.9: Total number of hits in the most muon like track in selected escaping events in the far detector data. The prediction is drawn in red with the systematic errors shown in the error bands. The major sources of background are shown in magenta and green.

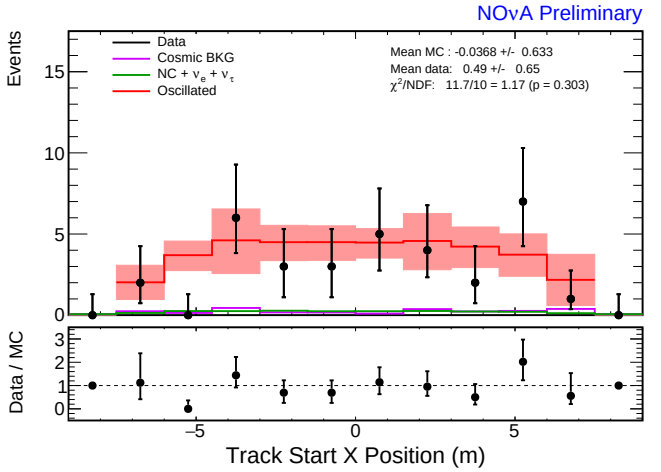

Figure 12.10: Track starting x position of the most muon like track in selected non QE events in the far detector data. The prediction is drawn in red with the systematic errors shown in the error bands. The major sources of background are shown in magenta and green.

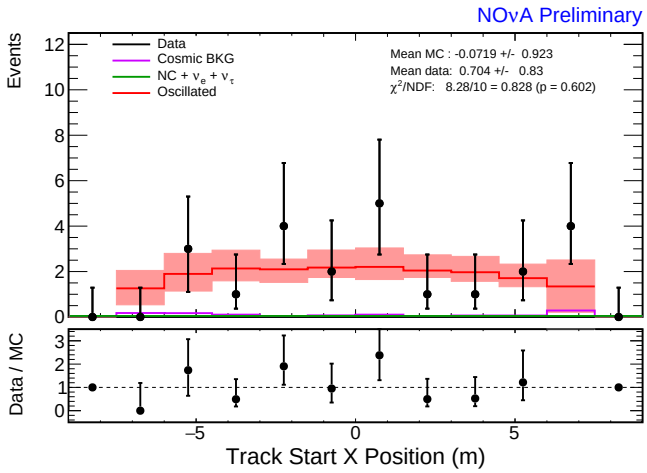

Figure 12.11: Track starting x position of the most muon like track in selected QE events in the far detector data. The prediction is drawn in red with the systematic errors shown in the error bands. The major sources of background are shown in magenta and green.

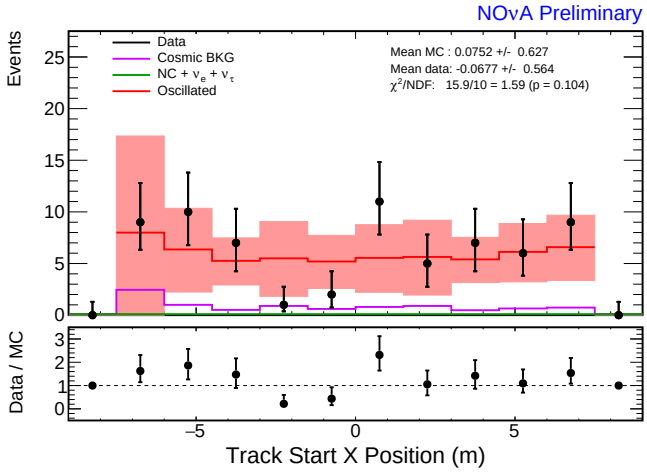

Figure 12.12: Track starting x position of the most muon like track in selected escaping events in the far detector data. The prediction is drawn in red with the systematic errors shown in the error bands. The major sources of background are shown in magenta and green.

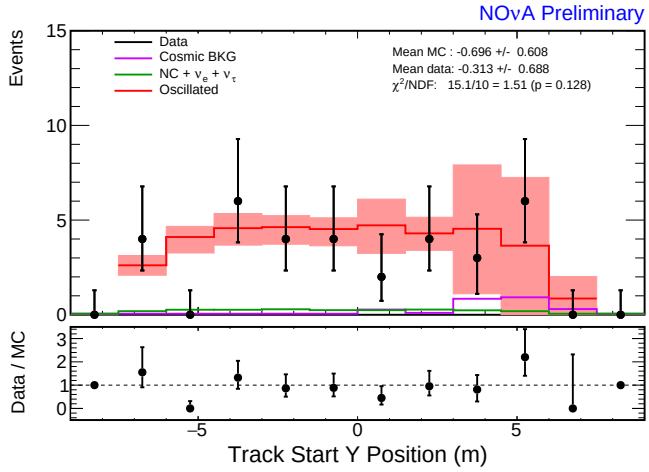

Figure 12.13: Track starting y position of the most muon like track in selected non QE events in the far detector data. The prediction is drawn in red with the systematic errors shown in the error bands. The major sources of background are shown in magenta and green.

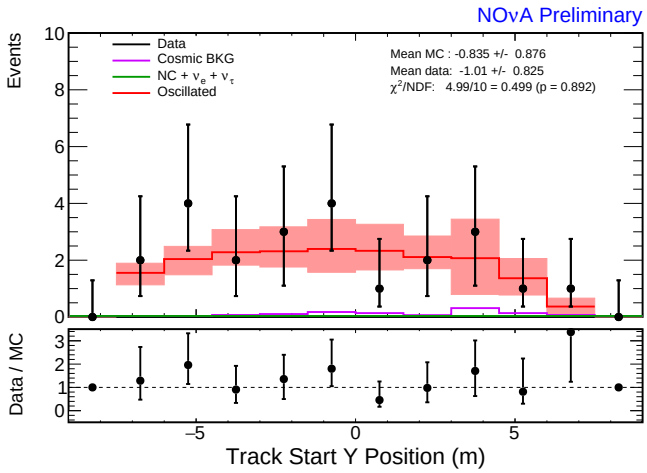

Figure 12.14: Track starting y position of the most muon like track in selected QE events in the far detector data. The prediction is drawn in red with the systematic errors shown in the error bands. The major sources of background are shown in magenta and green.

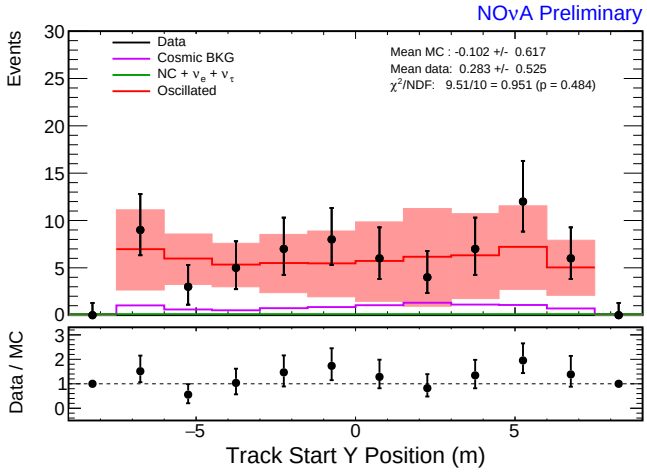

Figure 12.15: Track starting x position of the most muon like track in selected escaping events in the far detector data. The prediction is drawn in red with the systematic errors shown in the error bands. The major sources of background are shown in magenta and green.

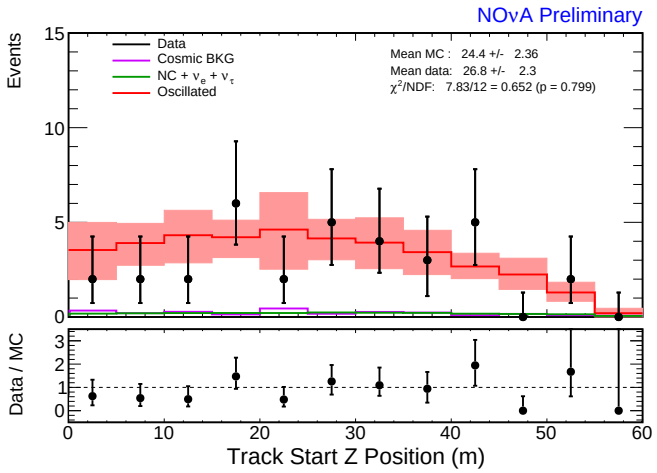

Figure 12.16: Track starting z position of the most muon like track in selected non QE events in the far detector data. The prediction is drawn in red with the systematic errors shown in the error bands. The major sources of background are shown in magenta and green.

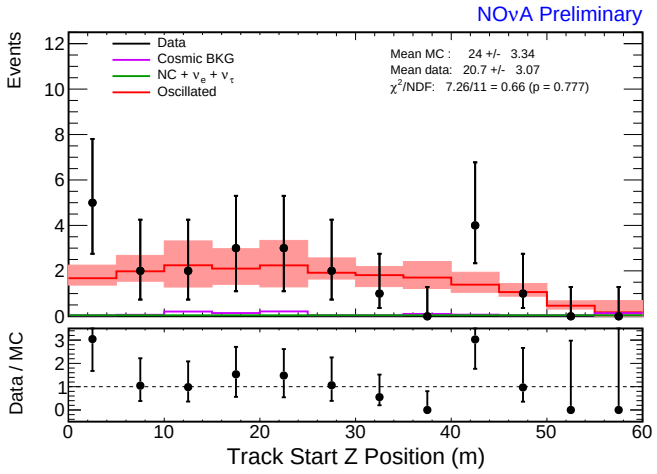

Figure 12.17: Track starting z position of the most muon like track in selected QE events in the far detector data. The prediction is drawn in red with the systematic errors shown in the error bands. The major sources of background are shown in magenta and green.

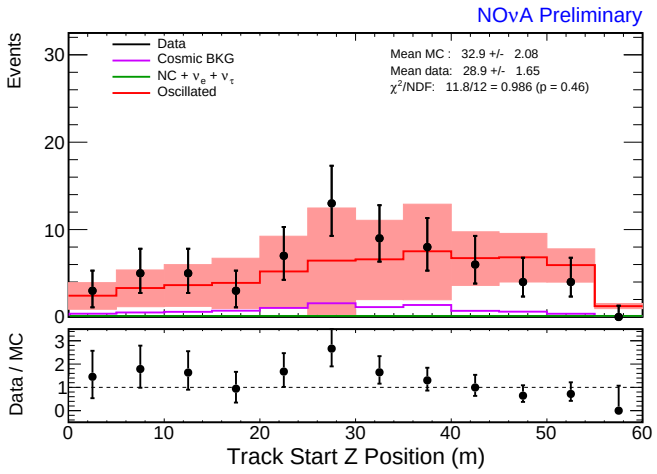

Figure 12.18: Track starting z position of the most muon like track in selected escaping events in the far detector data. The prediction is drawn in red with the systematic errors shown in the error bands. The major sources of background are shown in magenta and green.

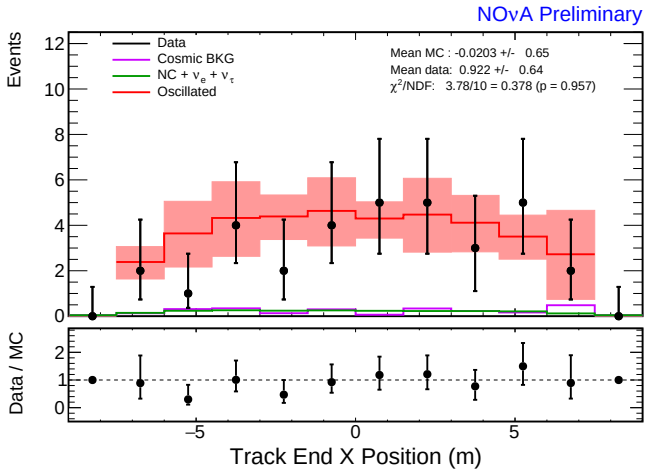

Figure 12.19: Track stopping x position of the most muon like track in selected non QE events in the far detector data. The prediction is drawn in red with the systematic errors shown in the error bands. The major sources of background are shown in magenta and green.

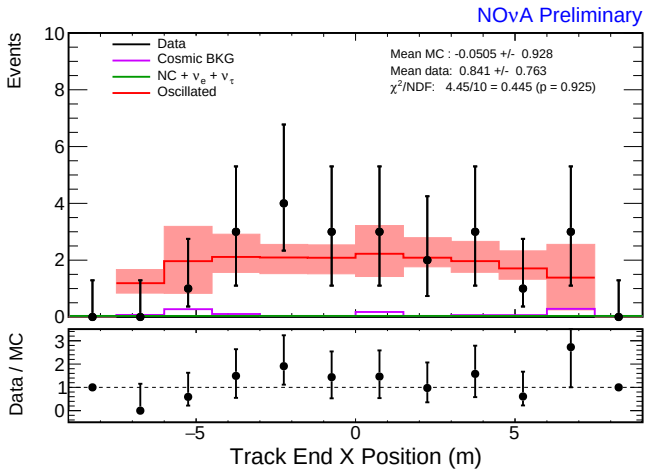

Figure 12.20: Track stopping x position of the most muon like track in selected QE events in the far detector data. The prediction is drawn in red with the systematic errors shown in the error bands. The major sources of background are shown in magenta and green.

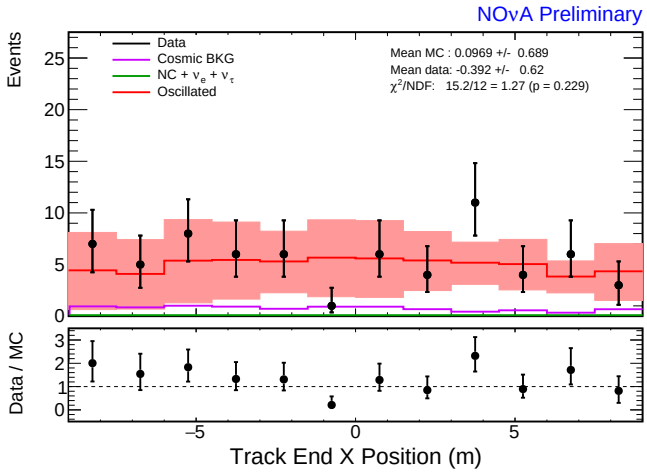

Figure 12.21: Track stopping y position of the most muon like track in selected escaping events in the far detector data. The prediction is drawn in red with the systematic errors shown in the error bands. The major sources of background are shown in magenta and green.

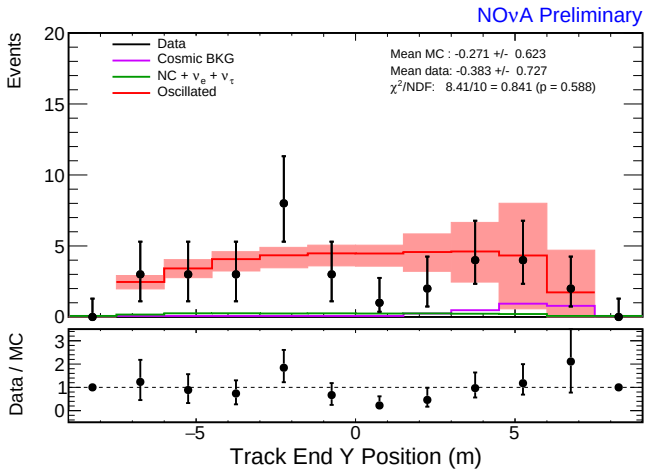

Figure 12.22: Track stopping y position of the most muon like track in selected non QE events in the far detector data. The prediction is drawn in red with the systematic errors shown in the error bands. The major sources of background are shown in magenta and green.

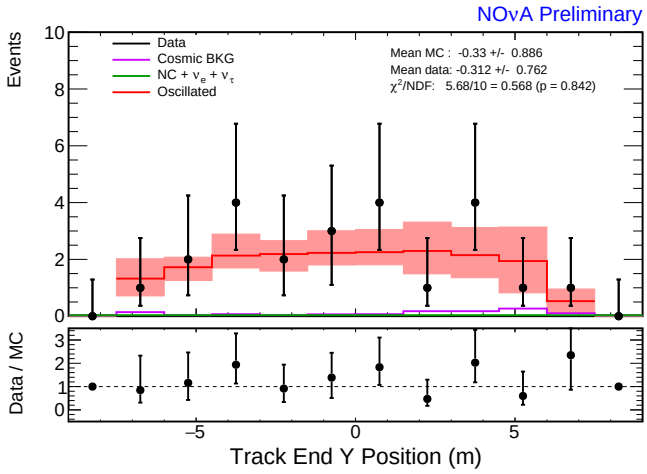

Figure 12.23: Track stopping y position of the most muon like track in selected QE events in the far detector data. The prediction is drawn in red with the systematic errors shown in the error bands. The major sources of background are shown in magenta and green.

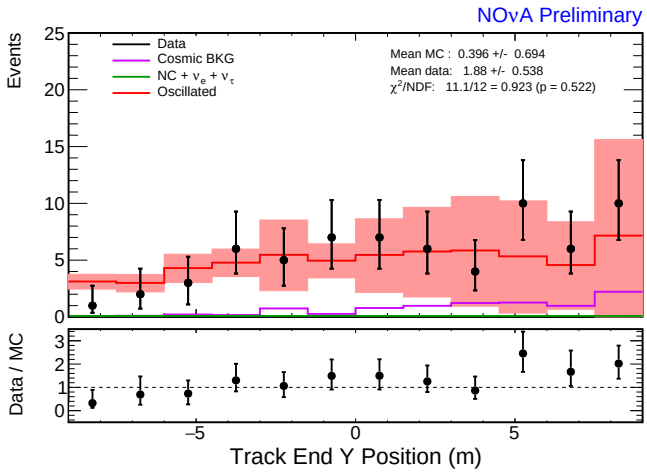

Figure 12.24: Track stopping x position of the most muon like track in selected escaping events in the far detector data. The prediction is drawn in red with the systematic errors shown in the error bands. The major sources of background are shown in magenta and green.

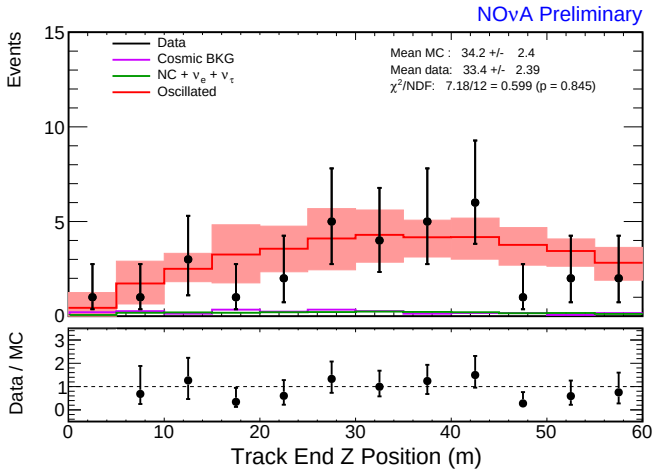

Figure 12.25: Track stopping z position of the most muon like track in selected non QE events in the far detector data. The prediction is drawn in red with the systematic errors shown in the error bands. The major sources of background are shown in magenta and green.

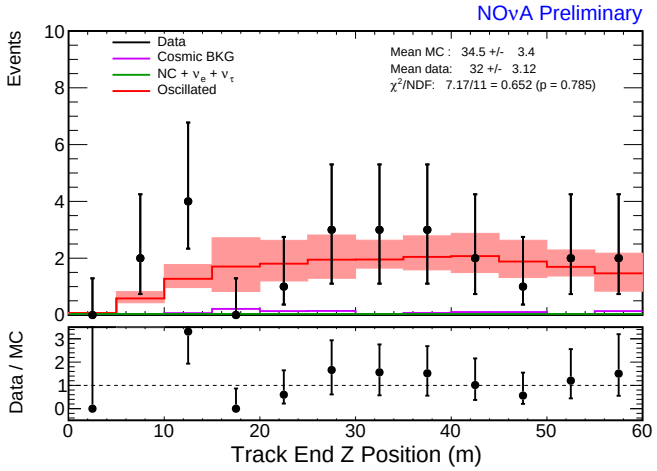

Figure 12.26: Track stopping z position of the most muon like track in selected QE events in the far detector data. The prediction is drawn in red with the systematic errors shown in the error bands. The major sources of background are shown in magenta and green.

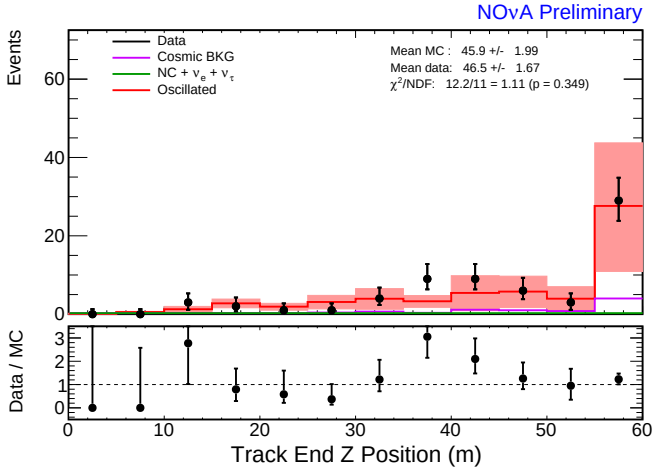

Figure 12.27: Track stopping z position of the most muon like track in selected escaping events in the far detector data. The prediction is drawn in red with the systematic errors shown in the error bands. The major sources of background are shown in magenta and green.

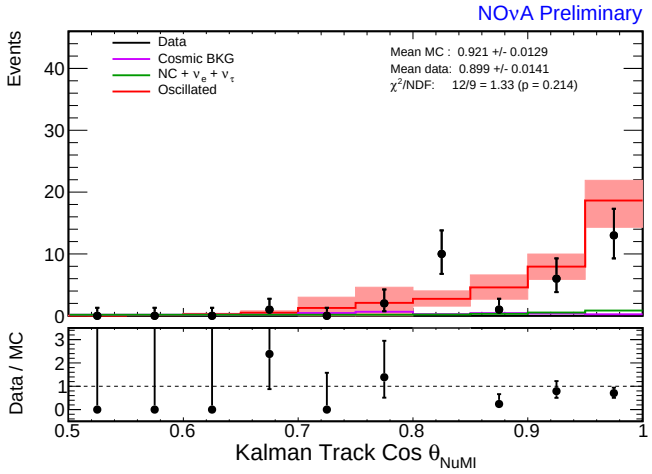

Figure 12.28: Direction with respect to the beam of the most muon like track in selected non-QE events in the far detector data. The prediction is drawn in red with the systematic errors shown in the error bands. The major sources of background are shown in magenta and green.

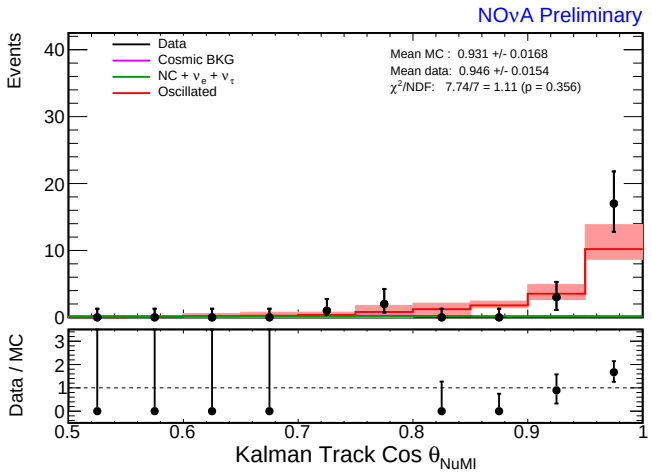

Figure 12.29: Direction with respect to the beam of the most muon like track in selected QE events in the far detector data. The prediction is drawn in red with the systematic errors shown in the error bands. The major sources of background are shown in magenta and green.

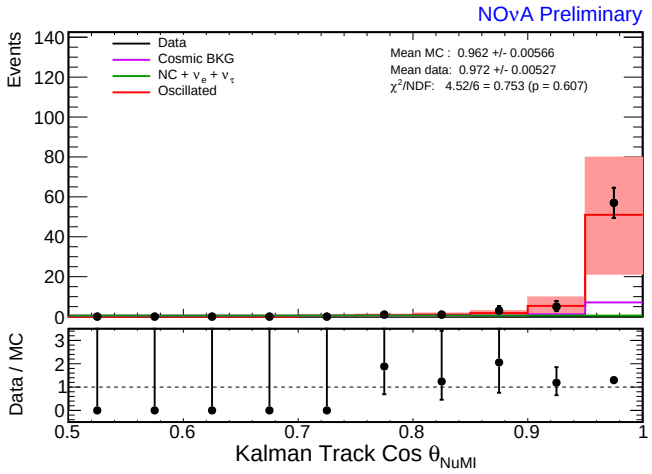

Figure 12.30: Direction with respect to the beam of the most muon like track in selected escaping events in the far detector data. The prediction is drawn in red with the systematic errors shown in the error bands. The major sources of background are shown in magenta and green.

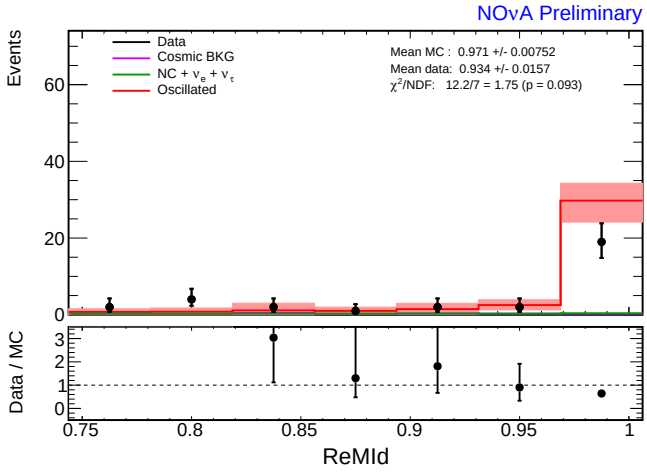

Figure 12.31: ReMId value of the most muon like track in selected non-QE events in the far detector data. The prediction is drawn in red with the systematic errors shown in the error bands. The major sources of background are shown in magenta and green.

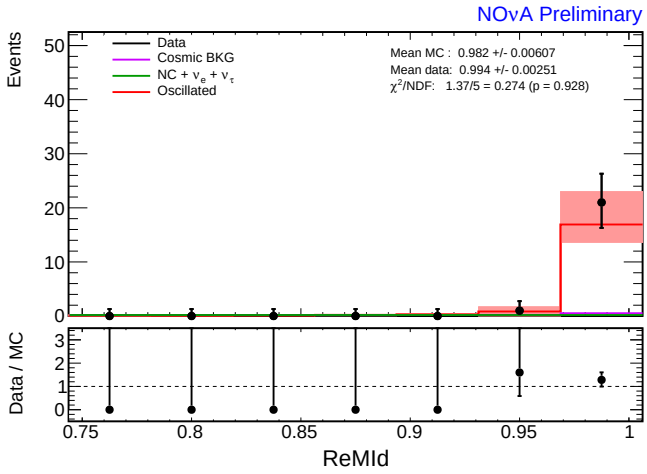

Figure 12.32: ReMId value of the most muon like track in selected QE events in the far detector data. The prediction is drawn in red with the systematic errors shown in the error bands. The major sources of background are shown in magenta and green.

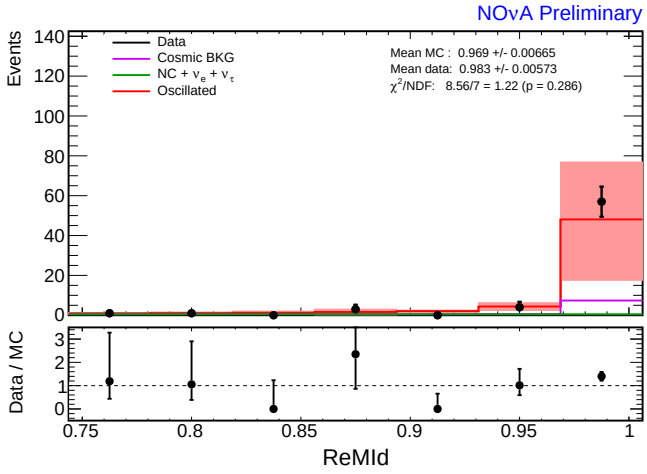

Figure 12.33: ReMId value of the most muon like track in selected escaping events in the far detector data. The prediction is drawn in red with the systematic errors shown in the error bands. The major sources of background are shown in magenta and green.

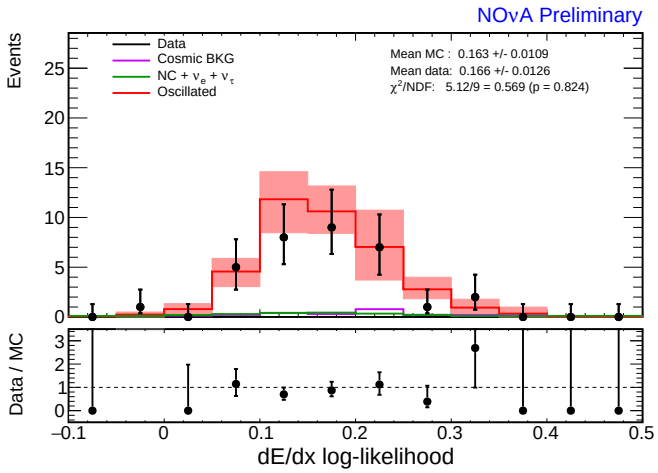

Figure 12.34: $\frac{dE}{dx}$ log-likelihood value of the most muon like track in selected non-QE events in the far detector data. The prediction is drawn in red with the systematic errors shown in the error bands. The major sources of background are shown in magenta and green.

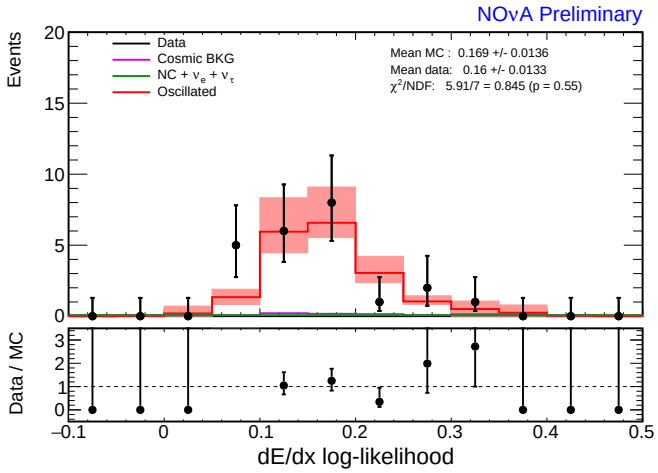

Figure 12.35: $\frac{dE}{dx}$ log-likelihood value of the most muon like track in selected QE events in the far detector data. The prediction is drawn in red with the systematic errors shown in the error bands. The major sources of background are shown in magenta and green.

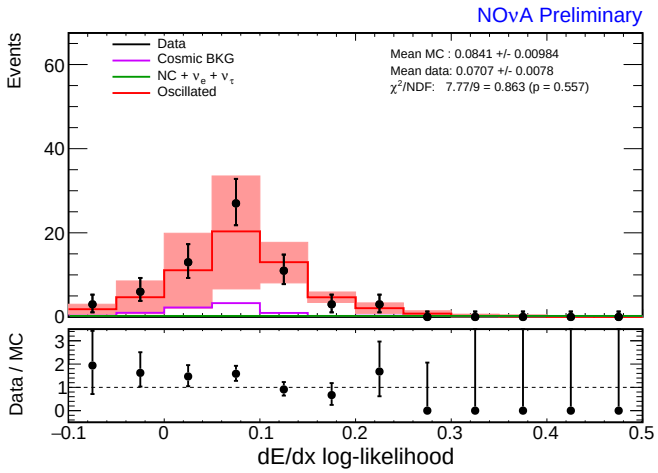

Figure 12.36: $\frac{dE}{dx}$ log-likelihood value of the most muon like track in selected escaping events in the far detector data. The prediction is drawn in red with the systematic errors shown in the error bands. The major sources of background are shown in magenta and green.

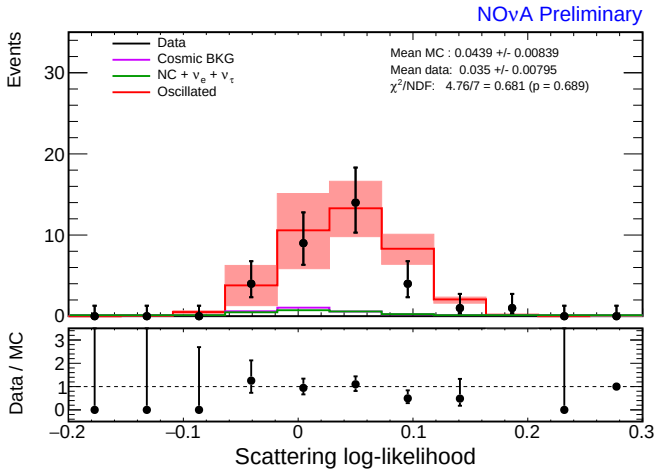

Figure 12.37: Scattering log-likelihood value of the most muon like track in selected non-QE events in the far detector data. The prediction is drawn in red with the systematic errors shown in the error bands. The major sources of background are shown in magenta and green.

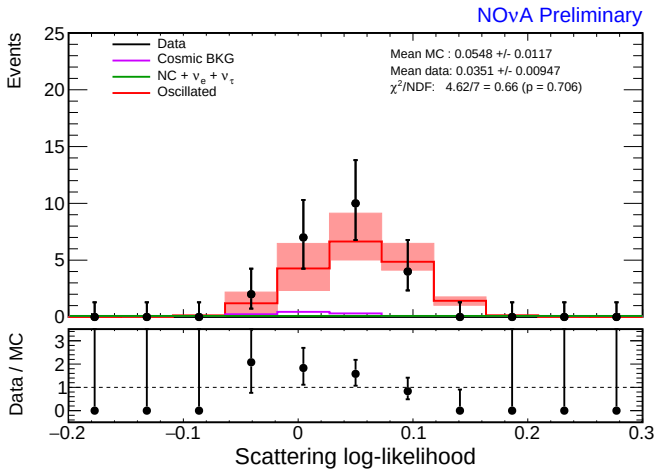

Figure 12.38: Scattering log-likelihood value of the most muon like track in selected QE events in the far detector data. The prediction is drawn in red with the systematic errors shown in the error bands. The major sources of background are shown in magenta and green.

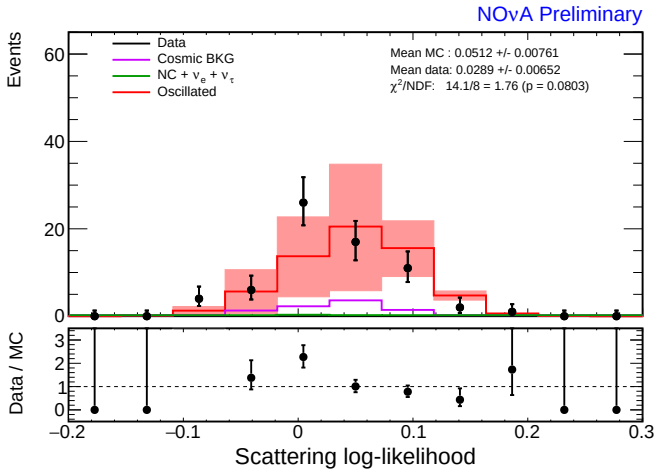

Figure 12.39: Scattering log-likelihood value of the most muon like track in selected escaping events in the far detector data. The prediction is drawn in red with the systematic errors shown in the error bands. The major sources of background are shown in magenta and green.

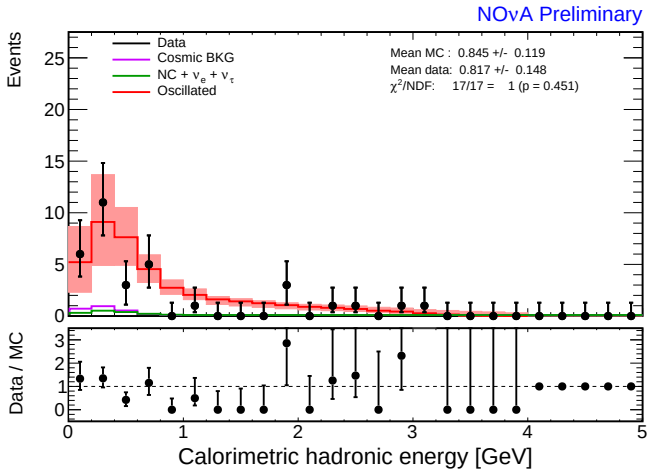

Figure 12.40: Hadronic energy in selected non-QE events in the far detector data. The prediction is drawn in red with the systematic errors shown in the error bands. The major sources of background are shown in magenta and green.

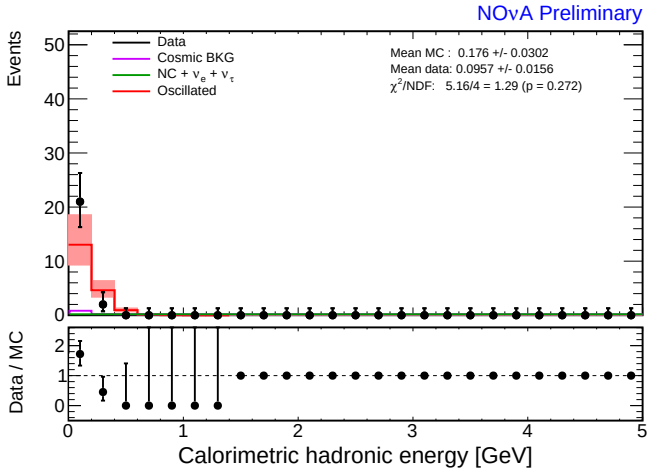

Figure 12.41: Hadronic energy in selected QE events in the far detector data. The prediction is drawn in red with the systematic errors shown in the error bands. The major sources of background are shown in magenta and green.

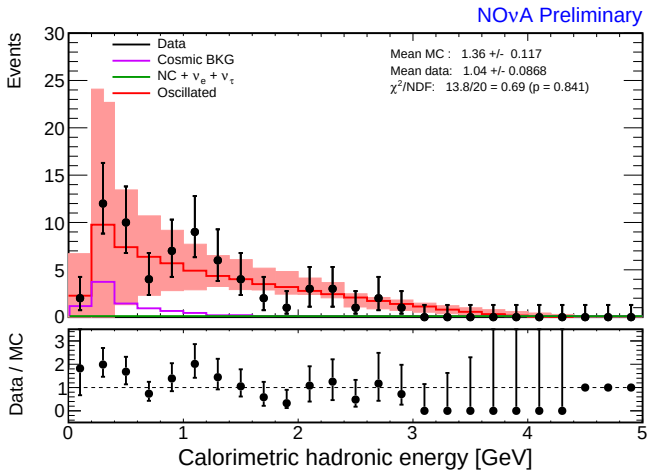

Figure 12.42: Hadronic energy in selected escaping events in the far detector data. The prediction is drawn in red with the systematic errors shown in the error bands. The major sources of background are shown in magenta and green.

12.2 Oscillation Parameter Measurement

The oscillation parameter measurement is performed from a binned maximum-likelihood fit to the reconstructed energy spectrum of the measured neutrino events. The reconstructed energy of the three samples used in this analysis are shown in figures 12.43-12.45. The fit marginalizes over the systematic errors in the analysis by determining the value of the systematic error, within the allowed values, of each parameter that minimizes the χ^2. Fits are performed for each of the three samples independently and the final log-likelihood surface is performed as a combined fit of the three spectrums simultaneously. The best fit point is determined from the minimum in the χ^2 in the two dimensional $\sin^2\theta_{23}$ and $\left|\Delta m^2_{32}\right|$ surface. For all measurements the normal mass hierarchy is assumed.

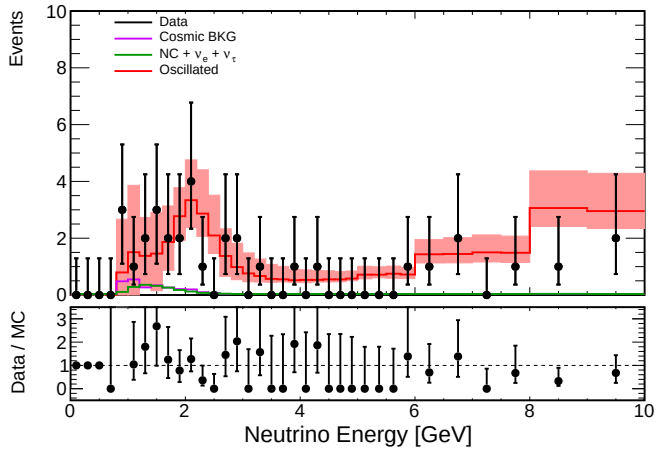

Figure 12.43: Neutrino energy in selected NonQE events in the far detector data. The prediction is drawn in red with the systematic errors shown in the error bands. The major sources of background are shown in magenta and green.

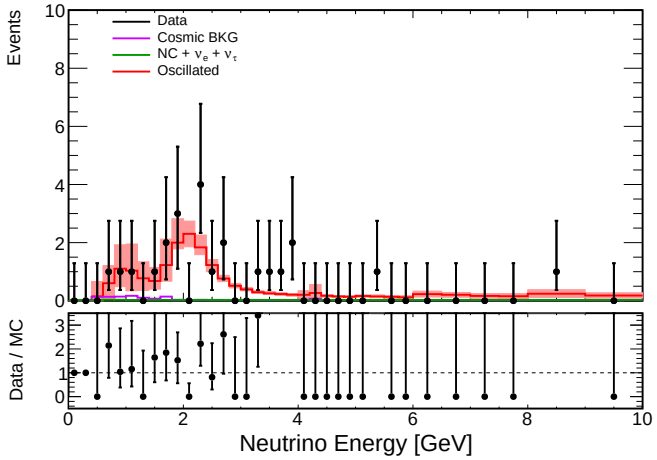

Figure 12.44: Neutrino energy in selected QE events in the far detector data. The prediction is drawn in red with the systematic errors shown in the error bands. The major sources of background are shown in magenta and green.

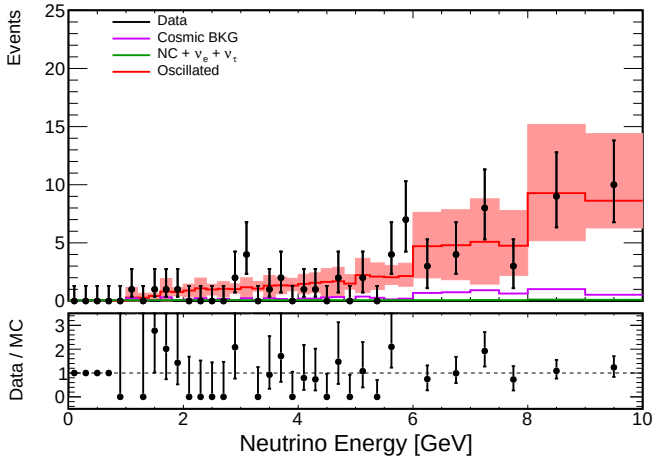

Figure 12.45: Neutrino energy in selected escaping events in the far detector data. The prediction is drawn in red with the systematic errors shown in the error bands. The major sources of background are shown in magenta and green.

12.2.1 Statistical Error Only Result

The result in the absence of systematic errors is shown in figure 12.46 as 90% confidence limits (C.L.) of values of the oscillation parameters. The best fit oscillation parameters were measured as $\sin^2\theta_{23} = 0.32\text{-}0.71$ and $\left|\Delta m^2_{32}\right| = 2.25\text{-}2.98\times10^{-3}$ eV^2 at 90% C.L. with the best fit point of $\sin^2\theta_{23} = 0.38$ and $\left|\Delta m^2_{32}\right| = 2.63\times10^{-3}$ eV^2. In the $\sin^2\theta_{23}$ dimension of the oscillation parameter plane the log-likelihood surface is nearly identical around 0.5 with only small asymmetries resulting from a non-zero value of $\sin\theta_{13}$. This results with a best fit point near $\sin^2\theta_{23} = 0.62$ fits the data nearly as well as the best fit point chosen.

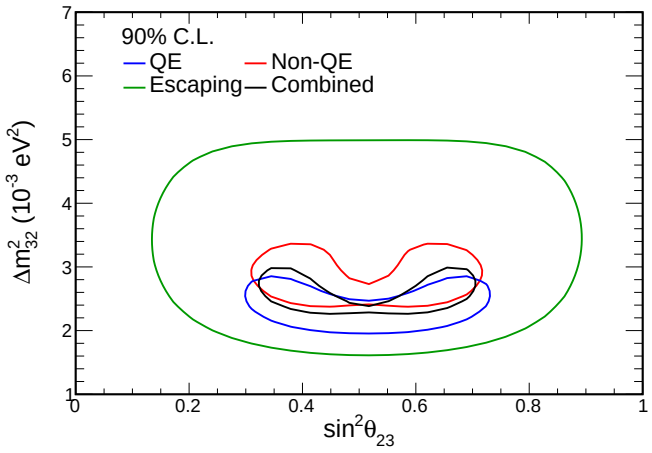

Figure 12.46: 90% confidence limits on the measurement of the oscillation parameters $\sin^2\theta_{23}$ and $\left|\Delta m^2_{32}\right|$ considering only statistical errors.

12.2.2 Systematic Error Result

This analysis is known to suffer from systematic errors as described previously. Including these systematic errors results in the 90% confidence limits of the values of the oscillation parameters shown in figure 12.47, with the best fit point measured as $\sin^2\theta_{23} = 0.31\text{-}0.71$ and $\left|\Delta m^2_{32}\right| = 2.15\text{-}2.91\times10^{-3}$ eV^2 at 90% C.L. with the best fit point of $\sin^2\theta_{23} = 0.41$ and $\left|\Delta m^2_{32}\right| = 2.50\times10^{-3}$ eV^2. As in the statistics only case there is a nearly equivalent

best fit point located near $\sin^2\theta_{23} = 0.59$ due to the symmetry of the contour. The best fit value for each systematic error found during the fitting procedure are listed in table 12.5. None of the best fits of the systematic errors are near one sigma deviations.

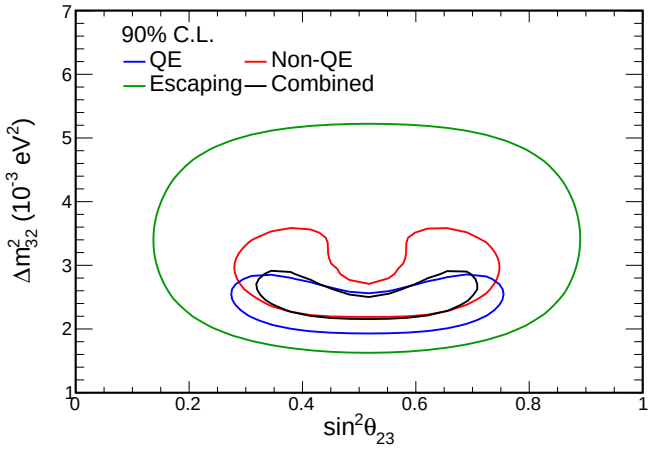

Figure 12.47: 90% confidence limits on the measurement of the oscillation parameters $\sin^2\theta_{23}$ and $|\Delta m^2_{32}|$ considering both statistical and systematic errors.

Figure 12.48 compares the result of the statistical error only result with the result that considers both statistical and systematic errors. The increase in area from the inclusion of systematic errors does not considerably increase the area of the 90% confidence limit. However, the result considering systematic errors does not favor a non maximal mixing measurement of $\sin^2\theta_{23}$ as strongly as the result considering statistics only. This is reflected in the best fit point being of $\sin^2\theta_{23}$ being closer to 0.5 when systematics are included.

Figure 12.49 compares the result of the measurements with and without the escaping sample included in the combined fit. While the difference between the contours with and without the escaping sample is small, the result including the escaping sample increases the lower bound of the contour by 0.003×10^{-3} eV^2 at the 90% C.L. over all values of $\sin^2\theta_{23}$. Additionally at $\sin^2\theta_{23} = 0.5$ the upper bound of the contour is reduced by 0.003×10^{-3} eV^2. At values of $\sin^2\theta_{23}$ further away from maximal mixing the upper bound on the contour sees an increase similar to that of the lower bound. As

Table 12.5: Best fit values of each systematic error from the marginalization fitting procedure in units of σ deviations defined for each systematic error.

Systematic Error	Best Fit [σ]
Beam	-0.120
M_A CC QE	+0.124
M_A CC RES	-0.287
M_v CC RES	-0.137
M_A NC RES	+0.066
M_v NC RES	+0.016
M_A NC Elastic	+0.043
Small GENIE	-0.039
Absolute Normalization	+0.003
Relative Normalization	+0.003
ND Absolute Energy	+0.291
FD Absolute Energy	-0.621
ND Hadronic Modeling	-0.234
FD Hadronic Modeling	+0.348

a result of the increase in precision of the measurement of $\left|\Delta m^2_{32}\right|$ near $\sin^2\theta_{23} = 0.5$ the measurement including the escaping sample is pushed towards non maximal mixing.

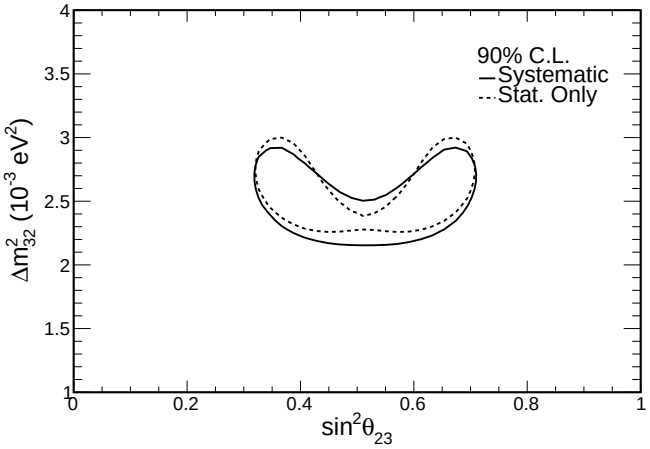

Figure 12.48: 90% confidence limits on the measurement of the oscillation parameters $\sin^2\theta_{23}$ and $\left|\Delta m^2_{32}\right|$ for the combined result of the statistical only and statistical and systematic error cases.

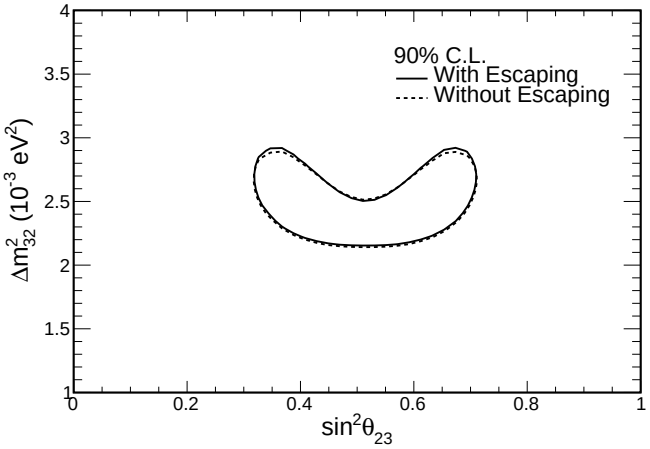

Figure 12.49: 90% confidence limits on the measurement of the oscillation parameters $\sin^2\theta_{23}$ and $\left|\Delta m^2_{32}\right|$ for the combined result including the escaping sample and not including the escaping sample.

12.2.3 Feldman-Cousins Anaylsis

Using the likelihood fitting technique described previously is not quite the correct method for this analysis. This analysis is a low statistics experiment measuring a parameter that has physical boundaries, i.e. neutrino oscillations can at most be maximal. For this situation the unified approach developed by Feldman and Cousins is the correct technique [92]. This technique uses many pseudo-experiments drawn from the simulation with true values of $\sin^2\theta_{23}$ and $\left|\Delta m^2_{32}\right|$ randomly drawn across the parameter space and the systematic errors drawn randomly from the error distributions. The maximum-likelihood fitting procedure is performed on each experiment and a $\left|\Delta\chi^2\right|$ map is created from the results of fitting all the experiments where $\left|\Delta\chi^2\right|$ is the difference between the χ^2 at the given values of oscillation parameters and the χ^2 at the values that maximize the probability of the observed outcome. To construct the C.L. at level α a critical $\left|\Delta\chi^2\right|$,$\left|\Delta\chi^2_c\right|$, is defined as having α of the experiments at that combination of oscillation parameters having $\left|\Delta\chi^2\right| < \left|\Delta\chi^2_c\right|$. The results of this approach give nearly identical results to the technique described previously with no change to the stated range of value of the oscillation parameters at the 90% C.L.. This technique is computing intensive and was only used to determine the final oscillation parameters and to validate the use of the likelihood fitting technique.

12.2.4 Comparison to MINOS and T2K

Figure 12.50 compares the results of this analysis with the current best measurement of the oscillation parameters from the MINOS experiment [7] and the T2K experiment [6] at the the 90% C.L.. This analysis is found to be in agreement with the measurements of both of these experiments. This result is comparable with the current best limits on the measurement of $\sin^2\theta_{23}$ and $\left|\Delta m^2_{32}\right|$ with only the 7% of the total expected NOνA POT. With increased exposure, NOνA will be able to rule out maximal mixing if the true value of $\sin^2\theta_{23}$ is near 0.4 or 0.6 [93].

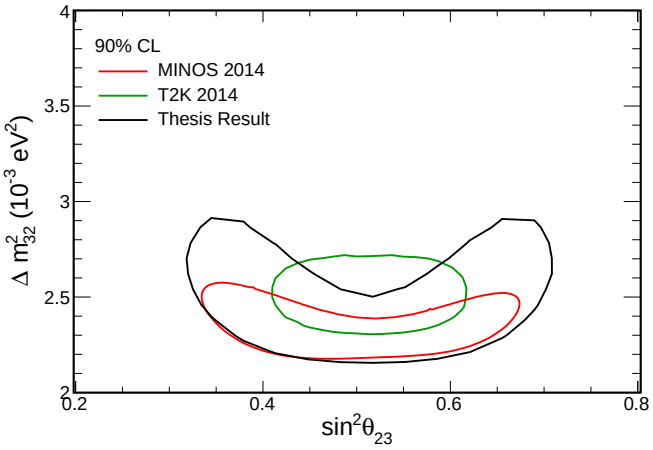

Figure 12.50: 90% confidence limits on the measurement of the oscillation parameters $\sin^2\theta_{23}$ and $\left|\Delta m^2_{32}\right|$ compared to measurements from the T2K and MINOS experiments with data taken from [6] and [7] respectively.

Chapter 13

Conclusion

Muon neutrino oscillations have been analyzed using the first data from NOνA experiment. This analysis shows clear evidence of neutrino oscillations and measured the oscillations parameters as $\sin^2\theta_{23}$ = 0.31-0.71 and $\left|\Delta m^2_{32}\right|$ = 2.15-2.91$\times 10^{-3}$ eV^2 at 90% C.L.. The results are comparable to existing measurements of these oscillation parameters using only 7% of the total exposure expected to be seen by the NOνA detectors. This analysis uniquely utilizes a sample of escaping neutrino interactions for the first time in the NOνA experiment. This sample adds additional statistical power to the limited statistics of this first data analysis and provides stronger evidence for non-maximal oscillations then when the contained neutrino interactions are considered by themselves.

In addition to statistical improvements on the measurements by using more exposure, future analysis can make other improvements on this analysis to increase the precision at which these oscillation parameters can be measured. These improvements come in two general forms, enhancements to event selection and reduction of systematic errors.

This analysis has its lowest efficiency for selecting ν_μ CC neutrino events at energies near the oscillation minimum and below. Improvements to the selection would allow for more events to be selected in this region allowing for better discrimination between maximal and non-maximal oscillations. In particular more precise reconstruction of low energy events would allow for better particle identification and event selection in this energy of interest.

The effect of systematic errors on future analysis also has potential for being reduced.

The largest systematic errors associated with this analysis come from hadronic modeling and absolute energy calibration. If the cause of the discrepancy between the modeling of the hadronic energy in simulation and what is observed in data is determined, this systematic could be greatly reduced. If the discrepancy is determined to arise from a hadronic physics process effect the simulation can be upgraded to include the effect. Additionally the effect should be present in both detectors and the systematic error should be taken as an absolute error without relative shifts between the detectors. Otherwise if the effect is determined to be from a mis-modeling of the detector response to the physics that is present in the detector, the simulation can be upgraded to improve the modeling of this particular feature once that feature is known. In this case the effect may or may not cancel between the two detectors depending on if the detector response modeling is the same between the detectors. In the case of the determination of the absolute energy calibration, the technique for the determining the calibration can be improved to include other calibration sources such as Michel electrons and the π° mass reconstruction which should improve the overall determination of the absolute energy scale.

Improving these components of the analysis is actively being pursued and should result in improvements to the systematic errors in future analysis. A second oscillation analysis should be released in the next year and even with the increase in statistical power that analysis should provide interesting scientific results.

References

[1] F. Capozzi et al. *Phys. Rev.*, D89:093018, 2015.

[2] Robert Miles Zwaska. *Accelerator systems and instrumentation for the NuMI neutrino beam*. PhD thesis, University of Texas, Austin, 2005.

[3] J. Cooper. Technical design report for cd-2/3a. NOνA Internal Note 2678, version 8, 2009.

[4] L. Mualem. Apd test board v.2 operation. NOνA Internal Note 40, version 1, 2007.

[5] J. A. Formaggio and G. P. Zeller. *Rev. Mod. Phys.*, 84:1307, 2012.

[6] K. Abe et al. *Phys. Rev. Lett.*, 112:181801, 2014.

[7] P. Adamson et al. *Phys. Rev. Lett.*, 112:191801, 2014.

[8] S.L. Glashow. *Nuclear Physics*, 22:579, 1961.

[9] P.W. Higgs. *Phys. Rev. Lett.*, 13:508, 1964.

[10] CMS Collaboration. *Phys. Lett. B*, 710:91, 2012.

[11] ATLAS Collaboration. *Phys. Lett. B*, 717:29, 2012.

[12] J. Chadwick. *Verh. d. D. Phys. Ges.*, 16:383, 1914.

[13] W. Pauli. Offener brief an die gruppe der radioaktiven bei der gauvereins-tagung zu tübingen [open letter to the group of radioactive people at gauvereins meeting in tübingen], 1930.

[14] C.L. Cowan et al. *Science*, 124:103, 1956.

[15] G. Danby et al. *Phys. Rev. Lett.*, 9:36, 1962.

[16] D. Decamp et al. *Phys. Lett.*, B231:519, 1989.

[17] K. Kodama et al. *Phys. Lett.*, B504:218, 2001.

[18] B. Pontecorvo. *Sov. Phys. JETP.*, 6:429, 1957.

[19] Z. Maki, M. Nakagawa, and S. Sakata. *Prog. Theor. Phys.*, 28:870, 1962.

[20] R. Davis. *Phys. Rev. Lett.*, 12:303, 1964.

[21] Y. Fukuda et al. *Phys. Rev. Lett.*, 82:2644, 1999.

[22] J. Boger et al. *Nucl. Instrum. Meth.*, A449:172, 2000.

[23] K. Eguchi et al. *Phys. Rev. Lett.*, 90:021802, 2003.

[24] G.L. Fogli et al. *Phys. Rev. D*, 78:033010, 2008.

[25] A. Bueno, M. Campanelli, and A. Rubbia. *Nucl. Phys. B*, 573:27, 2000.

[26] K. Abe et al. *Phys. Rev.*, D83:052010, 2011.

[27] B. Aharmim et al. *Phys. Rev.*, C81:055504, 2010.

[28] A. Gando et al. *Phys. Rev.*, D83:052002, 2011.

[29] A. Himmel. *AIP Conf. Proc.*, 1604:345, 2014.

[30] M. G. Aartsen et al. *Phys. Rev.*, D91:072004, 2015.

[31] M.H. Ahn et. el The K2K Collaboration. *Phys. Rev. D*, 74:072003, 2006.

[32] F. P. An et al. *Phys. Rev. Lett.*, 112:061801, 2014.

[33] Seon-Hee Seo [for the RENO Collaboration]. *AIP Conf. Proc.*, 1666:080002, 2015.

[34] J.I. Crespo-Anadon [for the Double Chooz Collaboration]. *Proceedings of the Neutrino Oscillation Workshop (NOW 2014)*, arXiv:1412.3698, 2014.

[35] K. Abe et al. *Phys. Rev. Lett.*, 112:061802, 2014.

[36] F. Di Lodovico [for the T2K Collaboration]. *Journal of Physics: Conference Series*, 556:012061, 2014.

[37] A.D. Sakharov. *Pisma Zh. Eksp. Teor. Fiz.*, 5:32, 1967.

[38] S.E. Kopp. *Particle Accelerator Conference Proceedings*, arXiv:physics/0508001, 2005.

[39] M. Martens. Overview and requirements of noνa target. NOνA Internal Note 4568, version 1, 2010.

[40] C. Backhouse. Generating nd cosmic ray mc. NOνA Internal Note 6250, version 1, 2011.

[41] R. Murphy. Updated nd rock rate. NOνA Internal Note 13247, version 1, 2015.

[42] E. Niner. Timing calibration technical note. NOνA Internal Note 12570, version 2, 2015.

[43] K. Bays. Cut flow tables for neutrino. NOνA Internal Note 11294, version 1, 2014.

[44] N. Raddatz. Hit efficiency tech note. NOνA Internal Note 10791, version 1, 2014.

[45] M. Messier. Timing shift summary. NOνA Internal Note 13364, version 1, 2015.

[46] A. Norman. Neutrino 2014 plenary talk. NOνA Note 11398, version 8, 2014.

[47] M. Campanella et al. First calorimeter simulation with the flugg prototype. Technical Report CERN-ALT-SOFT-99-004 CERN, 1999.

[48] T. Bohlen et al. *Nucl. Data Sheets*, 120:211, 2014.

[49] A. Ferrari et al. Fluka: A multi-particle transport code (program version 2005). Technical Report CERN-2005-010 CERN, 2005.

[50] S. Agostinelli et al. *Nucl. Instr. Meth.*, A506:250, 2003.

[51] J. Allison et al. *IEEE Trans. Nucl. Sci.*, 53:270, 2006.

[52] C. Andreopoulos et al. *Nucl. Instr. Meth.*, A614:87, 2010.

[53] C. Hagmann et al. *IEEE Nuclear Science Symposium Conference Record*, 2:1143, 2007.

[54] A. Aurisano. The noνa detector simulation. NOνA Internal Note 13577, version 3, 2015.

[55] M. Baird. Slicing module comparison tech note. NOνA Internal Note 9197, version 2, 2013.

[56] L. Suter. Numu nd selection tech note. NOνA Internal Note 13212, version 3, 2015.

[57] M. Baird. Near det pileup estimates for the first analysis. NOνA Internal Note 13293, version 1, 2015.

[58] C. Backhouse et. al. First analysis calibration technotes. NOνA Internal Note 13579, version 4, 2015.

[59] G. Davies. Cosmictrack review. NOνA Internal Note 6890, version 1, 2012.

[60] M. Messier. Neutrino detectors. NOνA Internal Note 9452, version 1, 2013.

[61] K. Sachdev. Mrcc tech note. NOνA Internal Note 9729, version 3, 2013.

[62] G.R. Lynch and O.I. Dahl. *Nucl. Instrum. Meth.*, B58:6, 1991.

[63] A. Hoecker et al. *PoS*, arXiv:physics/0703039:040, 2007.

[64] T. M. Cover and P. E. Hart. *IEEE Trans. Inform. Theory*, 1:21, 1967.

[65] N. Raddatz. Pid cuts for fd. NOνA Internal Note 9460, version 1, 2013.

[66] S. Lein. Numu charged current energy estimators. NOνA Internal Note 11208, version 1, 2014.

[67] K. Bays. Contours. NOνA Internal Note 9480, version 4, 2013.

[68] N. Raddatz. Numu event selection. NOνA Internal Note 8523, version 1, 2013.

[69] J. Liu. Crosstalk measurements with noνa apds. NOνA Internal Note 7992, version 1, 2012.

[70] S. Lein. Feb ring cut. NOνA Internal Note 12516, version 1, 2014.

[71] L. Goodenough and S. Phan-Budd. Technical note on the noνa beam monitoring for 2015 summer analysis. NOνA Internal Note 13572, version 2, 2015.

[72] J. Coelho and B. Chowdhury. Tech note: Good data selection. NOνA Internal Note 13546, version 2, 2015.

[73] X. Bu and K. Sachdev. Spill level data quality - technical note. NOνA Internal Note 12437, version 2, 2015.

[74] S. Lein. Dcm edge metric. NOνA Internal Note 13527, version 1, 2015.

[75] J. Lozier. Modularextrap technical note. NOνA Internal Note 12563, version 1, 2014.

[76] C. Alt et al. *Eur. Phys. J.*, C49:897, 2007.

[77] L. Goodenough. Discussion of beam quality cuts for use in pot counting. NOνA Internal Note 12474, version 1, 2014.

[78] C. Andreopoulos et al. arXiv:1510.05494, 2015.

[79] D. Rocco. Genie cross section systematics for numu analysis. NOνA Internal Note 13593, version 2, 2015.

[80] N. Raddatz. Fiducial mass systematic. NOνA Internal Note 13237, version 1, 2015.

[81] J. Musser. Detector mass modeling errors and systematics. NOνA Internal Note 13655, version 3, 2015.

[82] N. Raddatz. Muon energy scale systematic. NOνA Internal Note 13637, version 1, 2015.

[83] A. Radovic. Beam technote summary: Systematics for the first analysis. NOνA Internal Note 13617, version 1, 2015.

[84] N. Raddatz. Muon data-mc de/dx differences in numu analysis. NOνA Internal Note 13355, version 1, 2015.

[85] G. Davies. Pi-zero cross-checks on fa (s15-05-07a). NOνA Internal Note 13379, version 2, 2015.

[86] C. Backhouse and R. Patterson. Quick look at michel electrons in the nd and fd (calibration). NOνA Internal Note 13340, version 1, 2015.

[87] M. Tamestt. Calibration energy systematic. NOνA Internal Note 13410, version 1, 2015.

[88] B. Zamorano. Misalignment systematic uncertainty for the first analysis. NOνA Internal Note 13639, version 2, 2015.

[89] J.A. Sepulveda-Quiroz. Bad channels systematic technote. NOνA Internal Note 13663, version 3, 2015.

[90] D. Rocco. Geant4 systematic energy estimation. NOνA Internal Note 13539, version 1, 2015.

[91] K. Sachdev. Birks b/c mod fd. NOνA Internal Note 13647, version 1, 2015.

[92] G. Feldman and R. Cousins. *Phys. Rev. D*, 57:3873, 1998.

[93] A. Norman. *AIP Conf. Proc.*, 1666:110001, 2015.

Appendix A

Extrapolation

The following sections show the full suite of plots for all the major channels used in the extrapolation to a far detector prediction described in chapter 10 for both the Non-QE and QE samples in the near detector.

A.1 Near Detector Non-QE sample

A.1.1 $\nu_\mu \rightarrow \nu_\mu$ Channel

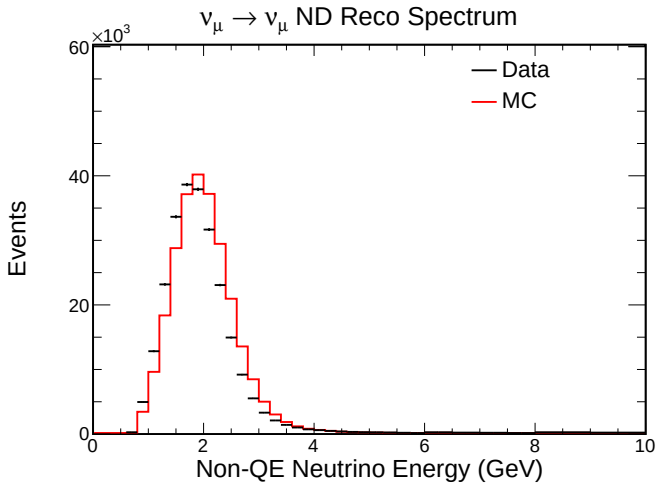

Figure A.1: Selected Non-QE events in near detector data and simulation.

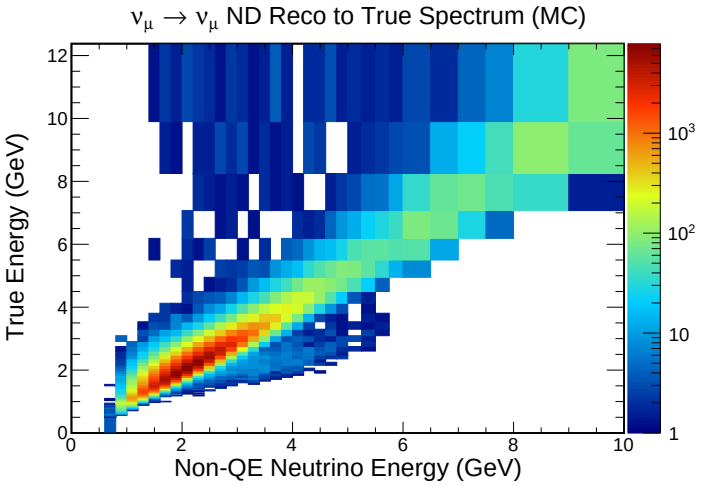

Figure A.2: Mapping of between reconstructed and true energy of selected Non-QE events in near detector.

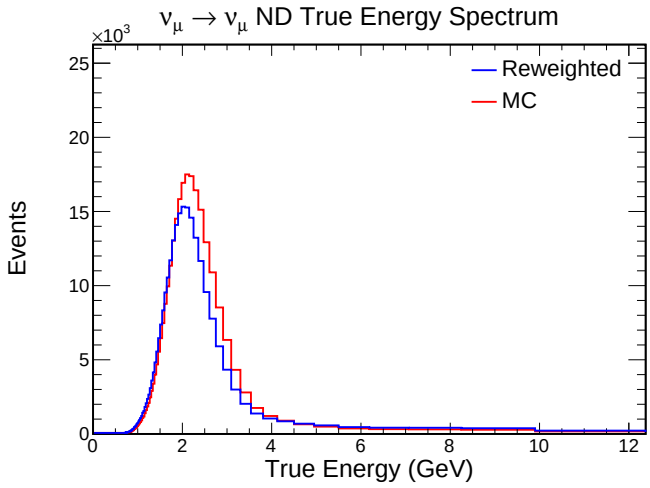

Figure A.3: True energy spectra of selected Non-QE events in near detector data and simulation. The reweighed spectrum is determined by the data selected events and the simulation spectrum is determined from the base simulation of near detector events.

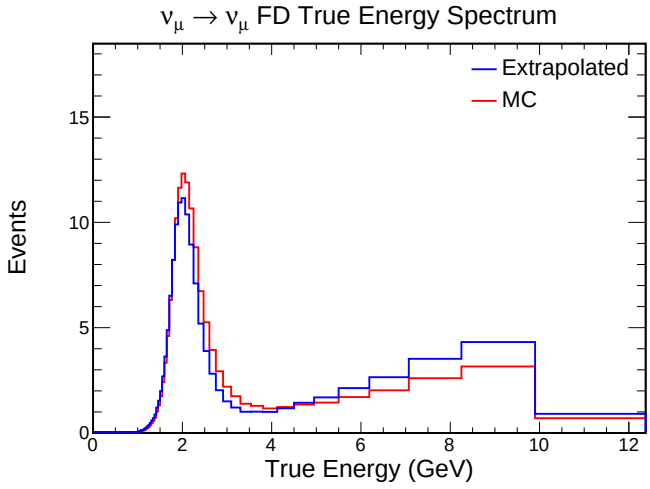

Figure A.4: True energy spectra of selected Non-QE events in far detector data and simulation. The extrapolated spectrum comes from extrapolated data events in the near detector and the simulation is from the base simulation of far detector events.

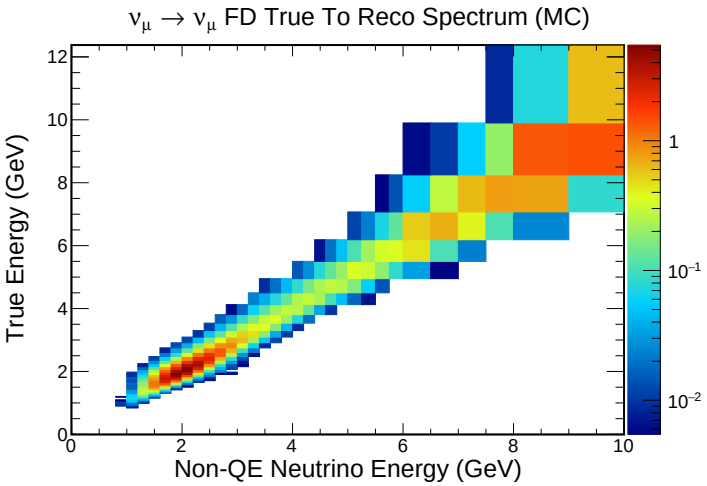

Figure A.5: Mapping of between reconstructed and true energy of selected Non-QE events in far detector.

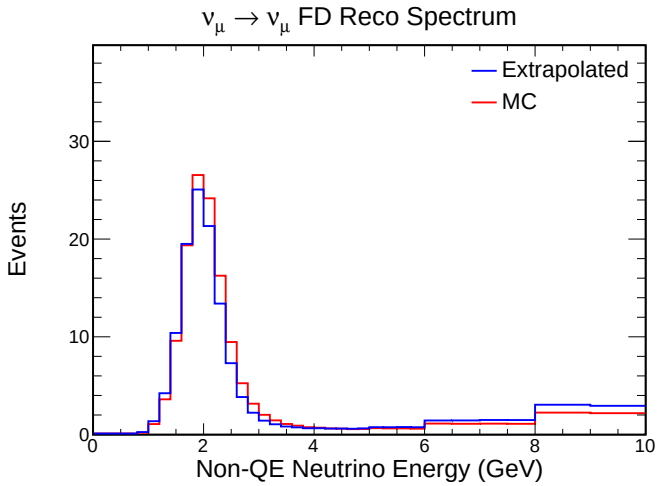

Figure A.6: Reconstructed energy spectra of selected Non-QE events in far detector data and simulation. The extrapolated spectrum comes from extrapolated data events in the near detector and the simulation is from the base simulation of far detector events.

A.1.2 $\bar{\nu}_\mu \rightarrow \bar{\nu}_\mu$ Channel

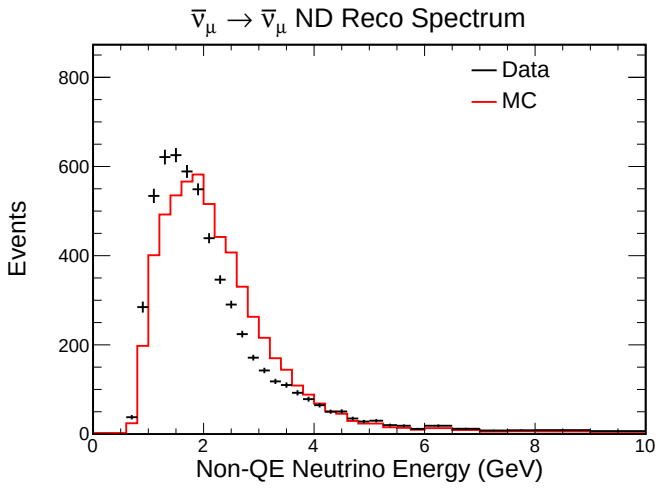

Figure A.7: Selected Non-QE events in near detector data and simulation.

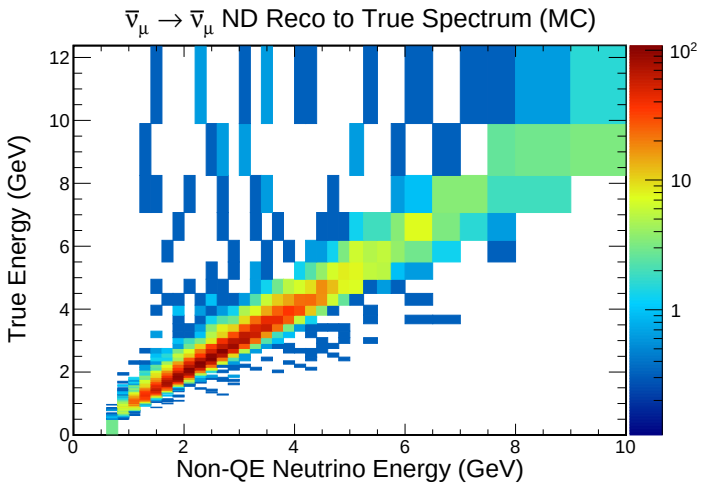

Figure A.8: Mapping of between reconstructed and true energy of selected Non-QE events in near detector.

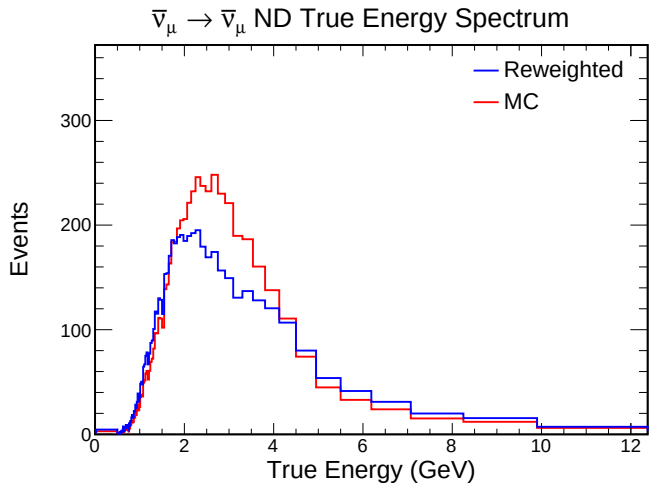

Figure A.9: True energy spectra of selected Non-QE events in near detector data and simulation. The reweighed spectrum is determined by the data selected events and the simulation spectrum is determined from the base simulation of near detector events.

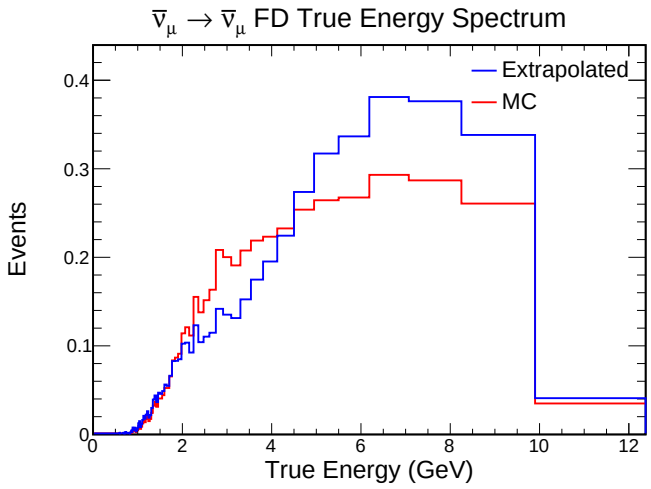

Figure A.10: True energy spectra of selected Non-QE events in far detector data and simulation. The extrapolated spectrum comes from extrapolated data events in the near detector and the simulation is from the base simulation of far detector events.

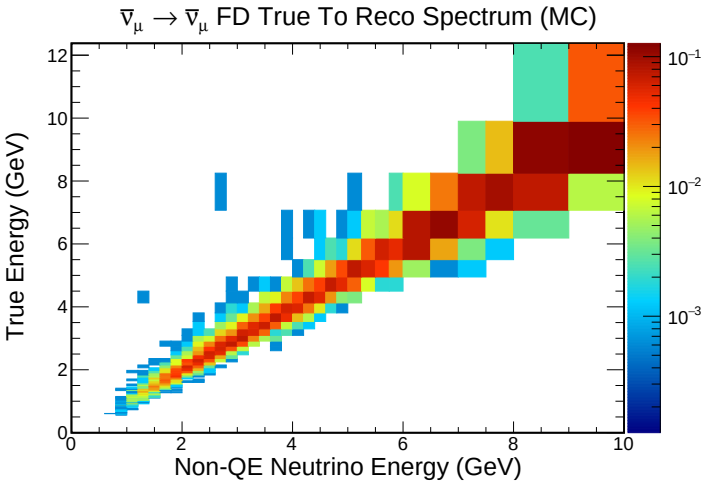

Figure A.11: Mapping of between reconstructed and true energy of selected Non-QE events in far detector.

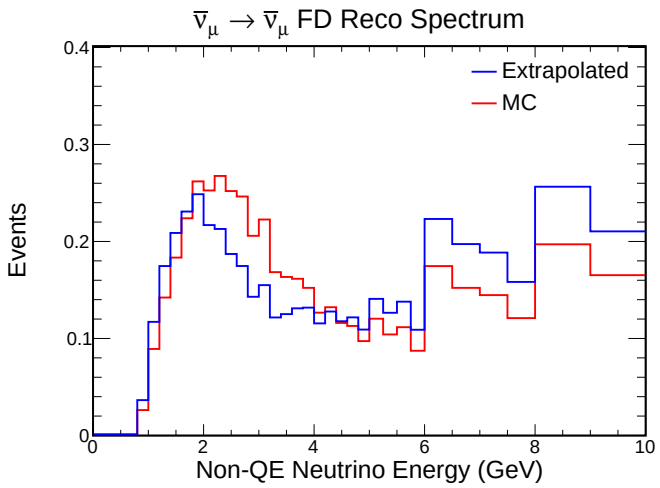

Figure A.12: Reconstructed energy spectra of selected Non-QE events in far detector data and simulation. The extrapolated spectrum comes from extrapolated data events in the near detector and the simulation is from the base simulation of far detector events.

A.1.3 NC $\rightarrow$ NC Channel

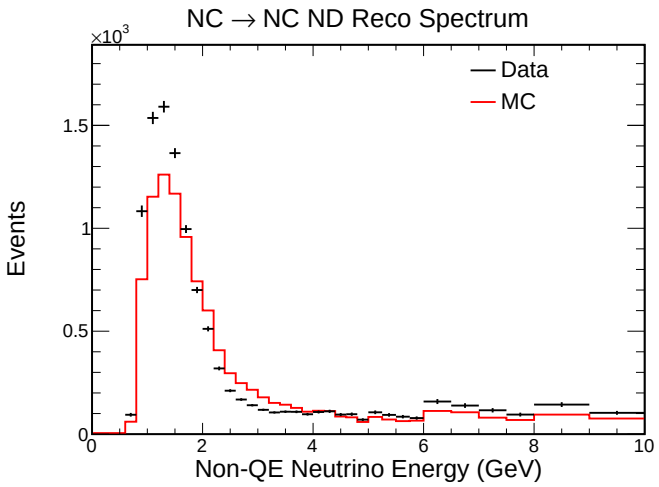

Figure A.13: Selected Non-QE events in near detector data and simulation.

A.2 Near Detector QE sample

A.2.1 $\nu_\mu \rightarrow \nu_\mu$ Channel

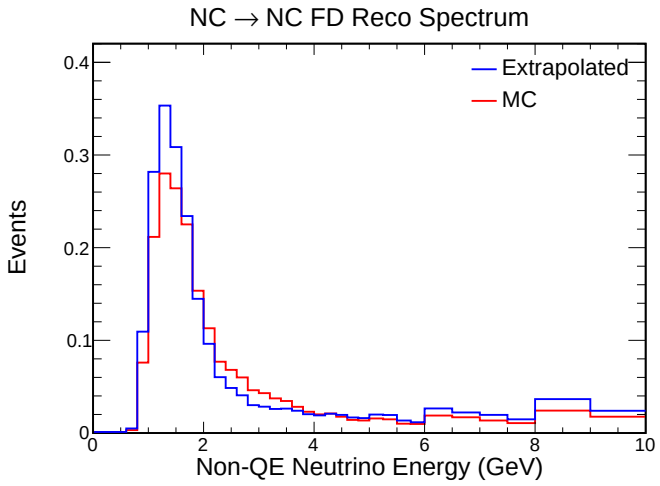

Figure A.14: Reconstructed energy spectra of selected Non-QE events in far detector data and simulation. The extrapolated spectrum comes from extrapolated data events in the near detector and the simulation is from the base simulation of far detector events.

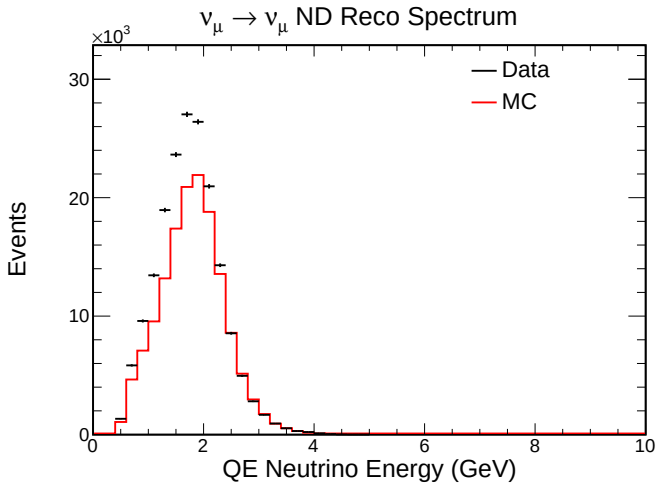

Figure A.15: Selected QE events in near detector data and simulation.

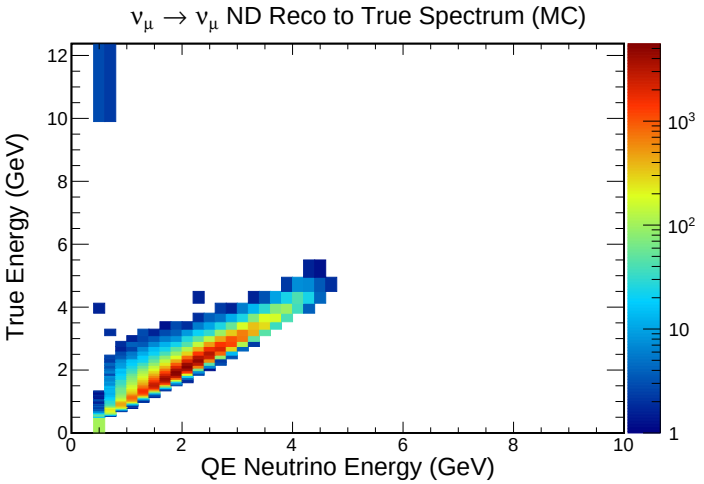

Figure A.16: Mapping of between reconstructed and true energy of selected QE events in near detector.

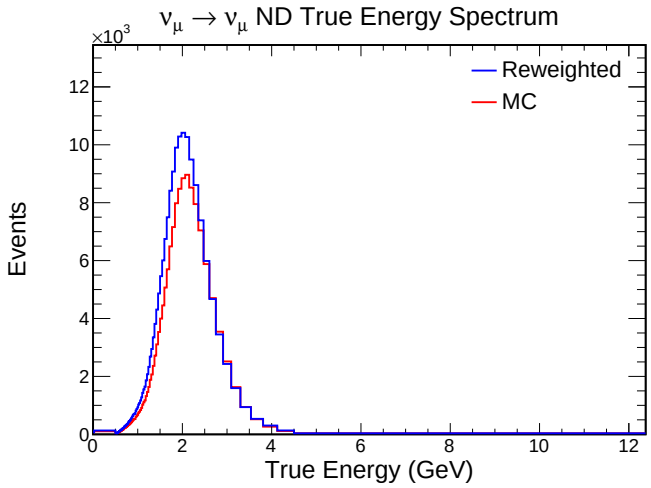

Figure A.17: True energy spectra of selected QE events in near detector data and simulation. The reweighed spectrum is determined by the data selected events and the simulation spectrum is determined from the base simulation of near detector events.

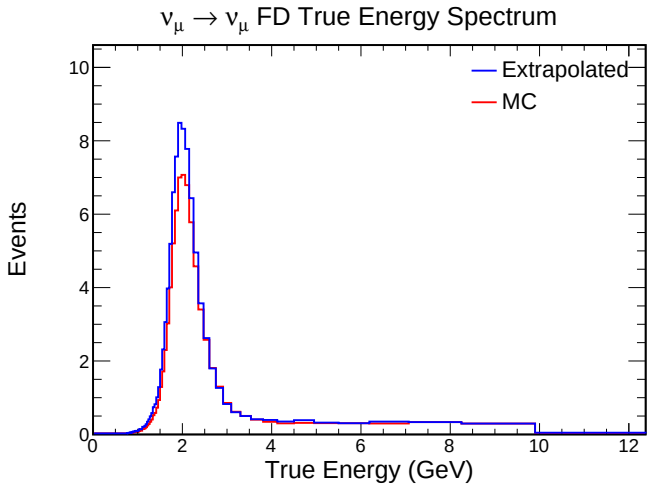

Figure A.18: True energy spectra of selected QE events in far detector data and simulation. The extrapolated spectrum comes from extrapolated data events in the near detector and the simulation is from the base simulation of far detector events.

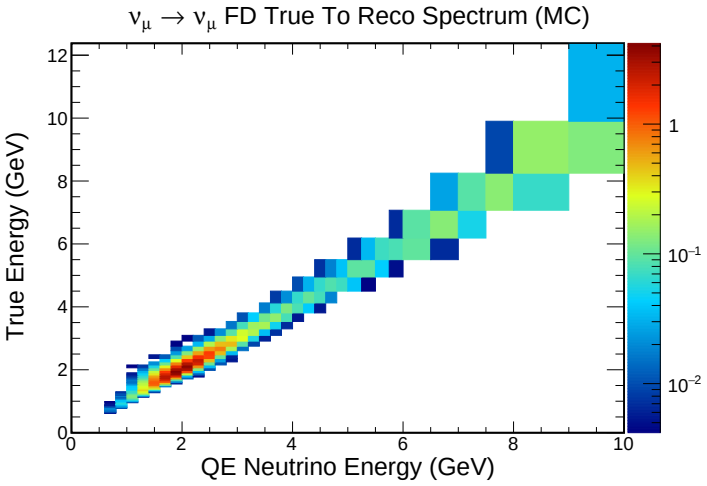

Figure A.19: Mapping of between reconstructed and true energy of selected QE events in far detector.

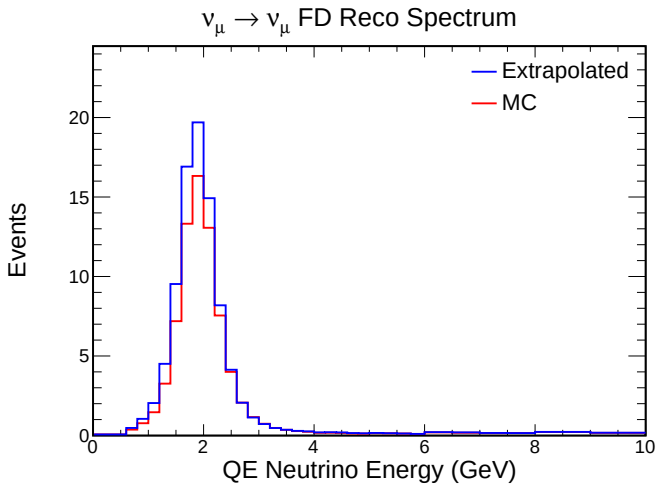

Figure A.20: Reconstructed energy spectra of selected QE events in far detector data and simulation. The extrapolated spectrum comes from extrapolated data events in the near detector and the simulation is from the base simulation of far detector events.

A.2.2 $\bar{\nu}_\mu \rightarrow \bar{\nu}_\mu$ Channel

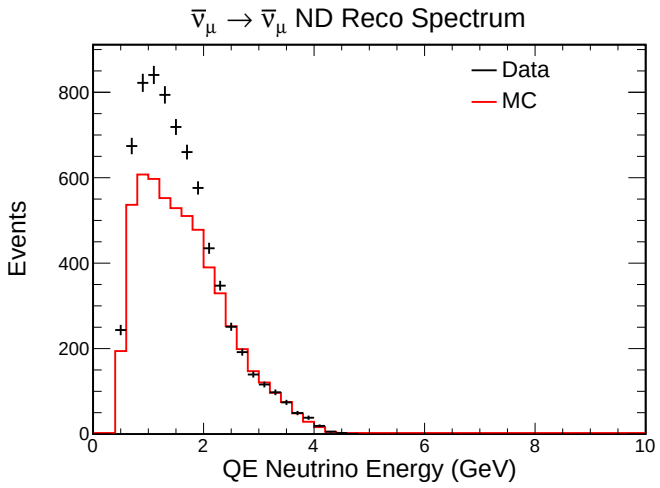

Figure A.21: Selected QE events in near detector data and simulation.

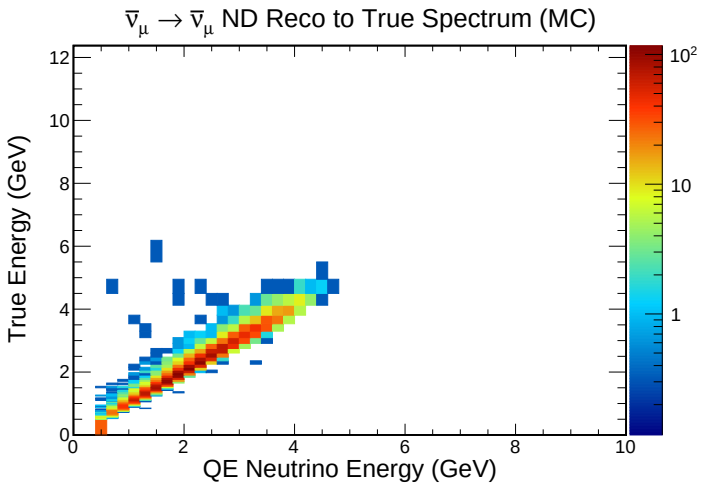

Figure A.22: Mapping of between reconstructed and true energy of selected QE events in near detector.

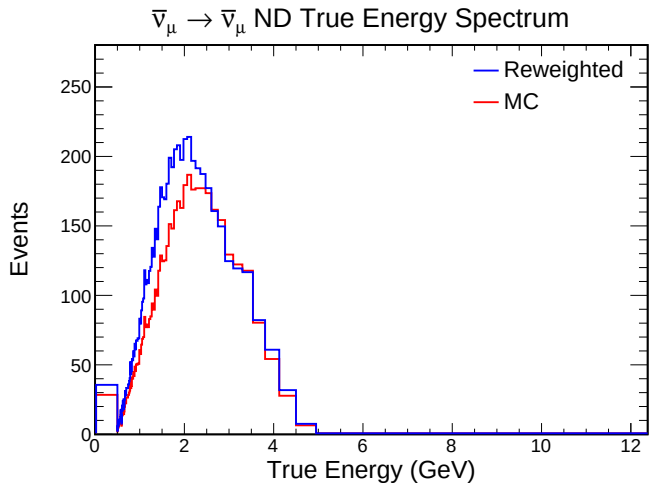

Figure A.23: True energy spectra of selected QE events in near detector data and simulation. The reweighed spectrum is determined by the data selected events and the simulation spectrum is determined from the base simulation of near detector events.

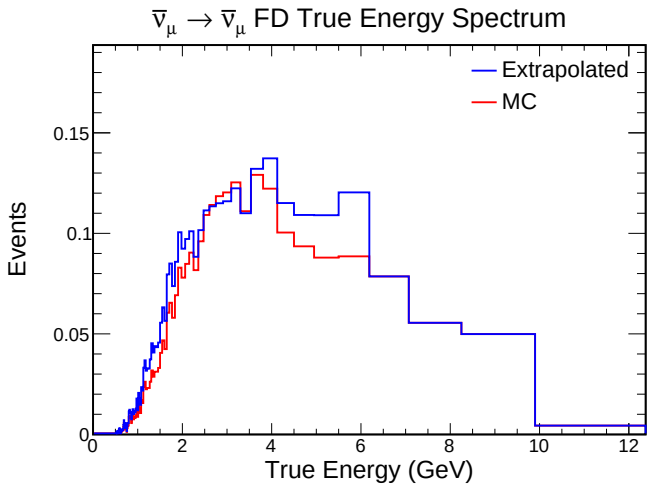

Figure A.24: True energy spectra of selected QE events in far detector data and simulation. The extrapolated spectrum comes from extrapolated data events in the near detector and the simulation is from the base simulation of far detector events.

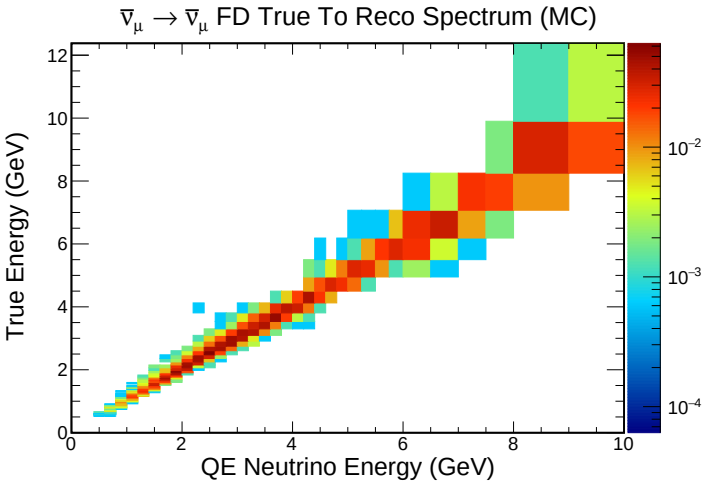

Figure A.25: Mapping of between reconstructed and true energy of selected QE events in far detector.

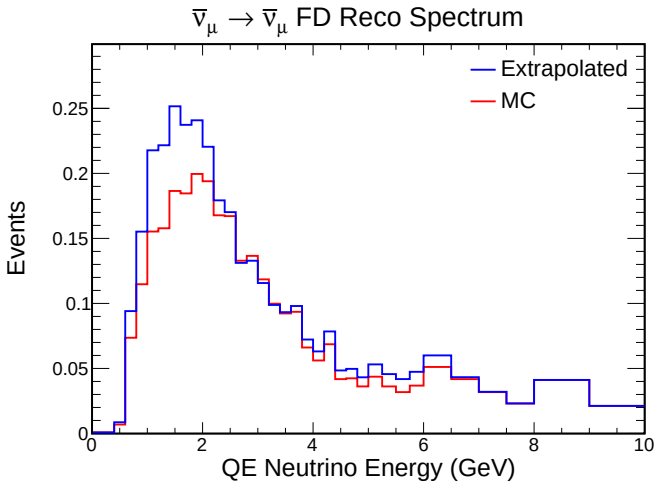

Figure A.26: Reconstructed energy spectra of selected QE events in far detector data and simulation. The extrapolated spectrum comes from extrapolated data events in the near detector and the simulation is from the base simulation of far detector events.

A.2.3 NC → NC Channel

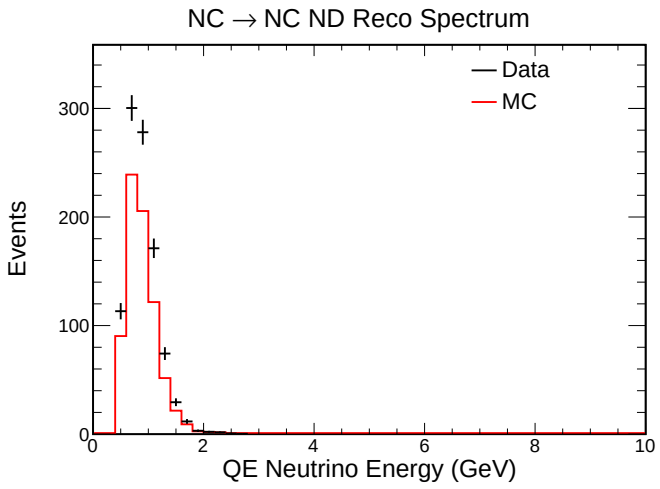

Figure A.27: Selected QE events in near detector data and simulation.

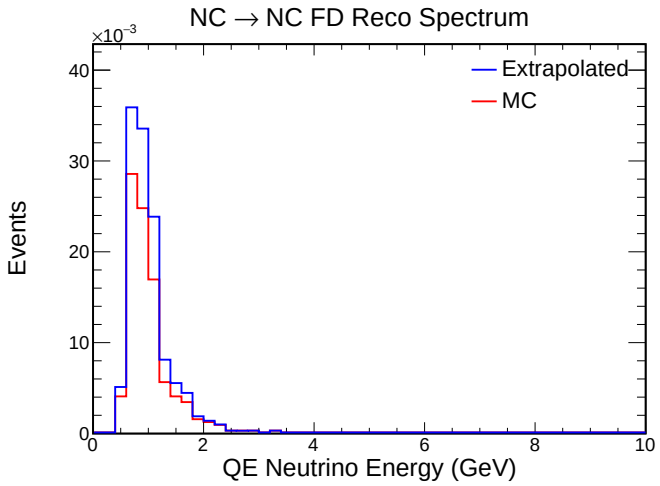

Figure A.28: Reconstructed energy spectra of selected QE events in far detector data and simulation. The extrapolated spectrum comes from extrapolated data events in the near detector and the simulation is from the base simulation of far detector events.

Appendix B

Systematics

The following sections show all plots individual systematic errors described in chapter 11 for both the QE,Non-QE, and escaping samples.

B.1 Beam

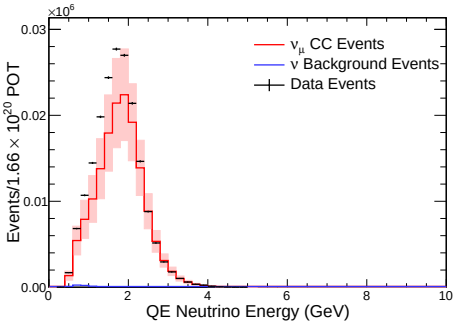

(a) Near Detector

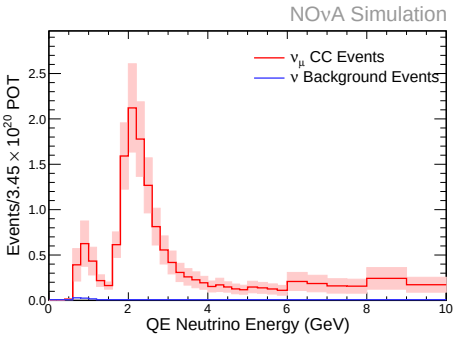

(b) Far Detector without Extrapolation

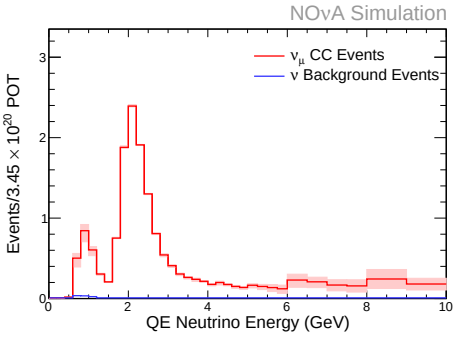

(c) Far Detector with Extrapolation

Figure B.1: Reconstructed energy of selected events in the QE sample with the systematic error band from beam uncertainties. All selected simulated events are shown in red with the a red systematic error band. The contribution to the selected events from background in the simulation is shown in blue. For the near detector the data is drawn in black with statistical error bars. For the far detector the oscillation parameters listed in table 2.1 are assumed.

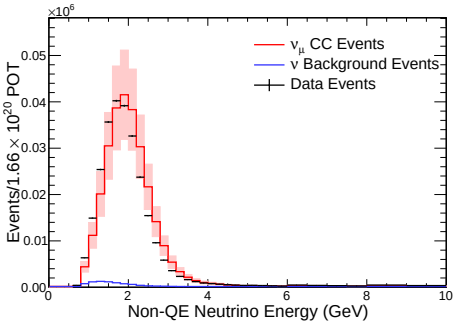

(a) Near Detector

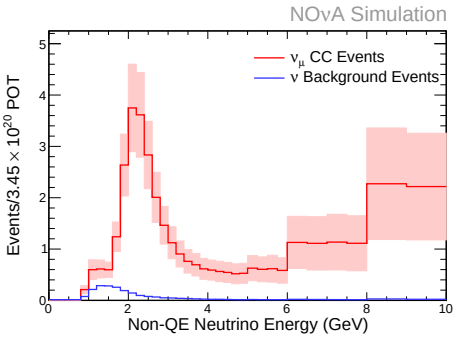

(b) Far Detector without Extrapolation

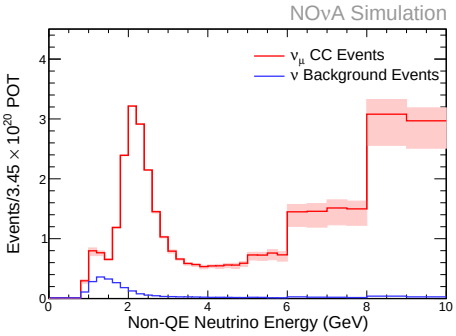

(c) Far Detector with Extrapolation

Figure B.2: Reconstructed energy of selected events in the nonQE sample with the systematic error band from beam uncertainties. All selected simulated events are shown in red with the a red systematic error band. The contribution to the selected events from background in the simulation is shown in blue. For the near detector the data is drawn in black with statistical error bars. For the far detector the oscillation parameters listed in table 2.1 are assumed.

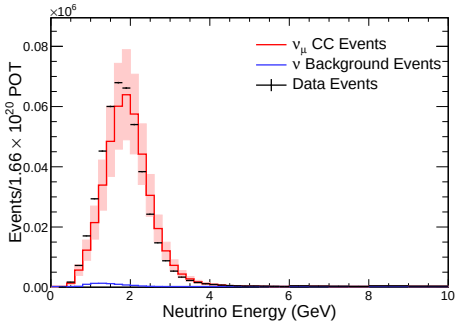

(a) Near Detector

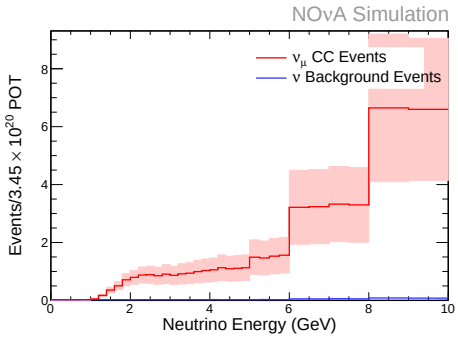

(b) Far Detector without Extrapolation

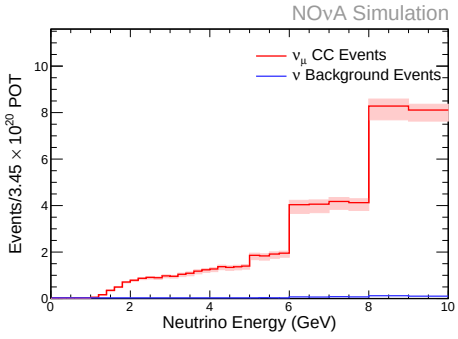

(c) Far Detector with Extrapolation

Figure B.3: Reconstructed energy of selected events in the escaping sample with the systematic error band from beam uncertainties. All selected simulated events are shown in red with the a red systematic error band. The contribution to the selected events from background in the simulation is shown in blue. For the near detector the data is drawn in black with statistical error bars. For the far detector the oscillation parameters listed in table 2.1 are assumed.

B.2 Large GENIE uncertainties

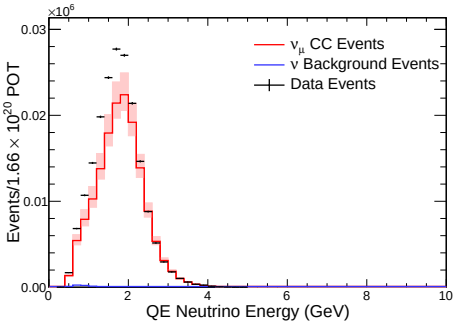

(a) Near Detector

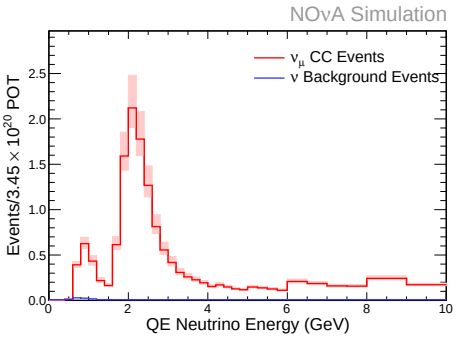

(b) Far Detector without Extrapolation

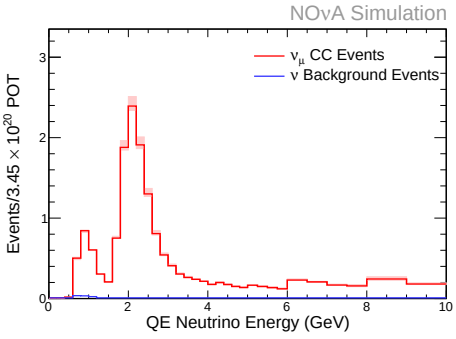

(c) Far Detector with Extrapolation

Figure B.4: Reconstructed energy of selected events in the QE sample with the systematic error band from M_A CC QE. All selected simulated events are shown in red with the a red systematic error band. The contribution to the selected events from background in the simulation is shown in blue. For the near detector the data is drawn in black with statistical error bars. For the far detector the oscillation parameters listed in table 2.1 are assumed.

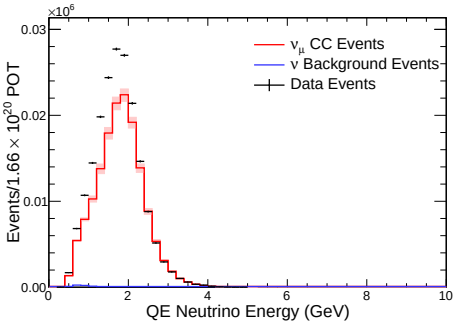

(a) Near Detector

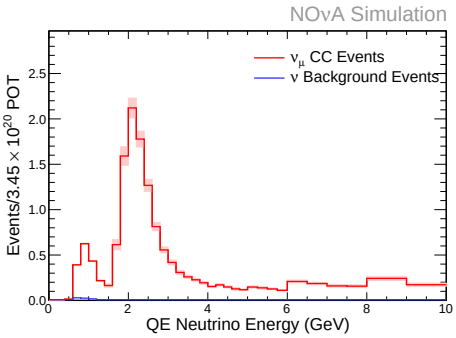

(b) Far Detector without Extrapolation

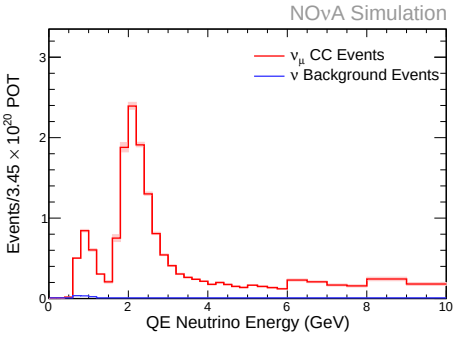

(c) Far Detector with Extrapolation

Figure B.5: Reconstructed energy of selected events in the QE sample with the systematic error band from M_A CC RES. All selected simulated events are shown in red with the a red systematic error band. The contribution to the selected events from background in the simulation is shown in blue. For the near detector the data is drawn in black with statistical error bars. For the far detector the oscillation parameters listed in table 2.1 are assumed.

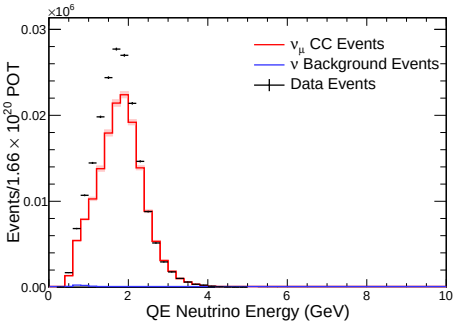

(a) Near Detector

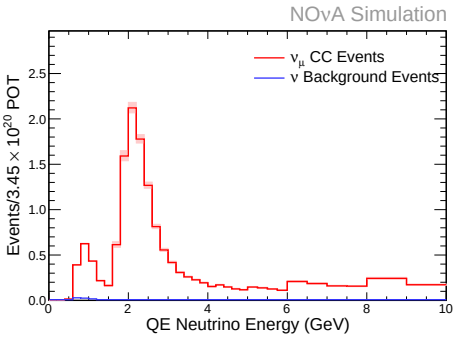

(b) Far Detector without Extrapolation

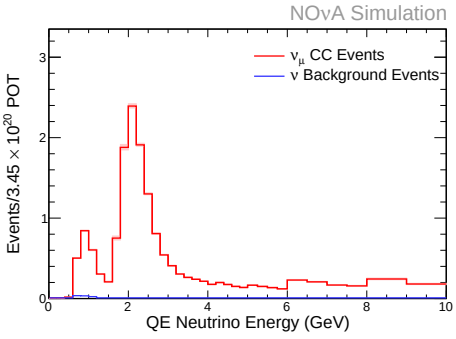

(c) Far Detector with Extrapolation

Figure B.6: Reconstructed energy of selected events in the QE sample with the systematic error band from M_v CC RES. All selected simulated events are shown in red with the a red systematic error band. The contribution to the selected events from background in the simulation is shown in blue. For the near detector the data is drawn in black with statistical error bars. For the far detector the oscillation parameters listed in table 2.1 are assumed.

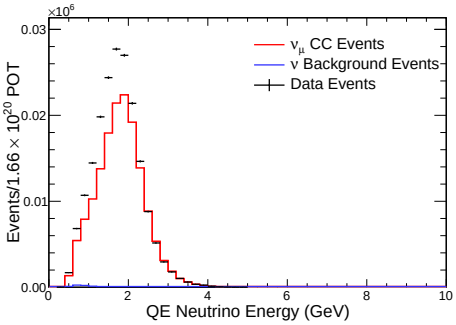

(a) Near Detector

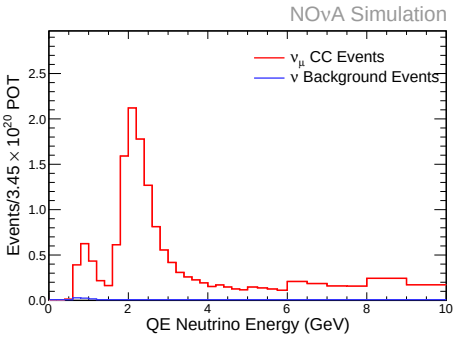

(b) Far Detector without Extrapolation

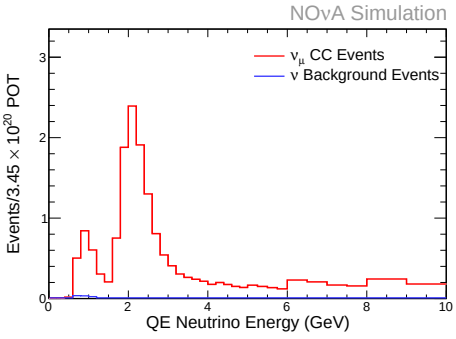

(c) Far Detector with Extrapolation

Figure B.7: Reconstructed energy of selected events in the QE sample with the systematic error band from M_A NC RES. All selected simulated events are shown in red with the a red systematic error band. The contribution to the selected events from background in the simulation is shown in blue. For the near detector the data is drawn in black with statistical error bars. For the far detector the oscillation parameters listed in table 2.1 are assumed.

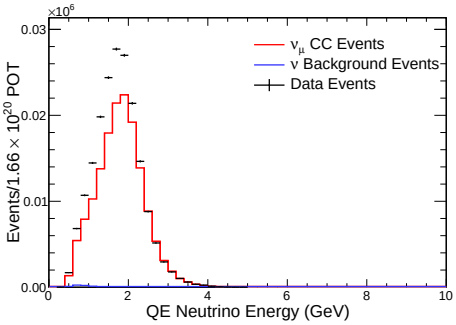

(a) Near Detector

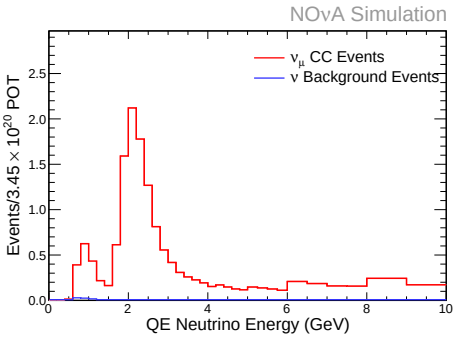

(b) Far Detector without Extrapolation

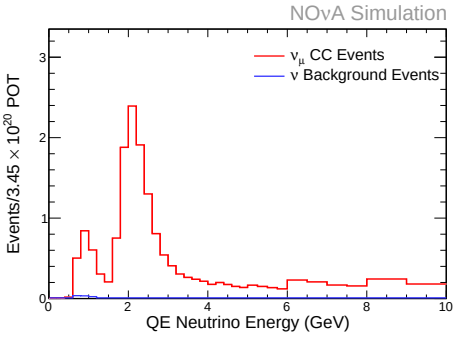

(c) Far Detector with Extrapolation

Figure B.8: Reconstructed energy of selected events in the QE sample with the systematic error band from M_v NC RES. All selected simulated events are shown in red with the a red systematic error band. The contribution to the selected events from background in the simulation is shown in blue. For the near detector the data is drawn in black with statistical error bars. For the far detector the oscillation parameters listed in table 2.1 are assumed.

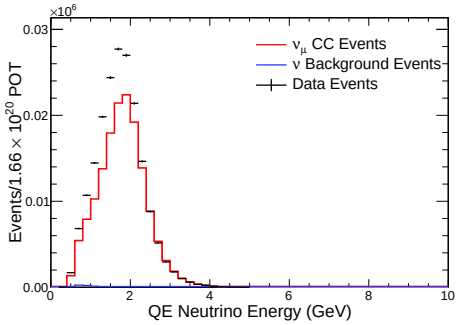

(a) Near Detector

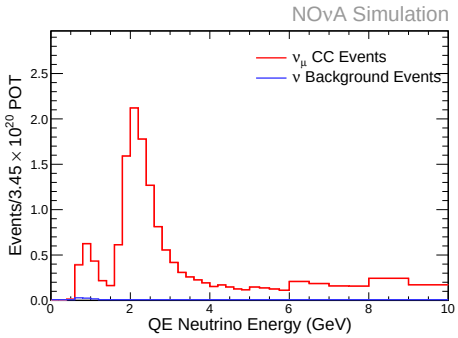

(b) Far Detector without Extrapolation

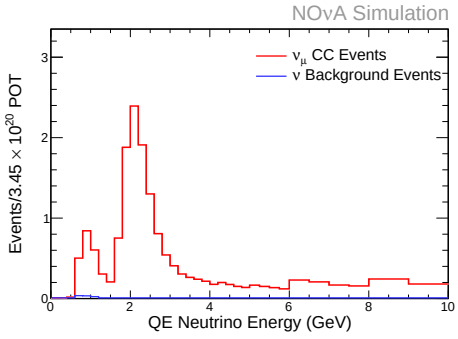

(c) Far Detector with Extrapolation

Figure B.9: Reconstructed energy of selected events in the QE sample with the systematic error band from M_A NC elastic. All selected simulated events are shown in red with the a red systematic error band. The contribution to the selected events from background in the simulation is shown in blue. For the near detector the data is drawn in black with statistical error bars. For the far detector the oscillation parameters listed in table 2.1 are assumed.

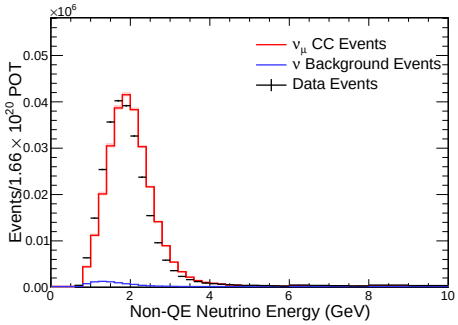

(a) Near Detector

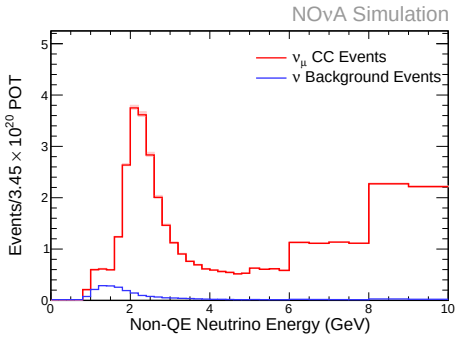

(b) Far Detector without Extrapolation

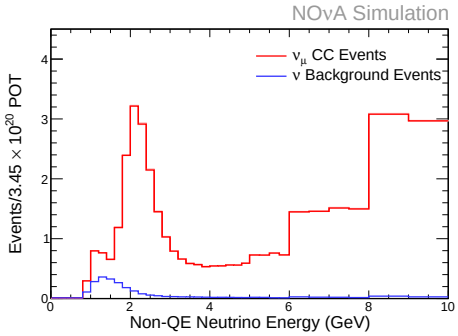

(c) Far Detector with Extrapolation

Figure B.10: Reconstructed energy of selected events in the nonQE sample with the systematic error band from M_A CC QE. All selected simulated events are shown in red with the a red systematic error band. The contribution to the selected events from background in the simulation is shown in blue. For the near detector the data is drawn in black with statistical error bars. For the far detector the oscillation parameters listed in table 2.1 are assumed.

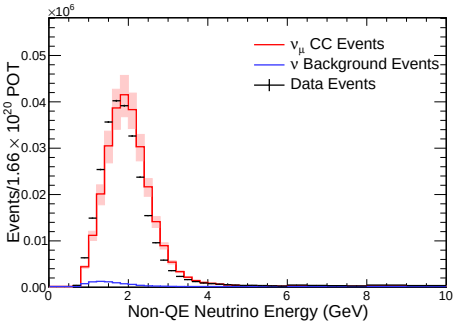

(a) Near Detector

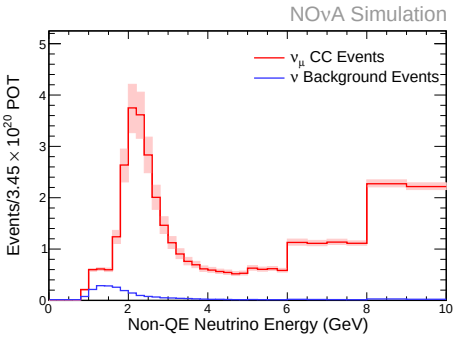

(b) Far Detector without Extrapolation

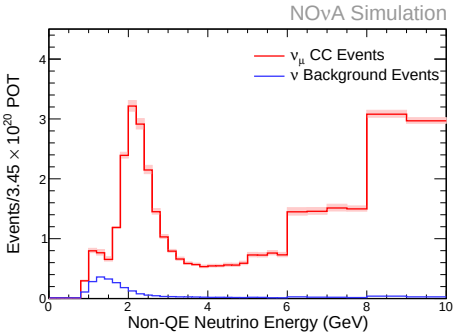

(c) Far Detector with Extrapolation

Figure B.11: Reconstructed energy of selected events in the nonQE sample with the systematic error band from M_A CC RES. All selected simulated events are shown in red with the a red systematic error band. The contribution to the selected events from background in the simulation is shown in blue. For the near detector the data is drawn in black with statistical error bars. For the far detector the oscillation parameters listed in table 2.1 are assumed.

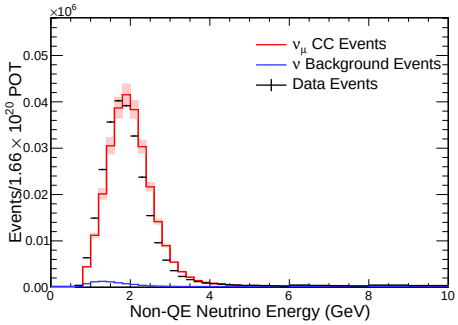

(a) Near Detector

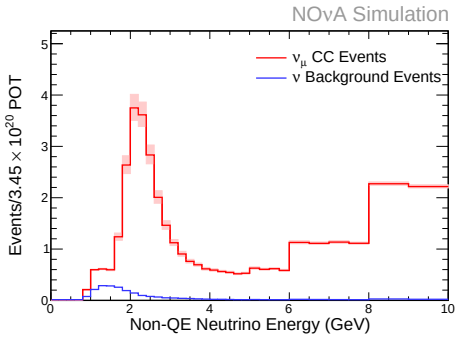

(b) Far Detector without Extrapolation

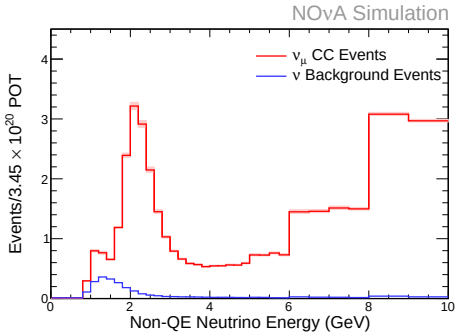

(c) Far Detector with Extrapolation

Figure B.12: Reconstructed energy of selected events in the nonQE sample with the systematic error band from M_v CC RES. All selected simulated events are shown in red with the a red systematic error band. The contribution to the selected events from background in the simulation is shown in blue. For the near detector the data is drawn in black with statistical error bars. For the far detector the oscillation parameters listed in table 2.1 are assumed.

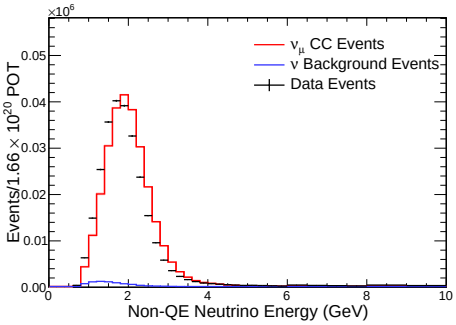

(a) Near Detector

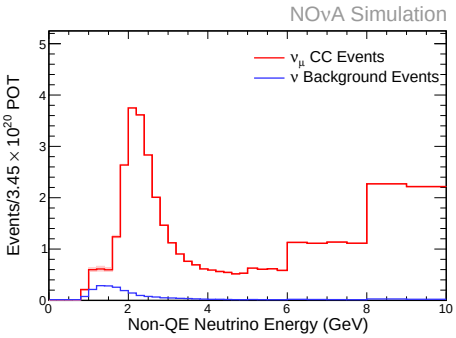

(b) Far Detector without Extrapolation

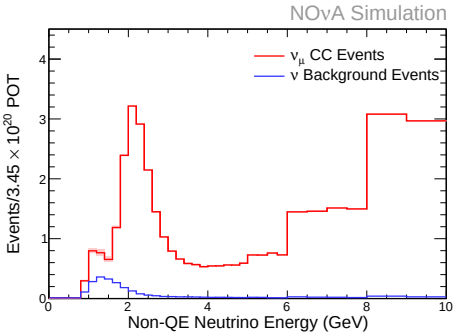

(c) Far Detector with Extrapolation

Figure B.13: Reconstructed energy of selected events in the nonQE sample with the systematic error band from M_A NC RES. All selected simulated events are shown in red with the a red systematic error band. The contribution to the selected events from background in the simulation is shown in blue. For the near detector the data is drawn in black with statistical error bars. For the far detector the oscillation parameters listed in table 2.1 are assumed.

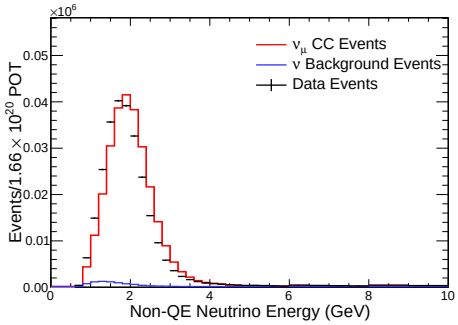

(a) Near Detector

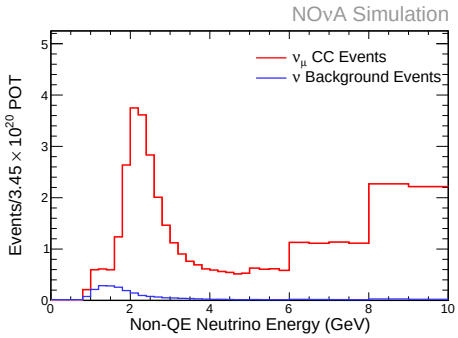

(b) Far Detector without Extrapolation

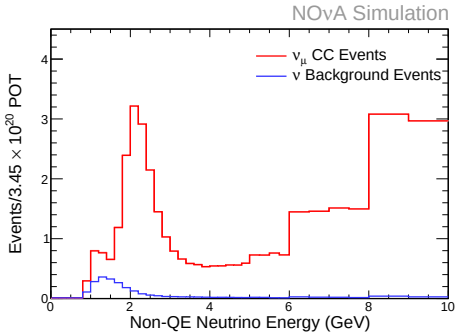

(c) Far Detector with Extrapolation

Figure B.14: Reconstructed energy of selected events in the nonQE sample with the systematic error band from M_v NC RES. All selected simulated events are shown in red with the a red systematic error band. The contribution to the selected events from background in the simulation is shown in blue. For the near detector the data is drawn in black with statistical error bars. For the far detector the oscillation parameters listed in table 2.1 are assumed.

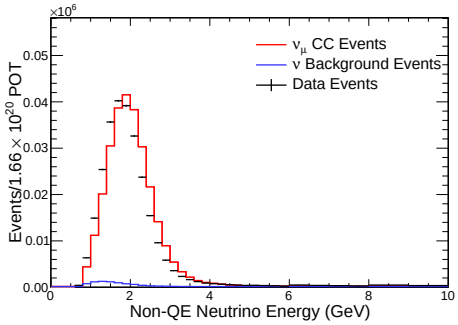

(a) Near Detector

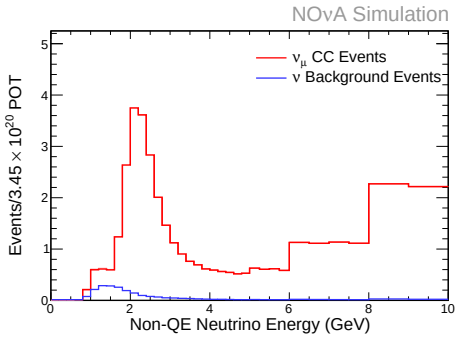

(b) Far Detector without Extrapolation

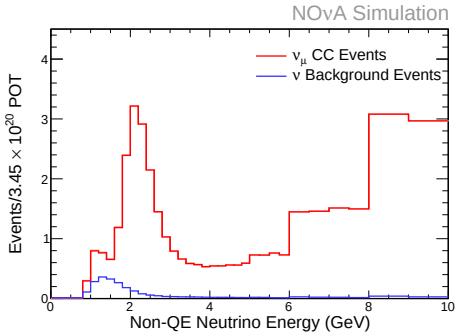

(c) Far Detector with Extrapolation

Figure B.15: Reconstructed energy of selected events in the nonQE sample with the systematic error band from M_A NC elastic. All selected simulated events are shown in red with the a red systematic error band. The contribution to the selected events from background in the simulation is shown in blue. For the near detector the data is drawn in black with statistical error bars. For the far detector the oscillation parameters listed in table 2.1 are assumed.

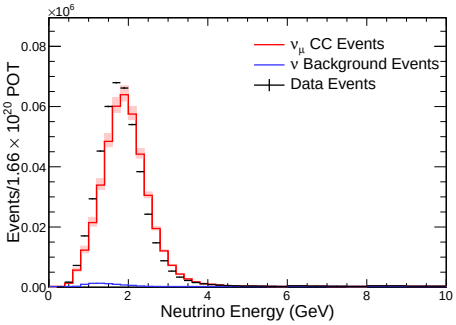

(a) Near Detector

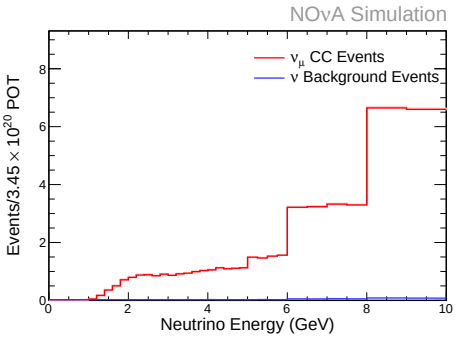

(b) Far Detector without Extrapolation

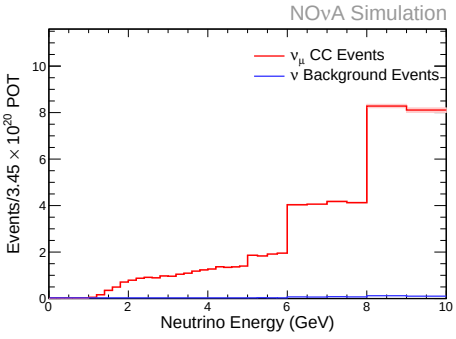

(c) Far Detector with Extrapolation

Figure B.16: Reconstructed energy of selected events in the escaping sample with the systematic error band from M_A CC QE. All selected simulated events are shown in red with the a red systematic error band. The contribution to the selected events from background in the simulation is shown in blue. For the near detector the data is drawn in black with statistical error bars. For the far detector the oscillation parameters listed in table 2.1 are assumed.

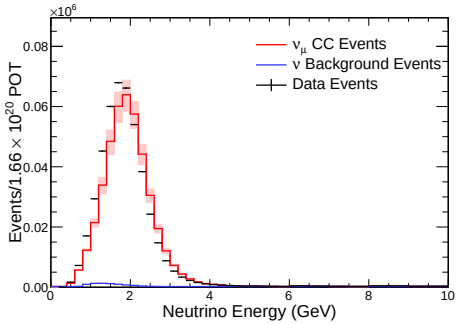

(a) Near Detector

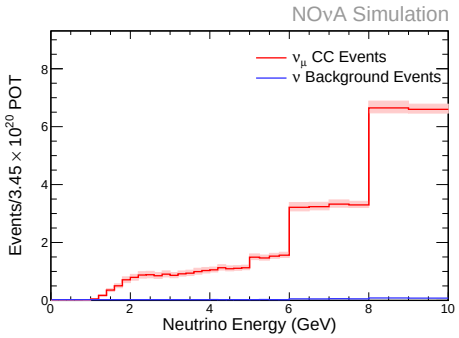

(b) Far Detector without Extrapolation

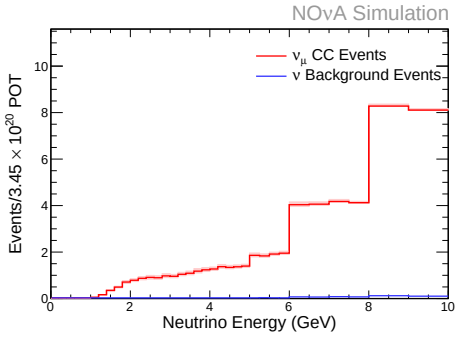

(c) Far Detector with Extrapolation

Figure B.17: Reconstructed energy of selected events in the escaping sample with the systematic error band from M_A CC RES. All selected simulated events are shown in red with the a red systematic error band. The contribution to the selected events from background in the simulation is shown in blue. For the near detector the data is drawn in black with statistical error bars. For the far detector the oscillation parameters listed in table 2.1 are assumed.

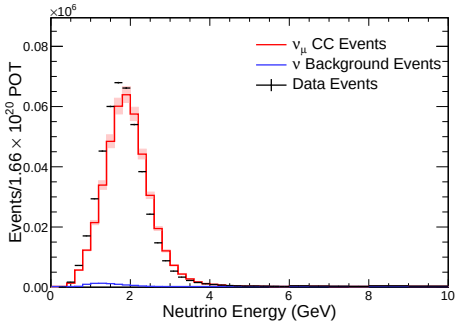

(a) Near Detector

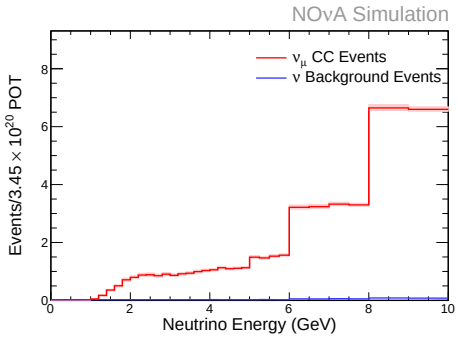

(b) Far Detector without Extrapolation

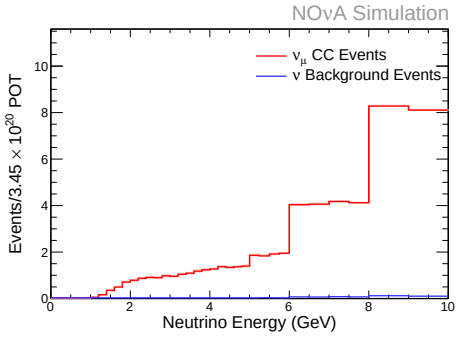

(c) Far Detector with Extrapolation

Figure B.18: Reconstructed energy of selected events in the escaping sample with the systematic error band from M_v CC RES. All selected simulated events are shown in red with the a red systematic error band. The contribution to the selected events from background in the simulation is shown in blue. For the near detector the data is drawn in black with statistical error bars. For the far detector the oscillation parameters listed in table 2.1 are assumed.

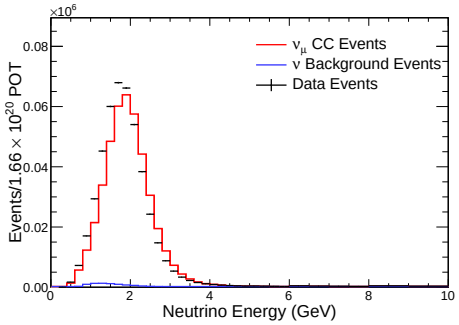

(a) Near Detector

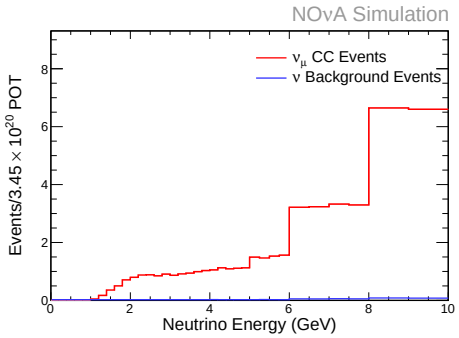

(b) Far Detector without Extrapolation

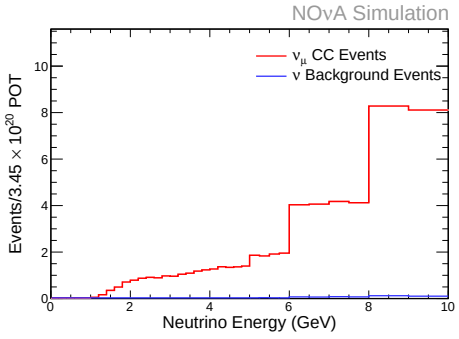

(c) Far Detector with Extrapolation

Figure B.19: Reconstructed energy of selected events in the escaping sample with the systematic error band from M_A NC RES. All selected simulated events are shown in red with the a red systematic error band. The contribution to the selected events from background in the simulation is shown in blue. For the near detector the data is drawn in black with statistical error bars. For the far detector the oscillation parameters listed in table 2.1 are assumed.

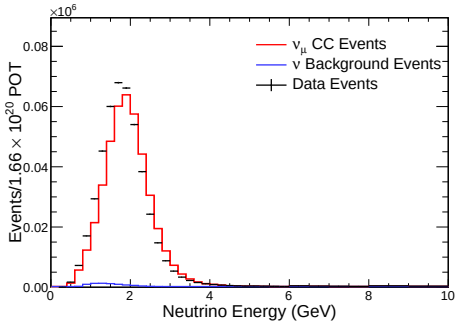

(a) Near Detector

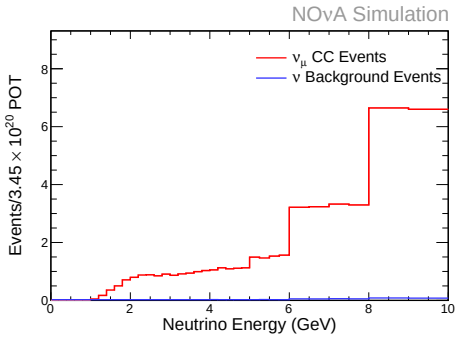

(b) Far Detector without Extrapolation

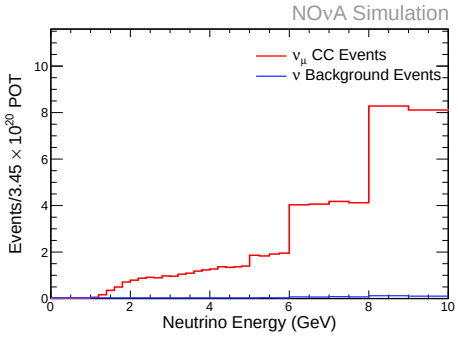

(c) Far Detector with Extrapolation

Figure B.20: Reconstructed energy of selected events in the escaping sample with the systematic error band from M_v NC RES. All selected simulated events are shown in red with the a red systematic error band. The contribution to the selected events from background in the simulation is shown in blue. For the near detector the data is drawn in black with statistical error bars. For the far detector the oscillation parameters listed in table 2.1 are assumed.

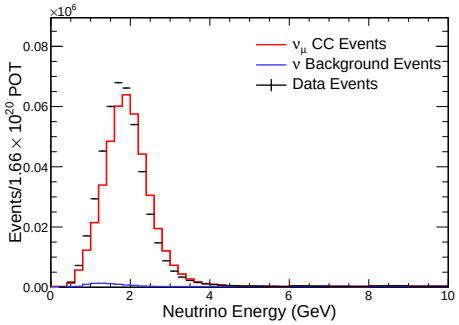

(a) Near Detector

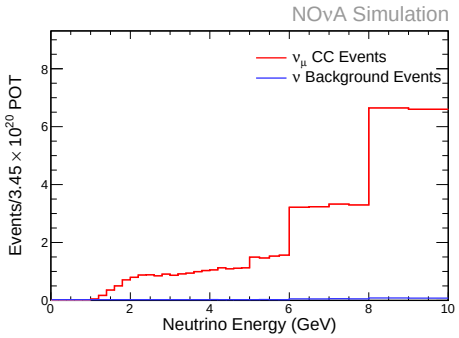

(b) Far Detector without Extrapolation

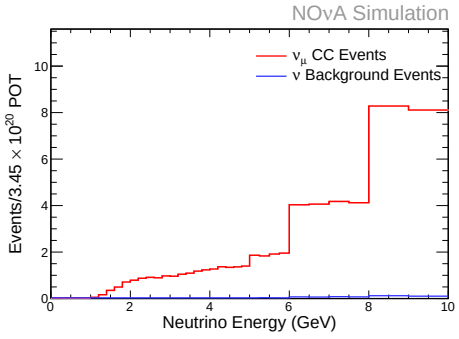

(c) Far Detector with Extrapolation

Figure B.21: Reconstructed energy of selected events in the escaping sample with the systematic error band from M_A NC elastic. All selected simulated events are shown in red with the a red systematic error band. The contribution to the selected events from background in the simulation is shown in blue. For the near detector the data is drawn in black with statistical error bars. For the far detector the oscillation parameters listed in table 2.1 are assumed.

B.2.1 Small GENIE uncertainties

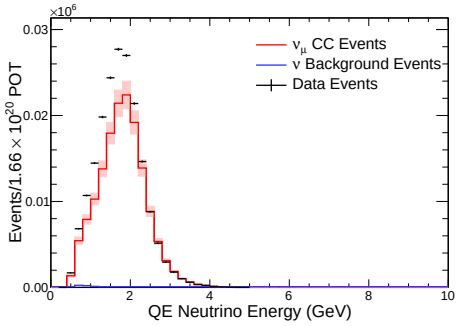

(a) Near Detector

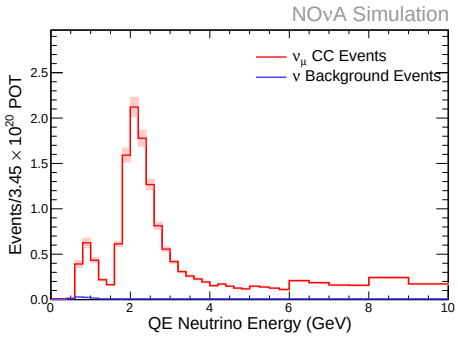

(b) Far Detector without Extrapolation

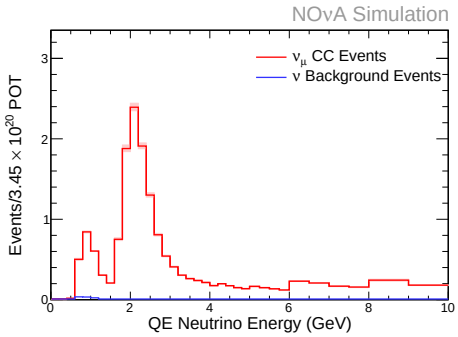

(c) Far Detector with Extrapolation

Figure B.22: Reconstructed energy of selected events in the QE sample with the systematic error band from the small GENIE uncertainties. All selected simulated events are shown in red with the a red systematic error band. The contribution to the selected events from background in the simulation is shown in blue. For the near detector the data is drawn in black with statistical error bars. For the far detector the oscillation parameters listed in table 2.1 are assumed.

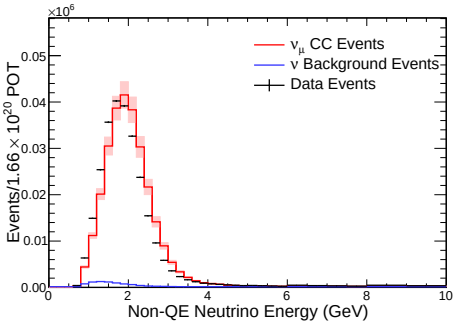

(a) Near Detector

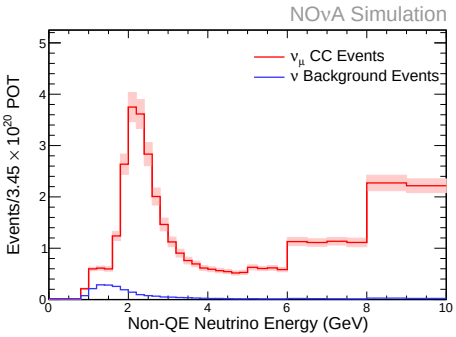

(b) Far Detector without Extrapolation

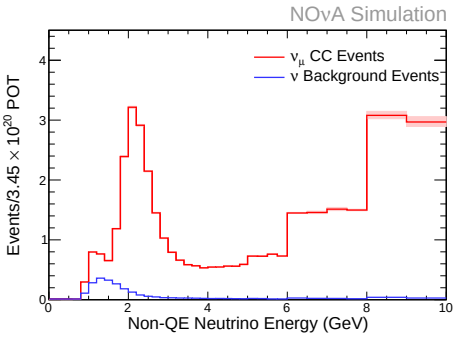

(c) Far Detector with Extrapolation

Figure B.23: Reconstructed energy of selected events in the nonQE sample with the systematic error band from the small GENIE uncertainties. All selected simulated events are shown in red with the a red systematic error band. The contribution to the selected events from background in the simulation is shown in blue. For the near detector the data is drawn in black with statistical error bars. For the far detector the oscillation parameters listed in table 2.1 are assumed.

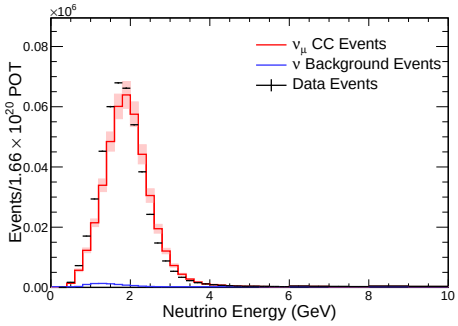

(a) Near Detector

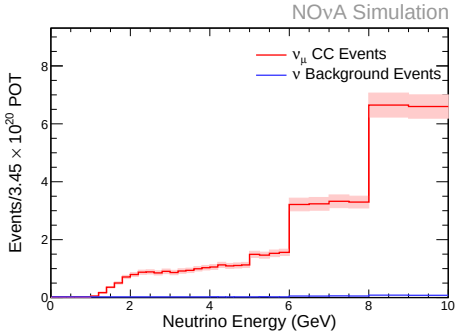

(b) Far Detector without Extrapolation

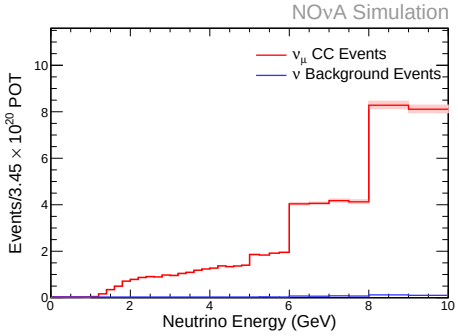

(c) Far Detector with Extrapolation

Figure B.24: Reconstructed energy of selected events in the escaping sample with the systematic error band from the small GENIE uncertainties. All selected simulated events are shown in red with the a red systematic error band. The contribution to the selected events from background in the simulation is shown in blue. For the near detector the data is drawn in black with statistical error bars. For the far detector the oscillation parameters listed in table 2.1 are assumed.

B.3 Normalization

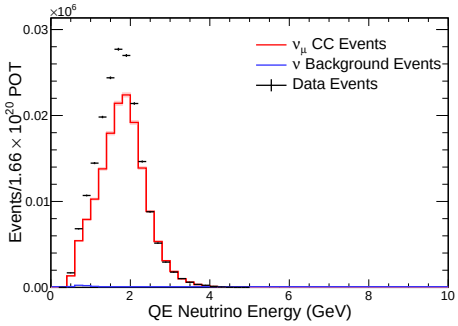

(a) Near Detector

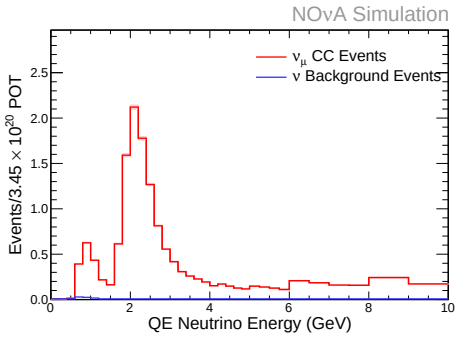

(b) Far Detector without Extrapolation

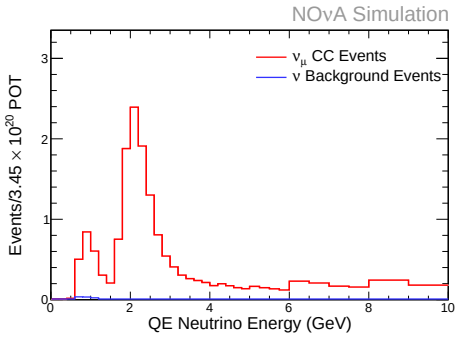

(c) Far Detector with Extrapolation

Figure B.25: Reconstructed energy of selected events in the QE sample with the systematic error band from the absolute normalization uncertainty. All selected simulated events are shown in red with the a red systematic error band. The contribution to the selected events from background in the simulation is shown in blue. For the near detector the data is drawn in black with statistical error bars. For the far detector the oscillation parameters listed in table 2.1 are assumed.

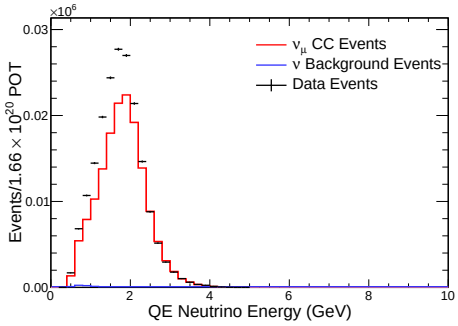

(a) Near Detector

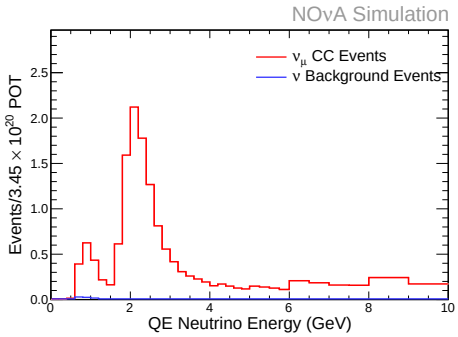

(b) Far Detector without Extrapolation

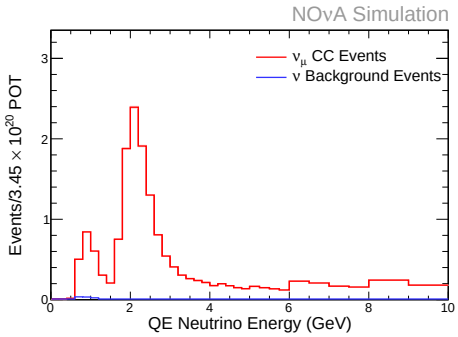

(c) Far Detector with Extrapolation

Figure B.26: Reconstructed energy of selected events in the QE sample with the systematic error band from the relative normalization uncertainty. All selected simulated events are shown in red with the a red systematic error band. The contribution to the selected events from background in the simulation is shown in blue. For the near detector the data is drawn in black with statistical error bars. For the far detector the oscillation parameters listed in table 2.1 are assumed.

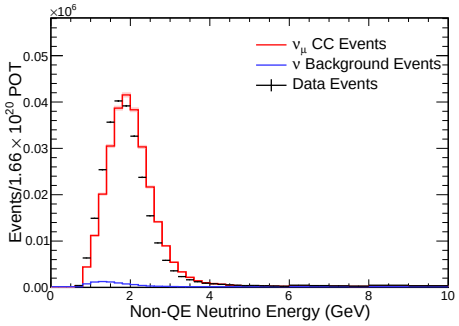

(a) Near Detector

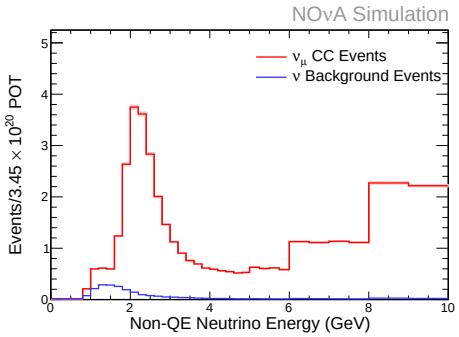

(b) Far Detector without Extrapolation

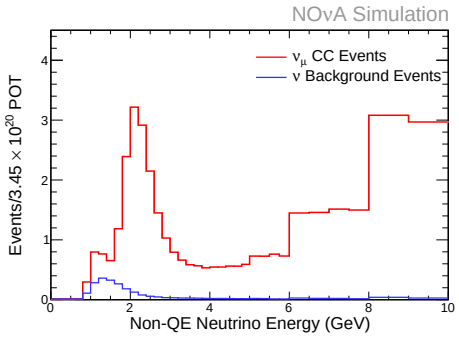

(c) Far Detector with Extrapolation

Figure B.27: Reconstructed energy of selected events in the nonQE sample with the systematic error band from the absolute normalization uncertainty. All selected simulated events are shown in red with the a red systematic error band. The contribution to the selected events from background in the simulation is shown in blue. For the near detector the data is drawn in black with statistical error bars. For the far detector the oscillation parameters listed in table 2.1 are assumed.

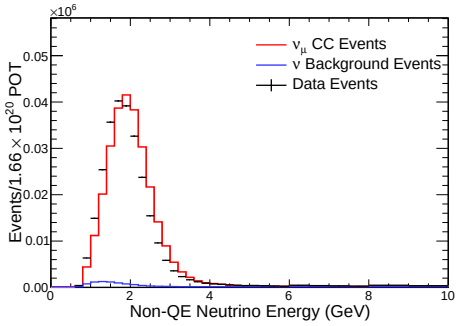

(a) Near Detector

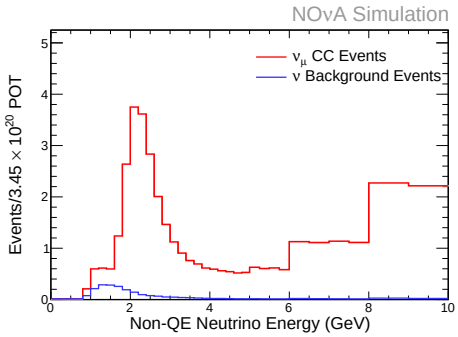

(b) Far Detector without Extrapolation

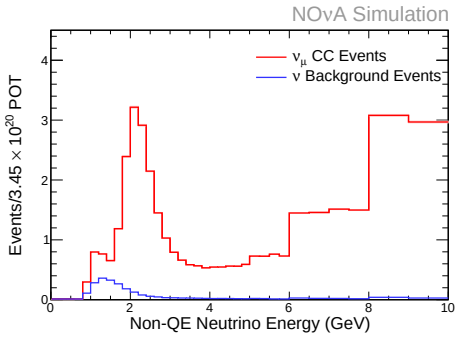

(c) Far Detector with Extrapolation

Figure B.28: Reconstructed energy of selected events in the nonQE sample with the systematic error band from the relative normalization uncertainty. All selected simulated events are shown in red with the a red systematic error band. The contribution to the selected events from background in the simulation is shown in blue. For the near detector the data is drawn in black with statistical error bars. For the far detector the oscillation parameters listed in table 2.1 are assumed.

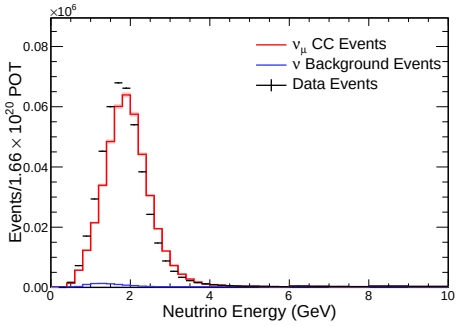

(a) Near Detector

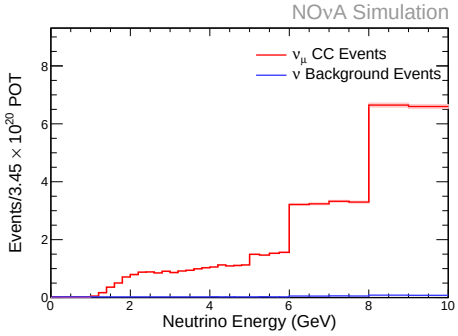

(b) Far Detector without Extrapolation

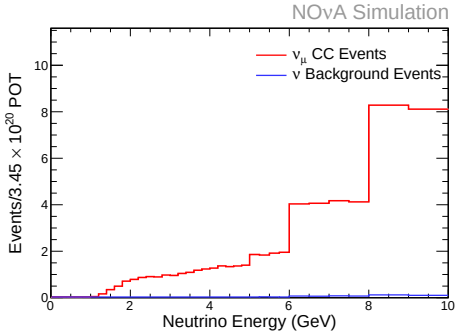

(c) Far Detector with Extrapolation

Figure B.29: Reconstructed energy of selected events in the escaping sample with the systematic error band from the absolute normalization uncertainty. All selected simulated events are shown in red with the a red systematic error band. The contribution to the selected events from background in the simulation is shown in blue. For the near detector the data is drawn in black with statistical error bars. For the far detector the oscillation parameters listed in table 2.1 are assumed.

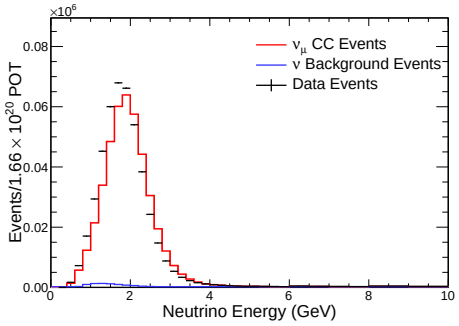

(a) Near Detector

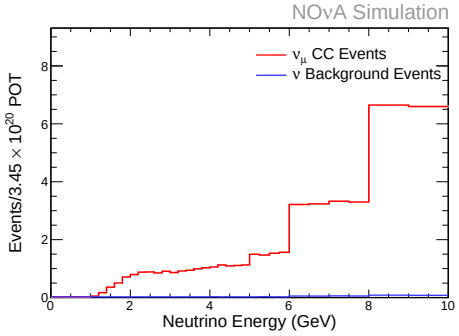

(b) Far Detector without Extrapolation

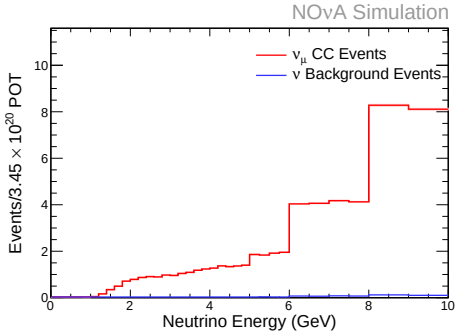

(c) Far Detector with Extrapolation

Figure B.30: Reconstructed energy of selected events in the escaping sample with the systematic error band from the relative normalization uncertainty. All selected simulated events are shown in red with the a red systematic error band. The contribution to the selected events from background in the simulation is shown in blue. For the near detector the data is drawn in black with statistical error bars. For the far detector the oscillation parameters listed in table 2.1 are assumed.

B.4 Absolute Energy Scale

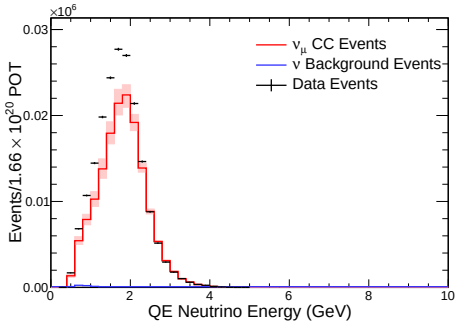

(a) Near Detector

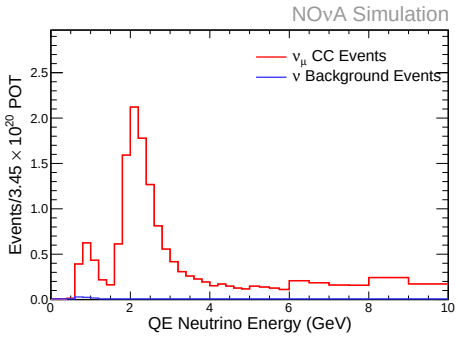

(b) Far Detector without Extrapolation

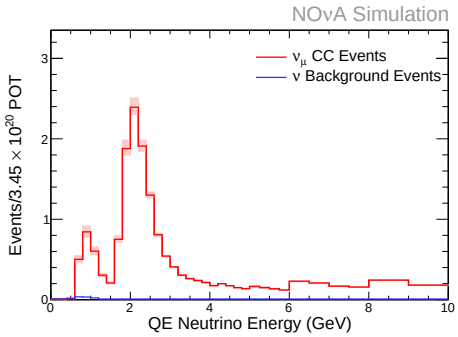

(c) Far Detector with Extrapolation

Figure B.31: Reconstructed energy of selected events in the QE sample with the systematic error band from the absolute energy uncertainty in the near detector. All selected simulated events are shown in red with the a red systematic error band. The contribution to the selected events from background in the simulation is shown in blue. For the near detector the data is drawn in black with statistical error bars. For the far detector the oscillation parameters listed in table 2.1 are assumed.

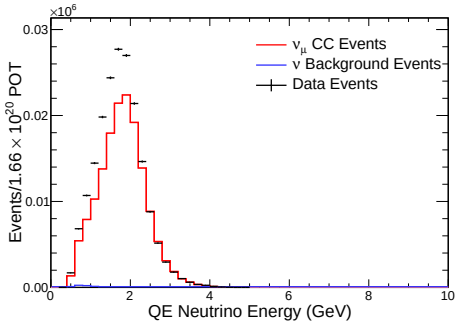

(a) Near Detector

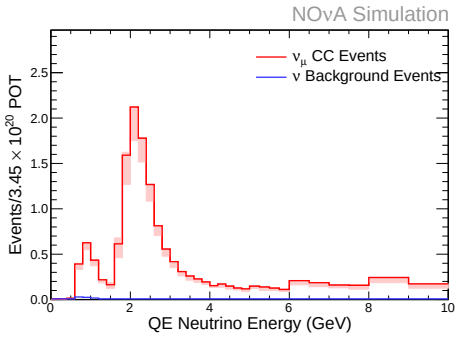

(b) Far Detector without Extrapolation

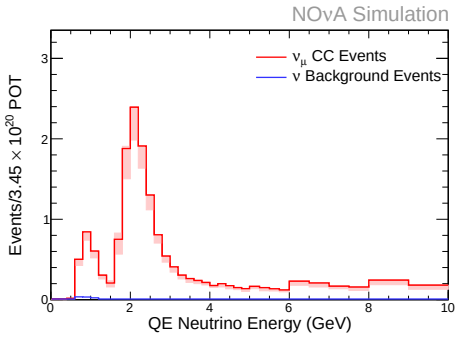

(c) Far Detector with Extrapolation

Figure B.32: Reconstructed energy of selected events in the QE sample with the systematic error band from the absolute energy uncertainty in the far detector. All selected simulated events are shown in red with the a red systematic error band. The contribution to the selected events from background in the simulation is shown in blue. For the near detector the data is drawn in black with statistical error bars. For the far detector the oscillation parameters listed in table 2.1 are assumed.

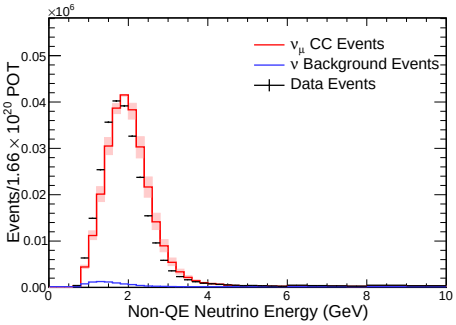

(a) Near Detector

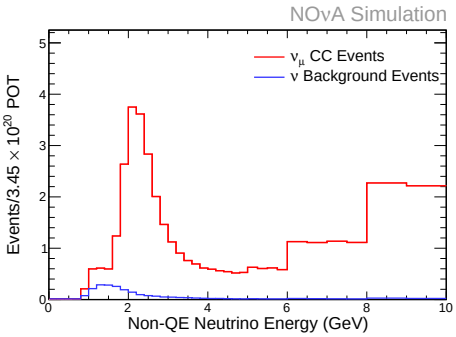

(b) Far Detector without Extrapolation

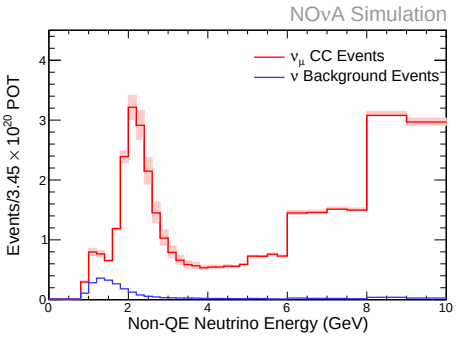

(c) Far Detector with Extrapolation

Figure B.33: Reconstructed energy of selected events in the nonQE sample with the systematic error band from the absolute energy uncertainty in the near detector. All selected simulated events are shown in red with the a red systematic error band. The contribution to the selected events from background in the simulation is shown in blue. For the near detector the data is drawn in black with statistical error bars. For the far detector the oscillation parameters listed in table 2.1 are assumed.

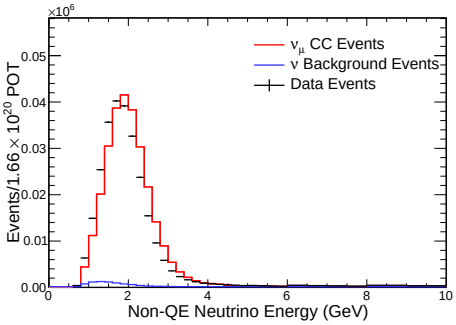

(a) Near Detector

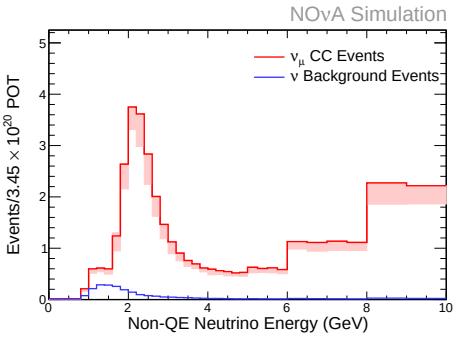

(b) Far Detector without Extrapolation

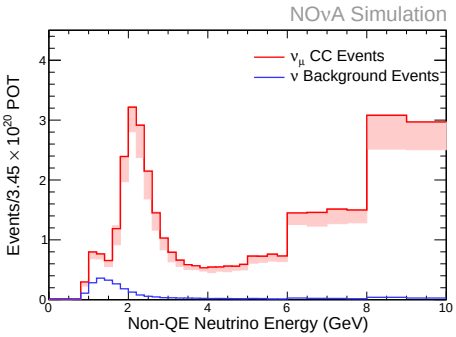

(c) Far Detector with Extrapolation

Figure B.34: Reconstructed energy of selected events in the nonQE sample with the systematic error band from the absolute energy uncertainty in the far detector. All selected simulated events are shown in red with the a red systematic error band. The contribution to the selected events from background in the simulation is shown in blue. For the near detector the data is drawn in black with statistical error bars. For the far detector the oscillation parameters listed in table 2.1 are assumed.

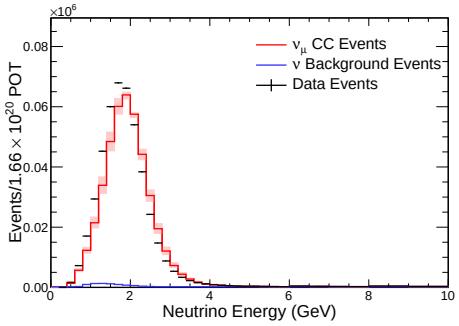

(a) Near Detector

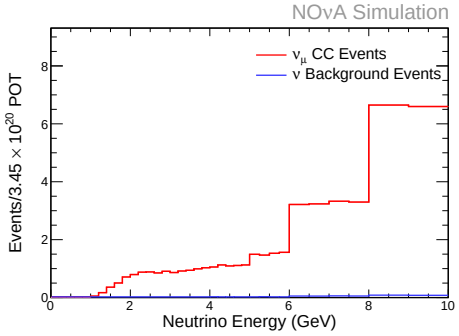

(b) Far Detector without Extrapolation

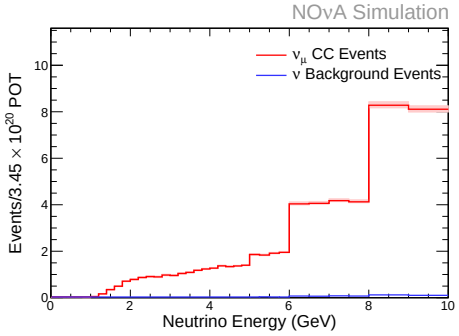

(c) Far Detector with Extrapolation

Figure B.35: Reconstructed energy of selected events in the escaping sample with the systematic error band from the absolute energy uncertainty in the near detector. All selected simulated events are shown in red with the a red systematic error band. The contribution to the selected events from background in the simulation is shown in blue. For the near detector the data is drawn in black with statistical error bars. For the far detector the oscillation parameters listed in table 2.1 are assumed.

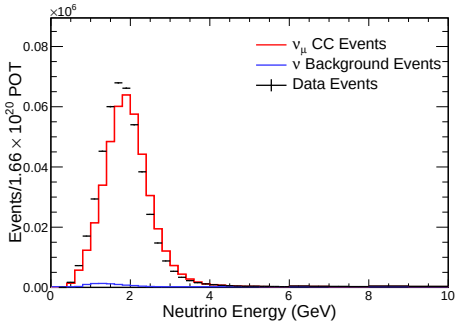

(a) Near Detector

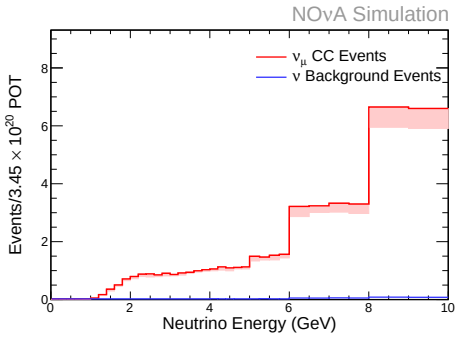

(b) Far Detector without Extrapolation

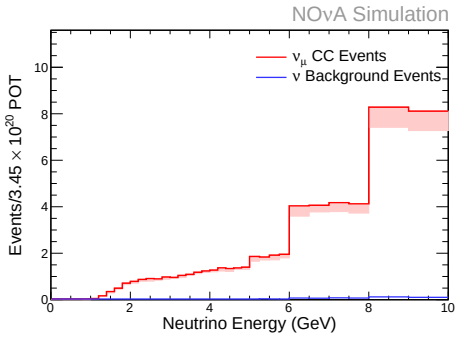

(c) Far Detector with Extrapolation

Figure B.36: Reconstructed energy of selected events in the escaping sample with the systematic error band from the absolute energy uncertainty in the far detector. All selected simulated events are shown in red with the a red systematic error band. The contribution to the selected events from background in the simulation is shown in blue. For the near detector the data is drawn in black with statistical error bars. For the far detector the oscillation parameters listed in table 2.1 are assumed.

B.5 Hadronic Hit

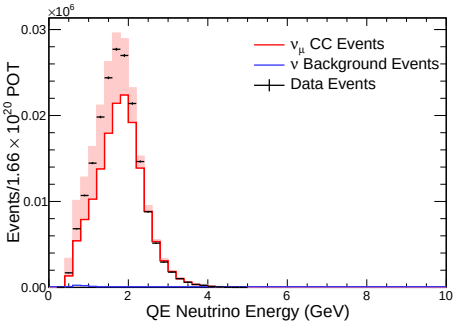

(a) Near Detector

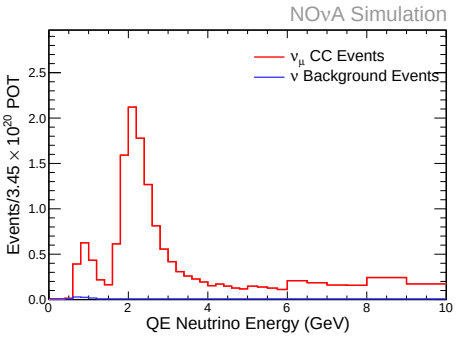

(b) Far Detector without Extrapolation

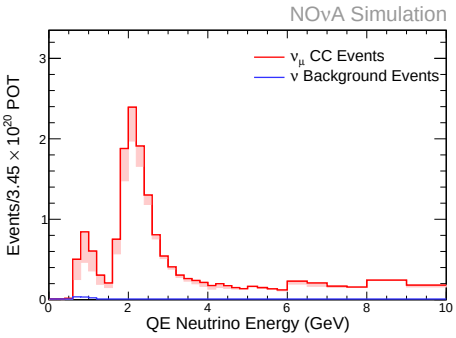

(c) Far Detector with Extrapolation

Figure B.37: Reconstructed energy of selected events in the QE sample with the systematic error band from the hadronic modeling uncertainty in the near detector. All selected simulated events are shown in red with the a red systematic error band. The contribution to the selected events from background in the simulation is shown in blue. For the near detector the data is drawn in black with statistical error bars. For the far detector the oscillation parameters listed in table 2.1 are assumed.

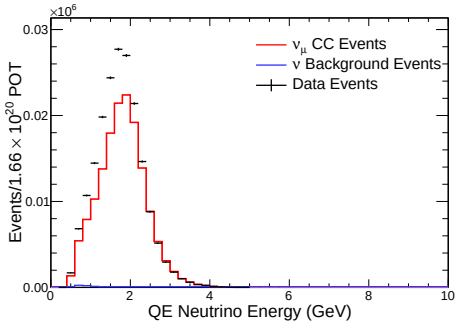

(a) Near Detector

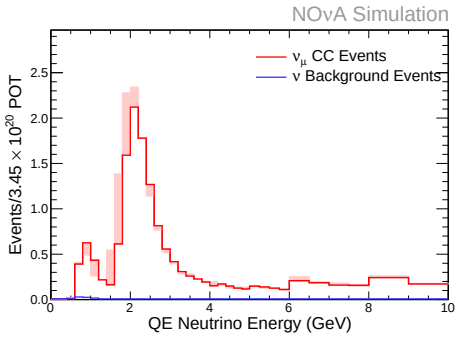

(b) Far Detector without Extrapolation

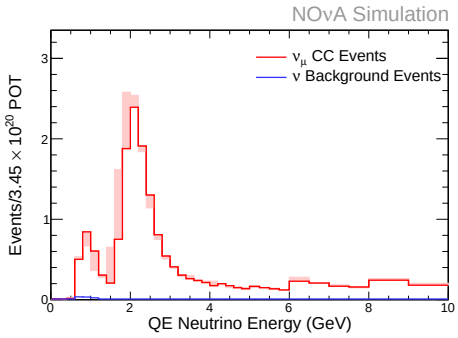

(c) Far Detector with Extrapolation

Figure B.38: Reconstructed energy of selected events in the QE sample with the systematic error band from the hadronic modeling uncertainty in the far detector. All selected simulated events are shown in red with the a red systematic error band. The contribution to the selected events from background in the simulation is shown in blue. For the near detector the data is drawn in black with statistical error bars. For the far detector the oscillation parameters listed in table 2.1 are assumed.

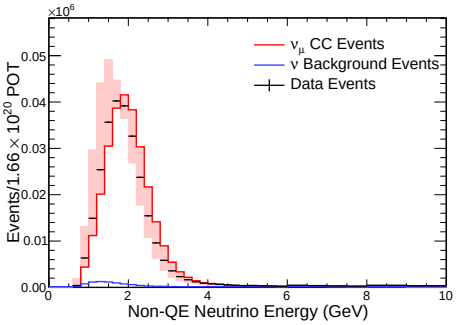

(a) Near Detector

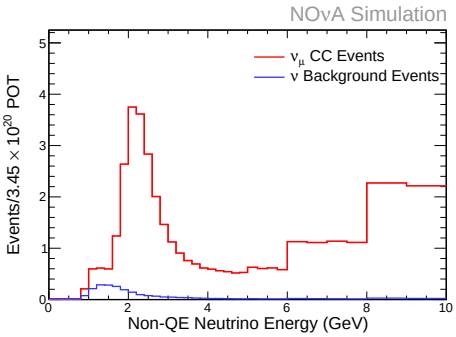

(b) Far Detector without Extrapolation

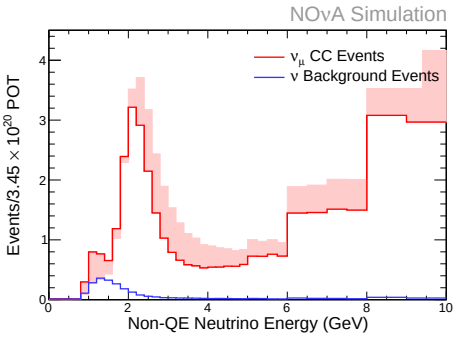

(c) Far Detector with Extrapolation

Figure B.39: Reconstructed energy of selected events in the nonQE sample with the systematic error band from the hadronic modeling uncertainty in the near detector. All selected simulated events are shown in red with the a red systematic error band. The contribution to the selected events from background in the simulation is shown in blue. For the near detector the data is drawn in black with statistical error bars. For the far detector the oscillation parameters listed in table 2.1 are assumed.

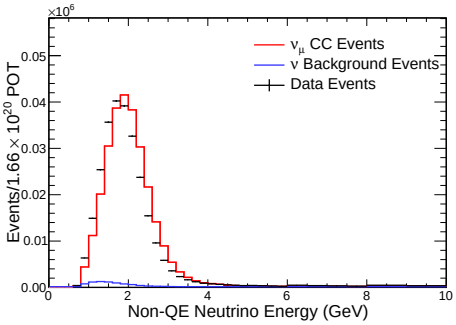

(a) Near Detector

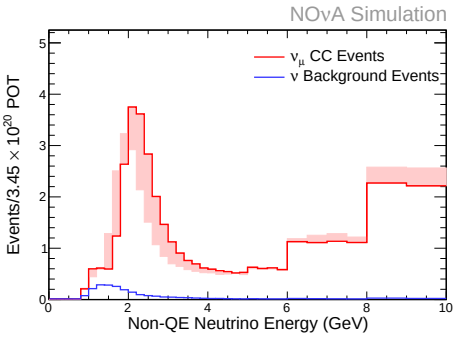

(b) Far Detector without Extrapolation

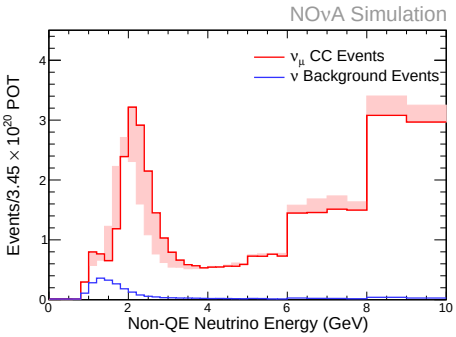

(c) Far Detector with Extrapolation

Figure B.40: Reconstructed energy of selected events in the nonQE sample with the systematic error band from the hadronic modeling uncertainty in the far detector. All selected simulated events are shown in red with the a red systematic error band. The contribution to the selected events from background in the simulation is shown in blue. For the near detector the data is drawn in black with statistical error bars. For the far detector the oscillation parameters listed in table 2.1 are assumed.

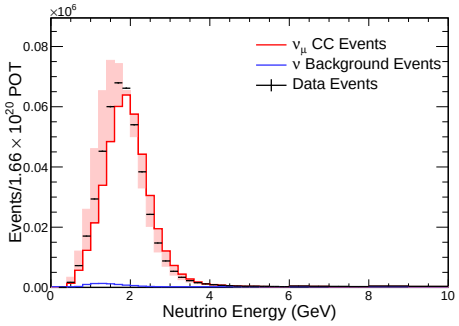

(a) Near Detector

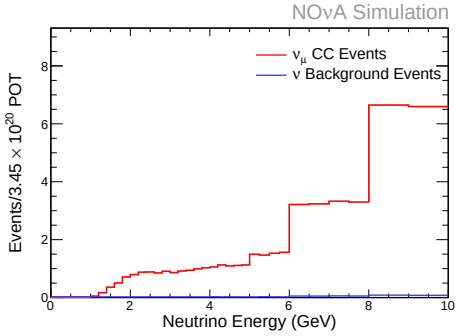

(b) Far Detector without Extrapolation

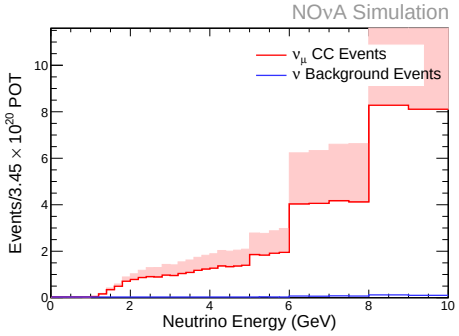

(c) Far Detector with Extrapolation

Figure B.41: Reconstructed energy of selected events in the escaping sample with the systematic error band from the hadronic modeling uncertainty in the near detector. All selected simulated events are shown in red with the a red systematic error band. The contribution to the selected events from background in the simulation is shown in blue. For the near detector the data is drawn in black with statistical error bars. For the far detector the oscillation parameters listed in table 2.1 are assumed.

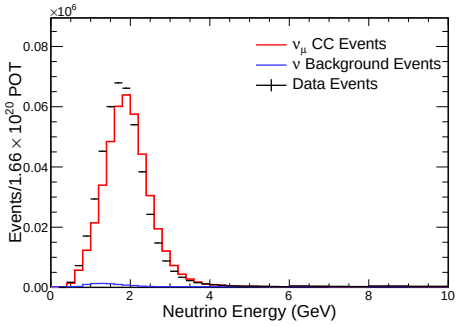

(a) Near Detector

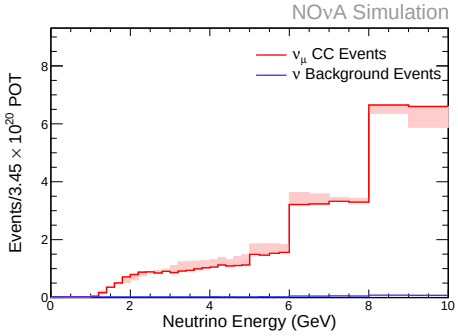

(b) Far Detector without Extrapolation

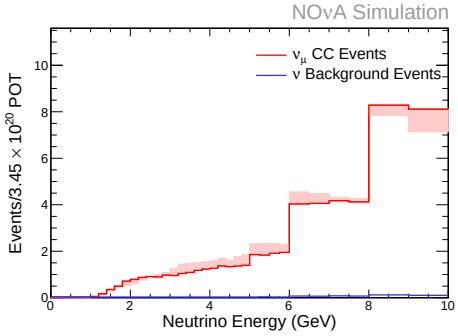

(c) Far Detector with Extrapolation

Figure B.42: Reconstructed energy of selected events in the escaping sample with the systematic error band from the hadronic modeling uncertainty in the far detector. All selected simulated events are shown in red with the a red systematic error band. The contribution to the selected events from background in the simulation is shown in blue. For the near detector the data is drawn in black with statistical error bars. For the far detector the oscillation parameters listed in table 2.1 are assumed.

Appendix C

Hadronic Model Systematic Simulation

The following plots show the data and simulation agreement of neutrino interactions in the near detector for the simulation used to estimate the hadronic modeling systematic.

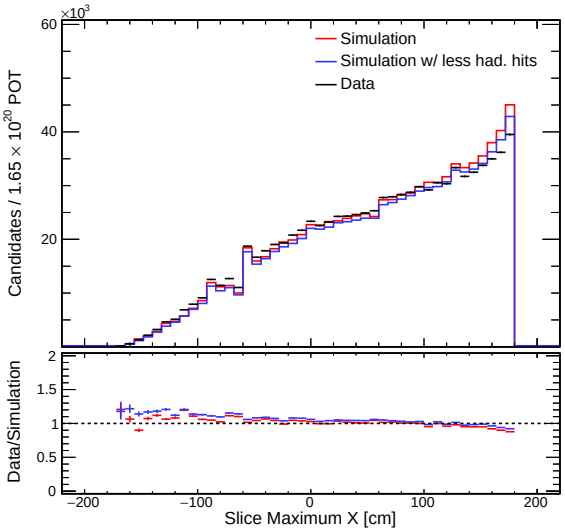

Figure C.1: Maximum position in the x direction of any hits in a contained slice.

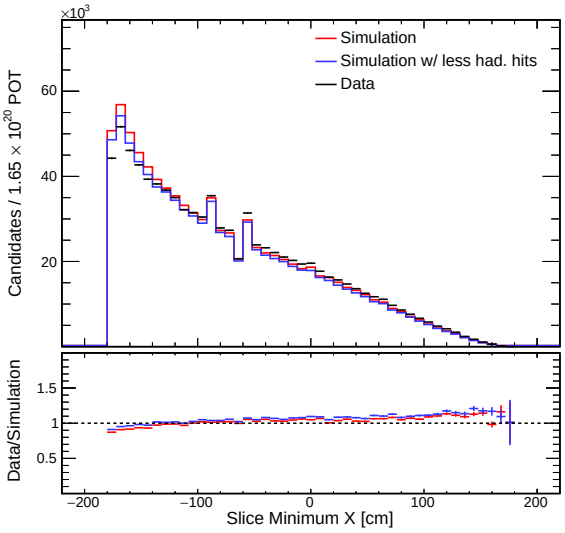

Figure C.2: Minimum position in the x direction of any hits in a contained slice.

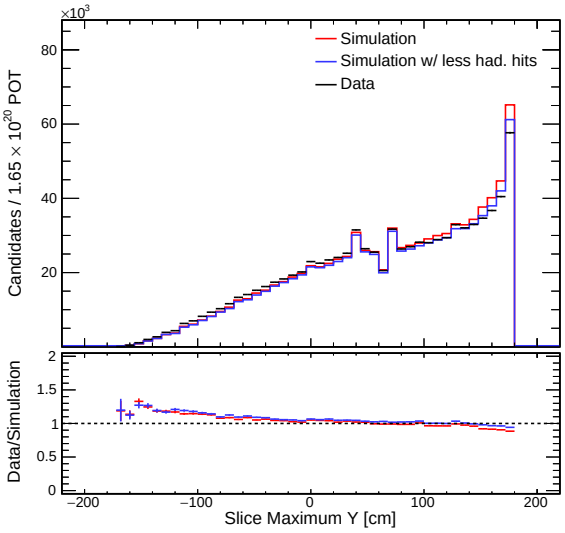

Figure C.3: Maximum position in the y direction of any hits in a contained slice.

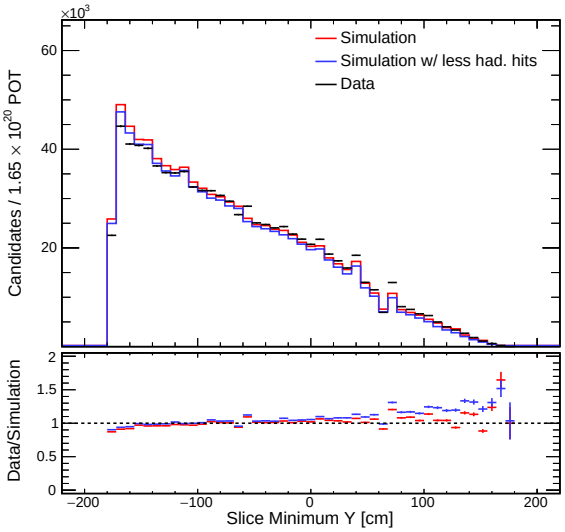

Figure C.4: Minimum position in the y direction of any hits in a contained slice.

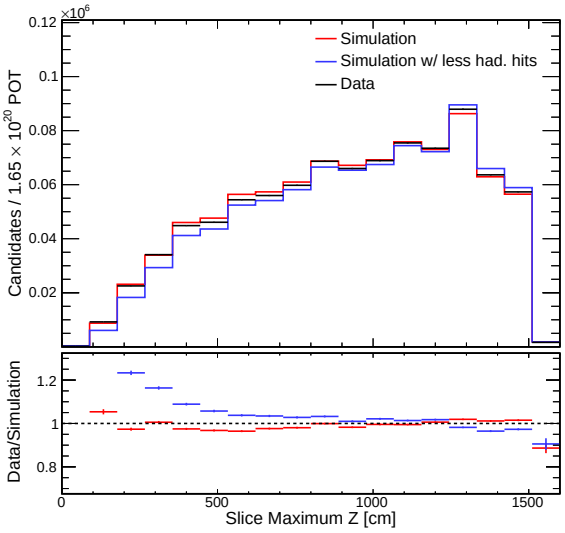

Figure C.5: Maximum position in the z direction of any hits in a contained slice.

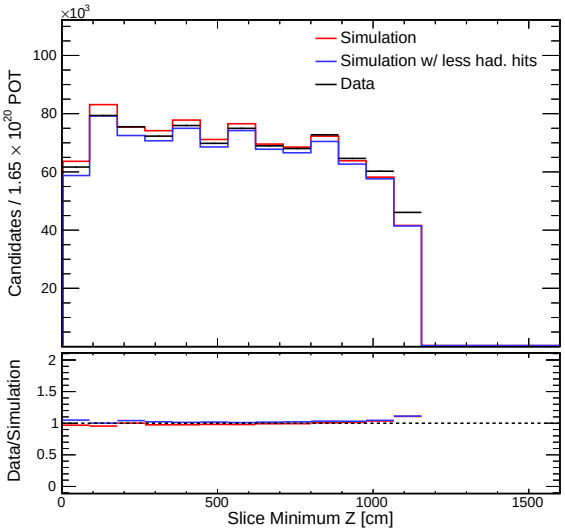

Figure C.6: Minimum position in the z direction of any hits in a contained slice.

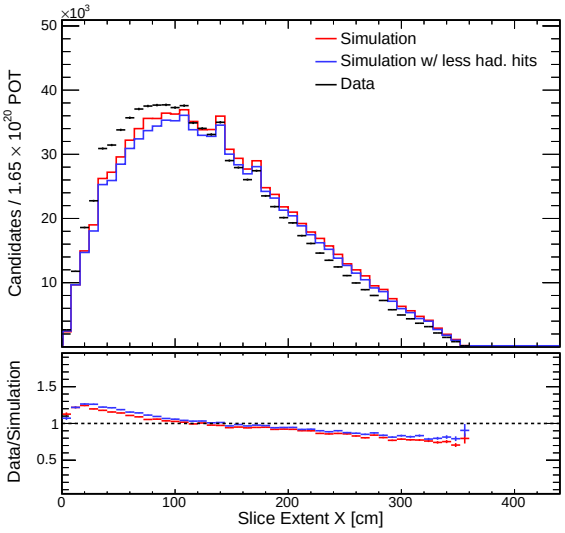

Figure C.7: Extent of hits of in a slice in the x direction in contained slices.

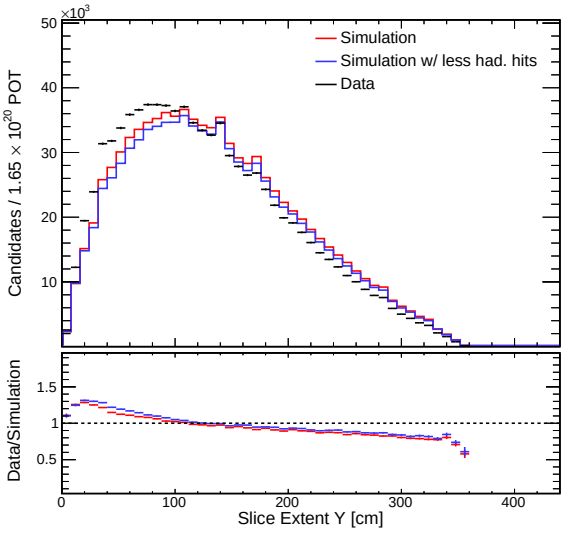

Figure C.8: Extent of hits of in a slice in the y direction in contained slices.

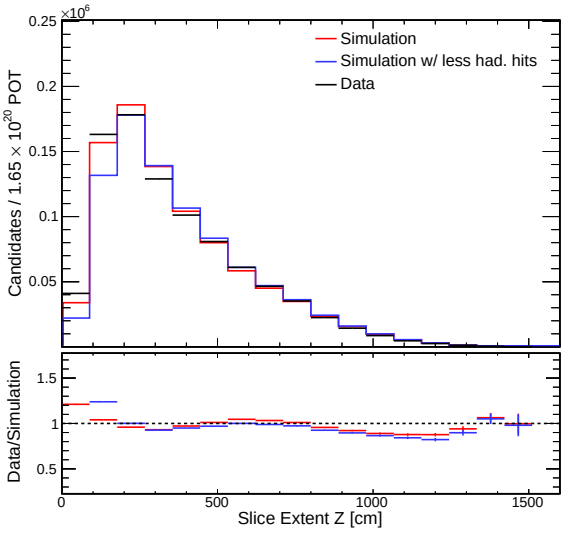

Figure C.9: Extent of hits of in a slice in the z direction in contained slices.

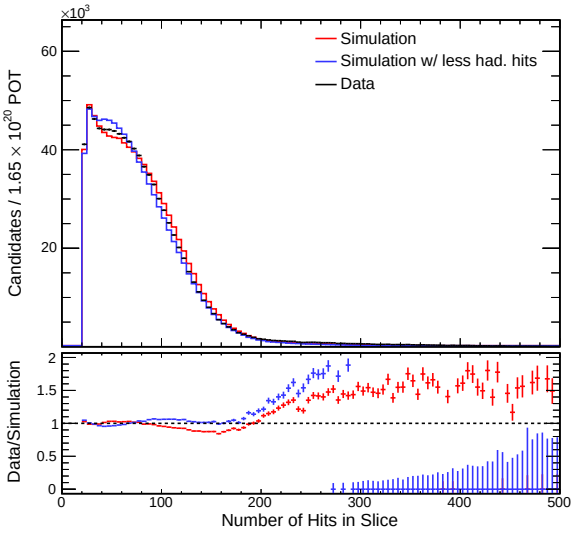

Figure C.10: Number of hits in contained slices.

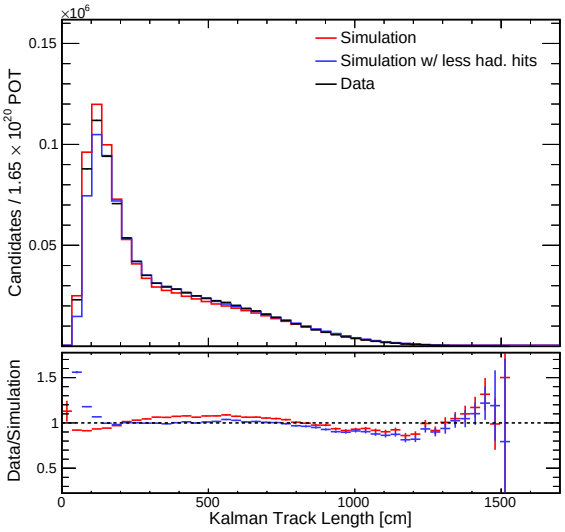

Figure C.11: Length of the most muon like track in contained slices.

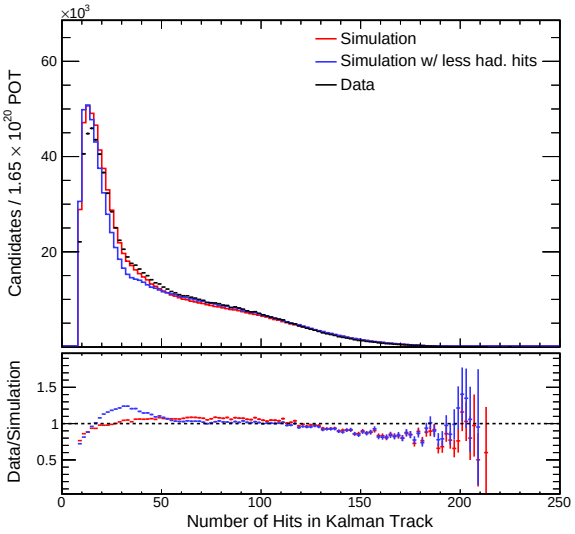

Figure C.12: Number of hits in the most muon like track in contained slices.

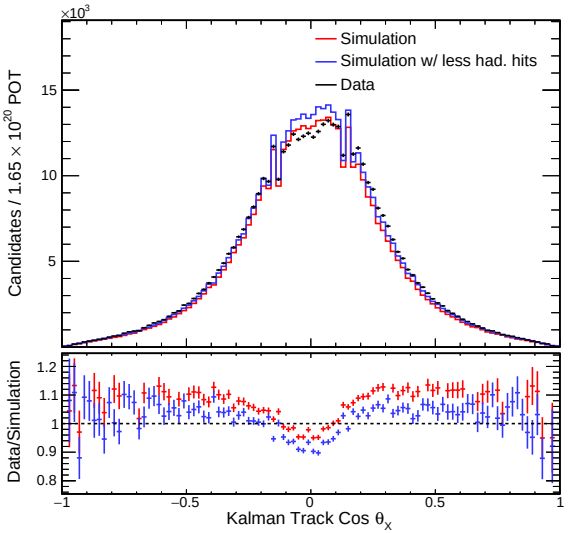

Figure C.13: Track direction with respect to the x direction in the most muon like track in contained slices.

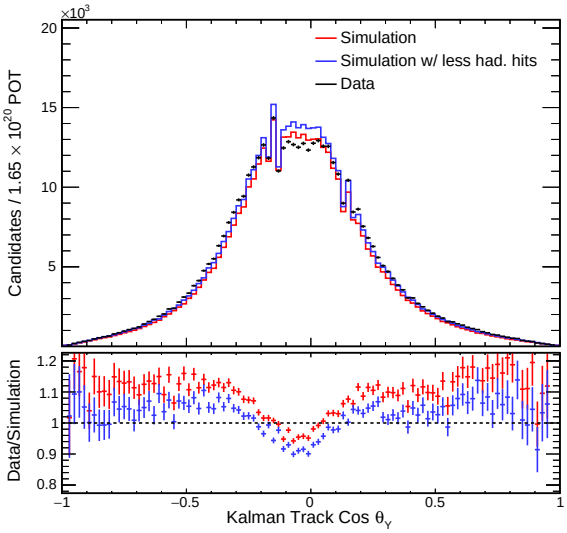

Figure C.14: Track direction with respect to the y direction in the most muon like track in contained slices.

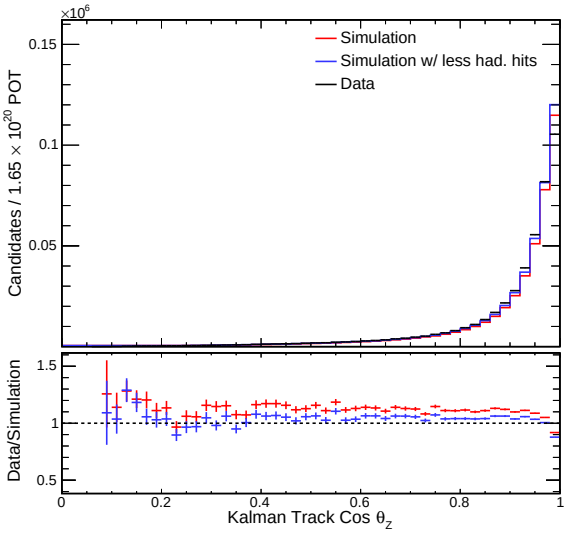

Figure C.15: Track direction with respect to the z direction in the most muon like track in contained slices.

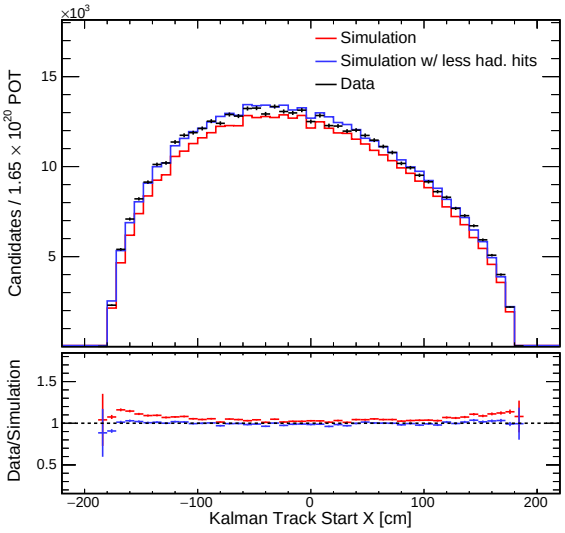

Figure C.16: Track start x position in the most muon like track in contained slices.

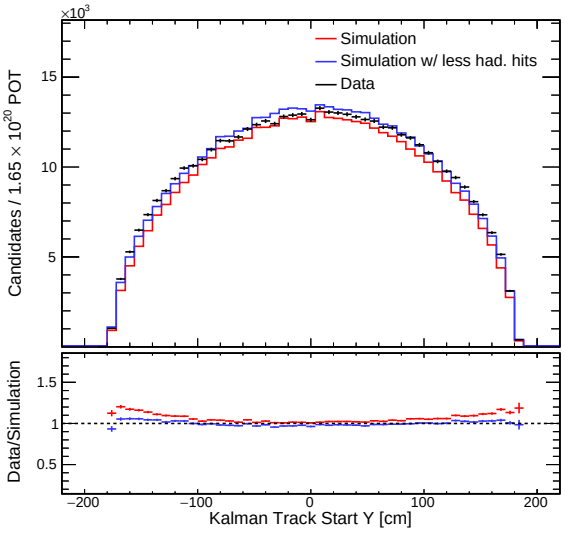

Figure C.17: Track start y position in the most muon like track in contained slices.

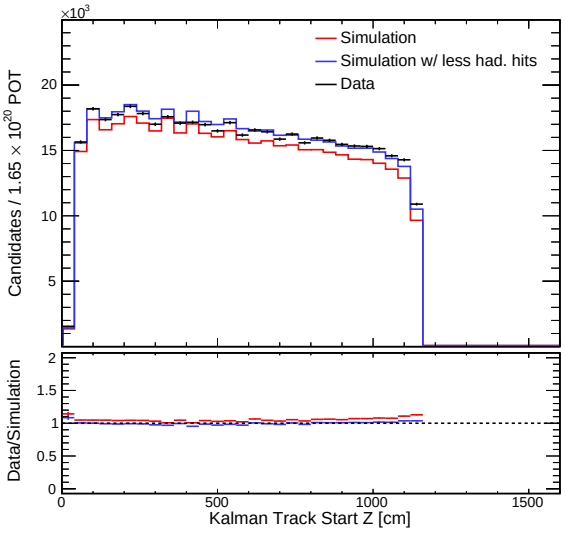

Figure C.18: Track start z position in the most muon like track in contained slices.

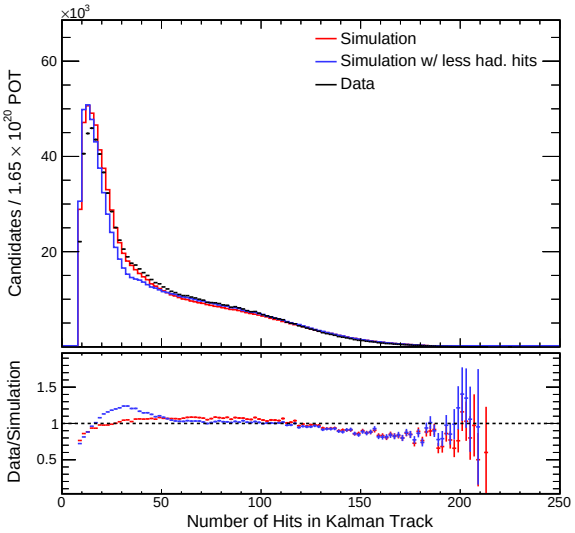

Figure C.19: Number of hits in the most muon like track in contained slices.

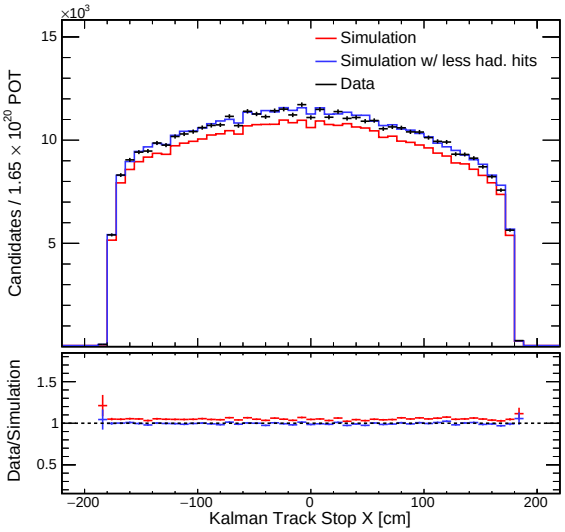

Figure C.20: Track end x position in the most muon like track in contained slices.

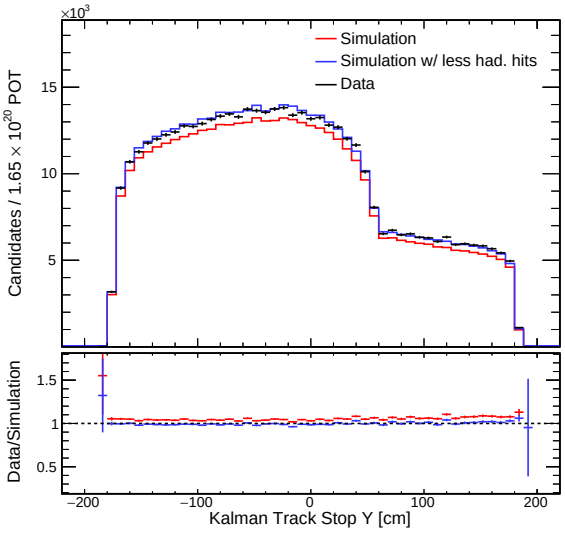

Figure C.21: Track end y position in the most muon like track in contained slices.

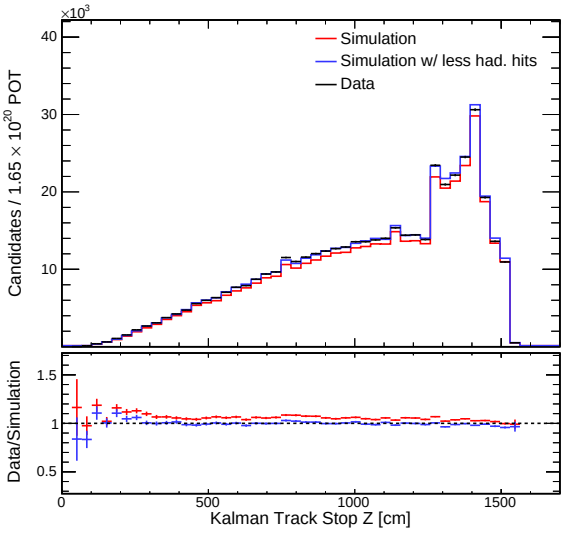

Figure C.22: Track end z position in the most muon like track in contained slices.

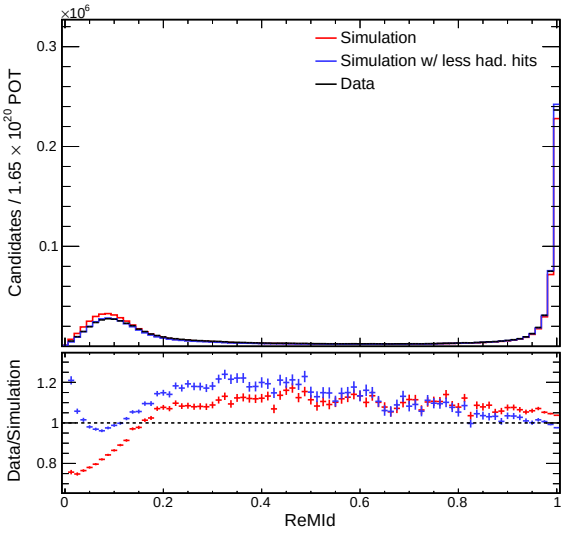

Figure C.23: ReMId distribution in contained slices.

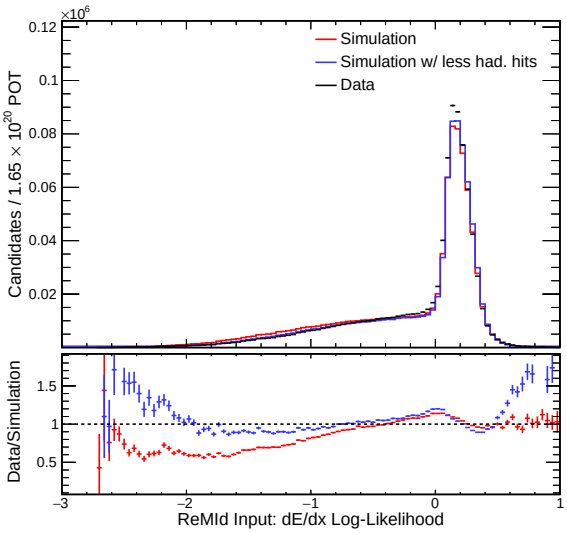

Figure C.24: ReMId $\frac{dE}{dx}$ LL distribution in contained slices.

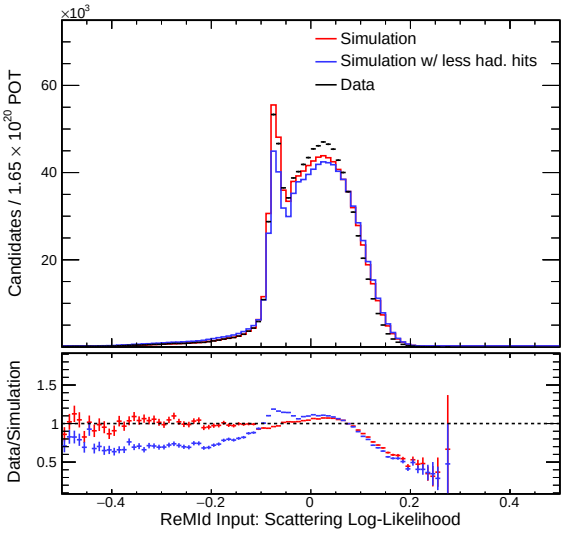

Figure C.25: ReMId scattering LL distribution in contained slices.

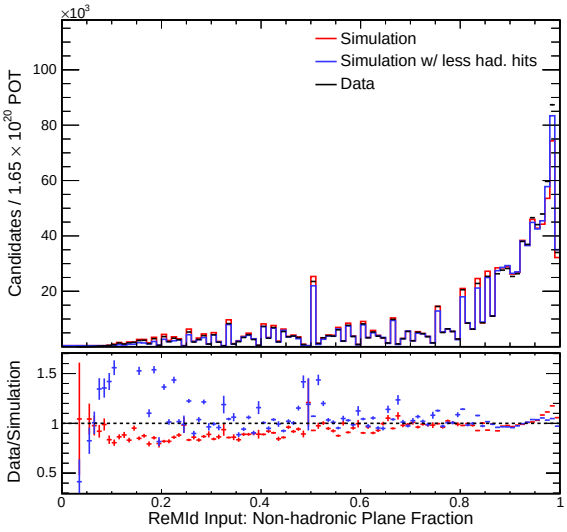

Figure C.26: ReMId non-hadronic plane fraction distribution in contained slices.

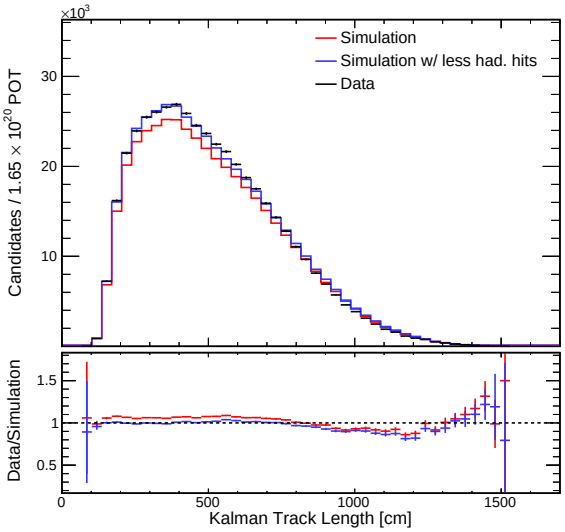

Figure C.27: Track length of muon track in contained slices passing ν_μ CC selection.

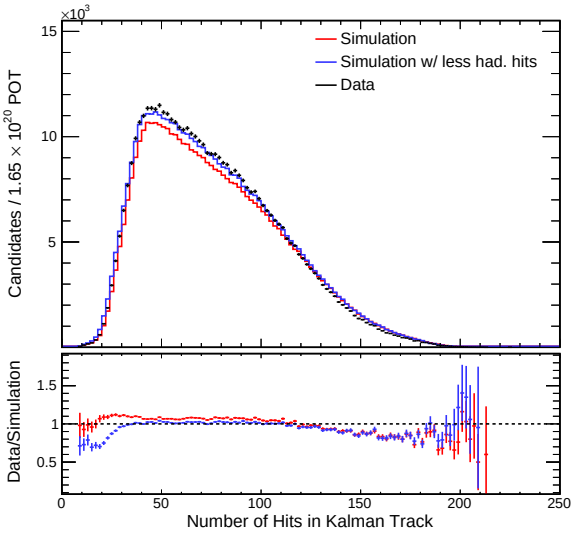

Figure C.28: Number of hits in the muon track in contained slices passing ν_μ CC selection.

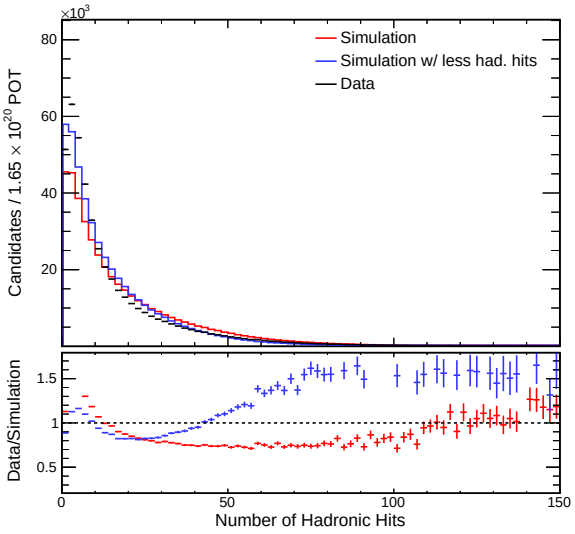

Figure C.29: Number of hadronic hits in contained slices passing ν_μ CC selection.

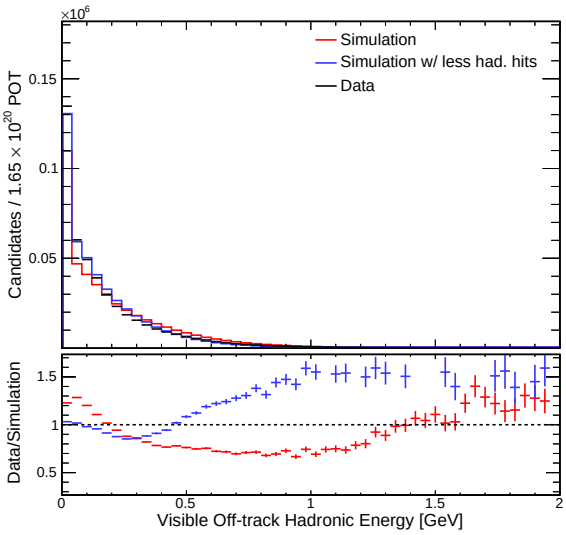

Figure C.30: Hadronic energy not overlapping with the muon track in contained slices passing ν_μ CC selection.

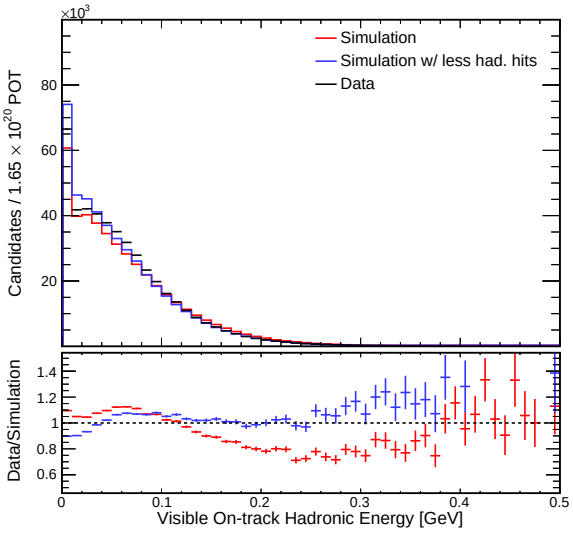

Figure C.31: Hadronic energy overlapping with the muon track in contained slices passing ν_μ CC selection.

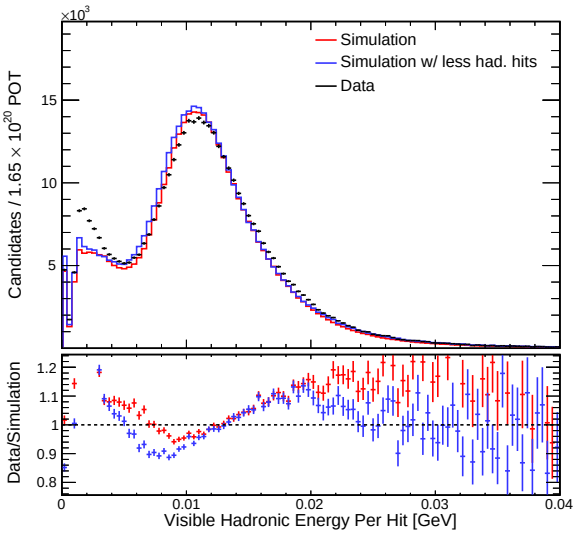

Figure C.32: Average visible hadronic energy per hadronic hit in contained slices passing ν_μ CC selection.

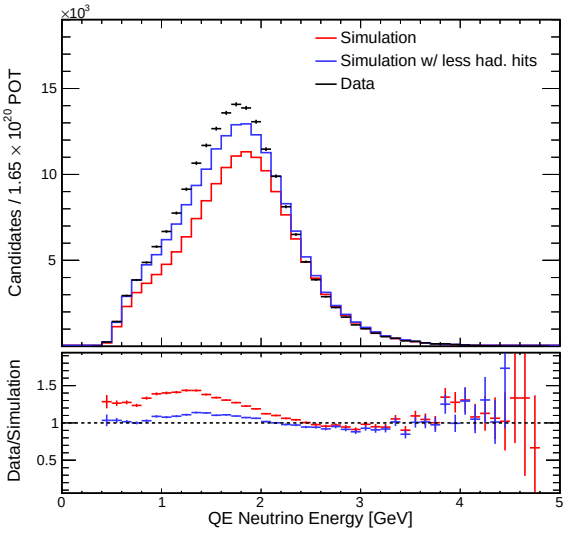

Figure C.33: Energy spectrum of QE selected events.

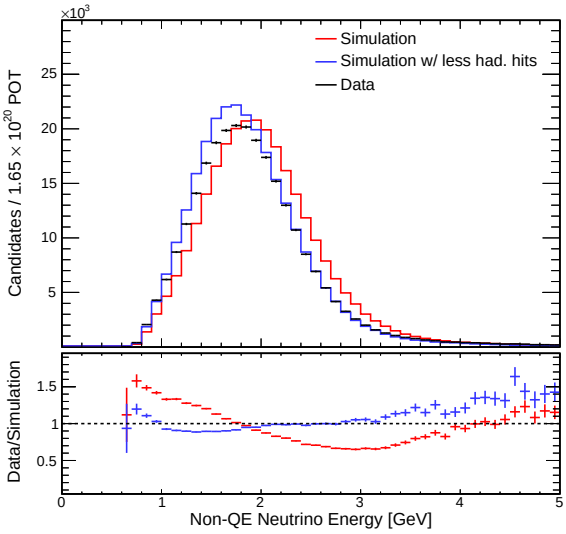

Figure C.34: Energy spectrum of Non-QE selected events.

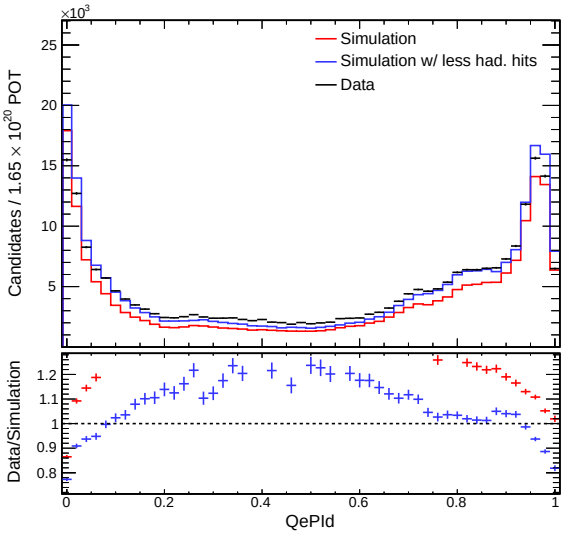

Figure C.35: QePID distribution in contained slices passing ν_μ CC selection with one reconstructed track.

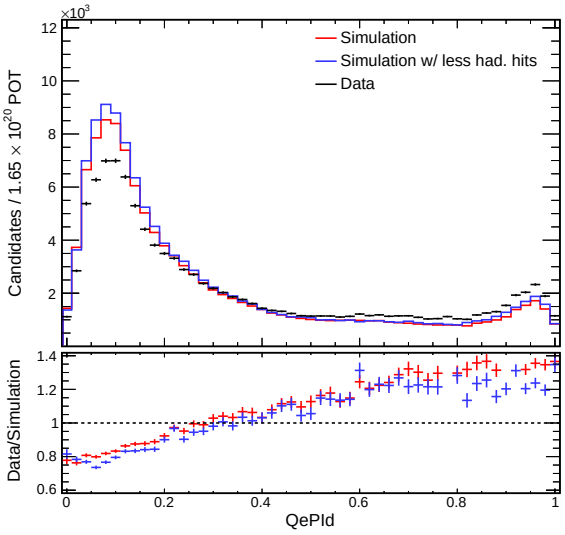

Figure C.36: QePID distribution in contained slices passing ν_μ CC selection with two reconstructed track.

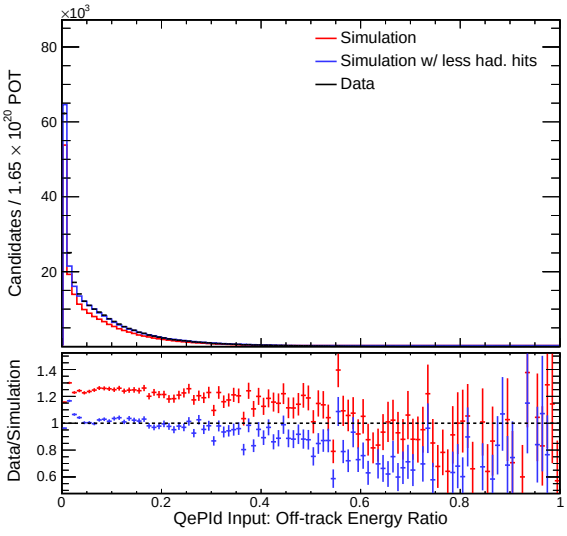

Figure C.37: Off-track energy ratio distribution in contained slices passing ν_μ CC selection with one reconstructed track.

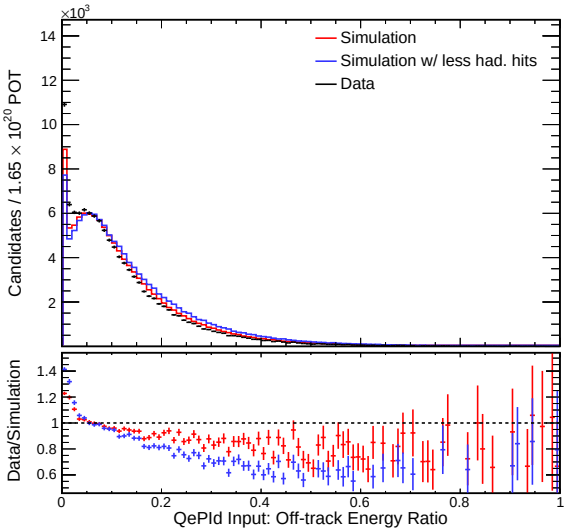

Figure C.38: Off-track energy ratio distribution in contained slices passing ν_μ CC selection with two reconstructed track.

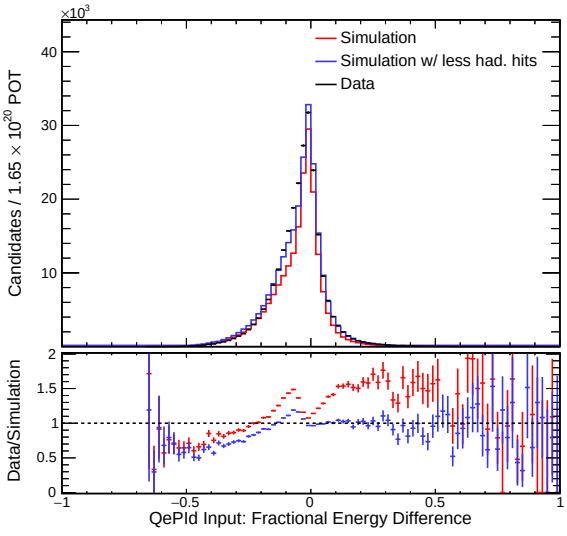

Figure C.39: Fractional energy difference distribution in contained slices passing ν_μ CC selection with one reconstructed track.

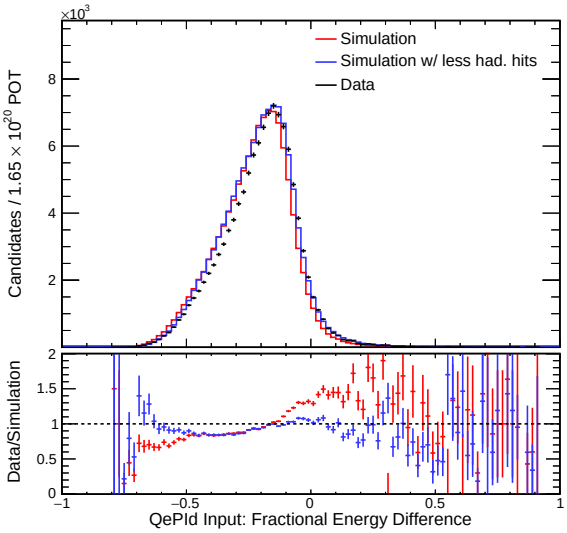

Figure C.40: Fractional energy difference distribution in contained slices passing ν_μ CC selection with two reconstructed track.

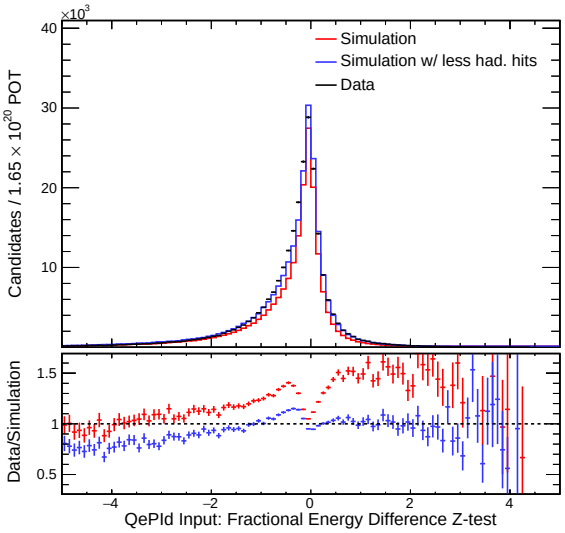

Figure C.41: Fractional energy difference z-test distribution in contained slices passing ν_μ CC selection with one reconstructed track.

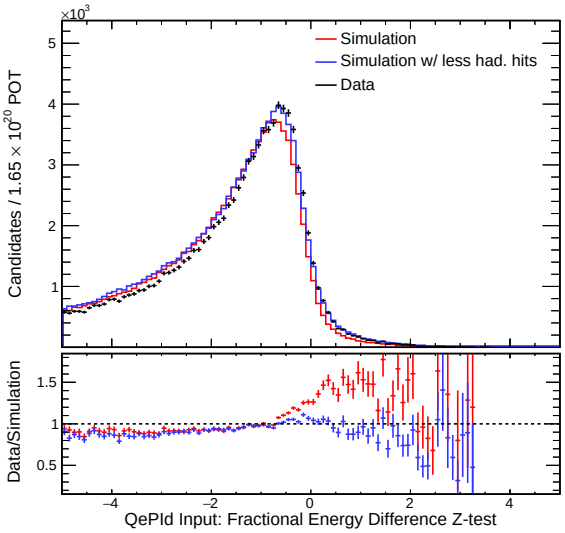

Figure C.42: Fractional energy difference z-test distribution in contained slices passing ν_μ CC selection with two reconstructed track.

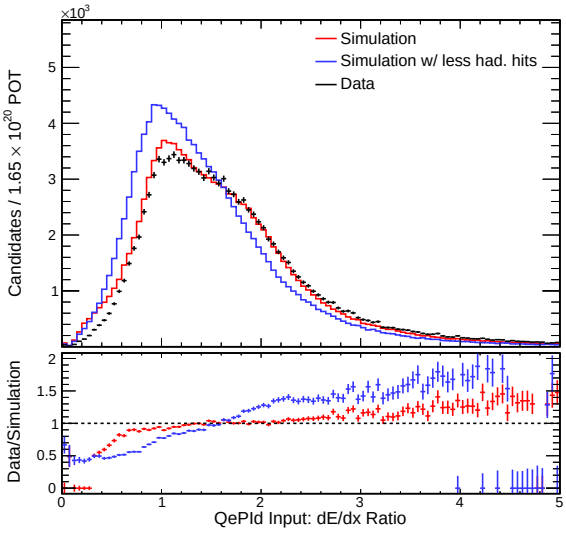

Figure C.43: $\frac{dE}{dx}$ ratio distribution in contained slices passing ν_μ CC selection with two reconstructed track.